UNIVERSITY OF LIVERPOOL

Density compensated small-field dosimeters – Evaluation in photon beams

Thesis submitted in accordance with the requirements of the University of Liverpool for the degree of Doctor in Philosophy

by Georgios Georgiou

April 2019

Abstract

Density compensated small-field dosimeters – Evaluation in photon beams

by Georgios Georgiou

Nowadays small photon fields are widely used in the delivery of advanced radiotherapy techniques to cancer patients. Accurate calculation of the radiation dose received by patients is critical to ensure effective radiotherapy treatments, while limiting as much as possible undesired complications due to over-irradiation of healthy tissue. Despite the upsurge in the use of small fields over the last decades, small-field dosimetry still remains a highly challenging task, especially in the absence of an ideal commercially available small-field dosimeter.

Silicon diodes are now considered suitable detectors for small-field dosimetry mainly because of their small sensitive volume. However, these dosimeters are made of materials with densities and atomic compositions different from those of water, causing them to over-respond when measuring dose in small fields, and thus departing from an ideal water-equivalent detector. Although the issues have been attributed to density, there is still some ongoing debate about the mechanism, but regardless of the mechanism, inclusion of air-gaps has been shown to change detector response in small fields. This thesis examines in detail the consequences of deliberately introducing thin air-gaps above the sensitive silicon, trying to identify the optimum air-gap thickness, and how well detectors with air-gaps and/or modified density/atomic composition respond in a wide range of small-field situations. Two different sets of silicon diodes, the PTW type 60017 and 60023 detectors, have been characterised at 6 and 15 MV, and their response has been both experimentally and computationally evaluated at different depths in water and for various positions off-axis and with the dosimeters oriented at a range of angles relative to the beam axis.

The validity of the (air-gap based) density compensation method is confirmed at both 6 and 15 MV, and at 5 and 15 cm deep. The inclusion of small air-gaps above the sensitive silicon substantially improves detector response, while very slightly affects the location of the dosimeter's effective point of measurement. Other (non-water equivalent) non-sensitive materials, which substantially affect detector response in small fields, need to be limited as much as possible and their amounts to be carefully controlled to avoid unexpected design issues.

The improved PTW type 60023 diodes perform substantially better than the type 60017 detectors with both the no air-gap and 0.6 mm air-gap 60023 diodes performing well as small-field dosimeters. More specifically, experimental and Monte-Carlo results show the no air-gap 60023 diode responding correctly to within ~ 2% on-axis in a 0.5x0.5 cm^2 field, whereas the Original PTW 60017 detector over-responds by about 9%. The no air-gap 60023 diode behaves as a slightly over-dense detector, while the 0.6 mm air-gap added in the PTW 60023 diode appears to be an over-correction. In conclusion, the no air-gap type 60023 PTW diode is a robust small-field dosimeter, which performs best on- and off-axis at 6 and 15 MV, at both 5 and 15 cm deep and continues to respond accurately even in a 0.3x0.3 cm^2 field, and when tilted at various angles relative to the beam axis. Both MC and experimental results suggest that a PTW 60023 diode with a small air-gap of approximately 0.3 mm thickness should perform optimally.

Acknowledgements

I would like to express my deepest gratitude to my primary supervisor at Clatterbridge Cancer Centre, Dr John Fenwick, for the continuous guidance, motivation and support throughout this work and for his patience during difficult periods of the project. I would also like to thank very much my other two supervisors, Dr Carl Rowbottom for valuable feedback and stimulating discussions throughout this work, and Prof. Tim Greenshaw for his help.

I would like to thank very much PTW, and especially Dr Jan Würfel for providing me all the necessary information for the design of PTW detectors. Many thanks also go to Dr Tracy Underwood and to my friend Dr Sudhir Kumar for their valuable help and advice regarding Monte-Carlo simulations. I would also like to thank Prof. Alan Nahum and Dr Colin Baker for giving me the opportunity to be part of Clatterbridge Cancer Centre, and to all people of the physics department at CCC who made my life as a PhD student easier. I would also like to thank very much my PhD examiners, Prof. Philip Mayles and Prof. Philip Evans, for their very valuable comments/suggestions/corrections contributing to the improvement of my final PhD thesis and for the very pleasant viva experience.

I wish to thank very much and express my very great appreciation to my Father and my Mother for their support, for believing in me, and for their invaluable advice over the years. Many thanks also to all my friends and family for their help and patience.

Finally, special thanks to Eleana for her continuous support, encouragement and endless patience. Thank you so much for everything, but especially for making my life more beautiful!

List of Abbreviations

AAPM	**A**merican **A**ssociation of **P**hysicists in **M**edicine
B-G	**B**ragg-**G**ray
CPE	**C**harged **P**article **E**quilibrium
CSDA	**C**ontinuous **S**lowing **D**own **A**pproximation
CT	**C**omputed **T**omography
EPOM	**E**ffective **P**oint **O**f **M**easurement
FWHM	**F**ull **W**idth **H**alf **M**aximum
IAEA	**I**nternational **A**tomic **E**nergy **A**gency
ICRU	**I**nternational **C**ommission on **R**adiation **U**nits and **M**easurements
IMRT	**I**ntensity **M**odulated **R**adiation **T**herapy
IPEM	**I**nstitute of **P**hysics and **E**ngineering in **M**edicine
LCPE	**L**ateral **C**harged **P**article **E**quilibrium
MC	**M**onte **C**arlo
MLC	**M**ulti **L**eaf **C**ollimator
MSR	**M**achine **S**pecific **R**eference
MU	**M**onitor **U**nit
NTCP	**N**ormal **T**issue **C**omplication **P**robability
OF	**O**utput **F**actor
PDD	**P**ercentage **D**epth **D**ose
PMT	**P**hoto **M**ultiplier **T**ube
SA	**S**pencer-**A**ttix
SBRT	**S**tereotactic **B**ody **R**adiation **T**herapy
SRS	**S**tereotactic **R**adio **S**urgery
SRT	**S**tereotactic **R**adio **T**herapy
SSD	**S**ource to **S**urface **D**istance
TCP	**T**umour **C**ontrol **P**robability
VMAT	**V**olumetric **M**odulated **A**rc **T**herapy

Contents

Chapter 1

Introduction

Cancer is a major cause of mortality worldwide. In 2016, more than one in four deaths (31%) were attributed to cancer in the U.K. (Cancer Research UK 2018, Office for National Statistics UK 2018). Radiotherapy is an effective cancer treatment method either by itself or in conjunction with other forms of treatment, such as chemotherapy or surgery. Radiotherapy uses high energy (ionising) radiation, i.e. photons, or particles (electrons or protons) to shrink the tumour, or even eliminate it, by damaging the DNA of cancer cells. The basic principle is to deliver sufficient dose to the cancerous tumour while at the same time adequately sparing adjacent normal tissues (Williams and Thwaites 2000). Radiation dosimetry focuses on the quantitative determination of the energy imparted to matter through interactions with ionizing radiation and the subsequent dose absorbed (Attix 1986a). The most important quantity in medical physics, due to its clear connection with macroscopic biological effects, is absorbed dose. According to the International Commission on Radiation Units and Measurements (ICRU 1980, 1998), absorbed dose, usually termed simply as dose, is defined as the mean energy imparted to matter per unit mass at a point. The unit of absorbed dose is the gray (Gy) which is equal to 1 Joule per kilogram (J/kg).

$$D = \frac{d\bar{\varepsilon}}{dm} \tag{1.1}$$

Accuracy in the measurement of the radiation dose delivered to the patient is critical to ensure the desired treatment outcome in radiotherapy. Due to the steep sigmoidal shape of the dose-response curves (Nahum 2007) for both tumour control probability (TCP) and normal tissue complication probability (NTCP), even small dosimetric errors can

lead to serious underdosage of the tumour, resulting in a less effective treatment in terms of failure to control/eliminate the tumour, or to significant undesired complications due to the over-irradiation of healthy tissue and vital organs of the human body (Boyer and Schultheiss 1988). The uncertainty on the measured dose should preferably be within 1-2%, with published recommendations advising to maintain dosimetric errors at the 2% level (IAEA 2016). This is important, so when uncertainties coming from dose-calculation accuracy are added in quadrature along with errors deriving from the patient positioning, target and organ definition, and the treatment machine mechanical tolerance, the dose delivered to the primary target is within ± 5% of the prescribed dose (Clark *et al* 2015, IAEA 2016).

Over the past several decades there has been significant progress in the field of radiotherapy thanks to the rapid growth of medical linear accelerator (linac) and imaging technologies, leading to reductions in normal tissue toxicity rates (Stark 2007). While radiotherapy develops and new more sophisticated techniques are introduced and used in medical centres around the world, it is equally important to ensure that the associated dosimetric challenges are successfully addressed and accurate determination of the dose delivered is achieved using suitable radiation detectors.

1.1 Small radiation fields widely used in modern radiotherapy

The implementation of small radiation fields was a great step towards the improvement of current radiation therapy, allowing radiation dose to be more tightly confined on tumours, making the successful treatment of smaller tumours diagnosed at an earlier stage of the disease feasible (Underwood 2013). Today, small fields are encountered in the delivery of two specialised forms of radiation therapy which can be broadly categorised into stereotactic therapies (SRS/SRT) and intensity-modulated radiotherapy (IMRT). These methods have been systematically used since 2000 (actually SRS since the early 1990s) and with more than two decades of development they have now become well-established techniques (Khan 2010a, 2010b, Lo *et al* 2012).

1.1.1 Small fields used in stereotactic treatments (SRS/SBRT)

Stereotactic treatments were initially performed to treat intracranial lesions, with the origin of the technique dating back to 1951 (Lo *et al* 2012). Nowadays, stereotaxy has evolved into a specialised form of radiotherapy that uses small radiation fields (sometimes on the order of a few millimeters, e.g. Gamma Knife, Cyberknife) precisely targeted at small tumours. The term stereotactic radiosurgery (SRS) is used to describe treatments delivered in a single-fraction (contrary to the conventionally fractionated radiotherapy), a non-invasive radiation therapy method used for treating small brain tumours with an extremely high degree of accuracy, sparing as much as possible the healthy parts of the brain (Solberg *et al* 2012). When multiple dose fractions are delivered the procedure is called stereotactic radiotherapy (SRT) (Khan 2010b). Technological advancements regarding imaging of the patient and image-guidance tools incorporated in radiotherapy (Stark 2007) helped to overcome problems related to inherent motion (e.g. respiratory movement) during treatment and allowed several groups after 1990 (Hamilton *et al* 1995, Uematsu *et al* 1998, Timmerman and Kavanagh 2005) to attempt the delivery of stereotactic radiotherapy to extracranial sites, as well as the brain. Stereotactic body radiation therapy (SBRT) is now widespread, utilising small fields to treat various organ sites such as the liver and the lung (AAPM 2010). SBRT is usually delivered in 1-5 fractions (hypofractionation), but in some cases up to 10 fractions may be used (Lo *et al* 2012).

1.1.2 Small fields in the implementation of IMRT

In the early 1990s the term intensity-modulated radiotherapy (IMRT) was proposed to describe the process of spatially varying the intensities of radiation beams in order to maintain uniform composite tumour dose distributions while better sparing normal tissues (Khan 2010a). IMRT was introduced to address a basic weakness of conventionally delivered external photon beam radiotherapy, namely its relative inability to restrict the region of high doses delivered to the tumour-bearing tissue. The main idea of IMRT is to treat the patient from several different directions combining many

radiation beams of non-uniform fluence (Khan 2010a). This is achieved by subdividing each beam into multiple beamlets, using small highly absorbing tungsten multi-leaf collimators (MLCs), and varying their individual intensities. These beamlets can sometimes be even less than 1 cm^2 depending on the complexity of the target (shape, size and position of the tumour). IMRT is now routinely used for static-gantry treatments or more often arc-based techniques like volumetric modulated arc therapy (VMAT) (Yu 1995, Khan 2010a).

1.2 Small-field dosimetry – a challenging task

As previously mentioned, accurate calculation of the dose received by cancer patients is crucial for successful radiotherapy treatments. The traditional radiation fields, dominating radiotherapy before 1999, range from 4x4 cm^2 to 40x40 cm^2 and dosimetry in these broad fields is based on widely adopted codes of practice (CoPs), like the AAPM TG-51 (1999) and the IAEA TRS-398 (2000), both recommending 10 cm as the in-water depth of the reference conditions, and the IPSM (1990), in which the reference depth is chosen to be 5 cm (like in the work presented in this thesis). In contrast, dosimetry within small radiotherapy fields, reduced down to a sub-centimeter range, is a challenging task generally known as "small-field dosimetry" and subject of much scientific research. The choice of an appropriate detector for small-field dosimetry is also difficult and quite confusing due to the large variety of radiation detectors commercially available and the lack of proper guidelines, as stated by Das *et al* (2008). Detectors commonly used in conventional radiotherapy fields, like the "Farmer" ionisation chamber, are not a reasonable choice for small-field dosimetry since their sensitive volume – with dimensions larger than 1 cm – can be wider than the whole field itself (volume averaging effect, described later in section 1.2.2).

By considering the upsurge in the use of small static photon beams over the last years it is easy to understand the importance of small-field dosimetry in radiotherapy. The growing interest in the development of dosimetry recommendations for small photon fields is shown by the fact that the International Atomic Energy Agency (IAEA) in

collaboration with the American Association of Physicists in Medicine (AAPM) recently published an extensive Code of Practice (CoP) (IAEA 2017) dedicated entirely to the dosimetry of small static fields used in modern radiotherapy techniques.

1.2.1 Defining a small field and beam-related problems in dosimetry

Historically, treatment fields smaller than 3x3 cm^2 have been considered small in radiotherapy (Das *et al* 2008). A much more scientific description, the result of a large number of publications on the use of small fields in radiotherapy, has emerged over the last years; we can generally define a small photon radiation field as a field with dimensions comparable to (or smaller than) the lateral range of the charged particles (electrons) generated initially by photon interactions, (figure 1.1) which contribute to the dose absorbed by a medium (Alfonso *et al* 2008, IPEM 2010). According to several publications (Das *et al* 2008, IPEM 2010, Andreo 2017) and the most recent attempt for a consensus definition in the IAEA CoP (2017), at least one of the following conditions must be true for a megavoltage (MV) photon field to be considered small:

i) There is loss of lateral charged particle equilibrium (LCPE) on the beam central axis, a phenomenon clearly linked with the range of secondary electrons.

ii) Partial occlusion of the primary photon source occurs: the collimating device shields part of the finite photon beam as viewed from the point of the detector.

iii) The size of the detector used is comparable to the dimensions of the photon field.

As stated in the IAEA CoP (2017), the first two conditions are related to the treatment beam, whereas the third one clearly depends on the size of the active volume of the detector chosen to determine the dose in a specific field.

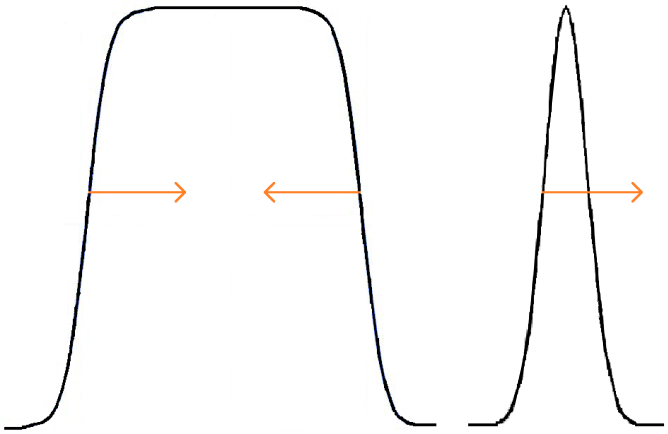

Figure 1.1: The size of a wide radiation field is larger than the range of secondary particles (left), thus lateral charged particle equilibrium (LCPE) is established almost throughout the entire field. In a narrow field (right) secondary electrons have enough kinetic energy to travel for a distance greater than the dimension of the field resulting in the breakdown of LCPE even on the central axis.

Despite the fairly straightforward definition of absorbed dose (Eq. 1.1), it would be naive to assume that the experimental determination of dose is equally easy, especially in small radiation fields. The physics of small MV photon fields differs greatly from the wider ones, mostly due to the loss of LCPE, meaning that the charged particles carrying a certain amount of energy out from a region of interest are not replaced by identical particles carrying the same amount of energy into the same region.

At this point it is worth emphasizing that the deposition of energy in matter by indirectly ionising radiation, such as a photon beam, is a two-step process (Attix 1986a). First, uncharged particles (i.e. photons, neutrons) interact with matter passing their energy to charged particles, which then impart that energy to matter through collisional or radiative (Coulomb-force) interactions. The electrons produced from a photon beam travel for a considerable distance before completely depositing their energy to matter via the generation of low energy secondary electrons and subsequent interactions. This distance can be larger than the dimensions of the radiation field, depending on the absorbing medium and the beam's nominal energy[1], invalidating the assumption of electronic equilibrium on the central axis. In wider fields, with dimensions considerably

[1] As a typical example consider a 1 MeV electron. Such 1 MeV electron, typical of those generated by Compton interactions of 2 MeV photons, the typical primary energy of a photon in a nominal 6 MV beam, can travel for approximately 0.5 cm in water (CSDA range) (Physics NIST 2018).

greater than the mean free path of secondary electrons (figure 1.1), we can say that lateral electronic equilibrium does exist in a specific volume on or close to the beam central axis, as the inward electron fluence is equal to the outward one and non-equilibrium conditions emerge only close to the field edge.

Both phenomena mentioned above, the loss of LCPE and occlusion of the primary photon source, strongly influence small-field dosimetry leading to a lower beam output as the field size decreases. The problem is exacerbated by increasing the energy of the photon beam or by decreasing the density of the absorbing medium (in both cases the range of the secondary electrons increases) (IAEA 2017).

1.2.2 Experimental considerations and detector-related problems in small-field dosimetry

An important experimental difficulty not encountered in wider fields is the geometric precision of the positioning of a detector in a small field. In the absence of a "flat" uniform dose region in the center of the field the precise positioning of the detector becomes critical to ensure the right on-axis dose determination. Otherwise, even a small positional error of the order of fractions of a millimeter can be significant because the maximum dose region is no longer included and that could potentially bias the value of measured dose (Li *et al* 2004).

As aptly stated by Das *et al* (2008), the most important problem associated with the small-field dosimetry is "the very presence of the detector itself". The existence of the detector in a small radiation field creates problems due to (i) the size of the sensitive volume which may be larger than the uniform region of the beam and (ii) the inevitable perturbation of the charged particle fluence in the absorbing medium (e.g. in water).

The size of the dosimeter used plays a key role for the measured dose distribution in a small field. Generally, the signal produced by a radiation detector is proportional to the absorbed dose (and thus charged particle fluence) averaged over its active volume (Nahum 2007). In a broad field, comprising a sufficiently large region of uniform dose,

the entire volume of the detector lies within the high-dose region meaning that averaging the dose over the active region has a minimal impact. On the other hand, in a narrow field with a peaked dose profile the detector volume is not covered by the high-dose region; hence, averaging may cause a reduction in the detector's reading on-axis compared to the true dose (IAEA 2017). This is known as "volume averaging effect" and its significant influence on dosimetry should not be overlooked because it can be responsible for serious clinical issues (Derreumaux *et al* 2008).

When any detector is introduced in a uniform medium to measure the absorbed dose at a specific point, it potentially perturbs the fluence of the charged particles, and thus the Bragg-Gray condition in not met (Attix 1986b) (as described later in 1.2.3) and complicated correction schemes are required to account for the effect on detector signal of the fluence perturbations (Bouchard *et al* 2009, Fenwick *et al* 2013, Fenwick *et al* 2018a). The perturbation of charged particle fluence occurs in small non-equilibrium fields because the detector materials have in general different physical densities than the absorbing medium, whereas in wide fields – that LCPE holds – the difference in the densities between the detector materials and the absorbing medium does not substantially affect the measured dose. The breakdown of LCPE and the non-uniform dose distribution across a small field make the fluence perturbations even larger and difficult to predict (IAEA 2017).

1.2.3 Classical dosimetry under broad field conditions – A brief synopsis of the Cavity Theories

In radiotherapy we are very often interested in measuring the dose at a specific point in a uniform medium of interest using a radiation detector (usually the medium is water because it is a reasonable radiological approximation of many human tissues, like muscle and fat)[2], and then the treatment planning software calculates the dose-to-biological-tissues. Therefore, it is important to get a detector that measures dose-to-water accurately, within the 2% tolerance levels. However, detectors do not measure the

[2] From now on we will always assume water as the absorbing medium.

dose to the medium directly (Nahum 2007, 2009) and for this reason a dosimetry theory, known as "cavity theory", is necessary to establish a relationship (Eq. 1.2) between the detector reading and the value of dose absorbed by water in a beam of quality Q.

The name cavity theory is used because the detector's sensitive volume can be thought of as a cavity introduced at a specific point in the water phantom (Nahum 2007), as illustrated in figure 1.2.

$$f_Q = \left(\frac{D_{water}}{D_{detector}}\right)_Q \tag{1.2}$$

The appropriate cavity theory to use for the determination of the factor f_Q depends on the size of the cavity (i.e. the sensitive volume of the detector). Cavities are considered either large or small in relation to the range of the secondary electrons generated by the indirectly ionising radiation. Detectors falling into the first category are known as "large photon detectors", whereas the small ones are usually described as "Bragg-Gray cavities" (Nahum, 2007). In these two extreme cases the relationship between the doses in the undisturbed water and the detector can be determined by deriving an exact expression for the cavity factor f_Q.

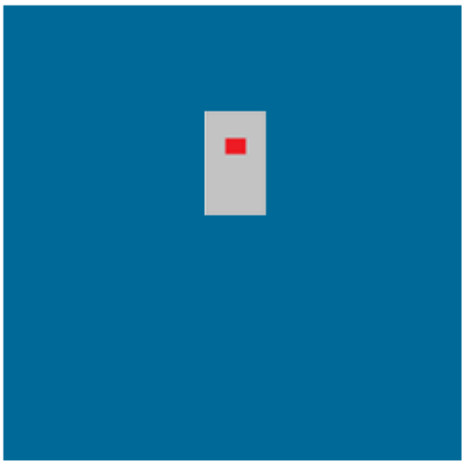

Figure 1.2: The detector is positioned at a specific depth in the water phantom to measure the dose deposited at that point. The detector's sensitive volume (shown in red) is considered as a cavity introduced in the uniform medium, i.e. water; consequently, any non-water equivalent materials of the detector greatly disturb the electron fluence making its response non-ideal.

When the detector's sensitive region is substantially larger than the range of the secondary electrons, charged particle equilibrium (CPE) is established in the cavity volume[3], and the absorbed dose can be calculated as the product of photon energy fluence $(\Psi^{\gamma})_{detector}$ and spectrally-averaged mass-energy-absorption coefficient $(\bar{\mu}_{en}/\rho)_{detector}$ of the sensitive material. Similarly, the dose absorbed by water at the same point and under CPE conditions but in the absence of the detector is given by multiplying the photon energy fluence $(\Psi^{\gamma})_{water}$ and the mass-energy-absorption coefficient of water. Making the key assumption that the detector negligibly affects the existing photon energy fluence in water, so that the two are now same, the ratio of doses and, therefore, the cavity factor in Eq. 1.2 becomes:

$$f_Q = \left(\frac{D_{water}}{D_{detector}}\right)_Q = \frac{(\bar{\mu}_{en}/\rho)_{water}}{(\bar{\mu}_{en}/\rho)_{detector}} \tag{1.3}$$

The bar in Eq. 1.3 is used to demonstrate the averaging over the spectrum of electrons. The last equation is often written in shorthand as the mass-energy-absorption coefficient ratio:

$$f_Q = (\bar{\mu}_{en}/\rho)_{water,detector} \tag{1.4}$$

[3] CPE exists in the cavity volume apart from a small "narrow rind region on either side of the detector wall" (Nahum 2007).

In the second situation, a detector which is small compared to the range of the secondary electrons, the Bragg-Gray (B-G) cavity theory (Bragg 1912, Gray 1929, 1936) can be used to determine the cavity factor f_Q. There is actually only one condition to consider a detector as a B-G cavity and that is (Attix 1986b, Nahum 2007):

> The cavity must be sufficiently small that it does not disturb the existing fluence of the charged particles (including its distribution in energy) in the medium in the absence of the cavity.

In this case the electron fluence is the same whether the cavity is present or not, and the ratio of absorbed dose by water and by the detector's sensitive volume becomes:

$$\frac{D_{water}}{D_{detector}} = \frac{(\bar{S}_{col}/\rho)_{water}}{(\bar{S}_{col}/\rho)_{detector}} \tag{1.5}$$

where $(\bar{S}_{col}/\rho)$ is the spectrally-averaged mass collisional stopping-power of water or the detector's sensitive material. The right part of Eq. 1.5 is known as the (water to detector) mass stopping-power ratio.

Spencer and Attix (1955) proposed an extension of the B-G cavity theory in order to take into account the range of the generated delta rays. The initial B-G theory, which examines losses only under the continuous-slow-down-approximation (CSDA), assumes that all energy lost is deposited locally within the cavity. According to Spencer and Attix (1955) the electron spectrum can be divided into electrons with energies above a cutoff energy Δ which escape the cavity and the ones below Δ; all collisional interactions that result in energy transfers below the value Δ are assumed to deposit their energy locally, i.e. in the cavity. For the calculation of this local energy loss the **restricted** (to losses less than the cutoff **Δ**) mass collisional stopping power is used and replaces the mass collisional stopping power $(\bar{S}_{col}/\rho)$ of the B-G theory as it is in Eq. 1.5. The restricted mass collisional stopping power is denoted as $(\bar{L}_{\Delta}/\rho)$.

The energy deposited by electrons which are generated in the cavity, but with energies below the cutoff Δ, is not considered in the Spencer-Attix cavity theory. For this reason, an additional term, known as the "track-end term", was added by Nahum (1978) to take into account their energy. Under the Spencer-Attix theory and the Nahum extension (shown in brackets below) the ratio of doses in Eq. 1.5 becomes (Nahum 2007):

$$f_Q = \frac{D_{water}}{\overline{D}_{detector}} = \frac{\int_{\Delta}^{E_{max}} \Phi_E^{e,tot} \left(\frac{L_\Delta(E)}{\rho}\right)_{water} dE + \left[\Phi_E^{e,tot}(\Delta)\left(\frac{S_{col}(\Delta)}{\rho}\right)_{water}\Delta\right]}{\int_{\Delta}^{E_{max}} \Phi_E^{e,tot} \left(\frac{L_\Delta(E)}{\rho}\right)_{detector} dE + \left[\Phi_E^{e,tot}(\Delta)\left(\frac{S_{col}(\Delta)}{\rho}\right)_{detector}\Delta\right]} \quad (1.6)$$

The ratio in Eq. 1.6 is known as the "Spencer-Attix-Nahum stopping-power ratio" and the much shorter form $s^{SA}_{wat,det}$ was established later (ICRU 1984) for practical reasons.

Apart from these two extreme scenarios, a detector may also be of an intermediate size. For these intermediate cavities (detectors) a "General Cavity Theory" was proposed by Burlin (1966) to overcome the problem of detectors that cannot be thought either as small (B-G cavities) or as large cavities (photon detectors). A parameter "d" related to the size of the cavity was proposed and the theory can be thought as a weighted average of the mass collisional stopping-power ratio and the mass-energy-absorption coefficient ratio (Attix 1986b):

$$1/f_Q = d \cdot s^{SA}_{det,wat} + (1-d)\left(\frac{\overline{\mu}_{en}}{\rho}\right)_{det,wat} \quad (1.7)$$

Burlin's cavity theory is important for the calculation of doses in geometrically small cavities of high density (i.e. detectors with sensitive volumes made of dense materials compared to water), in which secondary electron ranges are reduced. Detectors falling into this category, while should be treated as intermediate cavities, include the silicon diode detectors used in this project.

1.3 Detector selection for small-field dosimetry – Silicon diodes suggested as an appropriate candidate

Although small fields are now an integral part of radiotherapy and many attempts have been made to build fully ideal detectors, there is still no "perfect" commercial small-field dosimeter available. Over the last couple of decades the use of solid state (semiconductor) detectors for small-field dosimetry has been increasingly suggested, due to certain properties of these detectors.

First of all, the sensitivity of semiconductor detectors is higher in comparison to other types of detectors because of the higher densities of their active materials (e.g. 10^3 times denser than air in ion chambers). This allows semiconductor detectors to have smaller sensitive volumes, which is beneficial for spatial resolution (Knoll 2010a). Both characteristics, the high sensitivity and good spatial resolution of a detector, are very important when measuring small fields. Furthermore, semiconductor detectors are more efficient when compared to other types of solid state detectors such as scintillators. In scintillator detectors the energy of the incoming radiation is converted into visible light (called "scintillation light") which then needs to be detected and amplified by a photomultiplier tube (PMT) so the final amplified signal can be observed. In contrast, when the incident radiation interacts with the semiconductor material it generates a "cloud" of charge carriers which are responsible for producing the observed signal, a one-step process that will always be more efficient (Tsoulfanidis 1995, Knoll 2010b).

More specifically, silicon diodes are used as dosimeters because they can produce an electric signal when exposed to ionising radiation. The silicon (i.e. the semiconductor material) crystal comprises a valence and a conduction band. Electrons in the valence band have low energy and are bound to specific sites of the crystal. Conversely, electrons in the conduction band have higher energy and migrate through the crystal. These two bands are separated by an energy gap, small (≈ 1 eV) in the case of semiconductors, which no electrons can occupy. When an impurity is added to the silicon crystal the semiconductor is "doped" and based on the type of doping it can be either of p-type or n-type. The p-type refers to an elemental impurity with fewer valence electrons than the semiconductor in which it is added, and for n-type the opposite is true.

In a silicon diode detector one part of the chip is p-type and the other is n-type (known as "p-n junction") and the different doping types can create a potential difference across the junction. Absorption of ionising radiation provides sufficient energy to electrons that they can move from the valence to conduction band, leaving empty positions which are called "holes". The "holes" are considered as "positively charged" in contrast to the electrons which of course have a negative charge. The electric field formed across the p-n junction separates electrons and "holes" formed by radiation interactions in the junction, and directs them to different parts of the diode; the electrons move to the n-type part (acceptor doped) and "holes" to the p-type (donor doped) part of the diode, both contributing in generating an electric signal sufficiently strong to be detected (Attix 1986c, Knoll 2010a).

Several authors (McKerracher and Twaites 1999, 2002, Das *et al* 2008, Cranmer-Sargison *et al* 2012, Charles *et al* 2013) have recommended silicon diodes for measuring dose in small fields mainly because of their small (compared to ion chambers) sensitive volume.

1.3.1 Differences between responses of various detectors in small photon fields

In 1999, McKerracher and Thwaites compared the performance of several different detectors in circular fields (used for stereotactic treatments) ranging from 40 to 12.5 mm produced by a 6 MV photon beam. The detectors they compared included an unshielded electron diode, a new (at that time) "mini" diode with an active diameter of 0.6 mm, and three different ionisation chambers. Specifically, they compared output factors (OF) measured using these detectors. We can define the output factor (Eq. 1.8) as the ratio of the dose per monitor unit (MU) for any field size of interest to that for a reference field at the same source to surface distance. All output factors of their study were measured relative to a standard 10x10 cm^2 square field, at a 100 cm SSD and a constant depth of dose maximum of 1.5 cm.

$$OF = \frac{[Dose/MU]_{field\ size}}{[Dose/MU]_{10x10\ cm^2}} \tag{1.8}$$

They found that the output factors for the various detectors used decreased while decreasing the field size, and fell substantially as the size of the field approached 1 cm. They were not concerned at all about the spectral variation between the small fields and the 10x10 cm^2 reference field because it was too small to account for their findings. Instead, differences mentioned above were attributed to the different volumes of the detectors, with McKerracher and Thwaites concluding that none of the detectors used is ideal for measuring relative output factors, which "presents the largest problem". Ion chambers, which are generally preferred for measuring relative output factors, proved to be inappropriate in smaller fields. Their large size means that part of the detector lies outside the central uniform dose region of the radiation field, thereby causing the underestimation of the dose measured. On the other hand, an unshielded silicon diode detector (placed with its long axis parallel to the beam central-axis, CAX) seemed to be the best choice at the moment, with the new "mini" diode showing promising results for field-sizes even smaller than 12.5 mm, primarily due to its small size.

1.3.2 Establishing a generalised methodology for small-field dosimetry – The IAEA/AAPM formalism for reference dosimetry in small fields

With the use of small fields being an established practice both for stereotactic treatments (SRS/SBRT) and intensity modulated radiation therapies (IMRT), the need for a universal standardised set of recommendations for small field dosimetry was apparent. Towards this direction, in 2008, a group consisting of members from the IAEA and the AAPM proposed a formalism (Alfonso *et al* 2008) for reference dosimetry of small and non-standard fields. Under this formalism, the reference field is denoted as f_{ref} and is the conventional reference field used in dosimetry CoPs (usually a 10x10 cm^2 field (IAEA TRS-398, AAPM TG-51)). For small static photon fields they introduced the concept of machine-specific-reference field, f_{msr}, and the small field-of-interest, known as the clinical field, and denoted as f_{clin}. The determination of dose in a clinical field under specific, non-conventional conditions (e.g. in a non-equilibrium small photon field) relative to the dose measured under specific reference conditions is known as "relative dosimetry".

The f_{msr} was first introduced for novel treatment machines that are not able to establish the conventional 10x10 cm^2 reference field at around 100 cm source-to-surface distance (Alfonso *et al* 2008). Moreover, in small-field dosimetry f_{msr} can form a useful intermediate step between the conventional broad reference field, in which lateral electronic equilibrium exists but the fluence spectra may differ from that of a small field, and the small sub-equilibrium clinical field for which the dose needs to be accurately measured. The f_{msr} step allows the calibration of small-field dosimeters in a smaller than traditional 10x10 cm^2 fields ("daisy-chaining", IAEA 2017) in order to minimise the effects of photon spectral variations with field-size (Fenwick *et al* 2013, Fenwick *et al* 2018a). For instance, a 4x4 cm^2 field (used also in this project as the reference field) is appropriate as the machine-specific-reference field because it is sufficiently wide for lateral electronic equilibrium to be achieved, but at the same time the photon spectral differences with small fields will be limited compared to the typical 10x10 cm^2 field used for reference dosimetry (Fenwick *et al* 2018b).

This formalism was recently developed in the CoP published by the IAEA (2017), and as described by Fenwick *et al* (2018a), based on it and taking into account the changes in the detector response in small fields, the absorbed dose to a point of water in a clinical field f_{clin} of quality Q_{clin} is given by the equation:

$$\left(D_{wat-point}\right)_{Q_{clin}}^{f_{clin}} = M_{Q_{clin}}^{f_{clin}} \, N_{Q_{msr}}^{f_{msr}} \, k_{Q_{clin},Q_{msr}}^{f_{clin},f_{msr}} \tag{1.9}$$

where M is the reading of the detector at a specific depth in water in the clinical field, N is the absorbed dose to water calibration coefficient obtained for the detector in a msr field (f_{msr}) and $k_{Q_{clin},Q_{msr}}^{f_{clin},f_{msr}}$ is the correction factor that should be applied to correct for any differences in the response of the detector between the measured clinical field and the msr field. The $k_{Q_{clin},Q_{msr}}^{f_{clin},f_{msr}}$ correction factor is given by:

$$k_{Q_{clin},Q_{msr}}^{f_{clin},f_{msr}} = \left[\frac{(D_{wat-point})_{Q_{clin}}^{f_{clin}} \;/\; M_{Q_{clin}}^{f_{clin}}}{(D_{wat-point})_{Q_{msr}}^{f_{msr}} \;/\; M_{Q_{msr}}^{f_{msr}}}\right] \quad (1.10)$$

As complicated as it may seems the correction factor in Eq. 1.10 is simply the ratio of doses to points of water in the clinical field-of-interest and reference field, divided by the ratio of detector readings in the same fields. This factor is essential in small-field dosimetry and can be determined either experimentally or, as increasingly often in the last years, computationally by running Monte-Carlo (MC) simulations.

1.3.3 Using *k* correction factors to account for differences in detector response between small and wider fields

Francescon *et al* (2011) used computational models to generate key on-axis $k_{Q_{clin},Q_{msr}}^{f_{clin},f_{msr}}$ factor data using two different 6 MV beam models. Their Monte-Carlo (MC) calculations showed heavily divergent behavior of ionisation chambers and diode detectors for field sizes smaller than 1.5x1.5 cm^2 for both beam models. The various detectors were fully modelled using the "egs_chamber" MC user-code, part of the "EGSnrc" system (Kawrakow 2011). At field sizes greater than 2 cm in width, the $k_{Q_{clin},Q_{msr}}^{f_{clin},f_{msr}}$ correction factor did not differ much amongst the detectors. These findings were similar to those of Scott *at el* (2008) about output factors both experimentally measured and computationally calculated for a higher beam energy (15 MV).

1.3.4 Density plays a dominant role in detector response in small non-equilibrium fields

Scott *et al* (2012) published MC calculated data showing differences in the response of detectors between small and larger fields using a 15 MV photon beam model. The

detectors modelled were schematic, consisting only of the different active volumes, diamond, silicon and air, representing this way a diamond detector, a silicon diode and a pinpoint ion chamber, respectively. For the purpose of this work they defined a "density correction" factor, "$F_{detector}$", which simply is the ratio of absorbed dose-to-water to dose-to-detector-in-water, both at 5 cm deep in a water phantom, and for the same field size. In agreement with the MC results of Francescon *et al* (2011), they observed that for field sizes above 2x2 cm^2 the quantity $F_{detector}$ remains relatively constant (and independent of the densities), i.e. less than ~ 2% variation for all the different active volumes tested, but varies substantially, i.e. by tens of percent, in smaller fields. Regarding the non-equilibrium small fields, the two high-density active volumes show similar response, i.e. both $F_{detector}$ ratios decrease, meaning that detectors over-read relative to wider fields, while the low-density ion chamber under-reads (the $F_{ion\text{-}chamber}$ ratio increases).

To further investigate the impact of differences in the atomic composition and the physical density of the active volumes compared to water, Scott *et al* (2012) created voxels in which the different sensitive volumes were modelled with their real densities but the atomic composition and both the mass-stopping powers (L_Δ/ρ) and the mass-energy-absorption coefficients (μ_{en}/ρ) of unit density water. Calculating the different $F_{detector}$ ratios for the new voxels of "modified density water" they found same trends as before. In larger fields there is a small variation between the calculated ratios. In small fields the ratios differ from those in large fields, to an extend that depends on the density of the modelled material.

Considering that the spectral variation between small fields is limited (Scott *et al* 2008, Bouchard *et al* 2009, Crop *et al* 2009, Ding and Ding *et al* 2012) and having previously shown that the Spencer-Attix mass stopping-power ratio of water to silicon $(L_\Delta/\rho)_{Water:Silicon}$ changes insignificantly with field size and depth (Scott *et al* 2008), a result also confirmed by Sánchez-Doblado *et al* (2003) and Bouchard *et al* (2009), Scott *et al* reached the conclusion that the physical density, rather than atomic composition, of the sensitive volume plays the dominant role in the response of detectors in small radiation fields relative to wider fields compared to water. The dependence on mass-

density of detector response in small photon fields in which LCPE breaks-down was further explained by Fenwick *et al* (2013) using cavity theory.

The studies published by Scott *et al* (2008, 2012) and Francescon *et al* (2011) provided important results regarding our understanding of detector response in small MV photon fields. It is now clear that there are large differences between the responses of small-field dosimeters in non-equilibrium fields smaller than 1 cm across, relative to wider reference fields. Moreover, spectral variation amongst different small fields has a small effect in dosimetry; the number of scattered low energy photons is very limited in small fields (in contrast to wider fields), so absorbed doses vary less with the atomic number *(Z)* (IAEA 2017, Fenwick *et al* 2018b) and these differences are not entirely due to the volume averaging effect.

The most important finding of the work of Scott *et al* (2012), that the non-ideal detector response in small non-equilibrium photon fields relative to wider fields is mainly driven by the physical density of the active volume and not the atomic number, was later further confirmed by the computational work of Underwood *et al* (2013a) for various small-field detectors, and recently by the Monte-Carlo calculations of Fenwick *et al* (2018a) studying the response of the widely used "PTW 60017" electron diode detector.

In fact it is not only the active volume of the detector (e.g. silicon in the case of diode detectors) that is causing significant changes in the response of a detector in small fields relative to wider ones that LCPE holds, but the other non-water equivalent materials in the close proximity of the sensitive volume as well. These materials will also perturb the secondary electron fluence, and in this way have a considerable impact in the instrument's response (Bouchard and Seuntjens 2004, Cranmer-Sargison *et al* 2012, Francescon *et al* 2012, Underwood *et al* 2013a, 2013b).

1.3.5 The importance of Monte-Carlo calculations in small-field dosimetry

Apart from the very useful findings previously described, the importance of Monte-Carlo (MC) simulations in small-field dosimetry is also obvious from the publications

discussed. Classical dosimetry was based on well-established theories, like the B-G cavity theory: ion chambers, which have been the "backbone" (Alfonso *et al* 2008) of conventional radiotherapy dosimetry, mostly behave as B-G cavities in megavoltage photon beams.

However, for small-field dosimetry the case is totally different; there is no solid state detector that behaves entirely as a B-G cavity. Gafchromic film (e.g. EBT3) or alanine dosimeters, which can be used to measure dose accurately in small fields, require very careful and consistent handling or need to be send to the National Physical Laboratory (NPL) for the readout of dose. Furthermore, the big differences in the response of detectors in small fields and the lack of a theoretical framework means that there has not been an experimental gold standard for small-field dosimetry and there is no other way besides detailed MC simulations to confirm/predict dosimetric results for small fields.

MC techniques can be used to accurately simulate the transport, interaction and the subsequent energy deposition of individual particles in matter. This is done by averaging huge numbers of randomly sampled particle histories – often more than 10^9 – approximating this way the result of probabilistic events (Jenkins *et al* 1988, Landau and Binder 2009). The more histories *(N)* simulated the more statistically precise MC results will be but always with the compromise of time-consuming calculations. The statistical uncertainty (standard deviation) of MC simulations is proportional to one over the square root of the histories simulated $\left(1/\sqrt{N}\right)$. In radiotherapy the estimation of dose (and fluence) distributions is of great interest and MC simulations provide an excellent alternative for situations in which real experimental measurements are too complicated or even impossible. In addition, MC calculations are much more accurate than analytical cavity theories (Mobit *et al* 1997) especially under non-equilibrium conditions where electrons transport becomes really complex, and they can provide useful information regarding the understanding of radiation physics and detector response. Finally, MC simulations prove to be a very useful tool in attempts to improve the existing small-field detectors, and have been extensively used in this work for this purpose as well.

Monte-Carlo has played an increasing role in medical physics for more than half a century (Rogers 2006). Nowadays, many different code systems are available for

performing MC simulations, such as PENELOPE (Baró *et al* 1995), MCNP (Brown 2003), GEANT (Allison *et al* 2006) and of course EGSnrc (Kawrakow *et al* 2011), which is the most widely used MC package and was chosen for this project too.

1.4 Improving silicon diode response in small fields – The idea of density compensation

The field-size dependent correction factor $k_{Q_{clin},Q_{msr}}^{f_{clin},f_{msr}}$ proposed by Alfonso *et al* (2008) was shown to depend on the energy of the beam used and on the position and orientation of the detector within the field, i.e. depth, distance and direction off-axis (Underwood *et al* 2013a). Determining different factors for so many conditions is very difficult and time-consuming even if MC simulations were to be performed (Francescon *et al* 2012, Pantelis *et al* 2012, Underwood *et al* 2013a, Benmakhlouf *et al* 2014, Francescon *et al* 2014). For this reason, it would be ideal to build a detector that is independent of all these variations under non-equilibrium conditions, in order to achieve correction-free small-field dosimetry. Attempts towards this goal, focusing on the case of silicon diode detectors, are discussed in section 1.4.1.

It is now established that an ideal small-field dosimeter should have a small sensitive volume, in order to limit volume averaging, and comprise components with densities as close as possible to unity (ideally equal to 1 g cm^{-3} so that the detector is totally water-equivalent) and of low *Z* materials to limit spectral effects (which are anyway limited in small fields and further controlled by the intermediate calibration fields, as previously described in 1.3.2, 1.3.4). Classically, it was the atomic number that was thought to be critical for a dosimeter to respond ideally and measure dose accurately in water, but for small fields it is the density of the detector materials that plays a dominant role, and can potentially cause significant perturbations to the charged particles fluence if it differs substantially from the unity density of water. Considering that the first two factors mentioned above are primarily responsible for the non-ideal response and that detectors with very small sensitive volumes (less than 0.05 mm^3 in silicon diodes) exist today, the biggest challenge for silicon diodes remains the non-water equivalent density of the

active volume which leads to detector over-responding in small fields. A promising solution to this problem was proposed recently; the basic concept is to offset the higher density of the sensitive volume with that of other non-sensitive materials of the detector (Underwood *et al* 2013b).

1.4.1 Small air-gaps: a solution to silicon's higher density compared to water

The idea of detector density compensation in order to improve the response of small-field dosimeters is relatively new; it was first proposed in 2012 by Underwood *et al* (2012), stating that detectors with high-density sensitive volumes can be improved by adding a judiciously chosen amount of low-density material, and vice versa for the low-density detectors such as ion chambers. Since then, a number of experimental and computational studies have been published further investigating the concept of "mass-density compensation" (Underwood *et al* 2013b) and trying to identify the optimum strategies and detector designs for achieving an ideal density compensated electron diode for small-field dosimetry (Charles *et al* 2013, Charles *et al* 2014, Underwood *et al*, 2015).

The validity of the density compensation concept for silicon diodes (both shielded and unshielded) was first confirmed by the computational work of Charles *et al* (2013), who showed that introducing a thin air-gap above the sensitive region of the detector can compensate for the high density of silicon (2.33 g cm^{-3} compared to 1 g cm^{-3} for water) and substantially improve the instrument's response in small fields.

Underwood *et al* (2013b) further investigated the "mass-density compensation method" for ion chambers and diamond detectors by computationally calculating $k_{Q_{clin},Q_{msr}}^{f_{clin},f_{msr}}$ correction factors using for different detector geometries (spherical and cuboidal) in a 6 MV beam. Being particularly concerned to separate the effects of non-water equivalent detector materials and volume averaging, Underwood *et al* (2013b) also calculated $[k(D_{vol})]k_{Q_{clin},Q_{msr}}^{f_{clin},f_{msr}}$ correction factors for the different detector scenarios, with the (D_{vol}) being the dose to a specific volume of water with exactly the same dimensions as

the sensitive area of each detector. Based on the results of this study they concluded that the densities of both the active volume and surrounding materials have a considerable impact on the detector response in small fields, and that the density compensation method should be applied considering whether these densities are lower or higher compared to the density of water. The sensitive volume of a density-compensated detector should be very carefully designed since both its shape and size has a significant influence too: the modifications studied by Underwood *et al* (2013b) had an improved performance for spherical volumes than for cuboidal ones.

Regarding silicon diodes the first experimental validation of the density compensation method, by adding thin layers of air above the dense silicon active volume, was carried out by Charles *et al* (2014). In their work two modified diode detectors were characterised and air-gaps were "added" using an adjustable "air-cap", allowing the gap thickness to be varied. The goal was to design a small-field silicon diode detector with optimum air-gap thickness, so that there is no need for any correction factor to account for the non-water density of silicon. Similar work was done later by Underwood *et al* (2015) using again silicon diodes, but now the air-gaps (of different thicknesses) were included in the detectors placed at a point above the silicon active volume. A set of diode detectors was evaluated both computationally, performing MC simulations, and experimentally, by comparing the values of dose measured using the detectors and EBT3 gafchromic film. Both studies showed that the thickness of the air-gap introduced in the diodes should be close to 1 mm.

The work of Charles *et al* (2013, 2014) and Underwood *et al* (2015) aimed at building a correction-free silicon diode detector for small-field dosimetry, despite the existence of a high density sensitive volume (compared to water) and other components whose densities differ substantially from that of water. This approach is based on the idea that although the detector is not made of water-equivalent materials (including sensitive and non-sensitive ones) all the different perturbations of the electron fluence will be balanced, resulting in a detector response very close to that of a point water volume (i.e. having $k_{Q_{clin},Q_{msr}}^{f_{clin},f_{msr}}$ factors equal to one).

1.4.2 Overall aim and objectives of this project

Although it is widely accepted that density (in combination with the volume averaging effect), rather than atomic composition, plays a dominant role in the response of a detector in small non-equilibrium fields relative to wider (reference) fields, there is still some controversy regarding this issue (Andreo and Benmakhlouf 2017, Benmakhlouf and Andreo 2017, Andreo 2017, Fenwick *et al* 2018a, 2018b, Andreo and Benmakhlouf 2018).

Despite its significance in small-field dosimetry, the issue of mechanism is not relevant to the studies in this thesis, which focuses on ways of systematically improving the response of unshielded silicon diodes via the simple but rather revolutionary idea of air-gap based compensation (Underwood *et al* 2012). This work examines the consequences of deliberately introducing thin air-gaps above the active volume of silicon diodes, rather than the microscopic causes of the non-ideal behaviour of detectors in small fields.

The aim of the project is the detailed characterisation of two new sets of silicon diodes, manufactured by "PTW-Freiburg"; the comparison of their behavior to the unmodified "PTW 60017" diode; and the analysis of potential improvements in their design based on both experimental and Monte-Carlo (MC) simulation results. Fundamental modifications were made to the design of the first set of detectors, to further improve detector response, leading to the second set made by PTW in order to more closely approach a correction-free diode detector for small-field dosimetry.

Continuing the work of previous groups (Charles *et al* 2014, Underwood *et al* 2015) in the field, more needed to be done to confirm their 6 MV beam results and evaluate the response of the new density compensated diodes both for the same energy beam and for a higher energy (15 MV), at different depths in water and for various positions off-axis and with the detector oriented at a range of angles relative to the beam axis.

Chapter 2

Experimental and Monte-Carlo Methods

2.1 Detector geometry and modifications of the PTW silicon diodes

In the course of this project the performance of two sets of dosimetry diodes has been both experimentally and computationally evaluated. The detectors studied were unshielded (electron) diodes with sensitive volumes made of silicon, all manufactured by PTW.

The first set of detectors comprised the PTW 60017 Original diode (with no air-gap added above its sensitive volume) and the 1 mm air-gap "old" Prototype diode, both characterised by Underwood *et al* (2015), along with a set of six modified diode detectors (diodes "1162" - "1167") with air-gaps of different thickness introduced somewhere between the top surface of the detector and its sensitive volume. The second set of detectors available for study, provided again by PTW, included four new diodes (Type No. 60023) with improved design compared to the previous set; a diode detector with no air-gap and three modified ones with thin air-gaps added above the silicon sensitive volume.

2.1.1 First set of detectors – PTW 60017 Original diode and modified detectors

The PTW 60017 detector (figure 2.1) is a waterproof, cylindrically-shaped silicon diode appropriate for measurements in small radiation fields that can be used in air, solid phantoms and in water, as was the case for the experimental measurements of this project. The full detector consists of its main body, which contains the sensitive volume,

and of a cap made of water equivalent plastic (RW3[1]), a material used by PTW for the outer casing of the dosimeters. The geometry and the design of the modified diodes 1162 - 1167 is the same as the PTW 60017 Original diode, with the only difference being the thin air-gaps added at a point above the sensitive region.

Figure 2.1: The PTW 60017 un-modified (no air-gap) electron diode. The outer diameter of the whole detector, including the plastic RW3 cap, is approximately 7 mm (PTW 2018). The connection cable is about 2 m long so that the electrometer box, connected to the detector during measurements, can be placed far enough from the irradiation point (figure used with the permission of "PTW-Freiburg").

The sensitive volume of these diode detectors is a very thin cylinder whose axis is aligned with the detector long axis. Specifically, the sensitive volume has a cross-sectional area of 1 mm^2 and a thickness of 30 μm (nominal sensitive volume is 0.03 mm^3), and is made of silicon with a density of 2.33 g/cm^3 and atomic number Z = 14 (PTW 2018). The cylindrical sensitive region is a p-n junction as described in section 1.3, and lies at the top surface of a larger cuboidal block of silicon. The PTW 60017 Original diode and the modified ones are p-type silicon diodes, i.e. holes are the majority carrier. According to the manufacturer, for the Original diode the effective point of

[1] The density of RW3 is 1.045 g/cm^3. The exact atomic composition is not mentioned for confidentiality reasons.

measurement (EPOM) lies on the detector axis, at 1.33 mm below the top surface of the full detector (radiological depth[2]).

The entrance window of the PTW 60017 detector comprises 0.3 mm of RW3 plastic and approximately 0.4 mm of epoxy resin. In the modified diodes air-gaps of different thicknesses were deliberately added at a point between the detector main structures and the RW3 lid to compensate for the high density of silicon compared to water. The air-gap thicknesses of the modified 1162 - 1167 detectors are presented in table 2.1.

Detector	Air-gap thickness (mm)
1162	0.6
1163	0.8
1164	1.0
1165	1.2
1166	1.4
1167	1.6

Table 2.1: Air-gap thickness (in mm) of the 1162 - 1167 modified diode detectors. The air-gaps added above the sensitive volume of each diode vary so that the optimum thickness can be decided based on the response of the detectors in small radiation fields.

The difference in the design between the modified 1162 - 1167 detectors of this project and the four prototypes characterised by Underwood *et al* (2015), which included the "old" 1 mm air-gap Prototype diode, is the absence of PMMA (poly-methyl methacrylate) material. Within the "old" Prototype diode, a cylindrical PMMA ring of 4.7 mm in diameter was used to introduce the 1 mm thick air-gap between the main part

[2] The radiological depth is different from the actual one (real dimension) due to the densities of the materials used in the detector design.

of the detector and its RW3 casing. In this diode the air-gap was wider than the diameter of the sensitive silicon; thus, it extended beyond the sensitive region which had a diameter of approximately 1.2 mm. In the 1162 - 1167 modified detectors the PMMA material, previously used to form the "spacer" ring, was completely removed and RW3 plastic caps with thicker tops were used, significantly reducing this way the lateral width of the air-gaps compared to the prototypes characterised by Underwood *et al* (2015).

2.1.2 Second set of detectors – The PTW 60023 improved electron diodes

Following our testing of the first set of detectors tested, an additional set of improved diodes was manufactured by PTW. A material with density of about two times the density of water, and of thickness that inadvertently varied from detector-to-detector was present in the first set of modified diodes (described in 2.1.1), and affected the detector response and caused significant deviations between expected (based on the known air-gap thicknesses) and experimentally measured *k* correction factors.

Fundamental modifications were made to the design of the new set compared to the previous one to improve detector response. More materials with densities closer to the unity density of liquid water were used in the new detectors. Furthermore, the amounts of any existing materials whose densities differ from unity were better controlled, so that their thickness was kept constant and not variable between the four new detectors. The same material as before (RW3 plastic) was used for the outer casing of the detectors. Regarding the sensitive volume of the type 60023 PTW diode detectors, it is a very thin cylinder made of silicon which again is in contact with a larger silicon cuboid and lies perpendicular to the detector long axis (figure 2.2). However, the dimensions (both the thickness and the radius) of the silicon sensitive area were slightly modified in these new detectors. Although the exact sensitive volume dimensions of the PTW 60023 diodes were provided by PTW and used in the Monte-Carlo detector models, they are not included in this thesis for confidentiality reasons.

With the improvements in the design of the new set of detectors made by PTW smaller air-gap thicknesses were needed, compared to the first set of detectors, for the

compensation of the density perturbation. This time the maximum air-gap introduced in the diodes was 1 mm in thickness. In addition, the use of materials with densities even closer to unity than before, combined with the more carefully controlled amounts of higher density materials present in the detectors, slightly decreased the water-equivalent depth (radiological depth) of the EPOM. In the new PTW 60023 diode with no air-gap added, the EPOM lies, according to the manufacturer and subsequently confirmed by MC simulations, at about 0.95 mm below the top surface of the RW3 cap (whereas, as mentioned in 2.1.1, the elevated density of the material above the sensitive volume of the no air-gap PTW 60017 un-modified diode increased the radiological depth of the EPOM to 1.33 mm).

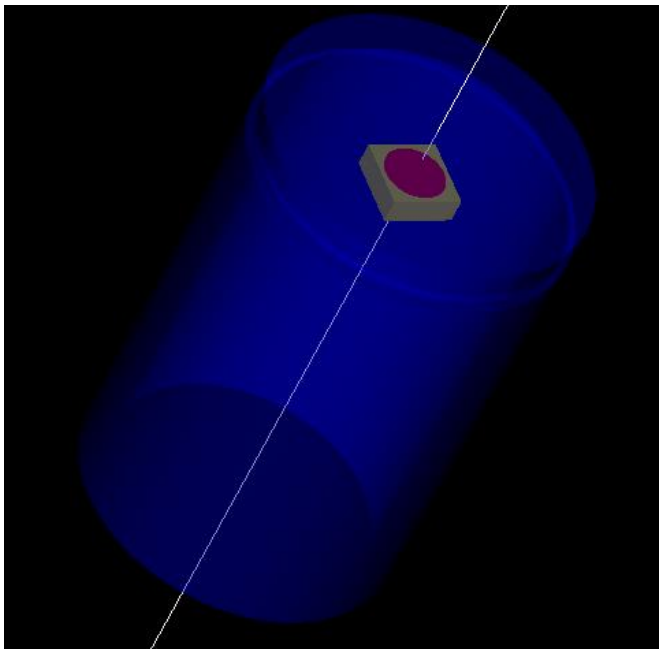

Figure 2.2: The geometry of the new, type 60023 PTW, no air-gap silicon diode. The cylindrical silicon sensitive volume (in red) is in contact with the larger silicon cuboid shown in yellow colour, both placed perpendicular to the detector axis. Several materials of the main body of the detector have been removed from this diagram to increase visibility and to keep the detailed detector design confidential.

Both for the experimental work and the computational studies completed in this project, only two of the four PTW 60023 diodes were characterised in detail and their response in small photon fields was evaluated: the diodes with serial numbers 1518_36 (no air-

gap added) and 1518_30 (0.6 mm air-gap added). These were the two detectors of the new set that performed best on-axis, i.e. had *k* correction factors closest to one in the 0.5x0.5 cm^2 clinical field.

2.2 Experimental methods and measurements

All detectors involved in this project, both the first set of silicon diodes and the improved ones, have been characterised and their performance has been experimentally evaluated. The detectors were labeled according to the thickness of their air-gap, stored in their special protective cases, and were always handled very carefully to avoid any damage of either the detector or its connection cable. The experimental work was done at Clatterbridge Cancer Centre (CCC), always on weekends (six in total) when no patients are being treated and the hospital linacs are available to use. Throughout the whole experimental process a photon beam of energy 6 or 15 MV was used, produced by a Varian ("TrueBeam") linear accelerator (Varian Medical Systems, Palo Alto, California) located in the VT2 room at CCC. The "Blue Phantom 2" scanning water tank in conjunction with the accompanying electrometer box and computer software ("OmniPro-Accept 7.4"), all made by "iba", were used for the experimental measurements of this project. Each detector was connected to the electrometer box via its own connection cable, and no bias voltage was applied since it is not necessary for diode detectors to operate.

The experimental data obtained using the two different sets of silicon diodes and for both beam energies (6 and 15 MV) comprise diode in-line and cross-line profiles (at 5 and 15 cm deep in water), output factors for various field sizes and percentage depth dose (PDD) data as well. Gafchromic (EBT3) film was used to measure the dose in small clinical fields (Underwood *et al* 2015, Fenwick *et al* 2018a) at a specific point in water – necessary for the calculation of diode on-axis *k* correction factors – and at various positions off-axis (beam profiles) in order to generate the off-axis *k* profiles for the diode detectors. All experimental measurements were completed without a reference detector and the different field sizes were set using just the collimator jaws and not the

MLCs, which were fully retracted. Once a specific (small) field size was set, the jaw settings of the linac were maintained until all diodes or EBT3 films were irradiated in this field at both depths before changing the position of the jaws to set the dimensions of the next radiation field. This was done to avoid any issues with the reproducibility of the exact field size, because even small differences (of the order of few tenths of a mm) can affect the obtained data (e.g. field width, on-axis dose) when measuring small fields.

2.2.1 Water tank and detector set-up – the "zero" depth position definition

Before making any experimental measurements the "Blue Phantom 2" tank was always placed below the linac head (gantry was at a 0° position) and was carefully centered by aligning the markers present on its side surfaces with the lasers of the treatment room. The next step was to apply both brakes on the wheels so that the tank remains in exactly the same position and finally fill it with water using the special pump cable. Once the tank was filled with water the source-to-surface distance (SSD) was measured using the field light of the linac. The "Blue Phantom 2" water tank is mounted on a mechanical base that makes possible the vertical movement of the whole tank allowing us to precisely and accurately adjust the SSD until the desired value of 100 cm was achieved, which was then maintained throughout the whole experimental process. The SSD has been regularly monitored during each day of experiments, because evaporation of water from the tank has the potential to slightly alter the exact SSD. However, the SSD was never found to differ from the 100 cm that was initially set.

The same procedure was followed for the set-up of each detector in the water tank to obtain all experimental data: the detectors were positioned vertically to the water surface, parallel to the beam axis, using the plastic holder of the "Blue Phantom 2", which is connected to a mechanism that enables the movement in all three dimensions. The exact position of the detector on the holder was carefully adjusted so that the main body of the instrument (with the sensitive volume inside) is far enough from the holder and is surrounded entirely by water. The clamps, responsible for holding the detector stable at exactly the same point, were then tightened to prevent any undesired movement

of the dosimeter during the measurements. The determination of the exact depth of the detector in the water tank plays a significant role, since even small errors can potentially bias dosimetric results. For this reason, particular attention was given to the definition of the "zero" depth position of the diodes in the water tank. Each detector was submerged into water and was then very slowly driven towards the surface; the point where the top of the detector just starts "breaking" the water surface was defined as the "zero" depth position. After allowing some seconds for the water surface to completely rest, the set-up of the detector was checked again and the "zero" depth position (of the detector top, but not its EPOM) was stored in the computer software. For any measurements made with the detector this was the position that was considered as the origin regarding the depth in water.

2.2.2 Calculation of on-axis $k_{Q_{clin},Q_{msr}}^{f_{clin},f_{msr}}$ correction factors

For the calculation of on-axis $k_{Q_{clin},Q_{msr}}^{f_{clin},f_{msr}}$ (Eq. 1.10) correction factors, at 5 and 15 cm deep in water, each detector's readings in both fields (i.e. output factors), the clinical (f_{clin}) and the machine-specific reference (f_{msr}), were used. The dose to a point of water was determined using EBT3 film in the small clinical fields and the f_{msr} field (film dosimetry discussed in detail later, section 2.2.5). For wider clinical fields that were also measured (3, 4, 6 and 10 cm square fields) the use of EBT3 films was not necessary, allowing us to use the "CC13" ion chamber (made by "iba") connected to a "KEITHLEY" electrometer box. All measurements, either using diodes or gafchromic film, were made at a 100 cm SSD. The correction factors were calculated using a 4x4 cm^2 field as the machine-specific reference field, 200 MUs, and for an SSD of 100 cm, at a depth of 5 cm in the water tank (reference conditions). Even when calculating correction factors at 15 cm deep in water for the various clinical field sizes, the reference conditions were always maintained the same (4x4 cm^2 field, 5 cm depth). Using the diode detectors $k_{Q_{clin},Q_{msr}}^{f_{clin},f_{msr}}$ values were calculated for several different clinical field sizes, small and wider ones (0.5x0.5 cm^2, 0.7x0.7 cm^2, 1x1 cm^2, 1.5x1.5 cm^2, 3x3 cm^2, 4x4 cm^2, 6x6 cm^2 and 10x10 cm^2). Since a 4x4 cm^2 was used as the reference field, the

correction factor for the same field at 5 cm deep is by definition equal to one for all the detectors tested. For each field size all the data were obtained on the same day to avoid any issues due to the beam variation from day-to-day. The statistical uncertainties on the values of film dose and diode readings (in both the reference and clinical fields) were determined as the result of repeated measurements. The final uncertainties on the $k_{Q_{clin},Q_{msr}}^{f_{clin},f_{msr}}$ values were calculated using the error propagation formula for division, i.e. add in quadrature the fractional uncertainties of the four values used to calculate each *k* correction factor.

The measurement depth of 5 or 15 cm corresponded to the exact position of the EBT3 film used and the (top of the) sensitive volume of each detector in experiment, e.g. for the first set of diodes, with the known EPOM radiological depth of 1.33 mm and according to the definition of the "zero" depth position as described in 2.2.1, the detector was driven so that its top lay at a depth of 49 mm and 149 mm, corresponding to its sensitive volume laying at 5 and 15 cm deep in water, respectively. Considering the experimental difficulties encountered in small fields (discussed in section 1.2.2), great care was also given to the accurate positioning of the diodes in the center of some of the clinical fields of interest, due to their small dimensions. Before obtaining any experimental data both in-line and cross-line profiles were measured at two different depths in water (5 and 15 cm) using each detector to ensure that it was well centered in the small field. If there was a discrepancy of more than 0.3 mm in the centering of the detector, adjustments were made accordingly and once the corrected detector position was confirmed, it was set as the centre of the beam.

2.2.3 Depth dose measurements – PDD curves

Depth doses have been measured for both beam energies, 6 and 15 MV, using the various silicon diodes down to 30 cm deep in the "Blue Phantom 2" water tank. When measuring the PDD data the diodes were set-up vertically to the water surface, parallel to the beam axis with their tops just breaking the water surface (as described in 2.2.1). Depth dose data were obtained for both the reference field (4x4 cm^2) and some of the

smaller ones (e.g. fields with side-lengths 0.5, 0.7 cm). The analysis of the PDD data, obtained using the silicon diodes, is of great importance for the experimental characterisation of the detectors in this project; it allows to investigate if the incorporation of thin air-gaps above the detector's sensitive region affects the overall shape of the observed PDD curves, and if the air-gaps of different thicknesses introduced in the detectors change the location of their points of measurement (EPOM shifts), and to what extent compared to the no air-gap PTW 60017 and 60023 diodes (i.e. the ones without air-gaps added between the top surface of the detector and its sensitive volume). In the reference field, i.e. 4x4 cm^2, PDD data were obtained using the PTW "Semiflex" ion chamber too as a comparison to the diode PDD data in the same field. Since ion chambers are not suitable for measurements in narrow fields, e.g. 0.5x0.5 cm^2, Monte-Carlo simulations were performed to measure the "true" PDD and compare it to the diode results.

2.2.4 Beam profile measurements – off-axis $k_{Q_{clin},Q_{msr}}^{f_{clin},f_{msr}}$ profiles

Profiles have also been measured using the un-modified PTW diodes and the modified prototypes, at 5 and 15 cm deep in the water tank, both for 6 and 15 MV photon beams. The accurate positioning of each diode in the centre of the radiation field was checked as described in 2.2.2, especially in the small fields (0.5, 0.7, 1 and 1.5 cm square fields). After its position in the water tank was confirmed, the detector was driven deeper in water, using the carriage mechanism of the "Blue Phantom 2", so that the (top of the) sensitive volume was located at 5 and then 15 cm, and both in-line and cross-line profiles were measured at these two depths. All profiles were measured some centimeters beyond the field edges in order to provide out-of-field data as well.

Beam profiles (6 and 15 MV energy) were obtained at both depths using gafchromic (EBT3) films as well, providing the necessary data to experimentally evaluate the response of the diode detectors at various points across a small radiation field. Using the profile data measured both with the PTW diode detectors and gafchromic films, $k_{Q_{clin},Q_{msr}}^{f_{clin},f_{msr}}$ (Eq. 1.10) correction values were later calculated, but now with the clinical

field data obtained at various positions off-axis. Error bars were added to the off-axis *k* profiles plotted for all the diodes to demonstrate the amount of random noise in the measurements, and thus explain any observed asymmetries in the profiles plotted. The stated uncertainties for the off-axis *k* profiles (graphs included in chapters 3, 4 and 5) were calculated based on the asymmetry (left-to-right side variation) of both the film and diode profiles at specific off-axis points (in the penumbra and the very low dose region of the profile, i.e. "middle" and "bottom" parts of the profiles). For a fixed number of points (N) in the "middle" and "bottom" parts of the profile the difference (d) in the dose values between the left and right side of both the film and diode profiles was estimated and the uncertainty at that region ("middle" or "bottom" part of the profile) was then calculated according to equation 2.1:

$$\delta_{L-R} = \frac{\sqrt{\frac{\sum_{i=1}^{N} d_i^2}{N}}}{2} \tag{2.1}$$

The final uncertainties (error bars shown in the off-axis *k* profiles) were calculated using the error propagation formula for division, to combine the errors determined according to equation 2.1 since the *k* profiles are calculated as the ratio of film to diode profile, and by also adding in quadrature the statistical error on dose due to the film-to-film variation.

Finally, the diode off-axis measurements at both 5 and 15 cm deep in water were necessary to get important data about the response of the different detectors tested, such as full width half maxima (FWHMs) and penumbra values, and compare them with the corresponding ones obtained from the EBT3 films.

During the irradiation process of both EBT3 films and detectors it was important to minimise the ripples caused by the movement of the carriage mechanism, which could potentially cause the distortion of the profiles measured. For this reason, the measurement (scanning) speed of the movement mechanism was set to low and the

sequence of the profiles measured was chosen carefully to limit as much as possible the movement of the carriage and therefore the perturbation of the water in the tank.

2.2.5 Film dosimetry – Gafchromic (EBT3) film methods

Gafchromic (EBT3) film was used as the reference dosimeter for the small fields studied in this project. EBT3 film has very good spatial resolution, near tissue equivalence and its response varies little between small and wider radiation fields (Bassinet *et al* 2013, Underwood *et al* 2015, Morales *et al* 2016, Fenwick *et al* 2018a), thus making it suitable for measuring dose in small fields. However, both the irradiation process and the subsequent film analysis can be quite challenging and time-consuming, requiring very careful and consistent handling to avoid any errors.

2.2.5.1 Irradiation of EBT3 film and calibration curves

More specifically, gafchromic film (EBT3) was used in the experimental work of this project to determine the dose to a point of water and measure beam profiles, following always the same process. For each set of measurements, large sheets of EBT3 film were taken out of the same box and were then cut into 6x6 cm^2 pieces under very limited light conditions and subsequently stored in dark envelopes. The 6x6 cm^2 EBT3 film pieces were placed in a metallic holder, which consists of a base and a lid with magnetic grids at the edges holding the film stable in a flat, horizontal position. The metallic holder was placed on the movement mechanism of the "Blue Phantom 2" water tank by slightly adjusting the set-up compared to the one used for the diode detectors. The clamps were then tightened in order to stabilise the whole metallic holder and avoid any undesired movement of the film during irradiation. The films were submerged into the water tank at depths of 5 and 15 cm (100 cm SSD), matching the set-up used for the diodes, irradiated in the water tank and then dried using normal paper tissue. The whole process of submerging, irradiating and drying each piece of EBT3 film used was completed in approximately the same amount of time (around 5 minutes) with the main lights of the

linac room turned off. Three to five films were irradiated for each field-size and depth combination. Particular attention was given to the removal of any air bubbles from both surfaces of the film that could potentially affect the film irradiation. Furthermore, the curvature of each irradiated piece of film was chosen to be the same (curve up), for consistency reasons. For all field sizes and the two different depths in water, the number of monitor units (MUs) was scaled so that the dose delivered to the EBT3 film was around 2 Gy.

EBT3 films were also irradiated to be used for calibration purposes for both beam energies (6 and 15 MV). For each beam thirty calibration films were irradiated in total, using a 4x4 cm^2 field at a water-depth of 5 cm at a 100 cm SSD and doses from 0.077 to 3.885 Gy (6 MV beam) and from 0.087 to 4.350 Gy (15 MV beam) adjusting the MUs of the linac. Eight films (four for each calibration curve) were not irradiated but only submerged and dried in the same way and amount of time as the other films in order to obtain experimentally consistent data for zero dose. The same procedure was repeated again, later in the project to generate the new calibration curves, for 6 and 15 MV energy beams, when the second set of PTW detectors was characterised.

2.2.5.2 Processing of EBT3 film

The next step, after irradiating the EBT3 films, was to scan them using the "EPSON V750 PRO" flatbed scanner located in the cyclotron department of CCC. The scanning procedure of the films requires skilled handling to avoid damaging the films, and to follow always the same protocol to avoid any significant inconsistencies in their processing, as described by several groups in the literature (Micke *et al* 2011, Lewis *et al* 2012, Papaconstadopoulos *et al* 2014). Throughout the irradiation and scanning procedures, all films were handled using rubber gloves and their exposure to light was kept at minimum levels. Both after the irradiation and scanning process all the films used were kept in dark envelopes minimising this way their exposure to light and dust.

Before the actual scanning process of the films five preview scans, separated by five minute intervals, were always carried out in order to warm-up the scanner. All films

were scanned approximately 48 hours after irradiation trying to be as consistent as possible regarding the positioning of each film on the scanner's glass surface. For this reason, a special Perspex jig was provided and placed at a specific position on the glass surface allowing us to keep the film fixed and flat at the centre of the scanner. The same scanning protocol was followed for all the films used in this work; professional mode, 48-bit colour scans, and a resolution of 150 DPI (dots-per-inch) were selected in the scanner software and the scanned images were saved as uncompressed ".TIFF" files (Papaconstadopoulos *et al* 2014, Underwood *et al* 2015). In addition, to avoid any distortion of the scanned image – which can affect the dose value obtained from the film – no image corrections were applied and any special image filters (such as "ICC profile") added by the scanner software were removed.

A MATLAB graphical user interface (GUI) was used to generate the calibration curve for both beams (6 and 15 MV) produced by the linac based on the calibration films previously described. Then, the calibration curve was loaded to a custom-written Python code which made possible the conversion of the scanned images of the films (".TIFF" files) into dose maps using triple channel (Red-Green-Blue) analysis (Micke *et al* 2011, Lewis *et al* 2012). The multichannel (3 channels) method for film dosimetry has been shown to be better compared to the one channel method used in the past: random noise is reduced and discrepancies caused by the non-homogeneity of the film are removed (Micke *et al* 2011).

For a specific (irradiated) film the Python code was used to calculate the average dose of a 3x3 pixels grid/area centered on each individual pixel of that film (for 150 DPI resolution, pixel size is 0.17 mm and the 3x3 area is 0.51x0.51 mm^2). By knowing the average dose of the 3x3 area around every single pixel of the film we could identify both the maximum average dose value of the film and the coordinates (Xmax, Ymax) of the centre pixel of the 3x3 area with that highest value of dose. On-axis dose values finally obtained were these maximum average doses for 0.5x0.5, 0.7x0.7 and 1.0x1.0 cm^2 films, and the average value of the geometric field-centre for the 1.5x1.5 and 4x4 cm^2 fields. In the smaller fields measured the peak of the profile is well defined and these maximum values needed to be used for the on-axis dose, as it is the only way to determine where

the field centre is. On the other hand, for the larger fields measured the average value of the geometric field-centre could be used, since it is not that critical to be exactly on the centre of the flat region of the field and the maximum dose value could potentially be the result of noise in these wider fields.

2.3 Monte-Carlo methods

The EGSnrc (Kawrakow *et al* 2011) code system was used for all the computational Monte-Carlo (MC) work completed within the project. MC beam models were used to simulate the irradiation of the two different sets of diode detectors; detailed detector models were "built" and several computational studies of their response were carried out. Detectors with slightly modified geometry of the air-gaps added were also modelled to investigate the effect on their response and some additional (non-standard) MC simulations were completed as well. All MC calculations were performed on a 64 core AMD 6378 Opteron-based computer, running with a "Scientific Linux" operating system.

2.3.1 Creating beam models with BEAMnrc and use of phase-space files

The BEAMnrc (Rogers *et al* 2011) MC system has previously been used to create 6 MV and 15 MV Varian Clinac iX (Varian Medical Systems, Palo Alto, California) accelerator beam models, which were utilised for the simulations of this work. Both beam models have been previously validated and the exact description of the models and their component modules (CMs) can be found in Scott *et al* (2008) and Underwood *et al* (2013a). For the BEAMnrc simulations, the photon and electron cut-off parameters (PCUT and ECUT) were set to 0.01 MeV and 0.7 MeV, respectively[3]. The number of histories – equal to the number of primary electrons hitting the target on top of the linac – was varied between the small (e.g. 0.5x0.5 cm^2) and the wider reference (4x4 cm^2) field in order to create sufficiently large phase-space files and run reasonably long

[3] For all ECUT values, the rest mass of electron, 0.511 MeV, is included.

simulations at the same time. Phase-space files generated with BEAMnrc need to be large enough, so that the subsequent MC calculations can be completed running the desired number of particle histories to get results with very low statistical uncertainties without "restarting" the phase space file used. The beam models produce phase-space files which then can be used as a source of particles for any other EGSnrc code by just selecting the appropriate "source type" within each code. The phase-space files are binary files, which contain all the information relating to the particles that exit the linac, such as particle position, energy, direction and charge. In the 6 MV beam model, phase space files were scored at a distance of 100 cm from the source, whereas the scoring plane was located 58 cm below the source in the 15 MV linac model.

For the BEAMnrc simulations, cross-section data of materials were taken from the "700 ICRU" PEGS4 data-file that is included in the EGSnrc installation (located in the "HEN_HOUSE" directory). For the remaining MC studies, new PEGS4 data-files were generated using the "EGSnrcMP" package (Kawrakow *et al* 2006, 2011), setting always the AP and AE thresholds to 1 and 512 keV, respectively and selecting the "ICRU density correction" option to apply the polarisation (density effect) correction. For some of the detector materials, density correction files were not available in the "HEN_HOUSE" directory; hence, appropriate density correction files were created in the "NIST" website (Physics NIST 2018) and were then used to generate the corresponding PEGS4 data-files.

2.3.2 Using the DOSXYZnrc user-code to calculate absorbed dose in water

The DOSXYZnrc (Rogers *et al* 2011) code was used to simulate the transport of particles in a Cartesian volume and score the energy deposition in specific water voxels. A 50x50x50 cm^3 water phantom was created (surrounded by 50 cm of air in each direction) to fully account for any scattered radiation, and Monte Carlo simulations were performed using the phase space files created in BEAMnrc as source inputs. For the 6 MV simulations the distance between the source and the isocenter (0,0,0) was set to zero, since the phase space file was scored at a 100 cm SSD. On the other hand, for the

15 MV DOSXYZnrc runs the "distance from source to isocenter" was set to be 42 cm, resulting in a total (58 cm + 42 cm) 100 cm SSD.

Global energy cut-off values of ECUT = 0.521 MeV and PCUT = 0.001 MeV were used throughout all the DOSXYZnrc simulations, and the most accurate electron-step transport (PRESTA-II) and boundary crossing (EXACT) algorithms were used. For the DOSXYZnrc calculations a higher ECUT value (i.e. 0.7 MeV) could have also been used to decrease simulation time, but the lower value of 0.521 MeV was finally set to be consistent with the egs_chamber simulatons (described later, section 2.3.3). The rest of the radiation transport parameters selected in DOSXYZnrc included Compton interactions for bound electrons, the effect of any atomic relaxation events, and relativistic spin effects in the multiple scattering of charged particles. Photon interaction cross-sections were taken from the XCOM database, and Bethe-Heitler (BH) differential cross-sections were used to sample photon energies in bremsstrahlung events.

PDDs, beam profiles (at 5 and 15 cm deep) and on-axis in water dose values at both depths were calculated in small fields (0.5x0.5 and 0.7x0.7 cm^2, since they are the ones in which detectors behave most non-ideally) and in a 4x4 cm^2 (machine-specific reference, msr) field using the DOSXYZnrc code. Water voxel dimensions have been selected carefully, depending on field size and the region of interest, to obtain results with good spatial resolution (even for the small fields) whilst minimising the computational time. In particular, for the small fields doses were calculated for a point-like water voxel of lateral dimensions 0.25x0.25 mm^2 and thickness 0.5 mm, whose centre lay on-axis at 5 and 15 cm deep in the water phantom. The whole profile, at both depths, was obtained using voxels of the same dimensions as for the on-axis dose to minimise volume-averaging. In all fields, for the PDDs a voxel depth (z-direction) of 1 mm was used close to the d_{max}, increased to 1 cm at depth greater than 20 cm in the water tank. Since the beam profile at the centre of a 4x4 cm^2 field is flat, a 2x2x0.5 mm^3 water voxel was used for computational efficiency to get the on-axis dose at 5 and 15 cm deep.

The output file of the DOSXYZnrc code is the ".3ddose" file that consists of 6 blocks. In the first block/row the number of voxels in x, y, z directions are represented by three

numbers (n_x, n_y, n_x). The next three blocks contain all the voxel boundaries (in cm) in the x, y, z directions represented by (n_x +1), (n_y +1) and (n_z +1) values. The last two blocks show all the dose (5th block) and 1 s.d. uncertainty (6th block) values, organized in arrays (n_x, n_y, n_x values) (Jabbari *et al* 2013). The ".3ddose" output files of the DOSXYZnrc simulations were loaded into MATLAB and analysed in order to extract all the desired PDDs and profiles.

2.3.3 Modelling the PTW diode detectors using the egs_chamber user-code

All the detectors studied in this project (both the un-modified and the modified prototypes of the two sets of PTW diodes) were modelled in detail within the egs_chamber (Kawrakow 2005, Wulff *et al* 2008) code using the EGS++ geometry package (Kawrakow 2005) according to the manufacturer's confidential technical drawings. Monte-Carlo simulations were then carried out using the egs_chamber code to calculate the response of all the detectors in small radiation fields of interest (especially in the 0.5x0.5 cm^2 field) and in the 4x4 cm^2 (machine-specific-reference, f_{msr} field). The phase space files generated in BEAMnrc for the 6 MV and the 15 MV beam models were again used as a source for each field size to irradiate the detectors.

The detectors were positioned in a 50x50x50 cm^3 water tank located at an SSD of 100 cm, aligned parallel to the beam, at the centre of each field (on-axis) with their sensitive-volumes at 5 and 15 cm depths (as shown in figure 2.3) to get static measurement dose values. For the beam profiles the detectors were positioned in exactly the same way but now sensitive-volume doses were calculated at various positions off-axis as well. To decrease the simulation time only half profiles were obtained since they can be considered to be completely symmetrical. For the PDD curves the detectors were simulated at first with their sensitive-volume at zero depth in water, and values of dose were calculated down to 35 cm deep in the virtual water tank. In order to make the PDD curves more realistic, a 0.5 cm thick air slab was "added" on top of the water tank and more data were obtained by now setting the detector's sensitive volume above the water

surface. In this way, it was possible to observe a sharp transition in the gradient of the PDD curve (a "kick") when the top of the detector is first submerged in the water tank.

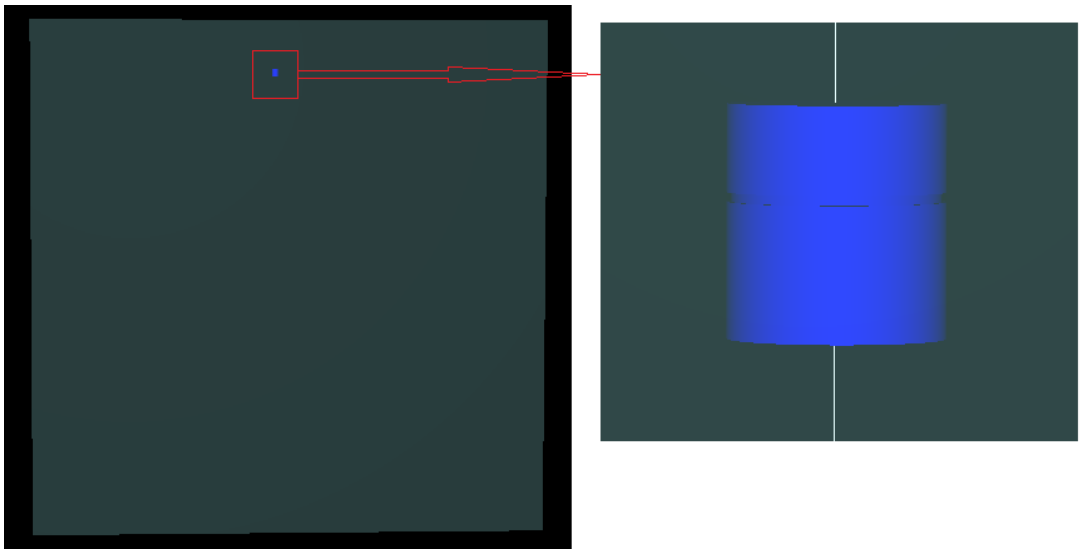

Figure 2.3: The diode detector is positioned in the virtual water tank (left), aligned parallel to the beam, with the top of its sensitive volume at a depth of 5 cm. In the image on the right the z-axis was added to clarify the detector's orientation. Both images were obtained within the egs_chamber code using the geometry viewer.

Considering the densities and thicknesses of the materials surrounding the diode sensitive volume and the range of particles, global ECUT and PCUT values were set to 0.521 and 0.001 MeV, respectively. To test the cut-off values used, egs_chamber simulations were also completed for selected detectors of both sets with ECUT = 0.512 MeV, proving that the lower ECUT value does not affect the calculated value of dose (results were in agreement within 1 s.d. statistical uncertainty). The photon cross-section enhancement (XCSE) variance reduction technique was used within a shell extending 2 cm beyond the sensitive-volume, with a 128 enhancement factor as described by Wulff *et al* (2008). Variance reduction techniques have been developed to substantially decrease the variance of a simulation's result for a given number of histories without introducing bias, thereby allowing MC calculations to be completed in a much shorter time.

The variance reduction technique used (XCSE) is very useful to speed-up MC simulations since it "forces" interactions of simulated particles in the specified region of interest (i.e. in the proximity of the detector's sensitive volume), or more accurately, substantially increases their probability of occurring, and then down-weights the resulting dose to avoid biasing the calculations. The radiation transport parameters and both the boundary crossing and electron-step algorithms were selected in a way to maintain consistency with the DOSXYZnrc simulations, and provide the most accurate results the EGSnrc code can produce (by activating all the available radiation transport parameters). As an additional check, selected simulations were repeated but now by setting the radiation transport parameters (e.g. atomic relaxations, spin effects etc.) off; no change was observed in the results for any of the MC calculations completed.

Running large numbers of particle histories for all the fields measured (small fields, e.g. 0.5x0.5 and 0.7x0.7 cm^2, and the 4x4 cm^2 reference field) we achieved a precision of better than ± 0.5% (2 s.d.) for the calculated doses for the static on-axis measurements at both depths and for both beam models. The statistical uncertainty in doses near the field edges (where the particle interactions are much less) was limited to less than 0.7% (2 s.d.). The statistical uncertainties on the results of all the MC simulations completed are the fractional errors reported by the different EGSnrc user-codes used. Values of correction factors $k_{Q_{clin},Q_{msr}}^{f_{clin},f_{msr}}$ were calculated for all the diode detectors positioned on-axis in the different small fields and calibrated in a 4×4 cm^2 machine-specific reference field, using equation 1.10 together with the detector sensitive-volume doses, $\overline{D}_{det}$, and point-like water voxel doses, $D_{wat\text{-}point}$ in the absence of the detector, computed in the small fields of interest and in the 4×4 cm^2 reference field.

2.3.3.1 Description of the modelled silicon diode detectors

The PTW 60017 Original diode detector was modelled first and then all the other detectors of the first set were "built" by introducing a precisely-formed air-gap (of different thickness as shown in table 1, section 2.1.1) between the main body of the detector and the RW3 cap. Regarding the second set of detectors, the PTW 60023 un-

modified detector (no air-gap added) model was created first and then the modified prototype with serial number 1518_30 was simulated, both according to PTW's confidential detector blueprints.

All the materials used in the detectors were added in the detector models by creating the necessary PEGS4 data-files and all the dimensions were set to match with reality. The different sensitive volumes of the two sets of diodes were simulated in detail and all the modifications in the geometry of the second set (compared to the first one) were made in the new detector model. According to the manufacturer's instructions the "old" 1 mm air-gap Prototype diode (characterised by Underwood *et al* 2015) was modelled with a cylindrical PMMA (poly-methyl methacrylate) ring of diameter 4.7 mm, which is not present in the rest of the modified detectors (1162 - 1167). As shown in figure 2.4, for detectors 1162 - 1167, the PMMA material was completely removed and RW3 plastic caps with thicker tops were used, in this way reducing the width of the air-gaps.

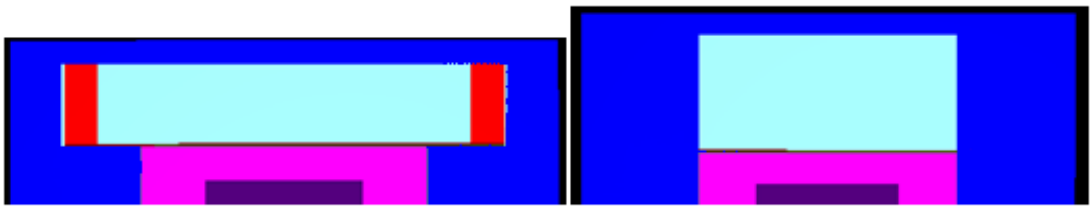

Figure 2.4: An illustration of the difference between the "old" Prototype 1 mm air-gap detector (left) with the PMMA spacer ring (in red colour) and the 1167 modified detector (right), with a 1.6 mm thick air-gap, but without any PMMA material and a RW3 plastic cap (in dark blue) with thicker top. The width of the air-gap in the "old" Prototype diode is 4.7 mm. Air is shown in light blue. The rest materials of the diode models are shown in dark blue, same as the RW3 plastic, and only the top parts of the detector models are shown for confidentiality reasons. The diagrams were obtained within the egs_chamber code using the geometry viewer.

In order to further investigate the effect of the air-gaps on the detectors' response the modified detectors of the first set (1162 - 1167 diode detectors) were modelled again, but now modifying the width (rather than thickness) of the air-gap. For this purpose, two different variants of the 1162 - 1167 detectors were "created" using the egs_chamber code, the "wider" air-gap detectors and the "even wider" ones. The variation in the width of the air-gap of the same detector, i.e. the 1167 diode, is presented in figure 2.5.

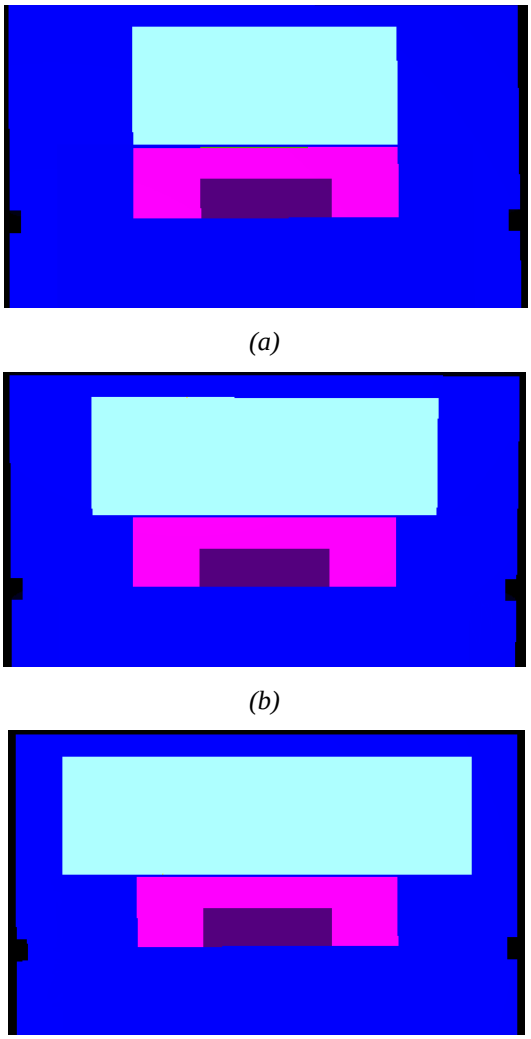

(a)

(b)

(c)

Figure 2.5: A schematic representation of the 1167 modified diode with (a) its real 3.6 mm wide air-gap, (b) the "wider" 4.7 mm, and the "even wider" 5.6 mm air-gap. Air is shown in light blue, the silicon cuboid in purple and the housing of the sensitive material in pink colour. All the remaining materials of the diode are shown in dark blue, same as the outer RW3 casing of the detector, to limit the complexity of the diagrams and to allow a more straightforward comparison between the widths of the air-gap and the detector's sensitive material in each case.

The diameter of the initial (real) air-gap was 3.6 mm (figure 2.5, part a). The "wider" air-gap was selected to be 4.7 mm (figure 2.5, part b) and the "even wider" one 5.6 mm (figure 2.5, part c) in diameter.

Chapter 3

Original set of detectors – 6 MV results

3.1 Introduction

Considering the increasing use of small radiation fields in modern radiotherapy and several previous publications (McKerracher and Twaites 1999, 2002, Das *et al* 2008, Cranmer-Sargison *et al* 2012, Charles *et al* 2013, 2014, Underwood *et al* 2015) pointing to the direction of silicon diodes as a good choice for small-field dosimetry, this chapter focuses on the detailed characterisation of a set of diode detectors provided by PTW. This set comprises the PTW 60017 Original diode (with no air-gap added) and the 1 mm air-gap "old" Prototype diode, both previously characterised by Underwood *et al* (2015), along with six new (Type No. 60017) modified diode detectors (diodes "1162" - "1167"). Based on the "mass-density compensation" principle (Underwood *et al* 2013b), first proposed by Underwood *et al* (2012) and later validated for silicon diodes both computationally (Charles *et al* 2013) and experimentally (Charles *et al* 2014), the PTW dosimetry diodes tested in this work were manufactured by deliberately introducing air-gaps of different thickness above their sensitive region to compensate for silicon's high density (compared to water) and eventually improve the dosimeter's response in small radiation fields.

The PTW 60017 Original diode with no air-gap added, the 1 mm air-gap "old" Prototype and six modified silicon diodes (1162 - 1167) with air-gaps ranging from 0.6 to 1.6 mm in thickness (section 2.1.1, table 2.1) have been thoroughly tested and the experimental and computational evaluation of their performance in the most commonly used nominal energy beam (6 MV) for external beam radiotherapy is the subject of this chapter. The data presented comprise on-axis *k* correction factors (under the Alfonso *et al* 2008 formalism), percentage depth doses (PDD curves) along with an analysis regarding

changes in the location of the detector's effective point of measurement (EPOM), and off-axis *k* diode profiles providing information about the detector's response across the measured radiation fields. The purpose of the work in this chapter is to confirm previous findings of other groups (Charles *et al* 2013, 2014, Underwood *et al* 2015) regarding the validity of the (air-gap based) density compensation method for silicon diodes, evaluate the response of the (not previously tested) 1162 - 1167 modified detectors, and identify the optimal air-gap thickness, for the PTW type 60017 modified diodes, attempting to identify a "correction factor free" small-field dosimeter.

Monte-Carlo simulations can be used as a comparison to experimentally obtained data, and to check the validity of experimental results especially when using not commercially available detectors whose response is not fully evaluated, as is the case for the modified diode detectors 1162 - 1167. Underwood *et al* (2015) published MC simulated results regarding density compensated silicon diodes that were in good agreement with their experimentally determined ones, and Charles *et al* (2013, 2014) used both experimental and computational methods to demonstrate improvements in the response of silicon diodes in small radiation fields when the air-gap based density compensation method is applied. For the computational studies of this chapter the EGSnrc (Kawrakow *et al* 2011) MC radiation transport code system was used; all the detectors of the first set were simulated in detail according to PTW's blueprints and several calculations were carried out, using a 6 MV beam model, providing results about their response and allowing comparisons with the experimentally-obtained data. Finally, computational methods were also used to further investigate the effect of the air-gaps on detector's response by creating additional diode models with air-gaps different to those physically manufactured.

3.2 Methods

3.2.1 Experimental methods for a 6 MV photon beam – measurement details

All the unshielded silicon diodes of the first set have been used to obtain the necessary experimental data for their characterisation in a 6 MV photon beam. Measurements were

completed with each detector positioned in the "Blue Phantom 2" scanning water tank, connected to the electrometer box via its connection cable, and without applying a bias voltage. After setting the dimensions of each field size using just the collimator jaws – the MLCs were fully retracted – each detector was carefully positioned in the centre of the field and was then irradiated. No reference detector was used at any point of the experimental work to avoid any additional perturbation of the charge particle fluence. All measurements for a specific field, either using the diode detectors or EBT3 gafchromic film, (including the measurements in the 4x4 cm^2 reference field) were made within two hours to minimise any issues with the possible variation in the accelerator output during the day.

For any type of measurements (output factors, PDDs or beam profiles), either in a small or in a wider square field, diodes were positioned vertically to the water surface, parallel to the beam axis, as also described by Beddar *et al* (1994), Scott *et al* (2008), Charles *et al* (2014) and Underwood *et al* (2015).

On-axis $k_{Q_{clin},Q_{msr}}^{f_{clin},f_{msr}}$ correction factors

Under the formalism established by the IAEA/AAPM group (Alfonso *et al* 2008) the on-axis correction factors were calculated according to Eq. 1.10:

$$k_{Q_{clin},Q_{msr}}^{f_{clin},f_{msr}} = \left[\frac{\left(D_{wat-point}\right)_{Q_{clin}}^{f_{clin}} \;/\; M_{Q_{clin}}^{f_{clin}}}{\left(D_{wat-point}\right)_{Q_{msr}}^{f_{msr}} \;/\; M_{Q_{msr}}^{f_{msr}}}\right]$$

using each detector's readings (M) in both the various clinical fields (f_{clin}) and the machine-specific reference field (f_{msr}) field, at 5 and 15 cm deep in water (SSD = 100 cm), and using EBT3 film to determine the dose to a point of water ($D_{wat-point}$) for the smaller clinical fields, i.e. 0.5x0.5 cm^2, 0.7x0.7 cm^2, 1x1 cm^2 and 1.5x1.5 cm^2, and the

machine-specific reference field, i.e. 4x4 cm^2, and the "CC13" ion chamber for the wider clinical fields measured (square fields of side-length above 3 cm). On-axis $k_{Q_{clin},Q_{msr}}^{f_{clin},f_{msr}}$ values were calculated for all the detectors of the first set, at both depths in water, to experimentally evaluate their response and decide the optimal air-gap thickness for the PTW type 60017 modified diodes. Both $(D_{wat-point})$ and (M) can be thought of as dose and reading per monitor unit (MU). Therefore, for each measurement a convenient number of MUs was set producing a clinically representative dose, of the order of a gray or two, and then corrected for differences between the MUs set. The reference conditions (4x4 cm^2 field, 200 MUs, 100 cm SSD and 5 cm deep in water) were kept the same even when calculating correction factors at 15 cm deep for the different clinical fields.

Percentage depth dose data (PDDs)

To obtain PDD data for any field size the long axis of the diodes was positioned perpendicular to the water surface in the "Blue Phantom 2", parallel to the beam axis at the "zero" depth position (defined in section 2.2.1) and doses were measured down to a depth of 30 cm in the water tank. A "global" shift of 1.33 mm was made to the PDD graphs (of all the detectors) based on the manufacturer's information about the location of the EPOM in the PTW 60017 Original diode.

Central axis depth doses have been measured using the diodes for the 6MV beam energy, in a 4x4 cm^2 field, to plot the PDD data for each detector and investigate if the existence of air-gaps of different thickness in the modified diodes causes any change in the location of the instrument's EPOM compared to the (no air-gap) 60017 Original diode. Additional PDD data were obtained for the 4x4 cm^2 reference field with the PTW "Semiflex" ion chamber, used at CCC to measure the Varian "TrueBeam" linac. The "Semiflex" ion chamber PDD data were added to the diode PDD plots as a comparison and to investigate if the air-gaps introduced in the modified diodes affect the overall shape of the measured PDD curve.

The same procedure, as for the reference 4x4 cm^2 field, was followed to acquire PDD data for all the diode detectors of the original set at smaller field-sizes (0.5x0.5, 0.7x0.7, 1x1, 1.5x1.5 cm^2) too; apart from the "global" 1.33 mm shift, which was again applied to the PDD curves of all the diodes, an additional small correction was made, when necessary, to move the "kick"[1] of the experimental data so that it occurs at a supposed measurement depth of 1.33 mm, i.e. the point at which it occurs for the no air-gap Original diode. The experimental PDD data were plotted focusing on different regions (depths in water) of the curves in order to observe any shift in the EPOM of the modified diodes due to the different air-gaps introduced. Graphs showing the build-up region of the PDD curves were generated providing useful results regarding changes in the location of the EPOM of the modified diodes.

Beam profiles – off-axis $k_{Q_{clin},Q_{msr}}^{f_{clin},f_{msr}}$ profiles

In-line and cross-line beam (6 MV) profiles were obtained using both the diode detectors and a number of EBT3 gafchromic films, at both 5 and 15 cm deep in water, providing information about the full-width half maximum (FWHM) and penumbra values of the different fields measured. For the smallest clinical field measured (0.5 cm square field, at 5 cm deep) graphs showing diode experimental data of the FWHM and penumbra values are presented, together with EBT3 film data added to the plots as a comparison.

Off-axis $k_{Q_{clin},Q_{msr}}^{f_{clin},f_{msr}}$ values, calculated according to Eq. 1.10 but now with the clinical field data obtained at various positions off-axis at 5cm deep, were plotted against the off-axis distance (in mm) to experimentally evaluate the performance of the diodes across a small (0.5x0.5 cm^2) and a wider (1.5x1.5 cm^2) field. In order to get the off-axis *k* profile plot for a diode in a specific field and depth, the average of the film profiles was divided by the diode profile (both normalised to one on-axis and interpolated onto the same x-axis, distance in mm) and then this "ratio" was multiplied by the on-axis *k* value that was calculated for this diode in the same field at the same depth. Off-axis *k* profiles were plotted for all the diode detectors in the 0.5x0.5 cm^2 field, and for the

[1] The "kick", i.e. a sharp transition in the gradient of the PDD curve, occurs when the diode top exits the water.

60017 Original diode and the "best" four ones (according to the 0.5x0.5 cm^2 experimentally determined on-axis *k* values) in the 1.5x1.5 cm^2 field, both at 5 cm deep in water.

For the smallest field measured (0.5x0.5 cm^2), the point of the film with the maximum value of dose was used as the on-axis point (x=0), because the peak is well defined and not that much affected by noise. On the other hand, in the 1.5x1.5 cm^2 field there is a quite flat region in the profile and noise has the potential to significantly bias the maximum dose value. For this reason, the geometric center of the film was considered as the origin of the film profile (x=0). Then, exactly the same procedure was followed for both field sizes to generate the off-axis *k* profiles; both the film and the diode profiles were plotted in the same graph and an appropriate shift (not greater than 0.4 mm for any of the diodes) was applied to the diode profile in order to get the best match between the two profiles. The last step was to use the (average) film and the (shifted) diode profiles to get the off-axis *k* profile for each diode and the corresponding dose error graphs (over-response of uncorrected diode readings when a dose of 1 Gy was delivered on-axis).

3.2.2 Monte-Carlo methods for a 6 MV beam model

A previously validated and utilised (Underwood *et al* 2013a, Fenwick *et al* 2018a) Varian Clinac iX 6 MV beam model, created with the BEAMnrc (Rogers *et al* 2011) MC code system, was used to generate the 6 MV phase-space files that were used as a source of particles for the simulations completed within the DOSXYZnrc and egs_chamber user-codes. For the original set of detectors MC simulations were completed mainly in the 0.5x0.5 cm^2 field, i.e. the one in which the detectors behave the most non-ideally, and in the 4x4 cm^2, the machine-specific reference field of this work. The phase-space files used for the 0.5x0.5 and 4x4 cm^2 fields contain 2.9 x 10^7 and 1.4 x 10^9 particles, respectively (Fenwick *et al* 2018a).

To score the energy deposition in specific water voxels of a 50x50x50 cm^3 virtual water phantom the DOSXYZnrc MC code was used with global energy cut-off values of

ECUT = 0.521 MeV and PCUT = 0.001 MeV. With the phase-space files being scored at a 100 cm SSD for the 6 MV beam model, the distance between the source and the isocenter was set and maintained to zero for all the DOSXYZnrc calculations. For the $k_{Q_{clin},Q_{msr}}^{f_{clin},f_{msr}}$ values determined computationally according to Eq. 1.10, the small field doses were calculated for a point-like water voxel with dimensions 0.25x0.25x0.5 mm^3, whose centre lay on the beam central axis at 5 and 15 cm deep in water at an SSD of 100 cm. The whole profile, at both depths, was obtained using voxels of the same dimensions as for the on-axis dose to minimise volume-averaging. For the PDD data a voxel depth (z-direction) of 1 mm was used close to the d_{max}, increased to 1 cm at depth greater than 20 cm in the water tank. Since the beam profile at the centre of a 4x4 cm^2 field is flat, a 2x2x0.5 mm^3 water voxel was used for computational efficiency to get the on-axis dose at 5 and 15 cm deep.

The detector models of the Original diode and all the modified detectors were created using the EGS++ geometry package (Kawrakow 2005) within the egs_chamber code (Wulff *et al* 2008) and MC calculations were completed with the detectors positioned in a 50x50x50 cm^3 water tank located at an SSD of 100 cm, aligned parallel to the beam, at the centre of each field (on-axis), to get static measurement (sensitive volume) dose values, at 5 and 15 cm deep, beam profiles[2] at both depths, and finally PDD data. The global ECUT and PCUT values were set to 0.521 and 0.001 MeV, respectively. For the egs_chamber MC calculations twelve different media were simulated in total and cross-sectional data were taken from the corresponding PEGS4 data-files, which either existed in the EGSnrc code system, e.g. water, or have been created (as described in section 2.3.1) using the EGSnrcMP package (Kawrakow *et al* 2006, 2011), e.g. RW3 plastic. For the geometry of each detector model approximately 1500 "regions" were specified and one of the simulated media was then assigned to each region.

[2] Only half profiles have been calculated with the detectors, since they can be considered to be completely symmetrical, substantially decreasing this way the simulation time.

3.3 Experimental results

3.3.1 On-axis $k_{Q_{clin},Q_{msr}}^{f_{clin},f_{msr}}$ correction factors

The on-axis $k_{Q_{clin},Q_{msr}}^{f_{clin},f_{msr}}$ correction factors (Alfonso *et a*l 2008), calculated using Eq. 1.10 at 5 cm deep in a 6 MV beam, for all the diode detectors of the first set are presented in figure 3.1. The $k_{Q_{clin},Q_{msr}}^{f_{clin},f_{msr}}$ values are plotted against the different clinical field sizes measured, spanning from 5 mm to 100 mm square fields. Detectors that under-respond in the small clinical fields, relative to the dose absorbed by a point of water, require a correction value greater than one, while for the ones that over-respond the calculated *k* value is less than one.

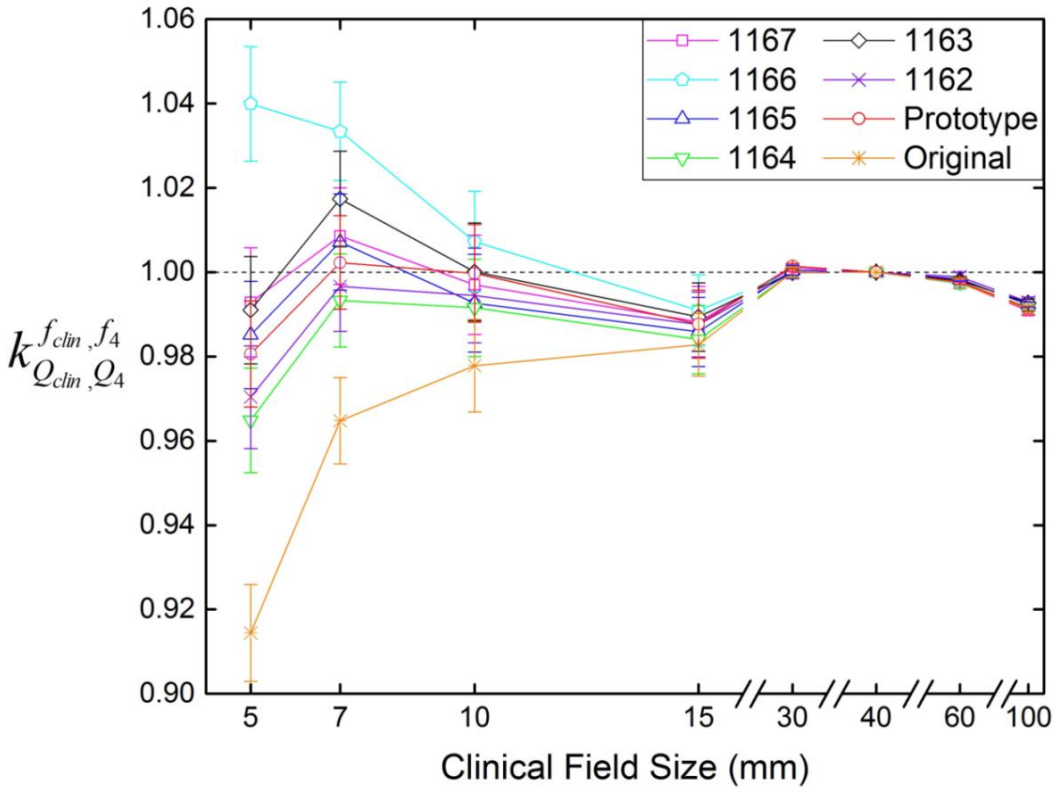

Figure 3.1: Experimental results for the on-axis correction factors for a 6 MV photon beam at ***5 cm deep*** *in water. All values were calculated using a 4x4 cm^2 as the machine-specific reference field, also measured at 5 cm deep; the correction factor for this field at 5 cm deep is by definition equal to one for all the detectors tested. Error bars show two standard deviations statistical uncertainties.*

From figure 3.1 it can be concluded that the detectors 1162, 1164, 1166 and the Original one are less good when measuring dose in small fields as their *k* values are quite far from one compared to the other four diodes. For this reason, those detectors showing less good response in small fields are deliberately omitted from figure 3.2 and the correction factors of only the "best" four diode detectors are shown. A small x-axis displacement has been introduced to this graph in order to separate the plots and increase clarity.

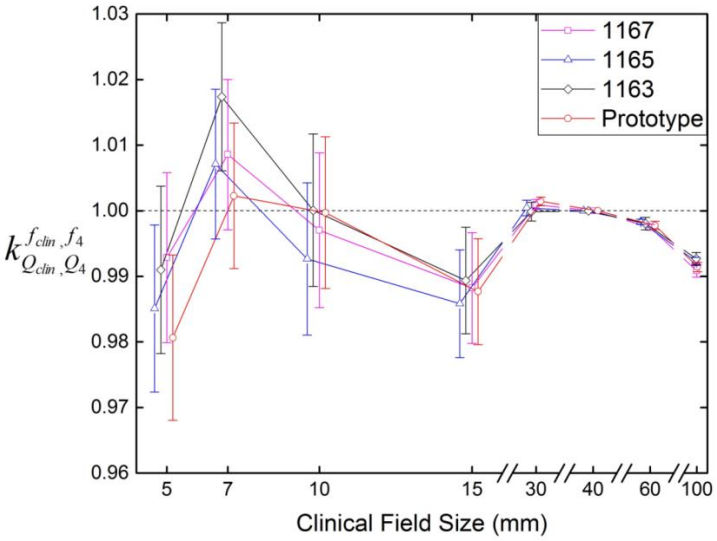

Figure 3.2: The on-axis correction factors for diodes 1167, 1165, 1163 and the "old" Prototype for a 6 MV beam at ***5 cm deep****. The* calculated correction factors of these detectors for any field size differ less than ± 2% from one. *The reference conditions are the same. The small displacement on the x-axis is done only to improve visibility of the graph. Error bars show two standard deviations statistical uncertainties.*

The (no air-gap) Original diode and the 1166 modified detector show the most non-ideal response with their *k* values in the smallest field measured, i.e. 0.5x0.5 cm^2, being 0.914 ± 0.011 and 1.040 ± 0.012 (2 s.d.), respectively. On the contrary, all *k* factors measured for the 1163, 1165, 1167 and the (1 mm air-gap) "old" Prototype detectors lie within ± 2% of 1.00, even for the smallest fields measured.

Similar trends are observed for the Alfonso *et al* (2008) on-axis correction factors at a greater depth in water (15 cm). The same experimentally-determined *k* values, but now with the EBT3 films used and (the top of) the sensitive volume of each diode at a water

depth of 15 cm in the various clinical fields measured, are presented in figure 3.3. Figure 3.4 comprises only the *k* values of the "best" four detectors (according to the 5 cm deep results) and the same, as in figure 3.2, small adjustment to the x-axis values has been made to improve the presentation.

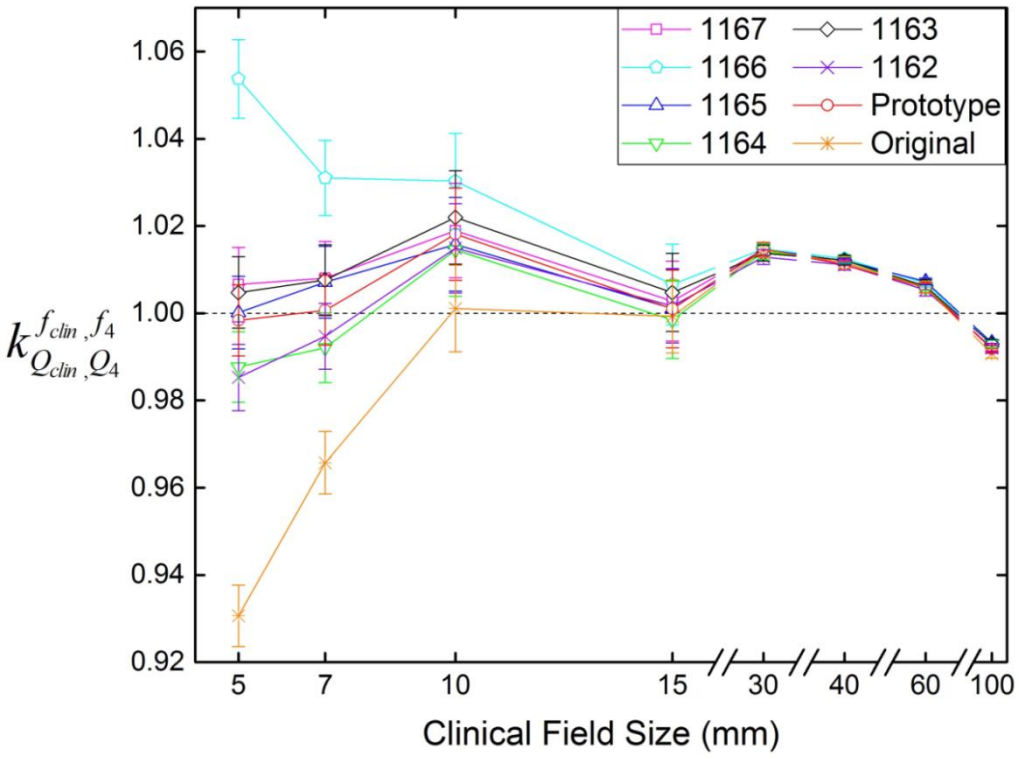

*Figure 3.3: Experimental results for the on-axis correction factors for a 6 MV beam at **15 cm deep** in water. All values are calculated using a 4x4 cm^2 machine specific reference (msr) field, measured at 5 cm deep. The k values calculated show divergent behavior of the diodes for field sizes smaller than 1.5x1.5 cm^2. Error bars show two standard deviations statistical uncertainties.*

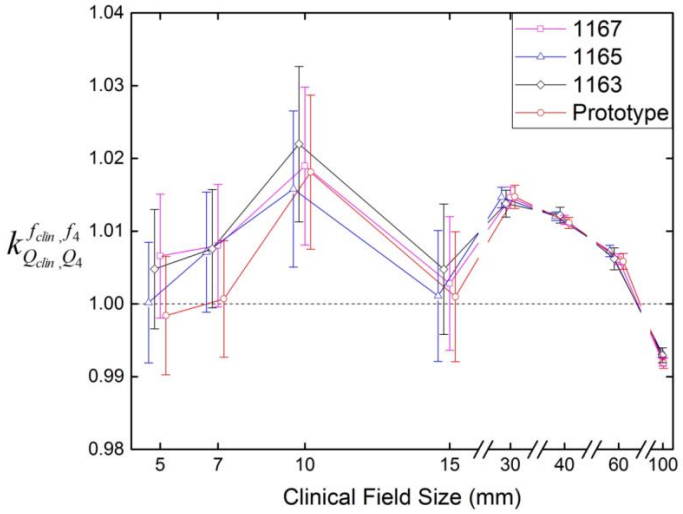

*Figure 3.4: The on-axis correction factors for diodes 1167, 1165, 1163 and the "old" Prototype for a 6 MV beam at **15 cm deep** in water. In agreement with the 5 cm deep results, all k values for these diodes lie within ± 2% of 1.00, apart from the 1163 detector in the 1x1 cm^2 field. The reference conditions are again the same (4x4 cm^2, 100 SSD, 5 cm deep). The small displacement on the x-axis is made only to improve visibility of the graph. Statistical uncertainties are shown at the ± 2 s.d. level.*

3.3.2 Percentage depth dose curves (PDDs) – EPOM shifts

For all the diode detectors of the first set the experimental PDD data in a 4x4 cm^2 field (i.e. the f_{msr} of this work) are presented in figure 3.5. All PDD curves for the diodes are plotted after applying the 1.33 mm shift based on the instructions of PTW regarding the effective point of measurement (EPOM) of the no air-gap 60017 Original detector. The data obtained with the PTW "Semiflex" ion chamber were also added to the plot (figure 3.5) in order to indicate the good agreement between depth dose curves measured for the 4x4 cm^2 field by the ion chamber and diode detectors.

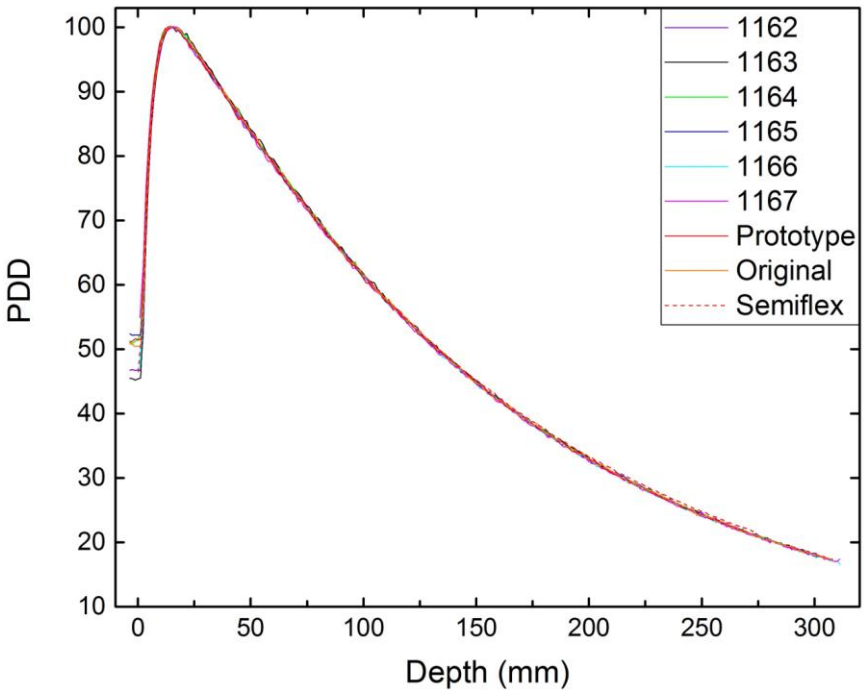

*Figure 3.5: Percentage depth dose (PDD) curves for all the diode detectors for a **4x4 cm²** field. The different thickness of the air-gap added in each modified diode does not affect the overall shape of the PDD curves; there is good agreement between the data measured with the "Semiflex" ion chamber and all the diodes tested.*

The same depth dose data in a 4x4 cm^2 field are plotted in figure 3.6 but now focusing on the build-up region of the PDD curves; it is evident from figure 3.6 that there is a difference (depth-shift) between the curve that rises first and the one that rises last.

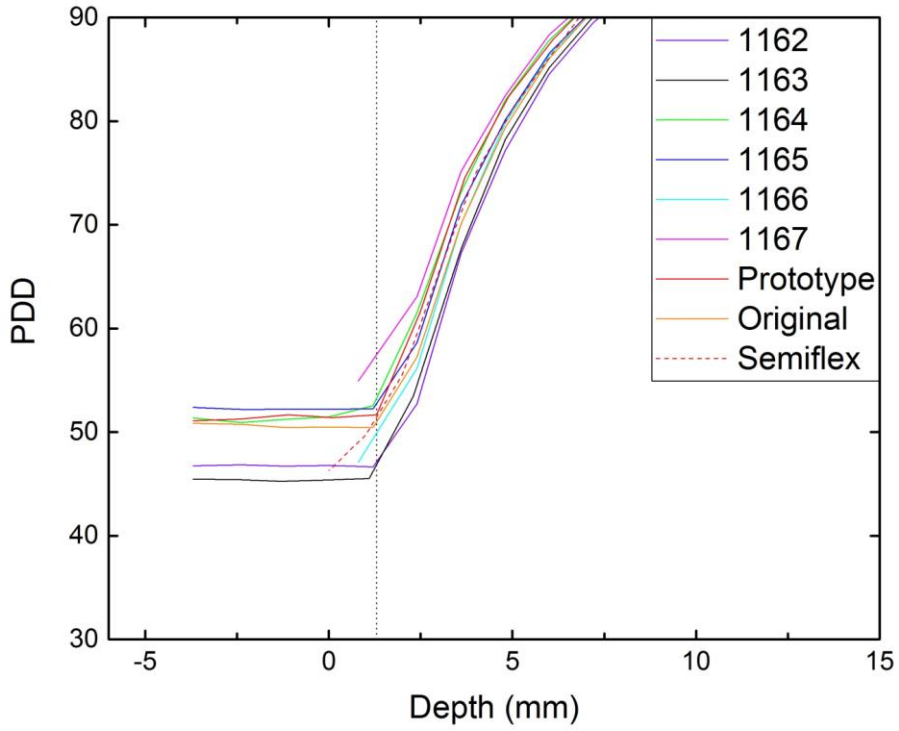

*Figure 3.6: PDD curves for a **4x4 cm²** field with a 1.33mm depth correction only. The dashed line indicates the 1.33 mm depth. The observed distance difference between the curves in the rising region means that the air-gaps added in the diodes affect the detectors' EPOMs.*

For the same field size (4x4 cm^2), PDD data in the d_{max} region obtained using all the detectors of the first set are plotted (figure 3.7a); in this region, the PDD curves are too noisy to observe any shift to the EPOM of the diodes due to the different air-gaps introduced. In addition, to investigate for potential EPOM shifts in the deeper region of the curves the PDD data at points deeper than the d_{max} are plotted for all the diodes (figure 3.7b).

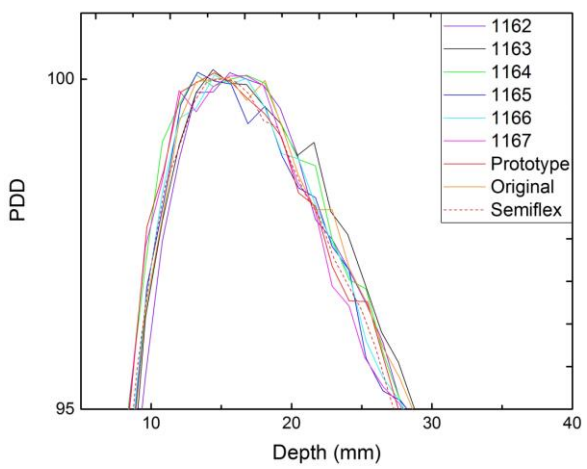

(a)

*Figure 3.7(a): PDD data for the **4x4 cm²** field shown in the d_{max} region only. Due to the noise, no shift could be observed at this point of the PDD curves.*

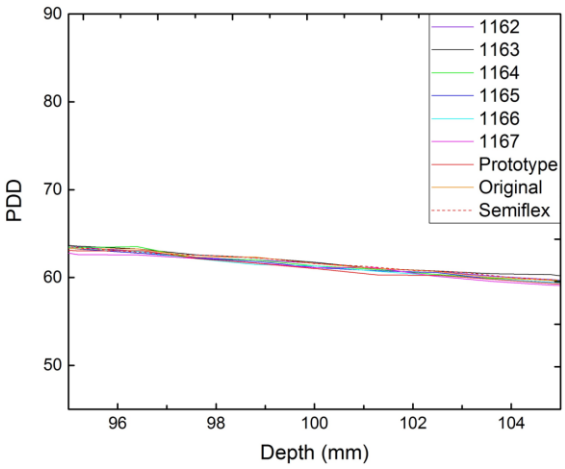

(b)

*Figure 3.7(b): PDD curves for **4x4 cm²**. The curves overlay in this region, there is no obvious shift after the d_{max} point for any of the modified detectors.*

PDD data were acquired using all the diodes at the smaller field-sizes (0.5x0.5, 0.7x0.7, 1.0x1.0 and 1.5x1.5 cm^2) too, for which data were measured at a finer depth-resolution (~ 0.3 mm) than for the 4x4 cm^2 field. For this reason, the location of the "kick" occurring when the diode top exits the water can only visually be corrected to within ± 0.5 mm for the 4x4 cm^2 field, compared to ± 0.15 mm for the other fields. Any better accuracy than this for the 4x4 cm^2 field would be due to our ability to set up the detectors more accurately than ± 0.5 mm. The improved resolution of the smaller fields allows to make, only when necessary, an additional small correction (apart from the "global" 1.33 mm one) to move the "kick" of the experimental data to a depth of 1.33 mm, the point at which it occurs for the un-modified (no air-gap) diode. The PDD data for the 0.5 cm square field (focused on the rising region of the curves) are presented in figure 3.8, whereas dose values obtained with the detectors at greater depths in water, after the d_{max} point, are shown in figure 3.9. The "kick" correction is made so that if the EPOMs of all the detectors were at the same depth as that of the Original (no air-gap) diode, then by arranging for all the "kicks" to occur at 1.3 mm depth where it really does for the Original diode, all the PDD curves would rise at the same point. As shown in figure 3.8 the curves do not rise at the same point, which means that there are EPOM differences between the detectors tested.

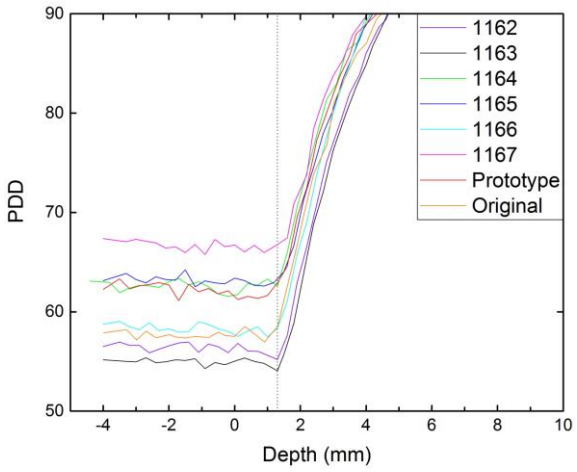

*Figure 3.8 (left): PDD curves for the **0.5x0.5 cm^2** field with each "kick" shifted to a depth of 1.33 mm. A ± 0.4 mm maximum distance (between the 1163, 1167 and the Original diodes) can be seen in the build-up region of the curves meaning the air-gaps added in the diodes slightly affect the detectors' EPOM.*

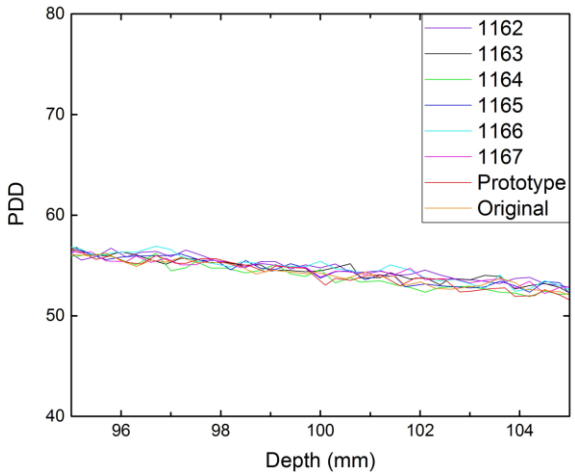

*Figure 3.9 (right): PDD curves for the **0.5x0.5 cm^2** field. Like in the 4 cm field, the curves overlay in this region, there is no obvious shift observed after the d_{max} point for any of the detectors.*

Similar observations regarding (small) changes in the location of the EPOM of the diodes were made for the PDD data in both the 0.7x0.7 and 1.5x1.5 cm^2 fields. In figure 3.10 the "kick" points region is presented for the 1.5x1.5 cm^2 field. As done with the 0.5 cm field PDD curves, additional slight "kick" corrections were applied to the data if necessary, moving the "kick" to a depth of 1.33 mm (indicated with a dashed line in the plot).

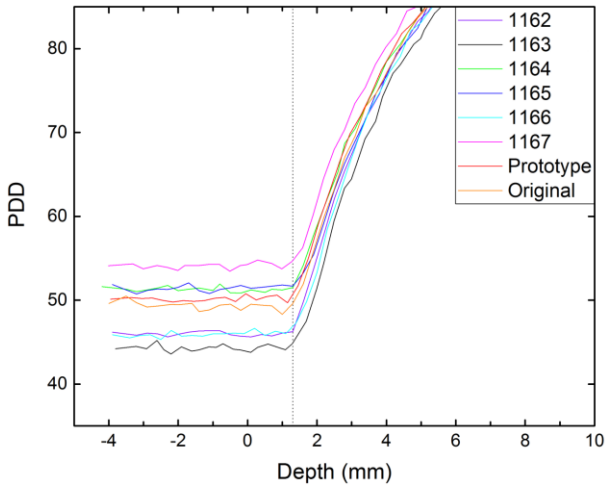

*Figure 3.10: PDD curves for the **1.5x1.5 cm^2** field with each "kick" shifted to a depth of 1.33 mm. A 0.4mm maximum distance (between the 1167 and the Original diode) can be seen again in the build-up region of the curves meaning the air-gaps added in the diodes slightly affect the detectors' EPOM.*

The observed PDD shifts (i.e. the distance between the PDD curve of the Original diode and all the others in the build-up region of the curve, at 80% of the max. dose) were calculated, and the corresponding EPOM shifts (having the opposite sign than the PDD shifts observed in figures 3.6, 3.8 and 3.10) are summarised in table 3.1. There is quite good agreement between the EPOM shifts measured in the three different (0.5, 1.5 and 4 cm square) fields, and especially for the "best" four diodes according to the 0.5x0.5 cm^2 *k* values **(1163, 1165, 1167 and "old" Prototype diodes)**.

	0.5x0.5 cm^2	1.5x1.5 cm^2	4x4 cm^2
DIODE	**EPOM shift (mm)**		
1162	-0.3	0.0	-0.3
1163	**-0.4**	**-0.3**	**-0.2**
1164	0.3	0.1	0.4
1165	**0.0**	**0.0**	**0.1**
1166	0.0	-0.1	0.1
1167	**0.4**	**0.4**	**0.5**
Prototype	**0.2**	**0.2**	**0.4**

Table 3.1: EPOM shifts (in mm) for the different field sizes measured at 6 MV. There is good agreement between the distances for the "best" 4 detectors, highlighted results, in all fields (~ 0.2mm consistency). No observed EPOM shift is larger than 0.5 mm. The negative sign indicates that a shift towards the water surface is necessary for the PDD curve of the modified detector (e.g. the 1163 diode) to match the data obtained using the Original diode.

The EPOM shifts previously shown (table 3.1) were calculated based on the PDD data of the diode detectors at the dose build-up region (before the d_{max} point). As mentioned before, figures 3.7(b) and 3.9 indicate that no obvious shift was observed for any of the detectors after the d_{max} point. However, it was considered necessary to further investigate the determination method of the EPOM shifts, trying now to identify the shift from the whole PDD curve. The idea of this new method was to apply the "pre-d_{max}" shift calculated for each detector (table 3.1) to the whole PDD curve and then compare all the PDD curves across a specific range of depths x_1 to x_2, where x_1 is the shallowest point at which all the curves overlay after applying the shift, and x_2 is the deepest point they were all measured. By then scaling each PDD curve so that the area under it between the depths x_1 and x_2 is the same, and interpolating all the PDD values onto the

same x points (depth in mm) it was possible to plot the ratio of the PDD data for each diode divided by the PDD data of the Original diode. This normalisation method is better than just normalising to 100% at d_{max}, because it is not influenced by noise in the vicinity of the d_{max} point. The graphs for the "best" four detectors according to the *k* factors (at 5cm deep) in the 0.5x0.5 cm^2 field are presented in figure 3.11.

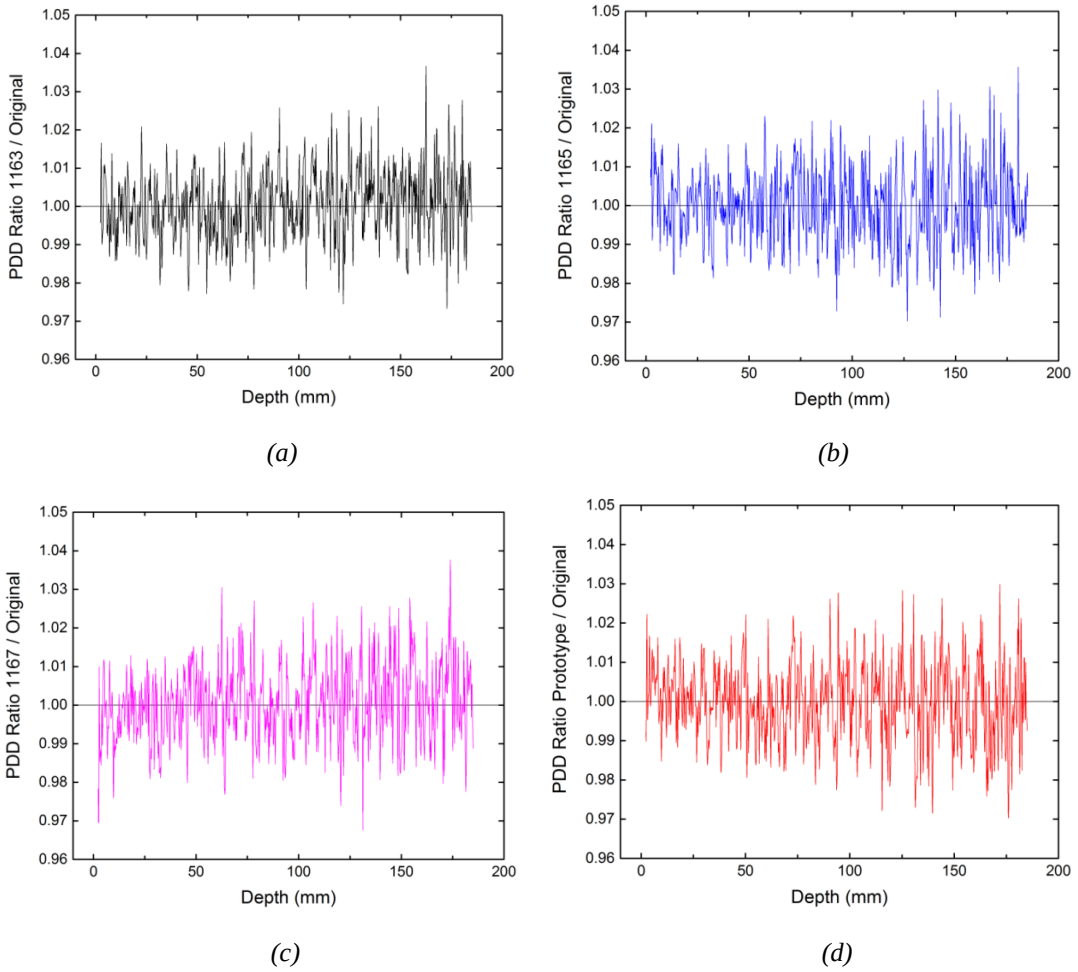

Figure 3.11: Ratios of the shifted (based on the pre-d_{max} observed EPOM shift) and scaled PDD data for diodes 1163 (a), 1165 (b), 1167 (c) and the 1 mm air-gap "old" Prototype (d) divided by the PDD data of the no air-gap 60017 Original diode in the 0.5x0.5 cm^2 field. The "pre-d_{max}" shift for each diode was applied to the whole PDD curve. No visible structure is observed in the plot of any of the diodes.

The same approach was considered to check the validity of the EPOM shifts calculated from the PDD curves before the d_{max} point in the reference, 4x4 cm^2 field. The "pre-

d_{max}" shifts for this field (shown in table 3.1 too) were applied to the whole of the PDD curve of each detector. The ratios of the PDDs were again plotted and only the graphs for diodes 1165 and the "old" Prototype are included in figure 3.12, to avoid presenting excessive amount of data all leading to the same conclusions.

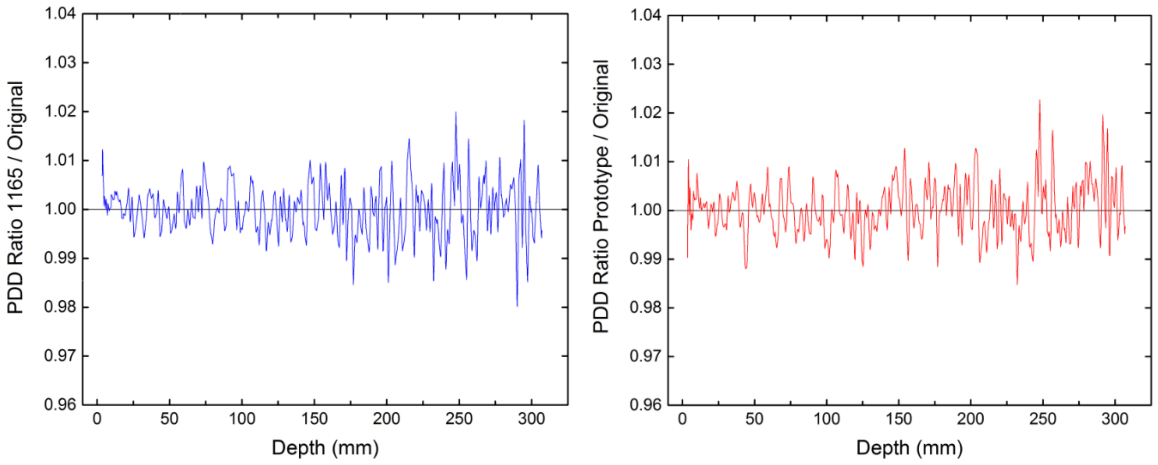

(a) *(b)*

*Figure 3.12: Ratios of the shifted and scaled PDD data for diodes 1165 (a) and Prototype (b) divided by the PDD data of the original diode all in the **4x4 cm^2** field. The "pre-dmax" shift for each diode was applied to the whole PDD curve. In agreement with the results of the 0.5 cm field PDD ratios, no visible structure can be seen for any of the diode detectors.*

To complete the PDD analysis and the detailed investigation for shifts in the diodes' EPOMs due to the existence of thin air-gaps, one final check was performed; the ratios of the PDDs in the 4x4 cm^2 field were plotted again but this time with the "pre-d_{max}" EPOM shifts of the 0.5x0.5 cm^2 field applied to the PDD curves of the modified diodes. The reason for this final check is to demonstrate that the PDD curves of the modified diodes and the PTW 60017 Original one overlay beyond d_{max}, irrespective of slight differences in EPOM shifts obtained from fields of different size. Consequently, there is no need to apply any additional EPOM shift to the PDD curves apart from the one calculated in the region before d_{max}. Selected graphs created for this check are presented in figure 3.13.

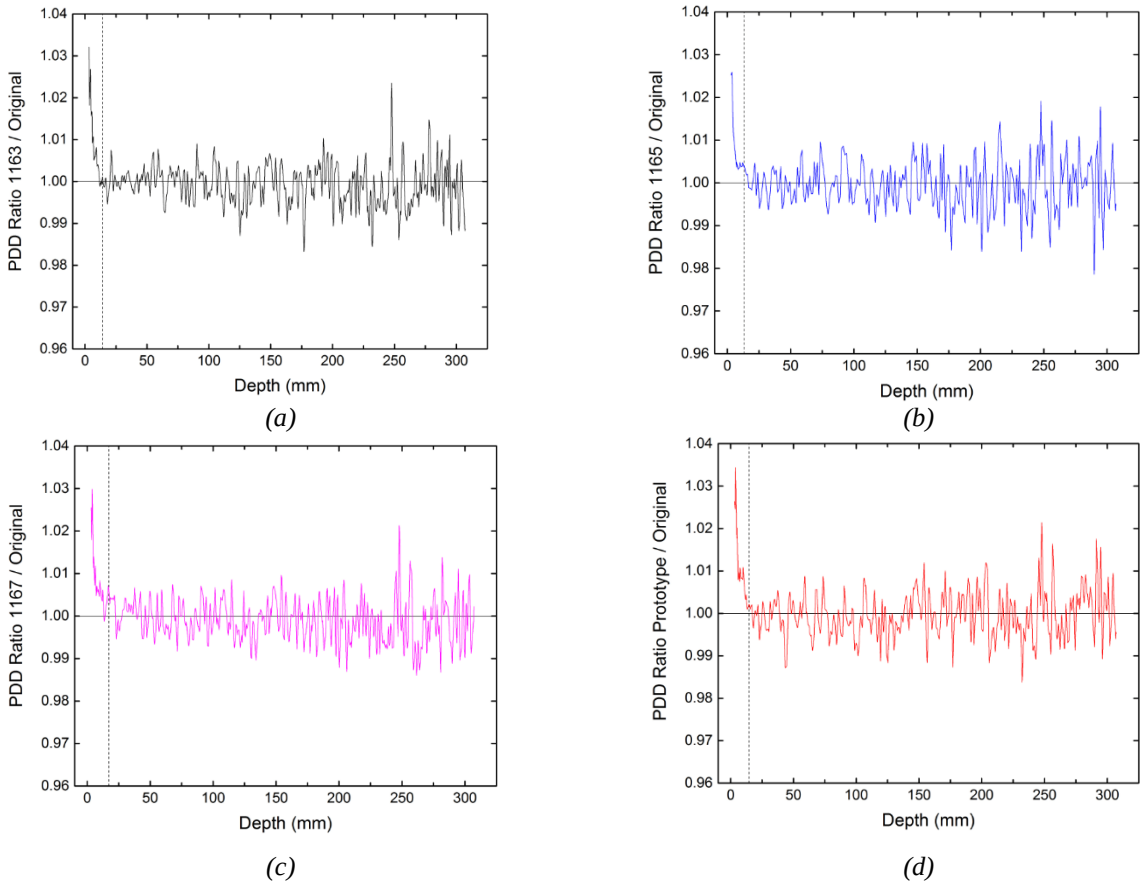

Figure 3.13: Ratios of the shifted and scaled PDD data for diodes 1163 (a), 1165 (b), 1167 (c) and "old" Prototype (d) divided by the PDD data of the Original diode all in a ***4x4 cm^2*** *field. The "pre-d_{max}" shift applied to each of the modified diodes PDD curve is the one calculated from the data of the 0.5x0.5 cm^2 field. No visible structure is observed beyond d_{max}, meaning that the PDDs of the modified diodes overlay quite well with the Original (un-modified) PDD curve in this region after applying the "pre-d_{max}" EPOM shifts. The mismatch of the data up to d_{max} can be attributed to the spatial sampling of the data causing slight spatial errors to the measurements. The vertical dashed lines indicate the d_{max} point for each of the modified diodes tested.*

3.3.3 Beam profile measurements – off-axis $k_{Q_{clin},Q_{msr}}^{f_{clin},f_{msr}}$ profiles

a) Full-width half maximum (FWHM) and penumbra values

In figure 3.14 the profile full width half maxima (FWHMs) values for the 6 MV beam in a 0.5x0.5 cm^2 field, at 5 cm deep, are presented. Data obtained experimentally using all the diode detectors are shown and EBT3 radiochromic film data are used as a comparison. The horizontal black lines represent the mean values obtained from the irradiation of ten EBT3 films in total. The one and two standard deviations from the mean value are indicated by the dark grey and light grey bands, respectively.

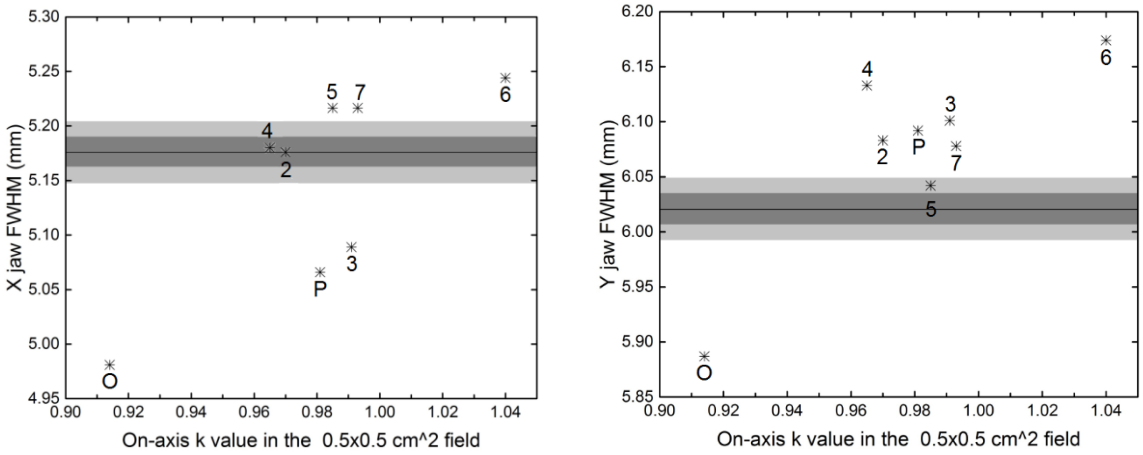

(a) *(b)*

Figure 3.14: Profile FWHMs (a) for X-jaw and (b) for Y-jaw of all the diodes in a ***0.5x0.5 cm^2*** *field at SSD = 100 cm and* ***5 cm deep****. Stars show the data of the diodes and the black horizontal line the average value of the irradiated EBT3 films. The dark and light grey bands show the 1 and 2 s.d. from the mean value. For the x-axis of both graphs the on-axis k values of the diodes in the 0.5x0.5 cm^2 field at 5cm deep were used. Diode names are shortened to improve presentation of the graphs, O: Original, P: Prototype, 1162 - 1167 diodes: 2 - 7.*

The full width at 20% of the maximum of the beam profile for each diode in the 0.5x0.5 cm^2 field was also plotted against the on-axis *k* value of each diode in the 0.5x0.5 cm^2 field (at 5 cm deep) and the graphs are presented in figure 3.15. The horizontal black lines indicate the average value obtained from the EBT3 films and the dark grey and light grey bands the one and two standard deviations from the mean value, respectively.

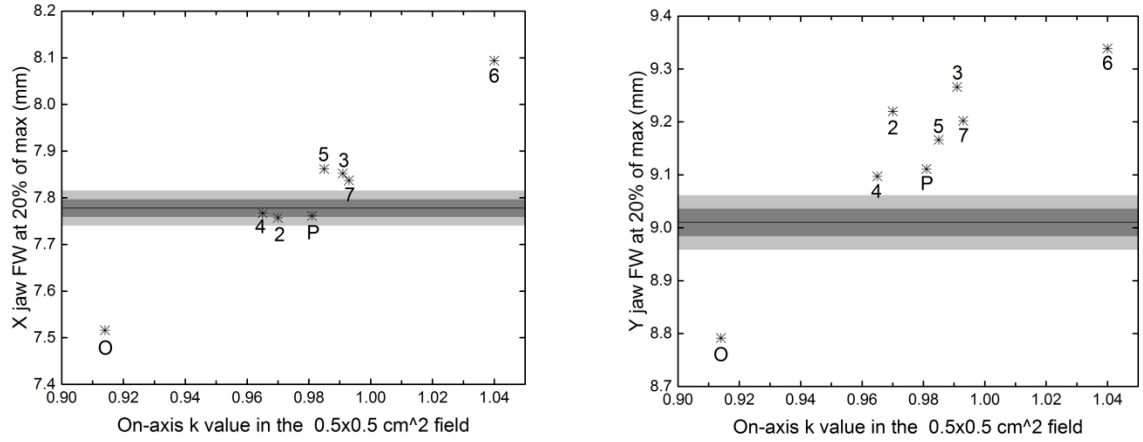

(a) *(b)*

Figure 3.15: Full Width at 20% of maximum (a) for X-jaw and (b) for Y-jaw measured with all the diodes in a ***0.5x0.5 cm^2*** *field at SSD = 100 cm and* ***5 cm deep.*** *O: Original, P: Prototype, 1162 - 1167: 2 - 7.*

Finally, the 20:80% penumbra values for all the diodes in the 0.5x0.5 cm^2 field, at 5 cm deep, are shown in figure 3.16.

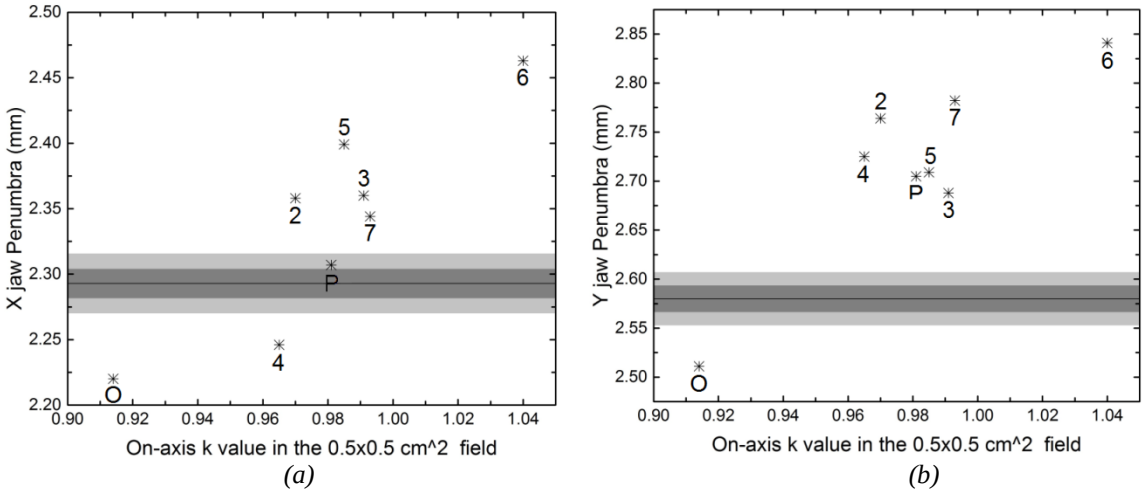

(a) *(b)*

*Figure 3.16: 20:80% Penumbra widths X-jaw (a) and Y-jaw (b) of all the diodes in a **0.5x0.5 cm^2 field** at SSD = 100 cm and **5 cm deep**. Stars show the data of the diodes and the black horizontal line the average value of 10 irradiated EBT3 films. Again, the one and two standard deviations from the mean value are shown by the dark grey and light grey bands, respectively. For the x-axis of both graphs the on-axis k values of the diodes in the 0.5x0.5 cm^2 field at 5cm deep are used. O: Original, P: Prototype, 1162 - 1167: 2 - 7.*

b) Off-axis *k* profiles

For the smallest field measured, 0.5x0.5 cm^2, the off-axis $k_{Q_{0.5},Q_4}^{f_{0.5},f_4}$ profiles (in the cross-line direction, with the X pair of jaws defining the field at the edges the detectors move) were plotted for all the diodes following the procedure described in section 3.2.1. Figure 3.17 shows the experimental results for the "old" Prototype (1 mm air-gap) diode. To provide a more complete illustration of the method used and the profile match, the film and Prototype diode profiles are plotted together against the same off-axis distance (top plot in figure 3.17). The errors bars in the off-axis *k* profile graph (middle plot) display the combined effects of fractional uncertainty of the film and the diode profiles, thus providing an estimate of the noise in three different parts of the *k* profile.

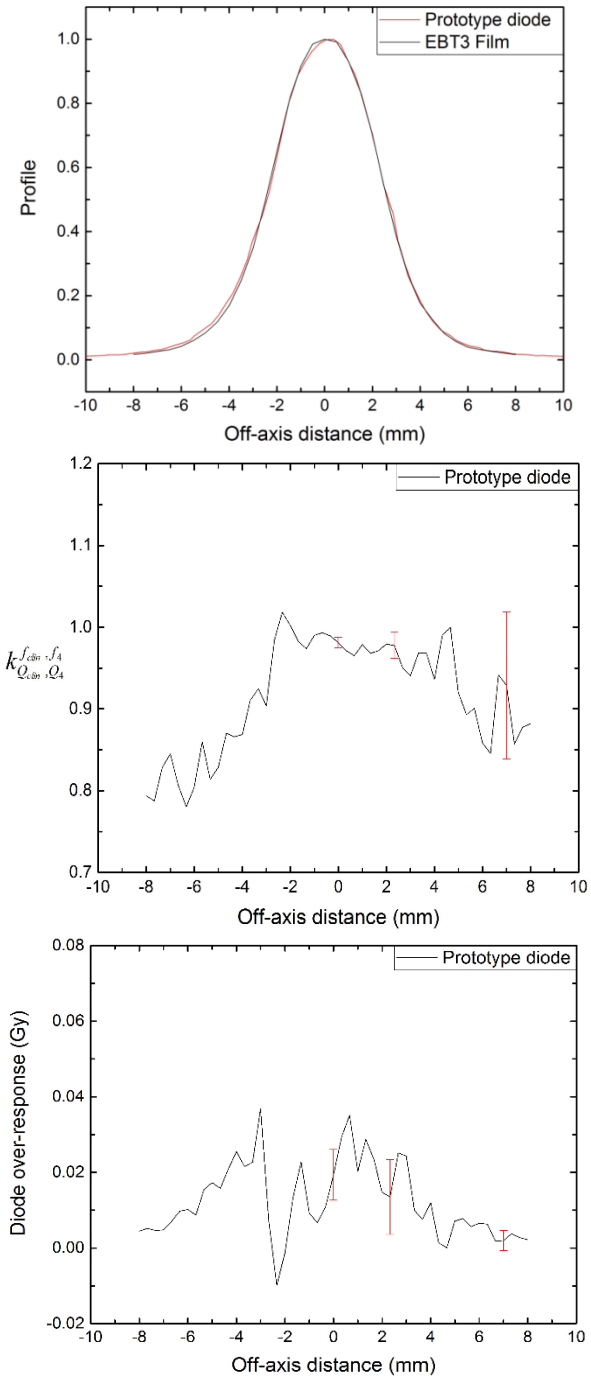

*<u>Figure 3.17:</u> Experimental data using EBT3 film and the Prototype diode, X-jaw, showing the detector reposne off-axis across a **0.5x0.5 cm^2** field, at 5cm deep, 100 cm SSD and 6 MV energy. The top plot shows the matching of the two profiles both normalized to 1 Gy on-axis. The middle plot shows the correction factor (relative to 4x4 cm^2 field) at various positions off-axis (off-axis k profile). The error bars (2 s.d.) indicate the signal to noise ratio. The bottom plot shows the over-response of the uncorrected readings of the prototype diode when a dose of 1 Gy was delivered on-axis.*

The off-axis *k* profiles with the corresponding over-response (of the uncorrected diode readings when a dose of 1 Gy was delivered on-axis) graphs for all the other diode detectors in the 0.5x0.5 cm^2 field, at a 5cm depth in water, are presented in figures 3.18 - 3.21. For the Original diode the *k* value varies substantially across the measured profile and an over-response of ~ 8.5% can be observed on-axis. Detector response substantially improves for off-axis measurements when modifying the diodes according to the air-gap based density compensation method. The "best" four diodes, 1163, 1165 1167 and the "old" Prototype perform reasonably well off-axis too.

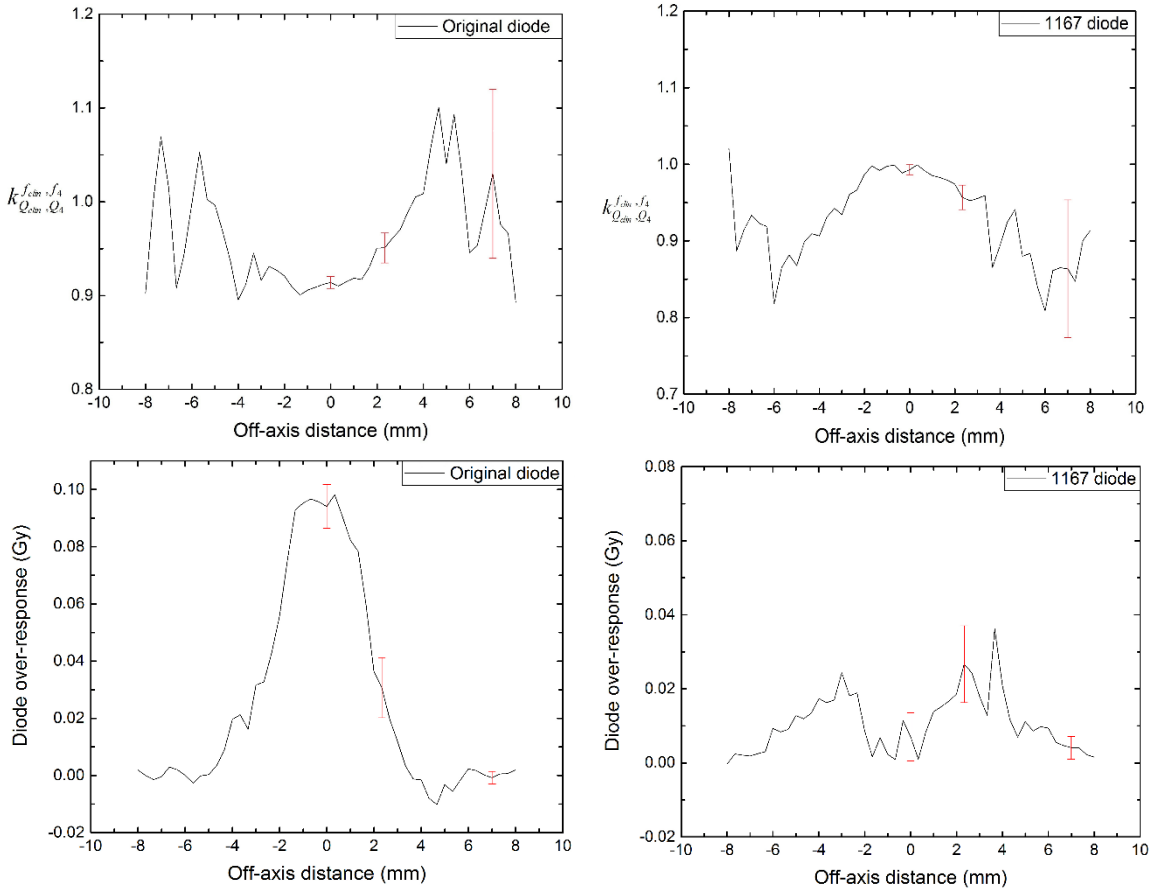

<u>Figure 3.18:</u> (a) Original diode off-axis k profile and over-response of uncorrected readings in a 0.5x0.5 cm^2 field, at 5 cm deep. (b) 1167 diode off-axis k profile and over-response of uncorrected readings in the same field. All errors bars show statistical uncertainties at the 2 s.d. level.

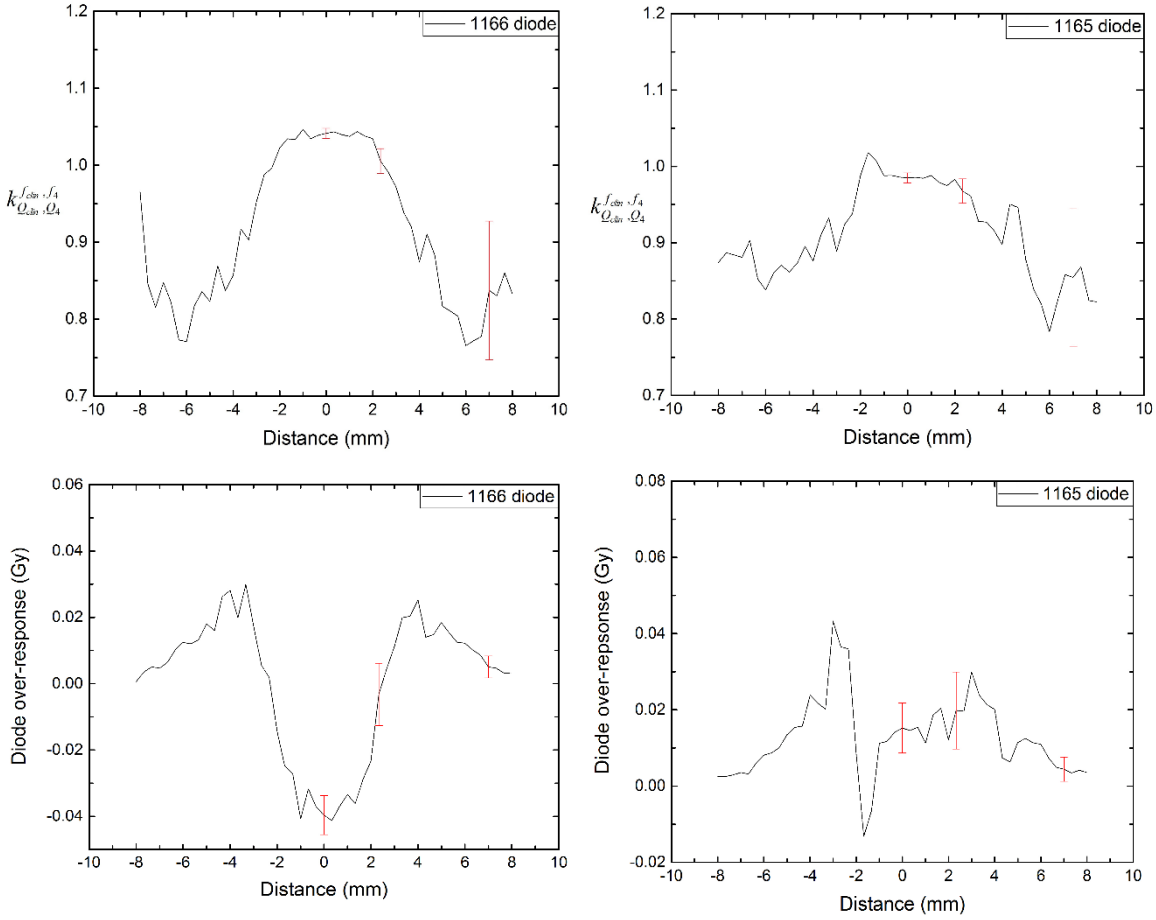

Figure 3.19: (a) 1166 diode off-axis k profile and over-response of uncorrected readings in a 0.5x0.5cm^2 field, at 5 cm deep, 100 cm SSD. (b) 1165 diode off-axis k profile and over-response of uncorrected readings in the same field and depth. Statistical uncertainties shown are ± 2 s.d.

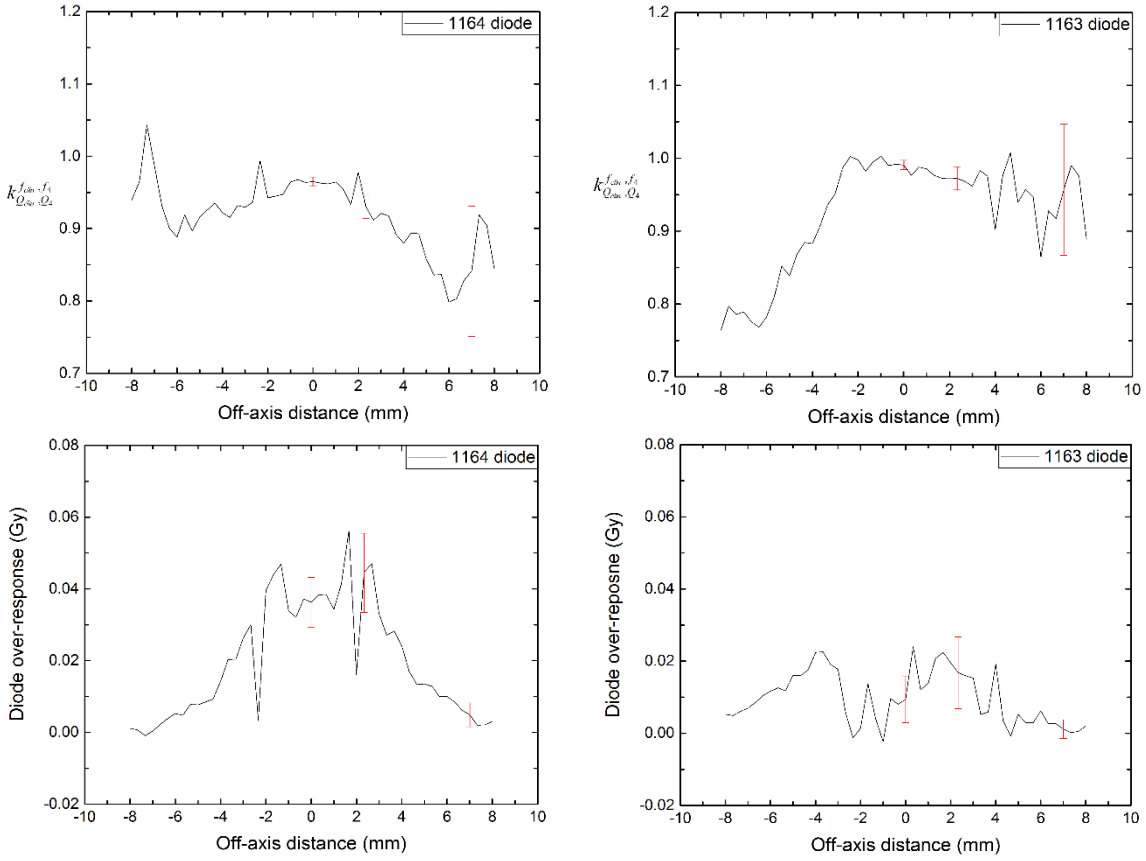

Figure 3.20: (a) 1164 diode off-axis k profile and over-response of uncorrected readings in a 0.5x0.5cm^2 field, at 5 cm deep. (b) 1163 diode off-axis k profile and over-response of uncorrected readings in the same field and depth. Statistical uncertainties shown are ± 2 s.d.

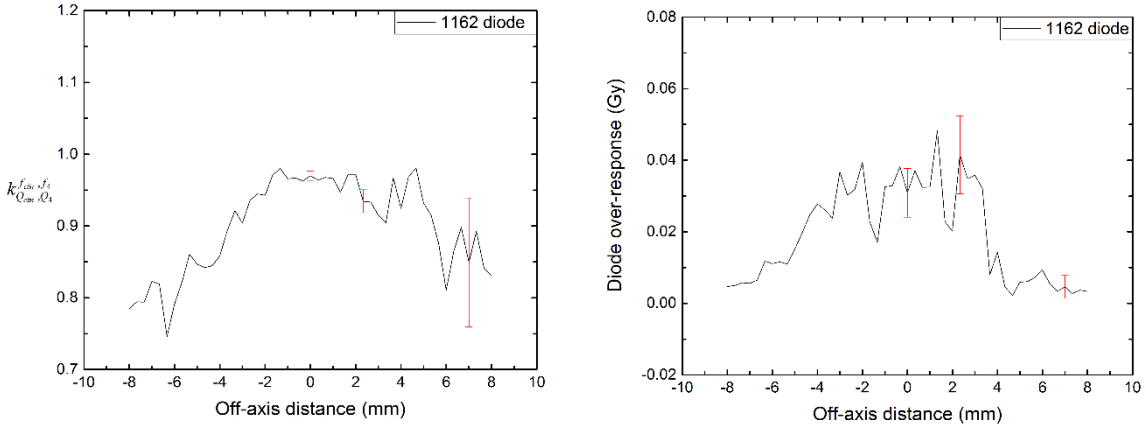

Figure 3.21: 1162 diode off-axis k profile (left) and over-response of uncorrected readings (right), 0.5x0.5 cm^2 field, 5cm deep, 100 cm SSD. Statistical uncertainties shown are ± 2 s.d.

Following the same procedure as in the 0.5x0.5 cm^2 field the off-axis *k* profiles, along with the corresponding dose error graphs, were plotted for selected diodes of the first set to evaluate their off-axis performance in a wider field (1.5x1.5 cm^2), at 5 cm deep. A 4x4 cm^2 field was again used as the reference field. First, the plots for the Prototype diode are presented (figure 3.22).

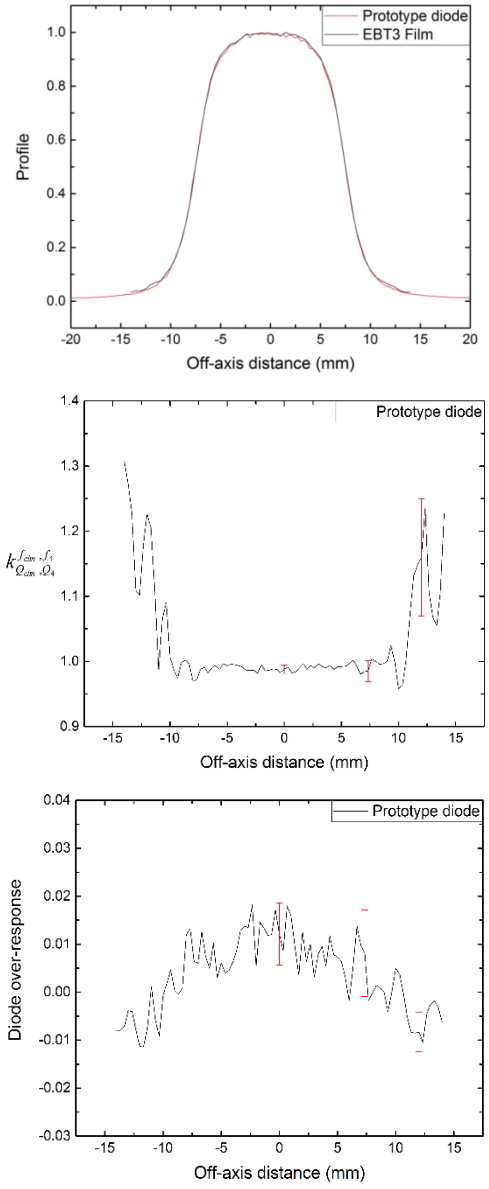

Figure 3.22: Experimental data using EBT3 film and the (1 mm air-gap) Prototype diode, X-jaw, showing the detector response off-axis across a ***1.5x1.5 cm^2*** *field at 5cm deep, 100 cm SSD and 6 MV energy. The top plot shows the matching of the two profiles both normalized to 1 Gy on-axis. The middle plot shows the correction factor (relative to 4x4 cm^2 field) at various positions off-axis (off-axis k profile). The error bars (2 s.d.) indicate the signal to noise ratio. The bottom plot shows the over-response of the uncorrected readings of the Prototype diode when a dose of 1 Gy was deliverd on-axis.*

Off-axis *k* profile data, at 5 cm deep, in the 1.5x1.5 cm^2 field are presented next (figures 3.23, 3.24) for the modified diodes 1163, 1165 and 1167 along with the Original diode. In this wider field all detectors behave less non-ideally, since the small-field effects are much more limited compared to the 0.5x0.5 cm^2 field.

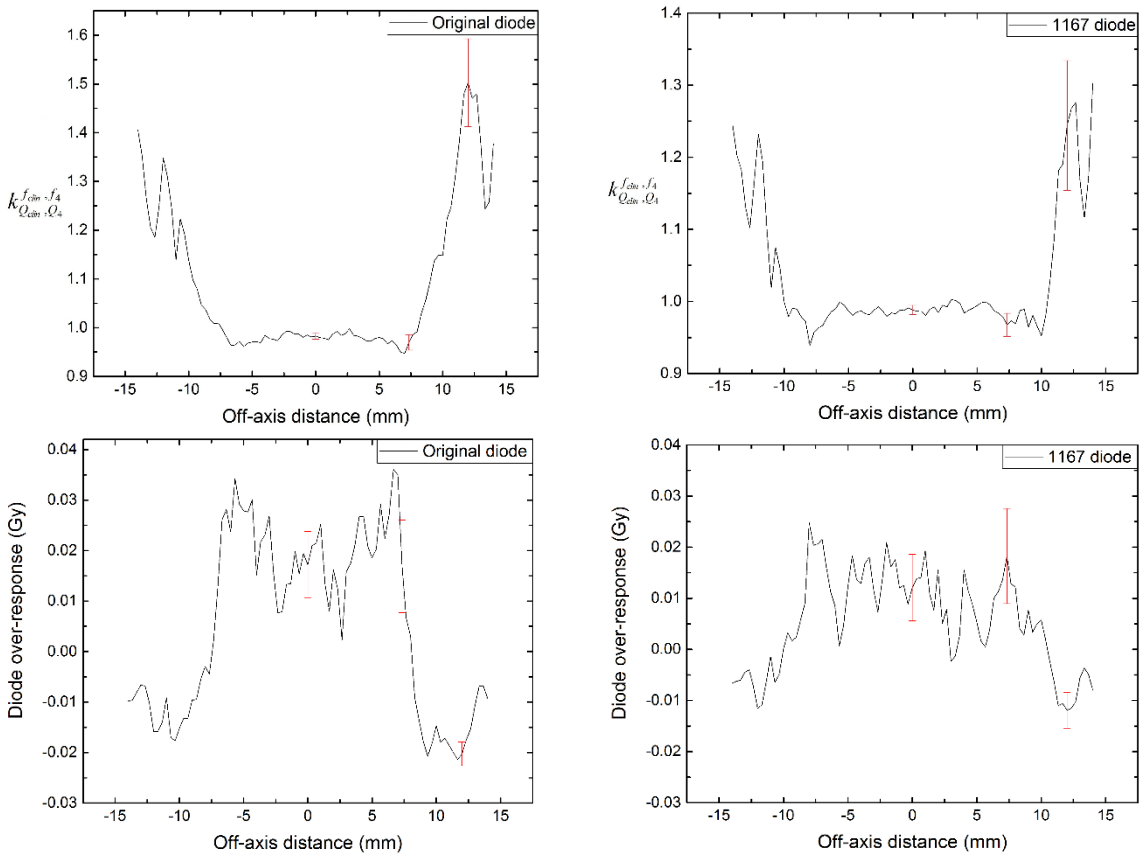

(a) *(b)*

Figure 3.23: (a) Original diode off-axis k profile and over-response of uncorrected readings (when a dose of 1 Gy was delivered on-axis) in a 1.5x1.5 cm^2 field, 5 cm deep. (b) 1167 diode off-axis k profile and over-response of uncorrected readings (when a dose of 1 Gy was delivered on-axis) in the same field and depth. Statistical uncertainties shown are ± 2 s.d.

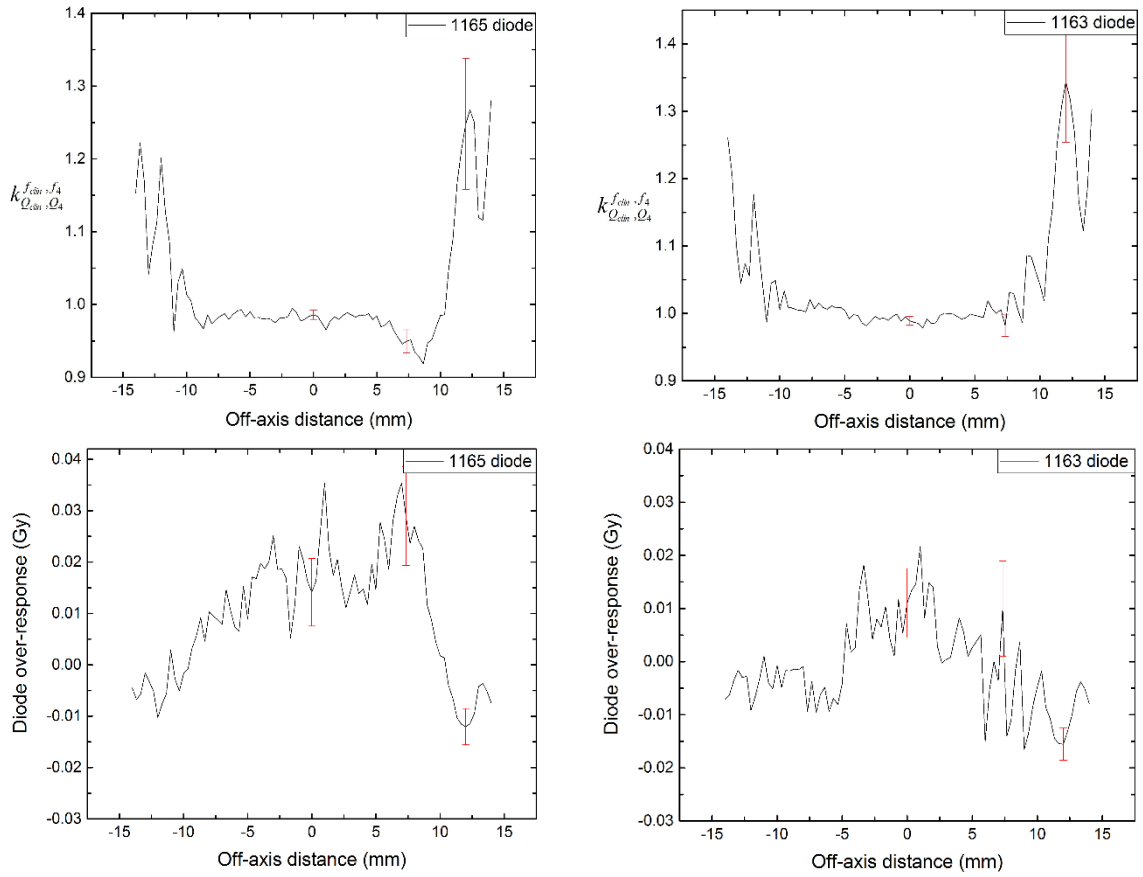

Figure 3.24: (a) 1165 diode off-axis k profile, in a 1.5x1.5 cm^2 field, at 5 cm deep, and over-response of uncorrected readings when a dose of 1 Gy was delivered on-axis. (b) 1163 diode off-axis k profile and over-response of uncorrected readings in the same field and depth. Statistical uncertainties shown are ± 2 s.d.

3.3.4 Discrepancies in *k* with respect to air-gaps – micro-CT imaging of the diodes

The 6 MV experimental results presented in sections 3.3.1, 3.3.2 and 3.3.3 confirm the substantial improvement on the response of silicon diodes in small radiation fields using the air-gap based density compensation method. Several modified detectors of the first set (1163, 1165, 1167 diodes) perform well both on- and off-axis at various depths in the smallest field measured in this work, the 0.5x0.5 cm^2 field. However, a detailed examination of the analysed data shows that the calculated on-axis *k* values reveal an unexpected pattern, at both depths, in the 0.5 and 0.7 cm square fields for the modified 1162 - 1167 diode detectors with respect to the expectation from the air-gap thicknesses.

On-axis *k* values for the 1162 - 1167 modified diodes do not change progressively with air-gap thickness as you might expect, but instead jump around, even after allowing for experimental uncertainties. In order to more clearly illustrate the discrepancies discussed above, the experimentally calculated on-axis *k* values for all the diodes of the first set in the 0.5x0.5 cm^2 field, at 5 cm deep, are summarised in table 3.2. The air-gap thickness of each detector is also included for clarification purposes. The same problem is also seen for the 15 cm deep on-axis *k* results.

Air-gap thickness (mm)	**Detector**	**Experimental on-axis $k_{Q_{0.5,4\ cm}}^{0.5,4\ cm}$ value**
-	60017 Original	0.914 ± 0.011
0.6	1162	0.970 ± 0.012
0.8	1163	0.991 ± 0.013
1.0	1164	0.965 ± 0.012
1.0	1 mm air-gap Prototype	0.981 ± 0.013
1.2	1165	0.985 ± 0.013
1.4	1166	1.040 ± 0.012
1.6	1167	0.993 ± 0.013

Table 3.2: Experimentally determined on-axis k values in a 0.5x0.5 cm^2 field, at 5cm deep. All statistical uncertainties shown are ± 2 s.d. The same data are presented in the plot of figure 3.1. The k values do not change progressively with the thickness of the air-gaps added.

The results for the 60017 Original and the "old" 1 mm air-gap Prototype diodes are in agreement with previous findings from Underwood *et al* (2015), implying that nothing was wrong in the experimental procedure of this work. Furthermore, the labeling and the sequence of the air-gaps in the diodes were checked with the manufacturer (PTW) to eliminate the possibility of any confusion. Finally, a micro-CT imaging of the detectors was performed in Oxford confirming that the air-gaps are in the right order, as expected.

However, by carefully looking at the CT images of the detectors, it has been observed that the thickness of a material almost two times denser[3] than water, overlying the square blocks of silicon, seems to vary from detector-to-detector, with detectors that over-read in small fields (compared to what was expected on the basis of their air-gap thickness) having thicker layers of this material. Therefore, this explains the discrepancies in experimentally determined *k* factors with respect to the air-gaps added for the modified diodes of the first set; the non-controlled thickness of the dense material overlying the silicon sensitive volume can change the detector response in small fields leading to unexpected results.

3.4 Monte-Carlo results

3.4.1 On-axis $k_{Q_{0.5,4\ cm}}^{0.5,4\ cm}$ correction factors

The calculated on-axis *k* values (Eq. 1.10), at 5 cm deep and a 100 cm SSD in a 0.5x0.5 cm^2 field, for all the detectors of the first set, including the modified 1162 - 1167 diodes and their variants with wider air-gaps are presented in Table 3.3. For the 60017 Original diode, the 1 mm air-gap "old" Prototype, and the detectors with *k* values within ± 2% of 1.00, more precise results were obtained by increasing the number of histories when running the egs_chamber code (results highlighted in table 3.3).

[3] The exact density of the material used by PTW is not included for confidentiality reasons.

Air-gap thickness (mm)	Detector	Real air-gap $k_{Q_{0.5,4\ cm}}^{0.5,4\ cm}$	Wider air-gap $k_{Q_{0.5,4\ cm}}^{0.5,4\ cm}$	Even wider air-gap $k_{Q_{0.5,4\ cm}}^{0.5,4\ cm}$
-	60017 original	**0.910 ± 0.005**	-	-
0.6	1162	0.941 ± 0.008	0.939 ± 0.009	0.945 ± 0.008
0.8	1163	0.956 ± 0.008	0.957 ± 0.008	0.962 ± 0.008
1.0	1164	0.975 ± 0.009	0.977 ± 0.009	0.976 ± 0.008
1.0	1 mm air-gap Prototype	-	**0.980 ± 0.006**	-
1.2	1165	0.971 ± 0.008	0.987 ± 0.007	0.989 ± 0.008
1.4	1166	0.979 ± 0.008	**1.006 ± 0.006**	**1.011 ± 0.006**
1.6	1167	**0.995 ± 0.006**	**1.017 ± 0.006**	1.019 ± 0.008

Table 3.3: k correction values calculated for all the detectors and their variants, for on-axis readings made at an in-water depth of 5 cm, 100 cm SSD, in a 0.5×0.5 cm^2 field, using a detector calibrated in a 4×4 cm^2 field. The results highlighted were obtained running more precise MC simulations. Uncertainties are shown at the ±2 s.d. level.

The computational results summarised in table 3.3 reveal three significant patterns regarding the on-axis response of the diodes. Firstly, and in full agreement with the experimentally determined *k* values in the same field, the air-gaps introduced in the modified detectors substantially improve their response, as expected based on the "mass-density compensation" principle, proposed by Underwood *et al* (2012, 2013b). Secondly, no significant differences are observed between the $k_{Q_{0.5,4\ cm}}^{0.5,4\ cm}$ values calculated for the real, the wider and the even wider variants of the diodes when the added air-gap is less than 1 mm in thickness. On the other hand, for air-gaps more than 1 mm thick, as

is the case for the 1165, 1166 and 1167 detectors, MC calculated *k* values differ notably between the real and the wider air-gap variants. And finally, the *k* values increase continuously as thicker air-gaps are added in the detectors above the sensitive silicon, with the 0.995 value of the (1.6 mm air-gap) 1167 Real diode being ~ 9% higher compared to the 0.910 value of the (no air-gap) Original diode.

As an additional check for the on-axis response of the modelled detectors, an imaginary diode with a considerably thicker air-gap (3 mm), but the same width as in the real existing diodes, was modelled using the egs_chamber code and the MC determined result for the on-axis $k_{Q_{0.5,4\ cm}}^{0.5,4\ cm}$ factor, at 5 cm deep and 100 cm SSD, was 1.038 ± 0.007 (2 s.d.). This was done to simply demonstrate that such an (excessive) increase in the thickness of the air-gap is not beneficial for the detector response causing the dosimeter to significantly under-estimate the dose measured in a small field.

Considering the on-axis performance of the diode detectors at 5 cm deep, the on-axis $k_{Q_{0.5,4\ \mathrm{cm}}}^{0.5,4\ \mathrm{cm}}$ factors were calculated at 15 cm deep in water as well under the same reference conditions (4x4 cm^2 field, 5cm deep, 100 cm SSD). On-axis *k* values at this greater depth were calculated only for the detectors that perform best at 5 cm deep, i.e. the 1167 Real diode and the 1166 Wider variant, along with the Original and "old" Prototype diodes. These results are shown in Table 3.4.

Air-gap thickness (mm)	Detector	Real air-gap $k_{Q_{0.5,4\ \mathrm{cm}}}^{0.5,4\ \mathrm{cm}}$	Wider air-gap $k_{Q_{0.5,4\ \mathrm{cm}}}^{0.5,4\ \mathrm{cm}}$
-	60017 Original	**0.913 ± 0.005**	-
1	1 mm air-gap Prototype	-	**0.981 ± 0.006**
1.4	1166	-	**1.009 ± 0.006**
1.6	1167	**0.997 ± 0.006**	-

Table 3.4: k correction values calculated for the original, 1 mm air-gap Prototype, and the "best" detectors, for on-axis readings made at an in-water depth of 15 cm in a 0.5×0.5 cm^2 field, using a detector calibrated in a 4×4 cm^2 field. Uncertainties are shown at the ± 2 s.d. level.

In agreement with the 5cm deep computational results (table 3.3) the air-gaps added above the sensitive volume of the un-modified, i.e. no air-gap added, detector substantially improve the response of the PTW 60017 Original diode, with all *k* values calculated for the Prototype, 1167 Real and 1166 Wider detector models being within 2% of 1.00, at both 5 and 15 cm deep in a 0.5 cm square field. The 1167 Real diode performs better than the other modified detectors, with no on-axis *k* value differing more than 0.5% from one.

3.4.2 Percentage depth dose curves (PDDs) and EPOM shift analysis

The Monte-Carlo PDD data of the 0.5 cm square field, both for a water voxel and the diode detectors, all normalised to their maximum value, are presented in Figure 3.25. In the top left plot (a), the reading of each detector is plotted against the depth of the detector's sensitive volume in water. The "kick" in the PDD curve (occurring when the detector is first submerged in water and no longer capped by air) is at different depth for each diode, depending on the amount of material present above the sensitive region. In the top right plot (b) of figure 3.25, the diode readings are shifted so each "kick" is occurring at zero depth in water. This is equivalent with plotting the detector readings against the depth of the top part of the detector (i.e. the detector just "breaking" the water surface). In part (c) all detector PDD data are shifted by 1.33 mm, according to the manufacturer's information about the location of the effective point of measurement (EPOM) in the original 60017 diode.

Comparing now the PDD curves of the detectors to the water voxel PDD curve, and focusing on the "build-up" region, it is clear from figure 3.25c that there is a very good match between the Original 60017 diode and the water voxel PDDs, confirming this way the position of the instrument's EPOM at 1.33 mm below the top surface of the detector. Regarding the modified diodes, 1166 Wider and 1167 Real, the existence of the air-gap does slightly change the location of the detector's EPOM; it is evident from figure 3.25c that there is a 0.45 mm distance difference (depth-shift) between the 1167 Real diode and the Original 60017 diode PDD curves. The statistical uncertainties of the MC

simulations were maintained below 0.55% (2 s.d.) and no error bars are added into the following plots in order to improve visibility of the graphs.

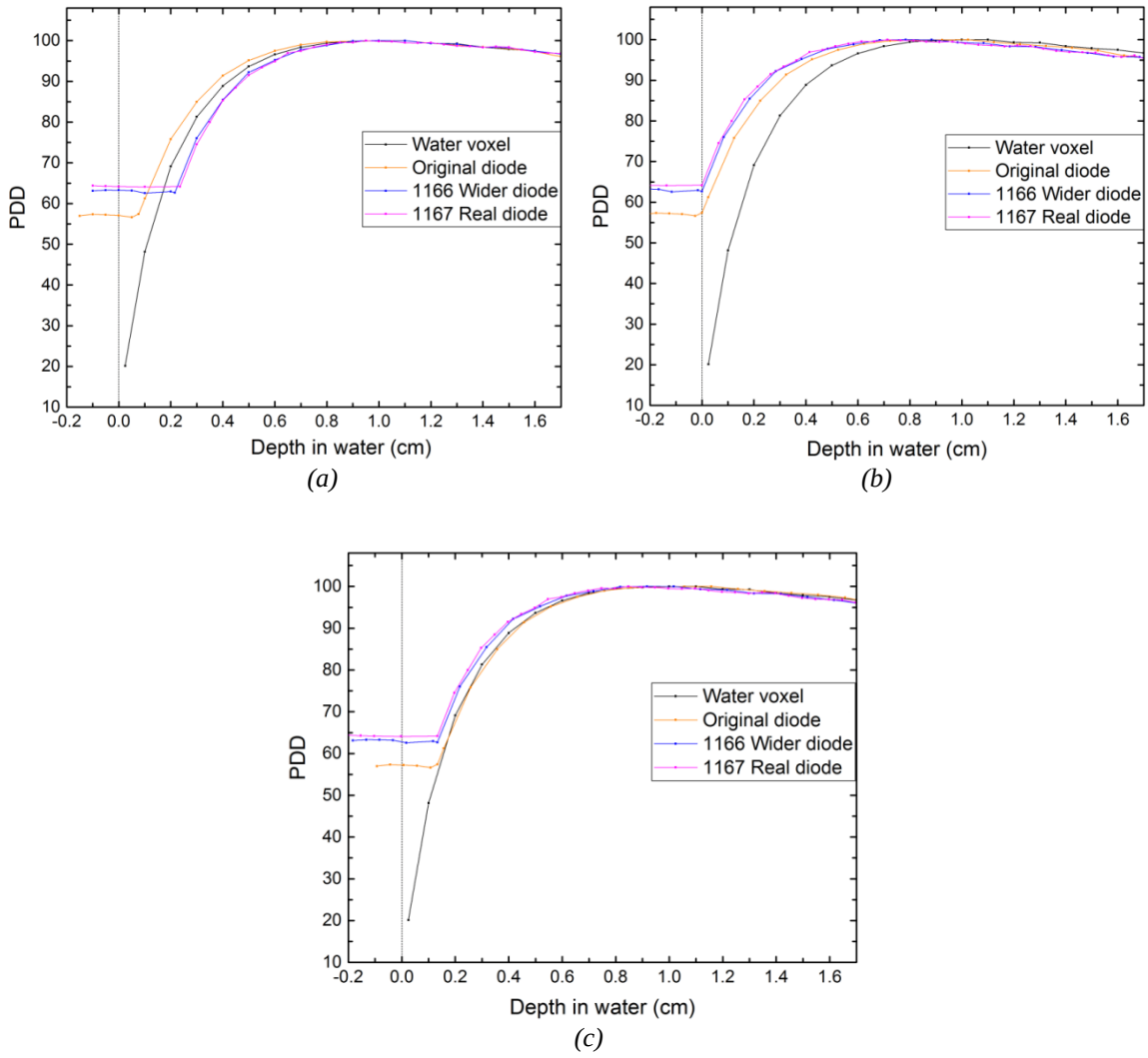

Figure 3.25: PDD data obtained by MC simulation for a 6 MV beam model. In part (a) the detectors' reading is plotted against the depth of the sensitive volume in water with the "kick" point occurring for each detector when it is first submerged. In part (b) all detectors PDD data are shifted so the "kick" occurs at zero depth in water. In part (c) the same data is plotted, but now with all detector readings shifted by 1.33 mm. The Original diode PDD curve is perfectly aligned with the water voxel PDD data; whereas, a 0.45 mm distance between the 1167 Real diode and the water voxel PDD can be seen in the build-up region of the curves meaning the air-gap added slightly affects the detector's EPOM.

In accordance with the experimental analysis presented in section 3.3.2 of this chapter, further investigation for the validity of the observed 0.45 mm EPOM shift for the 1167

Real diode was considered necessary. Therefore, a comparison was made between the PDD curve of this detector and the water voxel PDD curve at deeper depths, after the d_{max} point. After applying the 0.45 mm shift to the whole of the 1167 Real diode PDD curve the following graph, presented in Figure 3.26, was obtained. The two PDD curves were normalised to the three highest values "window" in order to prevent from any biasing of the max dose value due to noise close to the d_{max} point. The error bars (showing 2 s.d. statistical uncertainties) were added now to both plots.

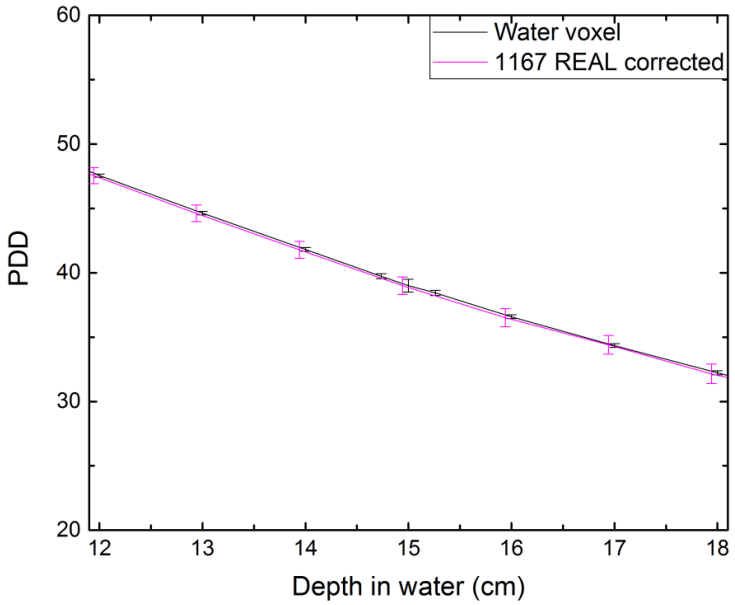

Figure 3.26: The water voxel PDD and the corrected (0.45 mm shift applied) 1167 Real diode PDD. The two curves overlay well in this region, no additional shift is required apart from the 0.45 mm one already applied to the curve.

3.4.3 Off-axis $k_{Q_{0.5,4\ cm}}^{0.5,4\ cm}$ profiles

With the detector's sensitive volume at various positions off the central axis of the 6 MV beam, at 5 and 15 cm deep in water, profiles for the Original diode were obtained. A comparison between the water voxel profile and the profile of the no air-gap Original 60017 diode, at 5 cm deep, is illustrated in the top plot of figure 3.27. The off-axis *k* profile, calculated according to equation 1.10, and the corresponding diode over-response graph for the same detector are presented in the middle and the bottom plots of

the same figure, respectively. The 2 s.d. statistical uncertainties (red error bars) of the MC calculations are included in the following graphs.

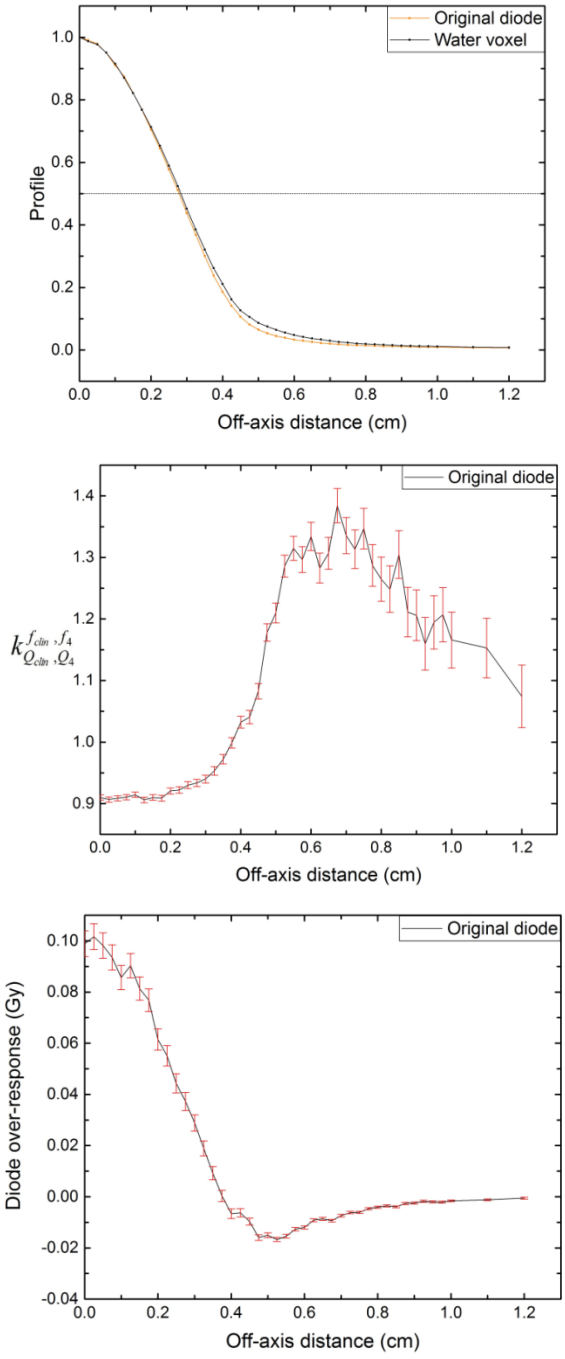

*Figure 3.27: MC data showing the detector response off-axis across a 0.5x0.5 cm^2 field at **5 cm deep** and 6 MV energy. The top plot is a comparison between the water voxel and the diode profiles both normalized to 1 Gy on-axis. The middle plot shows the correction factor (relative to a 4x4 cm^2 field) at various positions off-axis (off-axis k profile). The bottom plot shows the over-response of the uncorrected reading of the Original 60017 diode when a dose of 1 Gy was delivered on-axis. All error bars are 2 s.d.*

The same information is presented for the 1166 Wider and 1167 Real diodes in figure 3.28. The off-axis response of both of these detectors is substantially improved compared to the Original diode because of the air-gap introduced above the sensitive silicon in each detector. No over-response reading for these two detectors is more than 1.5% making it quite difficult to judge which one performs best.

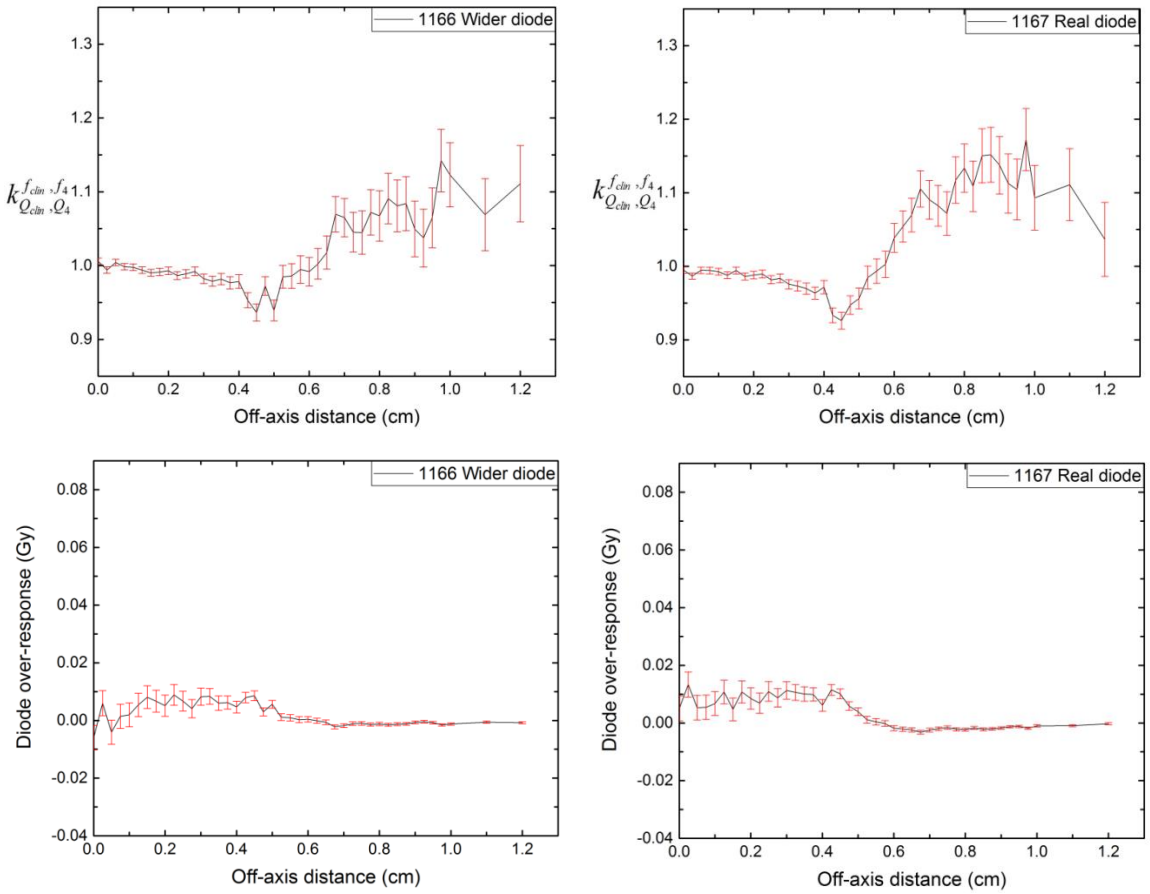

*Figure 3.28: Simulation data showing the detector response off-axis across a 0.5x0.5 cm^2 field at **5 cm deep** and 6 MV energy. The top plots show the correction factor at various positions off-axis (off-axis k profile) for the 1166 Wider diode (left) and the 1167 Real diode (right). A 4x4 cm^2 field is used as the f_{msr} field. The bottom plots show the over-response of the uncorrected reading of the 1166 Wider diode (left) and the 1167 Real diode (right) when a dose of 1 Gy was delivered on-axis. All error bars show 2 s.d. statistical uncertainties.*

Finally, similar graphs (figures 3.29 and 3.30) were created to illustrate the off-axis response of all the three detectors (Original, 1166 Wider and 1167 Real diodes) at an in-water depth of 15 cm. Same trends are observed with the modified diodes performing much better than the Original detector. At this depth the 1167 diode seems to perform best, with no over-response reading more than 0.8 %.

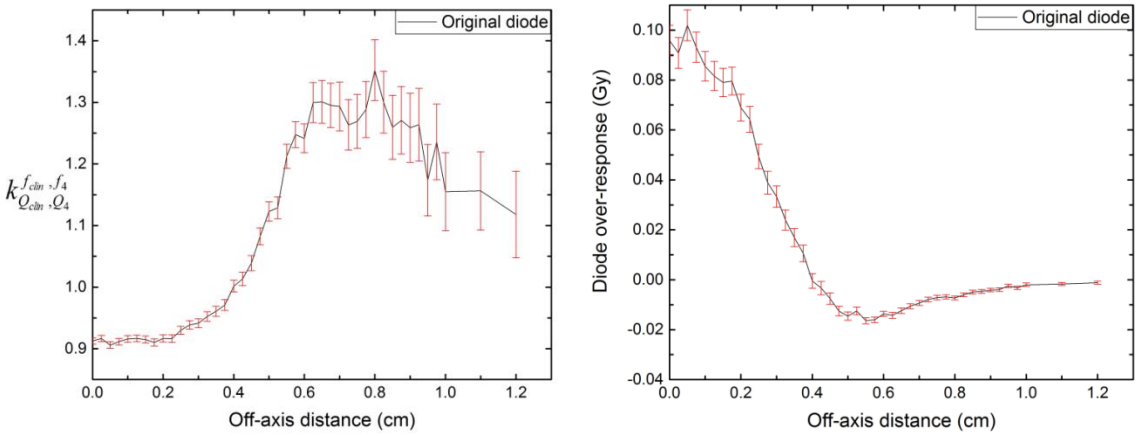

*Figure 3.29: MC data showing the Original diode off-axis k profile across a 0.5x0.5 cm^2 field at **15 cm deep** and 6 MV energy (left) and the over-response of uncorrected readings (right). All error bars show 2 s.d. statistical uncertainties.*

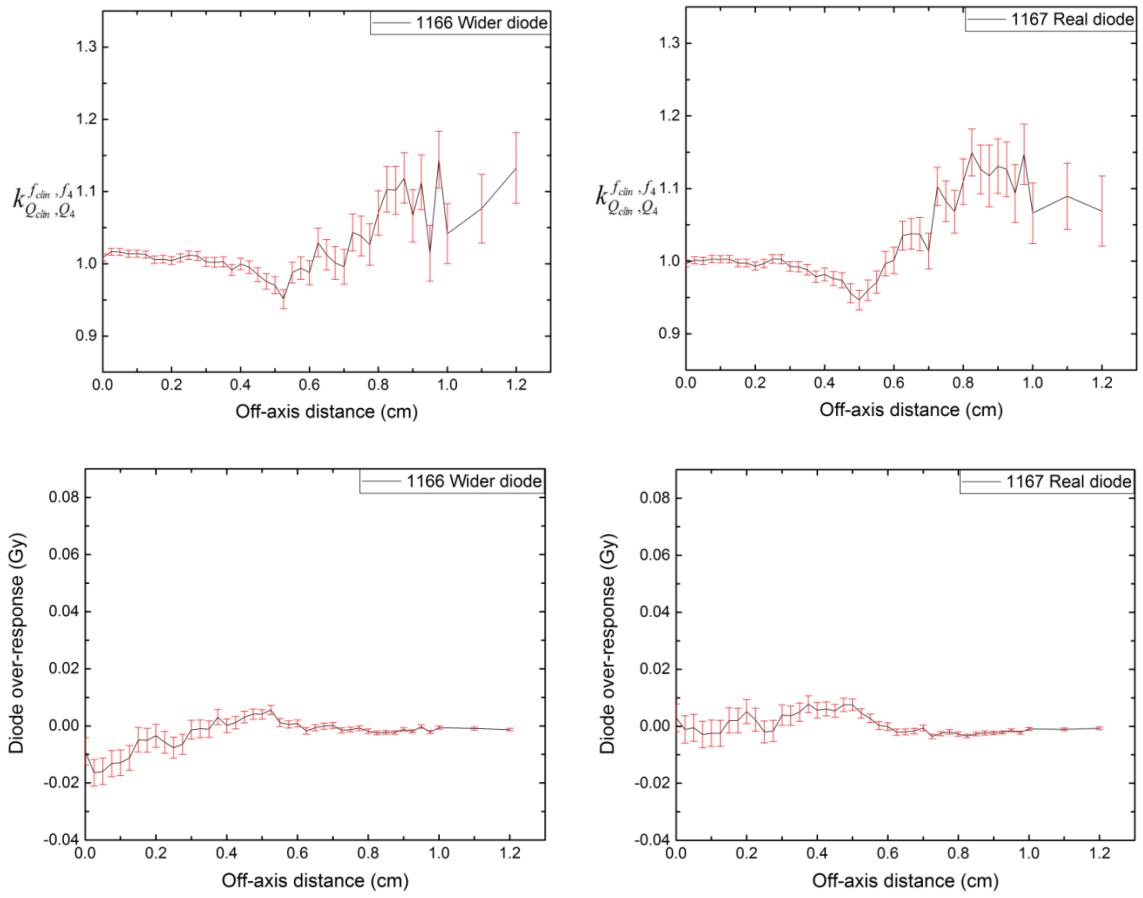

*Figure 3.30: (a) Simulation data for the 1166 Wider diode off-axis k profile across a 0.5x0.5 cm² field at **15 cm deep** and the over-response of uncorrected readings. (b) Similar data for the 1167 Real diode at the same field and depth. Comparing the two diode over-response graphs (bottom plots) it can be concluded that the 1167 Real diode performs better off-axis than the 1166 Wider diode with no over-response reading more than 0.8%.*

3.5 Discussion of 6 MV results

On-axis *k* correction factors, at two different depths in water, on-axis depth doses and off-axis *k* beam profiles have been both experimentally determined and computationally calculated for all the detectors of the first set. The responses of the various modified detectors vary for field sizes smaller than 1.5x1.5 cm^2 (figures 3.1, 3.3), a result in agreement with the findings of Francescon *et al* (2011) and Underwood *et al* (2015).

The experimental results for the on-axis *k* values of the PTW 60017 Original and the "old" 1 mm air-gap Prototype diodes, in a 0.5x0.5 cm^2 field at 5 cm deep, are in very good agreement (less than 0.5% difference) with the MC calculated ones. These results are also very close (within ± 1%) to the values published by Underwood *et al* (2015) and Charles *et al* (2013), if we also consider the different reference fields used in these studies (5x5 cm^2 for Charles *et al* 2014, and 10x10 cm^2 for Underwood *et al* 2015). For measurements at 15 cm deep the agreement between experiment and simulation is slightly poorer, but again values agree within the 2 s.d. error range. It is worth mentioning that experimental uncertainties on *k* values are quite considerable (typically ± 1.3%, 2 s.d.); this is mainly due to the limited precision of the EBT3 gafchromic film dosimetry. Regarding the experimental results of the modified diodes 1162 - 1167 similar trends are observed at both depths; all *k* factors measured for the 1165, 1167 and the "old" Prototype detectors lie within ± 2% of 1.00, with all values for the 1165 detector lying within ± 1.6% and for the 1163 diode within ± 2.2% of 1.00, implying that these detectors are suitable for measurements at both depths.

As discussed in section 3.3.4 experimental on-axis *k* values measured for the 1162 - 1167 modified diodes in the smaller fields are far from the expected ones on the basis of their air-gap thickness; this is also evident from the significant discrepancies between the experimentally determined and the computationally calculated *k* values in the 0.5x0.5 cm^2 field, at both depths. These discrepancies are attributed to the un-controlled thickness of the dense material overlaying the silicon square of the diodes and seriously affecting the response of the detectors; the image from the micro-CT scan performed in Oxford is presented in figure 3.31. Substantial regions of the detectors have been blocked out for confidentiality purposes.

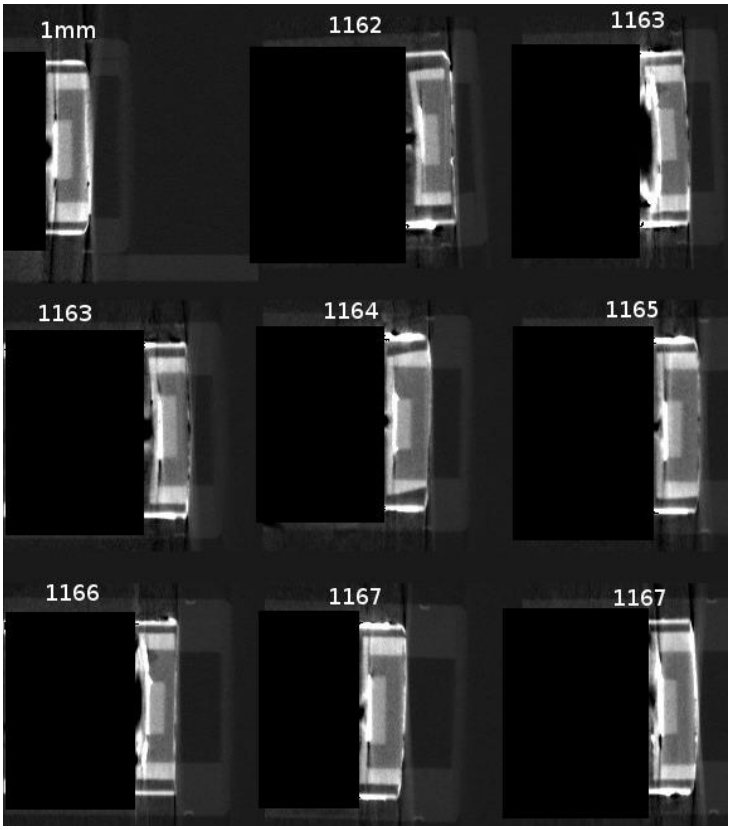

Figure 3.31: The micro-CT image from the imaging study completed in Oxford showing all the modified detectors of the first set. The thickness of the dense material (visible in dark grey) around the silicon square (light grey) is variable from detector-to-detector, thus significantly affecting the detector response and resulting in the unexpected k values experimentally determined.

From the analysis of the PDD data presented in this chapter it can be concluded that introducing an air-gap into each diode detector does not affect the overall shape of the observed PDD curves (very good agreement with the ion chamber PDD data in the $4x4cm^2$ field, figure 3.5). However, inclusion of air-gaps within the diodes leads to small changes in measured EPOMs of the detectors, all less than 0.5 mm (table 3.1). This finding is in agreement with the Monte-Carlo calculations of Underwood *et al* 2015, detailed examination of figure 6 of that paper showing a small (~ 0.2 mm) difference in EPOM between the (no air-gap) Original and modified (1 mm air-gap) type 60017 diode detectors. The EPOM shifts measured experimentally are also confirmed by the MC calculations (figures 3.25, 3.26).

It is clear from figures 3.11, 3.12 that there is lack of visible structure in these plots of the PDD ratios; the plots have values which are around one and no trend is observed (apart from the noise) for any of the diodes, indicating that there is no need to apply any other EPOM shift except for the one that was calculated from the PDDs before d_{max} and already applied to the whole of the PDD curves.

In addition, from figure 3.13 it can be concluded that applying the EPOM shifts calculated in the 0.5x0.5 cm^2 field to the data of the 4x4 cm^2 field does not have any impact on the response of the detectors beyond d_{max} (there is good agreement between the PDD data of the modified diodes and the 60017 Original in this region, with no visible structures of the plotted PDD ratios). Regarding the data before d_{max}, it is shown that applying the EPOM shifts calculated in a different field cause the occurrence of visible structures to the plots of the PDD ratios meaning that the PDD data of the modified diodes and the no air-gap Original one does not overlay in this region. This can be explained by either the fact that necessary shifts in the "pre-d_{max}" region differ with field size (table 3.1), or attributed to spatial errors on the experimental measurements, due to the spatial sampling of the obtained data. The difference between the PDD curve of the no air-gap type 60017 detector and the modified diodes can be seen in the "pre-d_{max}" data because dose changes much more sharply with depth at this region, but usually it is the dose at depth that is more important in dosimetry.

Finally, from the off-axis data of the various detectors characterised it can be concluded that the modified detectors perform significantly better off-axis compared to the Original diode. In both plots of figure 3.14 (for the X and Y pair of jaws), the FWHM values obtained with the no air-gap 60017 Original diode are significantly below the average value of EBT3 film, meaning that this un-modified "non-corrected" in terms of density-compensation detector, seems to over-sharpen the off-axis beam profiles, a result also observed by Underwood *et al* (2015). On the other hand, the 1166 diode (with a 1.4 mm thick air-gap and a 1.040 ± 0.012 on-axis *k* value in the 0.5 cm square field, 5cm deep) measures a much wider profile compared to the EBT3 film and the rest of the modified detectors. Apart from the 1166 detector, diode measurements (shown with the star symbols in figure 3.15) with the modified detectors lie within or close to the EBT3 film

2 s.d. confidence intervals. The asymmetries observed in some of the experimental off-axis *k* profiles (e.g. figures 3.17, 3.18 and 3.20) can be attributed to noise in the beam profile measurements using the films and the diode detectors. These asymmetries can be mainly seen in the very low dose regions of the *k* versus off-axis distance plots and the corresponding diode over-response graphs are much more symmetric with the uncertainties being suppressed at the regions where the dose is much lower compared to the on-axis point (i.e. beyond the field edges). The MC results for the off-axis *k* profiles indicate that both the 1166 Wider (1.4 mm thick air-gap) and the 1167 Real (1.6 mm thick air-gap) diodes are suitable for small-field measurements at both 5 and 15 cm deep in a 6 MV beam, with no over-response reading for the latter more than 1.2%.

3.6 Conclusions

The detailed characterisation of the diodes of the first set confirms findings from previous groups (Charles *et al* 2013, 2014 and Underwood *et al* 2015) regarding the mass-density compensation method; the response of silicon diodes in small radiation fields is substantially improved by deliberately introducing thin air-gaps above the sensitive region. The performance of all the diodes have been both experimentally and computationally evaluated; some of the modified detectors tested perform well both on- and off-axis at different depths in water.

However, unexpected design issues, revealed during the data analysis and later confirmed by a micro-CT scan of the detectors, led to unexpected experimental results making it quite difficult to identify the optimal air-gap thickness for the type 60017 modified diodes. As previously stated by several groups (Bouchard and Seuntjens 2004, Cranmer-Sargison *et al* 2012, Francescon *et al* 2012, Underwood *et al* 2013a, 2013b) it is not only the sensitive volume of the detector (e.g. silicon) that is causing significant changes in its response in small fields relative to wider ones, but the other non-water equivalent materials close to the active region as well. If the non-sensitive materials are not controlled too (in terms of density and thickness) there will be significant problems building the detector with the "correct" air-gap and achieving accurate results for small-

field dosimetry. Consequently, considering the results of this chapter a new and re-designed improved set of radiation detectors was built by the detector company (PTW), in which the thickness of the material causing difficulties was controlled and not variable from detector-to-detector, and also its density was substantially decreased to a value much closer to 1 g/cm^3. The characterisation of these improved detectors is the subject of chapter 5.

Chapter 4

Original set of detectors – 15 MV results

4.1 Introduction

All the dosimetry diodes of the first set provided by PTW, the 60017 Original, the 1 mm air-gap Prototype and the 1162 - 1167 modified detectors, have been tested at Clatterbridge Cancer Centre (CCC) using a 15 MV photon beam as well. The experimental and computational data presented in this chapter, providing information about the response of the silicon diodes characterised in small and wider radiation fields, comprise on-axis *k* values (Alfonso *et al* 2008), percentage depth doses (PDD curves), and off-axis *k* profiles.

Although a lot of work has been previously done and many results have been published in the past showing the response of silicon diodes in 6 MV photon beams (Francescon *et al* 2011, Bassinet *et al* 2013, Charles *et al* 2013, 2014, Benmakhlouf *et al* 2014, Underwood *et al* 2015) much fewer studies, and mainly computational ones (Underwood *et al* 2015, Fenwick *et al* 2018a), present data about the performance of silicon diodes in higher beam energies used for external beam radiotherapy. The aim of this chapter is to confirm the results of chapter 3 regarding improvements in the response of density compensated silicon diodes in small fields, further investigate the performance of the modified 1162 - 1167 diodes in a 15 MV beam, and finally demonstrate that the detectors behave similarly at this substantially higher beam energy.

4.2 Methods

For the characterisation of the original set of PTW dosimetry diodes in a 15 MV beam, output factors, PDD and beam profile data were obtained and analysed in the same way

as the 6 MV beam data. The Varian "TrueBeam" linac (Varian, Palo Alto, CA) located in the VT2 room at CCC was used again to produce a 15 MV photon beam with the MLCs fully retracted and using just the collimator jaws to set the different field sizes throughout the whole experimental process. Measurements were made with the diode detectors and EBT3 gafchromic film both at 5 and 15 cm deep in the "Blue Phantom 2" water tank, always in the absence of a reference detector. The diodes were positioned vertically to the water surface, parallel to the beam axis (as previously described in sections 2.2.1 and 3.2.1) to complete the experimental work for the 15 MV beam energy. In accordance with the 6 MV data, thirty EBT3 films[1] were irradiated in the reference field (4x4 cm^2, 5 cm deep, 100 cm SSD) for calibration purposes; by adjusting the MUs of the linac values of dose absorbed by the calibration films ranged from 0.087 to 4.350 Gy, and a new calibration curve was then generated for the 15 MV beam using MATLAB (as described in chapter 2, section 2.2.5.2).

Computational studies for the 15 MV beam model (Scott *et al* 2008) were completed within the egs_chamber (Kawrakow 2005, Wulff *et al* 2008) user-code only for selected diodes of the original set, the 60017 (un-modified) Original diode, the 1 mm air-gap "old" Prototype and the two modified detectors that performed best according to the 6 MV Monte-Carlo results of chapter 3 (section 3.4), i.e. the 1166 Wider and the 1167 Real diodes. The phase-space files used as a source of particles for the small (0.5x0.5 cm^2) and the machine-specific reference (4x4 cm^2) fields contain 6.7 x 10^6 and 3.6 x 10^8 particles, respectively (Fenwick *et al* 2018a). Both phase-space files were created using the experimentally validated 15 MV beam model of Scott *et al* 2008. The same water voxel dimensions as for the 6 MV calculations (0.25x0.25x0.5 mm^3 for the 0.5x0.5 cm^2 field) were chosen for the DOSXYZnrc simulations to obtain the on-axis small-field doses and beam profiles at both 5 and 15 cm deep (SSD = 100 cm) in a 50x50x50 cm^3 virtual water phantom. A 2x2x0.5 mm^3 water voxel was used for computational efficiency to calculate the on-axis dose at 5 and 15 cm deep in the 4x4 cm^2 reference field. Global energy cut-off values of ECUT = 0.521 MeV and PCUT = 0.001 MeV were set both for the DOSXYZnrc and egs_chamber calculations, and all radiation

[1] Four additional EBT3 films were not irradiated but only submerged and dried in the same way and amount of time as the irradiated ones in order to obtain experimentally consistent data for zero dose.

transport parameters and variance reduction techniques were kept exactly the same as for the 6 MV computational work (discussed in sections 2.3.2 and 2.3.3 of chapter 2).

4.3 Experimental results

4.3.1 On-axis $k_{Q_{clin},Q_{msr}}^{f_{clin},f_{msr}}$ correction factors

Figure 4.1 shows the Alfonso *et al* (2008) on-axis $k_{Q_{clin},Q_{msr}}^{f_{clin},f_{msr}}$ correction factors (Eq. 1.10) for all the diodes of the first set, calculated at 5 cm deep in a 15 MV photon beam. The reference conditions (4x4 cm^2 field, 200 MUs, 100 cm SSD and 5 cm depth) are exactly the same as for the 6 MV data. All *k* values are plotted against the various clinical fields measured and their experimental statistical uncertainties are shown at the ± 2 s.d. level.

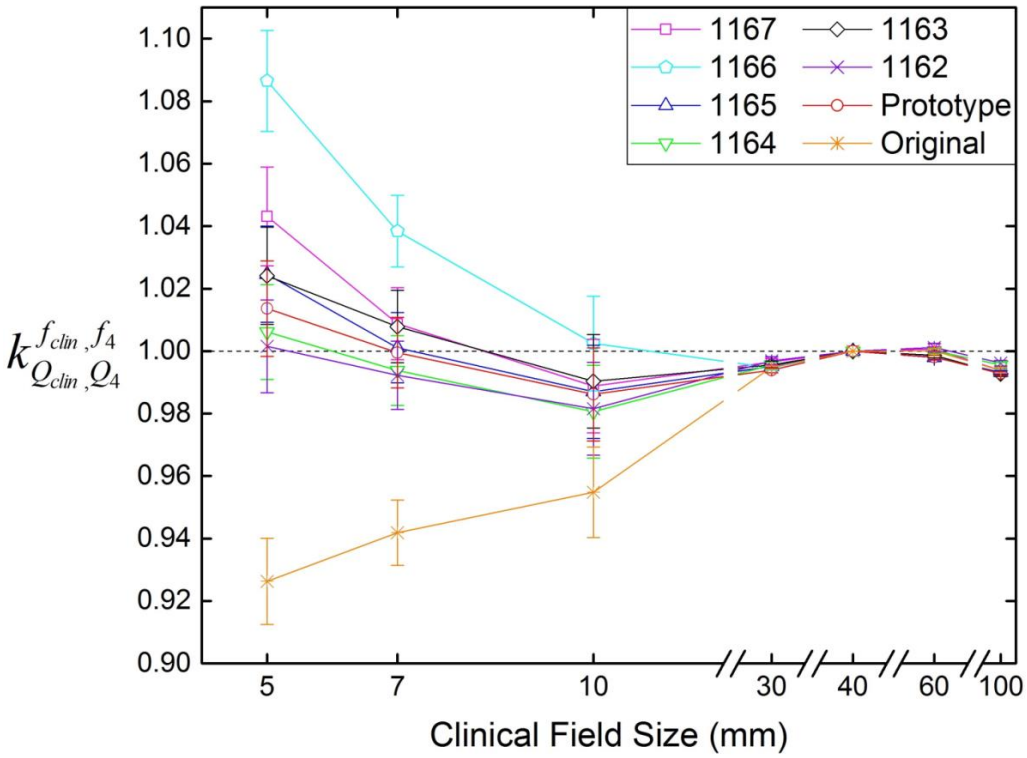

*Figure 4.1: Experimental values of the on-axis correction factors for a 15 MV photon beam at **5 cm deep** in water and 100 cm SSD. All values were calculated using a 4x4 cm^2 field as the machine-specific reference field, also measured at 5 cm deep. The Original (no air-gap added) and the 1166 diodes are the two extremes with the k values for all the other didoes somewhere in between.*

The on-axis *k* correction factors for each diode detector of the first set were calculated for various clinical field sizes at 15 cm deep in water as well. Reference conditions are exactly the same and *k* values are again plotted against the different clinical field sizes measured. Results are presented in figure 4.2.

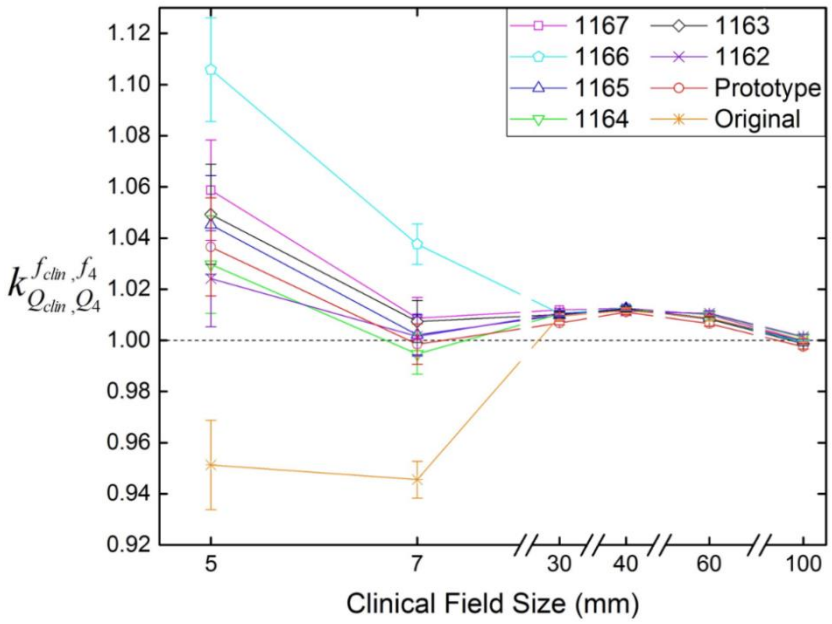

Figure 4.2: Experimental values of the on-axis correction factors for a 15 MV beam at ***15 cm deep,*** *100 cm SSD, in various clinical fields relative to a 4x4 cm^2 field. Error bars show two standard deviations statistical uncertainties.*

At depths of both 5 and 15 cm, similar trends are observed for the Alfonso *et al* (2008) *k* values; the 1166 diode (1.4 mm air-gap) is almost as far out in one direction (under-reads compared to the dose absorbed by a point of water) as the no air-gap Original diode is in the other direction (over-reads). The 1162 and 1164 diodes perform best at both depths in a 15 MV beam, since all their *k* factors lie within ± 3% of 1.00. In agreement with the 6 MV experimental results, on-axis *k* values for the 1162 - 1167 modified detectors do not change progressively with the air-gap thickness revealing a similar behaviour of the detectors at this higher beam energy. However, the detectors that work best at 6 MV, at both depths, (1163, 1165, 1167 and the "old" Prototype, as discussed in chapter 3) perform significantly worse in a 15 MV beam, with the 1167 diode under-reading by more than 4% in a 0.5x0.5 cm^2 field, at 5 cm deep in water, and by about 6% in the same field, at depth of 15 cm.

4.3.2 Percentage depth dose curves (PDDs) – EPOM shifts

The 4x4 cm^2 field PDD data obtained with the detectors[2] of the original set positioned in the "Blue Phantom 2" water phantom are presented in figure 4.3. The "global" 1.33 mm shift was applied to the PDD data of all the diodes based on the information provided by PTW about the location of the EPOM in the Original diode. The PDD curves were measured at a spatial resolution of ~ 0.3 mm, allowing to visually correct the location of the "kick" (occurring when the diode top exits the water) within ± 0.15 mm. When necessary, an additional small correction not greater than 0.4 mm (apart from the 1.33 mm one), was made to the PDD curves to move the "kick" of the experimental data so that it occurs when the top of the detector lies at the water surface, and thus the sensitive volume of the Original detector lies at depth of 1.3 mm.

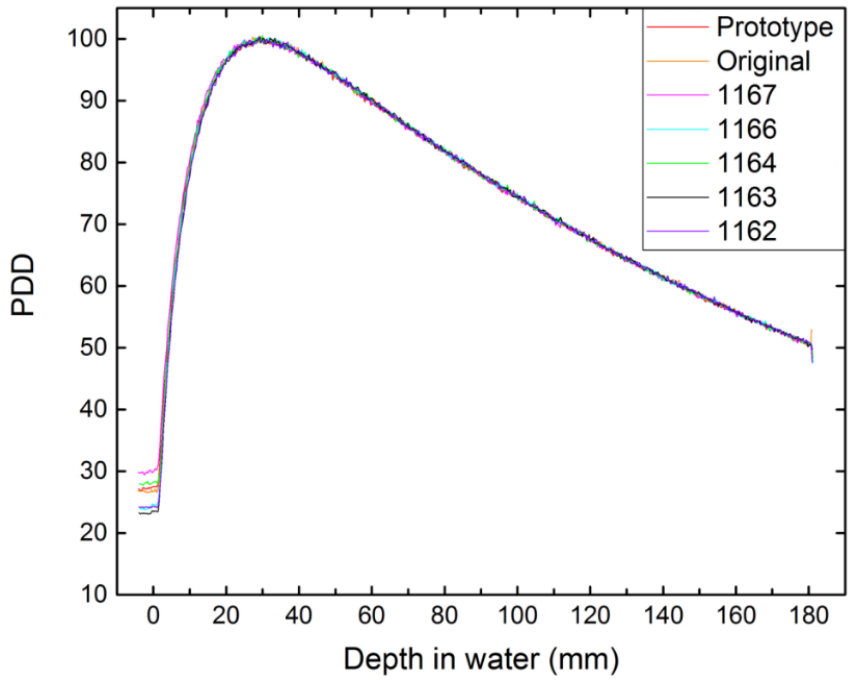

*Figure 4.3: Percentage depth dose (PDD) curves for the detectors of the first set in a **4x4 cm^2** field. The different thickness of the air-gap added in each diode does not affect the overall shape of the PDD curves, a result in agreement with the 6 MV data.*

[2] The PDD curve of the 1165 diode is missing from the graph in figure 4.3. Due to mis-positioning of the diode, close to the edge of the field, the values of dose were significantly lower than the ones of all the other detectors.

It is evident from figure 4.3 that introducing an air-gap into each diode, between the top surface of the detector and its sensitive volume, does not affect the overall shape of the measured PDD curves. However, further investigations were made of the PDD curves in the build-up region to observe potential EPOM shifts, considering that it is quite difficult for small shifts to be seen at greater depths, after the d_{max} point, due to the much slower variation of dose compared to the build-up region. Figure 4.4 demonstrates that there is a small distance difference (depth-shift) between the curve that rises first and the one that rises last for the PDD data in the 4x4 cm^2 field.

The same analysis, applying the "global" 1.33 mm shift to the PDD curves of all the diodes and then the additional small "kick" correction only when necessary, was done for the PDD data of the 0.5x0.5 cm^2 field; the experimentally obtained data for all the detectors of the first set are presented in figure 4.5. The distance between the PDD curve of the Original diode and all the other modified detectors in the build-up region of the curves, at 80% of the maximum dose, was calculated and the results for the EPOM shifts both in the small (0.5x0.5 cm^2) and reference (4x4 cm^2) fields are summarised in table 4.1.

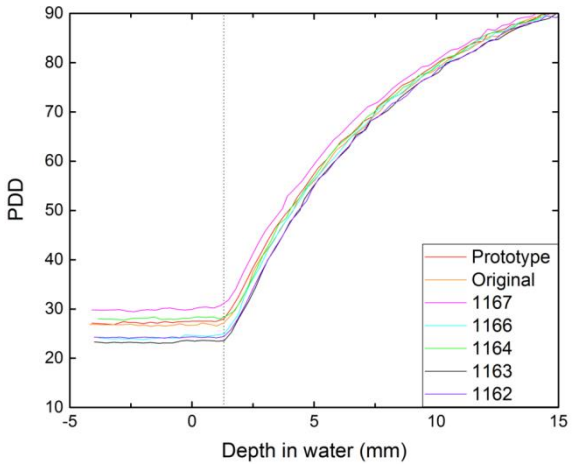

*Figure 4.4 (left): PDD curves for a **4x4 cm²** field with the "kick" point correction made. Very slight distance differences (depth-shifts) between the curves in the build-up region are observed meaning that the air-gaps affect the location of the EPOM in the modified diodes.*

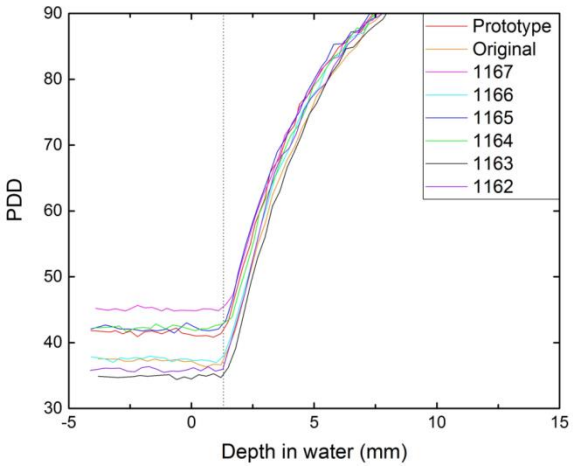

*Figure 4.5 (right): PDD curves for the **0.5x0.5 cm²** field with each "kick" shifted to a depth of 1.33 mm (dashed line). A +0.5 mm maximum distance (between the 1165, 1167, Prototype and the Original diodes) can be seen in the rising region of the curves.*

	0.5x0.5 cm^2	4x4 cm^2
DIODE	**EPOM shift (mm)**	
1162	0.0	-0.2
1163	0.0	-0.1
1164	0.4	0.2
1165	0.5	0.0
1166	0.3	-0.2
1167	0.5	0.5
Prototype	0.5	0.3

Table 4.1: EPOM shifts (in mm) estimated from the early (≤ 10 mm depth) part of the PDD curve for the two different fields measured in a 15 MV beam. No observed shift is larger than 0.5mm. The negative sign indicates that a shift towards the water surface needs to be applied to the PDD curve of the modified detectors (e.g. 1162, 1163 diodes in the 4x4 cm^2 field) to match the Original diode PDD data.

The shifts shown in table 4.1 are the shifts that need to be applied so that the PDD curve of each modified diode matches the PDD data of the (no air-gap) Original detector. For instance, in the 4x4 cm^2 field, the EPOM shift of the 1167 diode is +0.467 mm, i.e. the EPOM of the dosimeter lies at 1.33 + 0.467 ≈ 1.80 mm below the top surface of the detector.

As for the case of the 6 MV experimental data, the observed EPOM shifts for both fields were calculated based on the PDD data of the diode detectors at the dose build-up region (before the d_{max} point), because dose changes much more sharply with depth in this region. For this reason, a similar analysis based on the idea of identifying the EPOM shift from the whole PDD curve was completed for the 15 MV data as well. The ratio of the PDD data of each modified detector divided by the PDD data of the Original (un-modified) diode were plotted, after applying the calculated "pre-d_{max}" shifts presented in table 4.1. The normalisation method, of scaling each PDD curve so that the area under it between the depths x_1 (the shallowest point at which the PDD curves overlay after applying the shift) and x_2 (the deepest point that all the PDD curves were measured) is the same, was done again to avoid any bias of the dose by noise in the vicinity of the d_{max} point. For the 4x4 cm^2 field the graphs of the "old" 1 mm air-gap Prototype and the 1167 diodes are presented in figure 4.6.

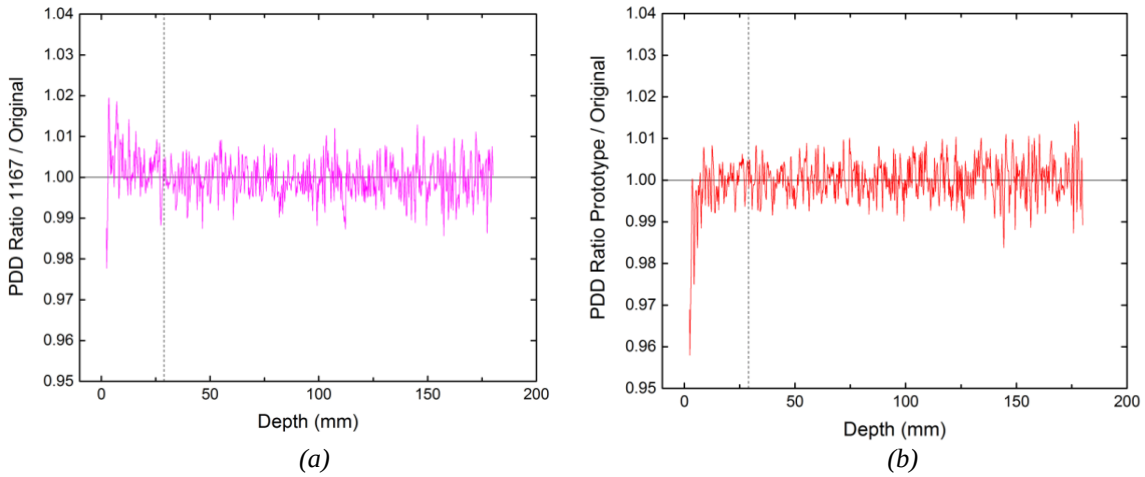

*Figure 4.6: Ratios of the shifted and normalised PDD data for diodes 1167 (a) and Prototype (b) divided by the PDD data of the Original diode in the **4x4 cm²** field. The calculated "pre-d_{max}" shift for each modified diode was applied to the whole PDD curve. The vertical dashed lines indicate the d_{max} point. No visible structure (apart from noise) can be observed beyond the d_{max} for either of the detectors.*

It is clear from figure 4.6 that both plots (a and b) have an average value within ± 1.5% of one – due to the normalisation method chosen – and some noise too. No structure is visible beyond the d_{max} point implying that there is no need to apply any additional EPOM shift to the PDD data apart from the one calculated at the build-up region of the curves. Similar graphs were created following exactly the same method for the rest of detectors in the 4x4 cm^2 field, all showing no visible structure beyond the d_{max} point, but are not included here to limit the amount of data presented in this chapter.

Regarding the 0.5x0.5 cm^2 field, the PDD data ratios of the modified diodes to the original (unmodified) one were also plotted to check if any systematic structures can be observed. In order to further investigate the validity of the calculated "pre-d_{max}" shifts in this field it was decided to plot the PDD ratios in two different ways: first, (a) with applying the "pre-d_{max}" shift, shown in table 4.1, to the whole PDD curve of each diode and then (b) without applying the shift at all. Both ways indicated that for the detectors with the smaller air-gaps ("old" Prototype and 1162 - 1165 diodes) applying the "pre-d_{max}" shifts makes no difference to the plotted ratios; all the ratio plots have an average value within ± 1.5% of one, and some noise too, without revealing any visible structure beyond the d_{max} point. Some representative graphs of the diodes with the "thinner" air-gaps are shown in figure 4.7 for the 0.5 cm square field.

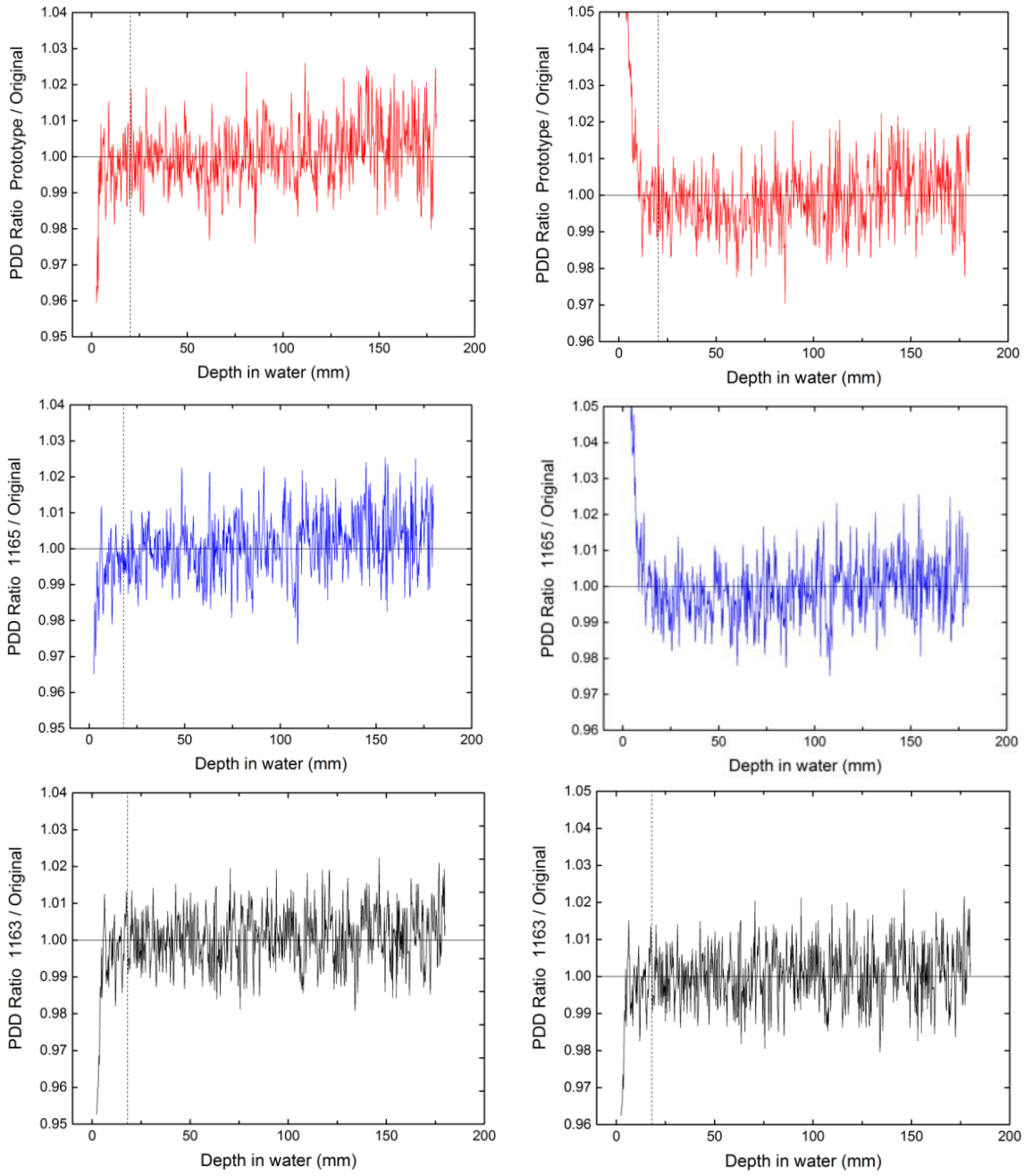

(a) with the shift applied ***(b) without the shift applied***

<u>Figure 4.7:</u> Ratios of the PDD data for diodes 1163, 1165 and the Prototype divided by the PDD data of the Original diode in the ***0.5x0.5 cm^2*** *field with (a) the "pre-d_{max}" shift applied and without (b) the shift. The vertical dashed lines show the d_{max} point. No visible structure, apart from noise, is observed either with or without the shift applied for any of these detectors beyond the d_{max} point.*

On the other hand, when plotting the PDD ratios for the detectors with the thickest air-gaps (1166 diode with 1.4 mm air-gap and 1167 diode with 1.6 mm air-gap) a slight visible structure can be seen both with and without the "pre-d_{max}" shifts applied. The corresponding graphs are presented in figure 4.8.

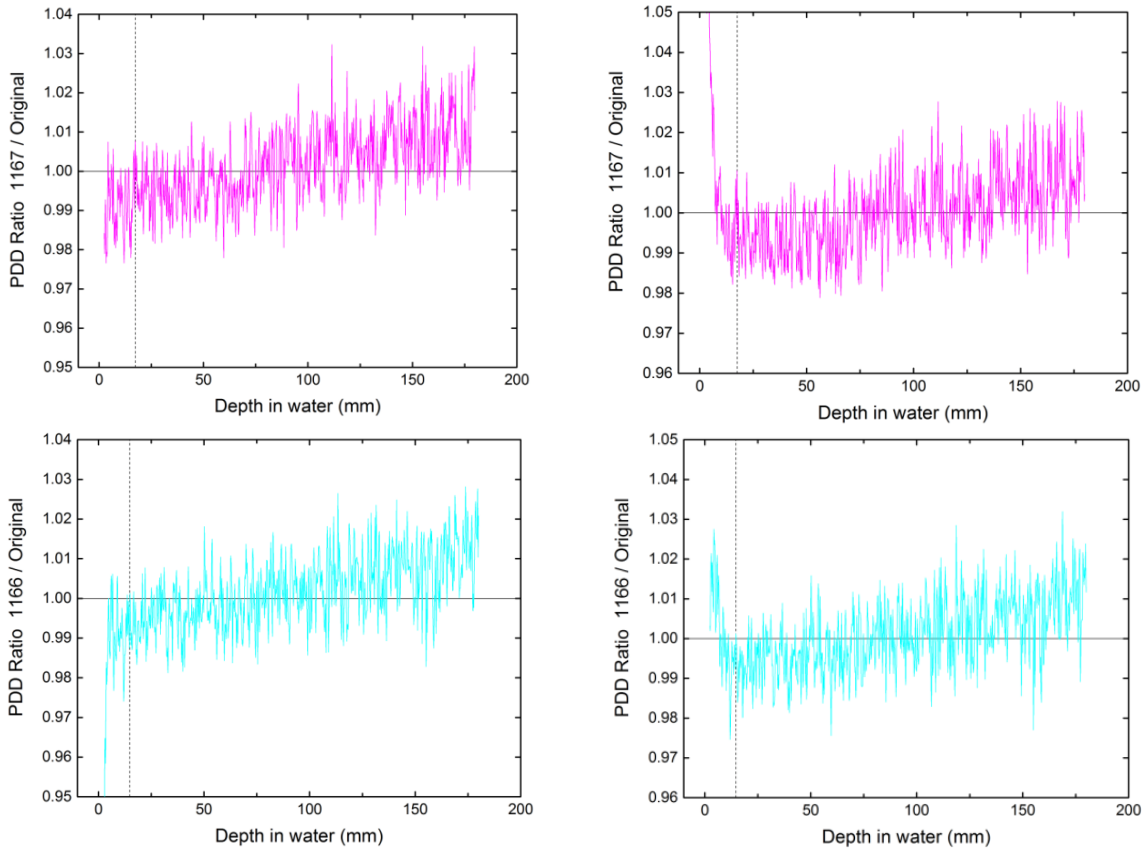

(a) with the shift applied ***(b) without the shift applied***

Figure 4.8: Ratios of the PDD data for diodes 1166 and 1167 divided by the PDD data of the Original diode in the ***0.5x0.5 cm^2*** *field with (a) the "pre-d_{max}" shift applied and without (b) the shift. The vertical dashed lines indicate the d_{max} point. Visible structures are observed for both detectors and applying the shift to the PDD curves makes the graphs even worse.*

4.3.3 Beam profile measurements – off-axis $k_{Q_{clin},Q_{msr}}^{f_{clin},f_{msr}}$ profiles

a) Full-width half maximum (FWHM) and penumbra values

In figure 4.9 the profile full-width half maxima (FWHMs) values for a 15 MV beam in a 0.5x0.5 cm^2 field at 5 cm deep are shown. The data were obtained experimentally using all the diode detectors of the original set and EBT3 film data are used as a gold standard. The horizontal black lines represent the mean values obtained from the irradiation of eleven EBT3 films in total. The one and two standard deviations from the mean value are indicated by the dark grey and light grey bands, respectively. For the detectors with on-axis *k* values differing less than ± 3% of 1.00, the width obtained at half maximum is accurate to 0.2 mm (0.1 mm for each side of the profile).

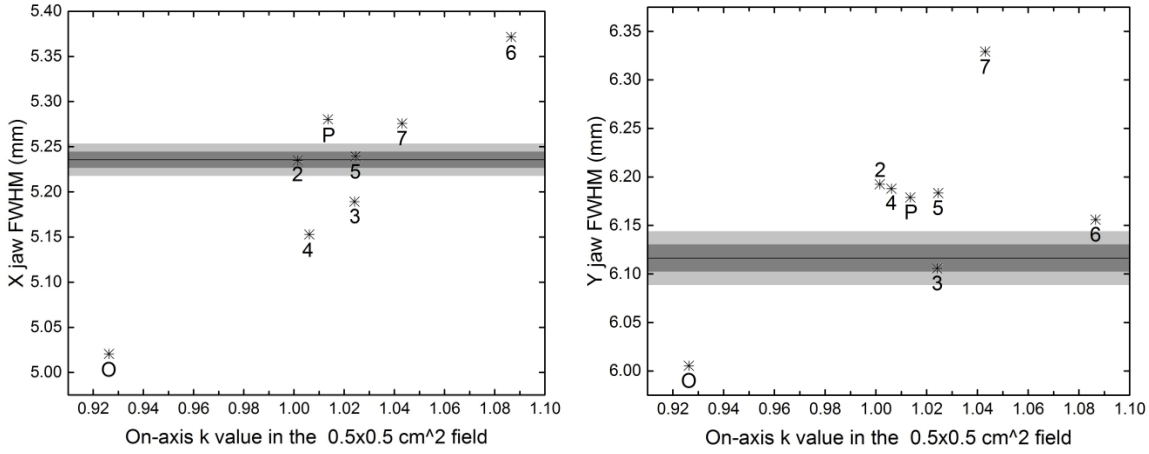

(a) *(b)*

*Figure 4.9: Profile FWHMs (a) for X-jaw and (b) for Y-jaw of all the diodes in a **0.5x0.5 cm²** field at SSD = 100 cm and **5 cm deep**. Stars show the data of the diodes and the black horizontal line the average value of the irradiated EBT3 films. For the x-axis of both graphs the on-axis k values of the diodes in the 0.5x0.5 cm^2 field at 5 cm deep are used. Diode names are shortened to improve visibility of the graphs, O: Original, P: Prototype, 1162 - 1167 diodes: 2 - 7.*

To be consistent with the 6 MV data presented in chapter 3, the full width at 20% of the maximum of the 15 MV beam profile for each diode in the 0.5x0.5 cm^2 field is also plotted against the on-axis *k* value of each diode in the same field (figure 4.10).

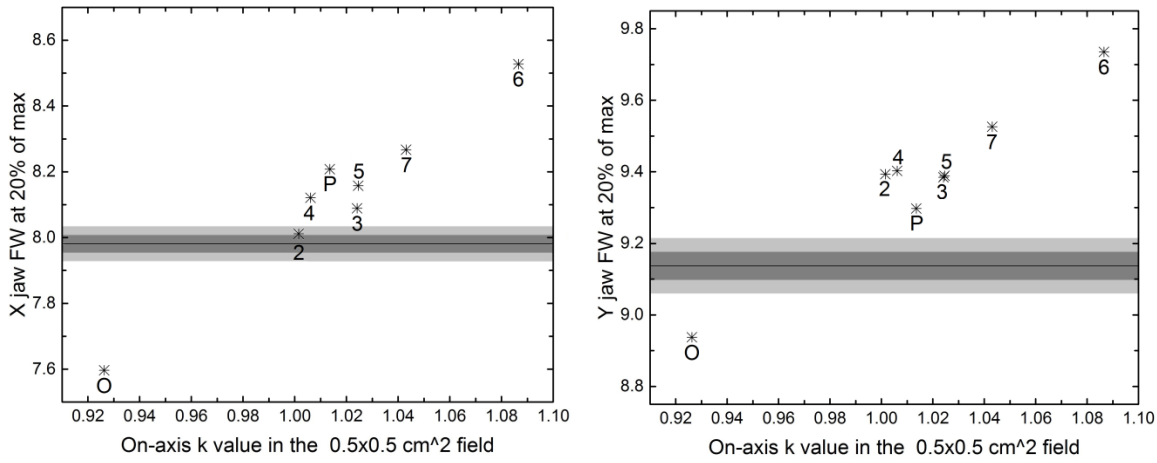

(a) *(b)*

Figure 4.10: Full Width at 20% of maximum of the 15 MV beam profile (a) for X-jaw and (b) for Y-jaw of all the diodes in a ***0.5x0.5 cm^2*** *field, at SSD = 100 cm and* ***5 cm deep.*** *The horizontal black lines indicate the average value obtained from the irradiation of eleven EBT3 films in total and the dark grey and light grey bands the one and two standard deviations from the mean value, respectively. O: Original, P: Prototype, 1162 - 1167 diodes: 2 - 7.*

Comparing the graphs of figures 4.9 and 4.10 it can be observed that there is a larger variation in the values of the full width at 20% of maximum of the profile than for the FWHM values between the diode detectors. In a narrow field (like the 0.5x0.5 cm^2) at 50% of the beam profile more electrons (that contribute to the measured dose) enter the cavity (i.e. the detector) on one side of the profile than on the other side, but at the same time the number of electrons that exit the cavity on one side is higher than the ones leaving the cavity on the other side so that the average number of electrons in the cavity is "right" resulting in the existence of (transient) charged particle equilibrium. On the other hand, in a "curved" region of the profile, like at the 20% of maximum, more electrons enter the cavity on one side of the profile than on the other and are not balanced by the number of electrons leaving the cavity. As a result non-equilibrium conditions exist there, meaning that for a dense detector, like the Original un-modified diode, electrons from outside the cavity travel less and the measured dose there is even lower compared to the over-reading of the detector on-axis, meaning that a much sharper penumbra is observed.

Finally, the 20:80% penumbra widths for all the diode detectors in the 0.5x0.5 cm^2 field, at 5 cm deep, are presented in figure 4.11. For each diode the value presented in these

graphs, is the average of the penumbra values of both sides of the profile; for detectors with *k* values within about ± 2% of 1.00 the penumbra values are right within 0.2 mm for each side of the profile.

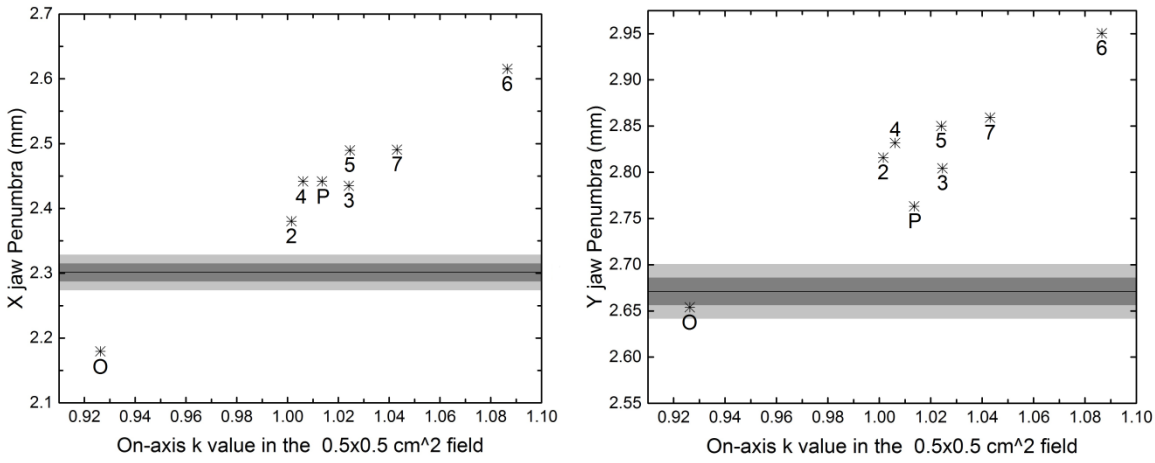

(a) *(b)*

Figure 4.11: 20:80 Penumbra values X-jaw (a) and Y-jaw (b) of all the diodes in a ***0.5x0.5 cm^2 field*** *at SSD = 100 cm and* ***5 cm deep****. Stars show the diode data and the black horizontal line the average value of the irradiated EBT3 films. One and two standard deviations from the mean value are shown by the dark grey and light grey bands, respectively. For the x-axis of both graphs the on-axis k values of the diodes in the 0.5x0.5 cm^2 field at 5 cm deep are used. O: Original, P: Prototype, 1162 - 1167 diodes: 2 - 7.*

b) Off-axis *k* profiles

Beam profiles obtained using both the diode detectors (moving in the cross-line direction, with the X pair of jaws defining the field at the edges the detector moves through) and EBT3 films were used to plot the off-axis *k* profiles for the diodes of the first set, according to the methodology described in section 3.2.1. Graphs for two different field sizes (0.5 and 0.7 cm square fields) are presented in the following figures (4.12 - 4.19). For both fields, the point of the film with the maximum value of dose was used as the on-axis point (x=0).For the smallest field measured (0.5x0.5 cm^2), off-axis *k* profiles (cross-line direction) are presented for all the diodes at 5 cm deep in water. Figure 4.12 shows the results for the "old" Prototype (1mm air-gap) diode at 5 cm deep. The error bars in the off-axis *k* profile graph (middle plot) display the (combined) fractional error of the film and the diode profiles, thus providing an estimate of the noise in three different parts of the *k* profile.

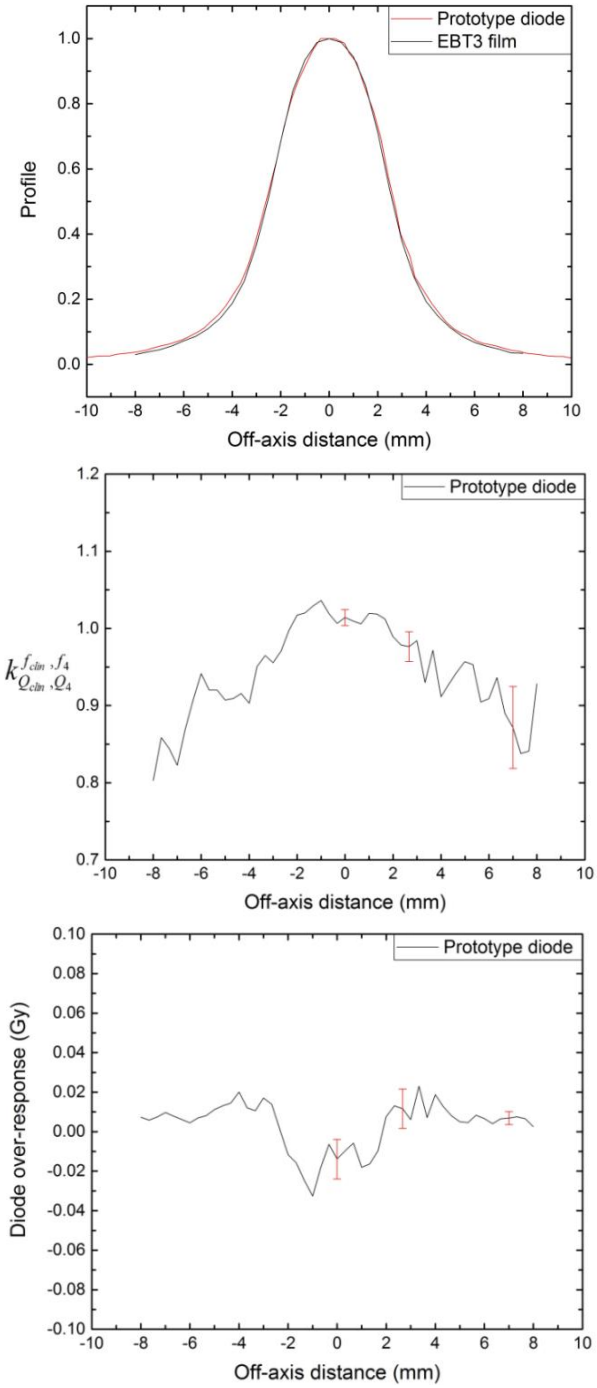

*<u>Figure 4.12:</u> Experimental data using EBT3 film and diode, X-jaw, showing the detector response off-axis across a **0.5x0.5 cm^2** field at **5 cm deep,** 100 cm SSD, in a 15 MV photon beam. The top plot shows the matching of the two profiles both normalized to 1 Gy on-axis. The middle plot shows the k correction factor (relative to 4x4 cm^2 field) at various positions off-axis (off-axis k profile). The error bars (2 s.d.) indicate the signal to noise ratio. The bottom plot shows the over-response of the uncorrected readings of the Prototype diode when a dose of 1 Gy was delivered on-axis.*

The off-axis *k* profiles with the corresponding over-response graphs for all the other diode detectors of the first set in the 0.5x0.5 cm^2 field, at 5 cm deep, are presented next. From figures 4.12 and 4.13 it is clear that detectors with $k \approx 1$ on-axis (like the "old" Prototype diode) perform better off-axis than the detectors with *k* values substantially different than one (e.g. the no air-gap Original diode).

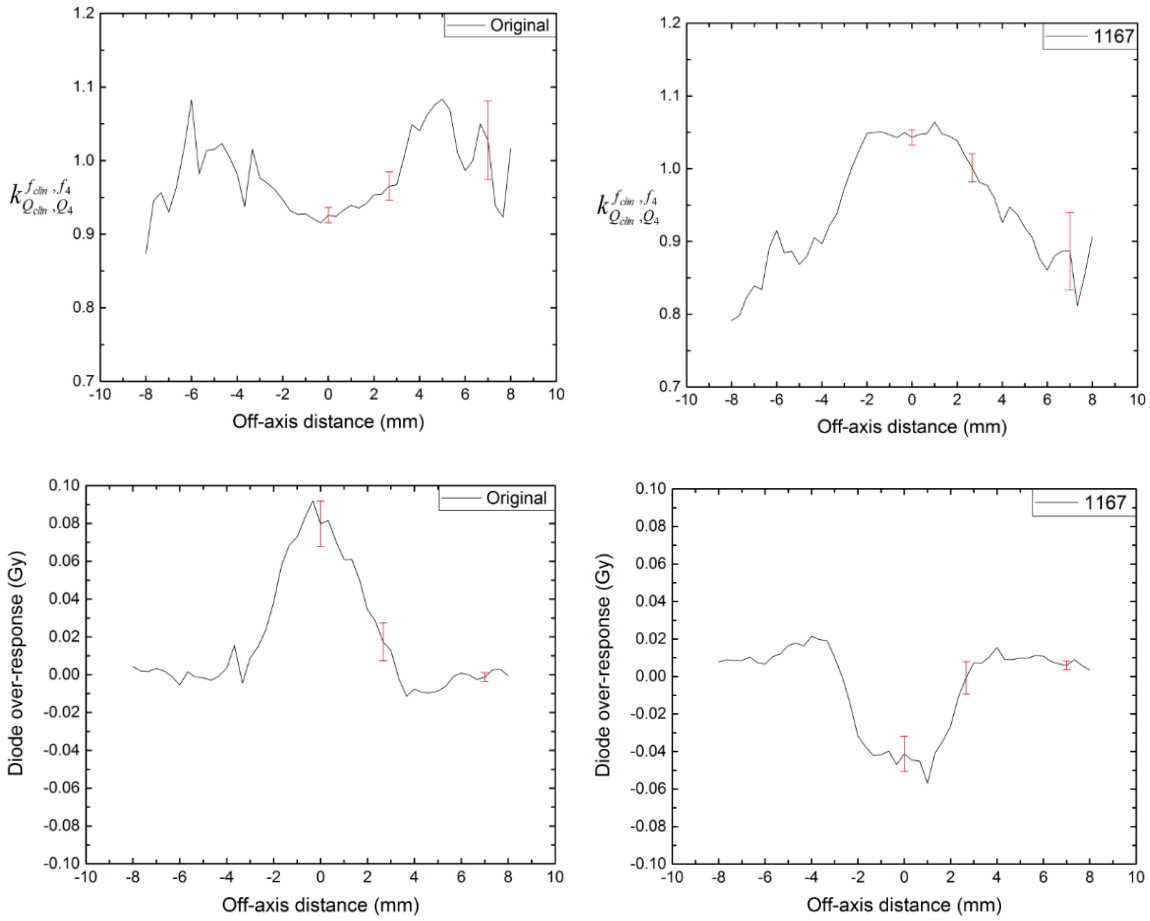

Figure 4.13: (a) Original diode off-axis k profile and over-response of uncorrected readings (when a dose of 1 Gy was delivered on-axis) in a 0.5x0.5 cm^2 field, at 5 cm deep, with a 4x4 cm^2 as the calibration field. (b) 1167 diode off-axis k profile and over-response of uncorrected readings (when a dose of 1 Gy was delivered on-axis) in the same field and depth. All error bars show statistical uncertainties at the 2 s.d. level.

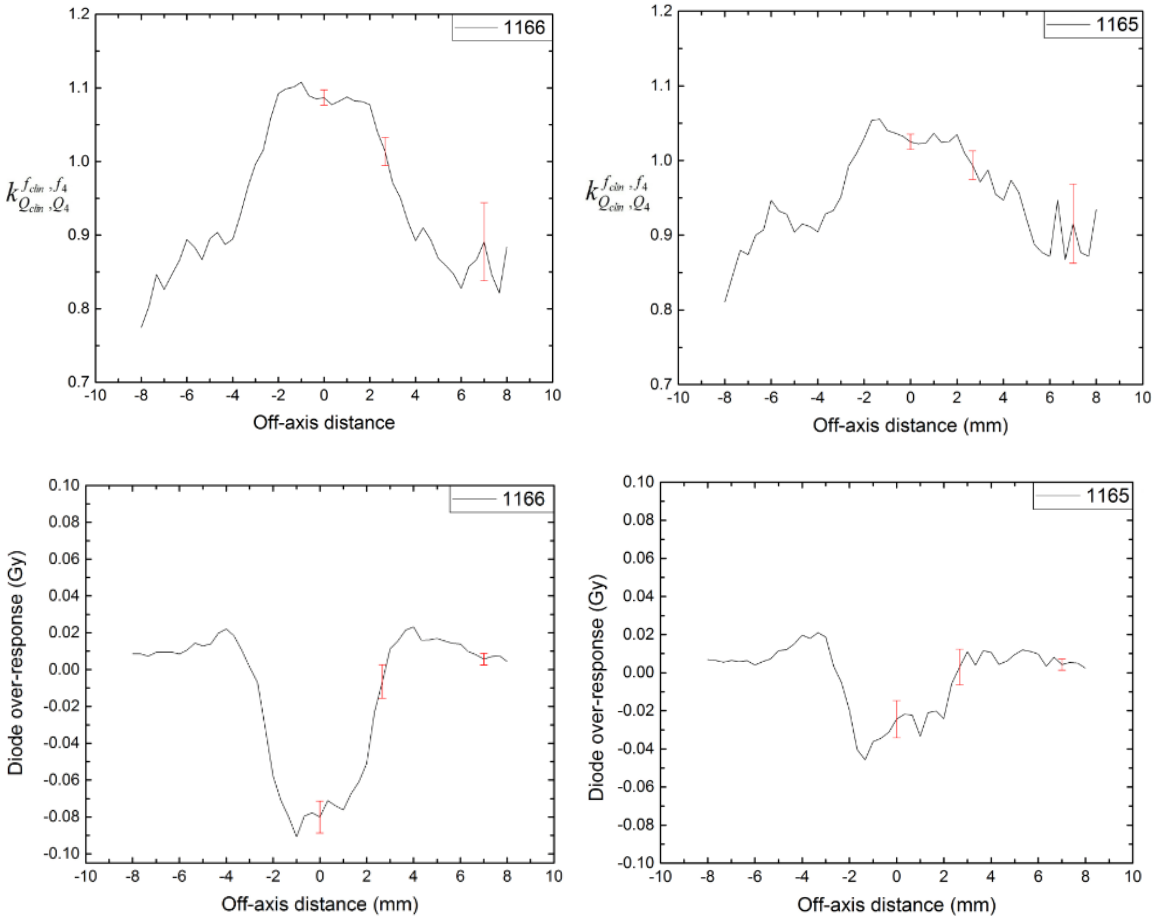

Figure 4.14: (a) 1166 diode off-axis k profile and over-response of uncorrected readings (when a dose of 1 Gy was delivered on-axis) in a 0.5x0.5 cm² field, at 5 cm deep, 100 cm SSD. (b) 1165 diode off-axis k profile and over-response of uncorrected readings (when a dose of 1 Gy was delivered on-axis) in the same field and depth. Statistical uncertainties shown are ± 2 s.d.

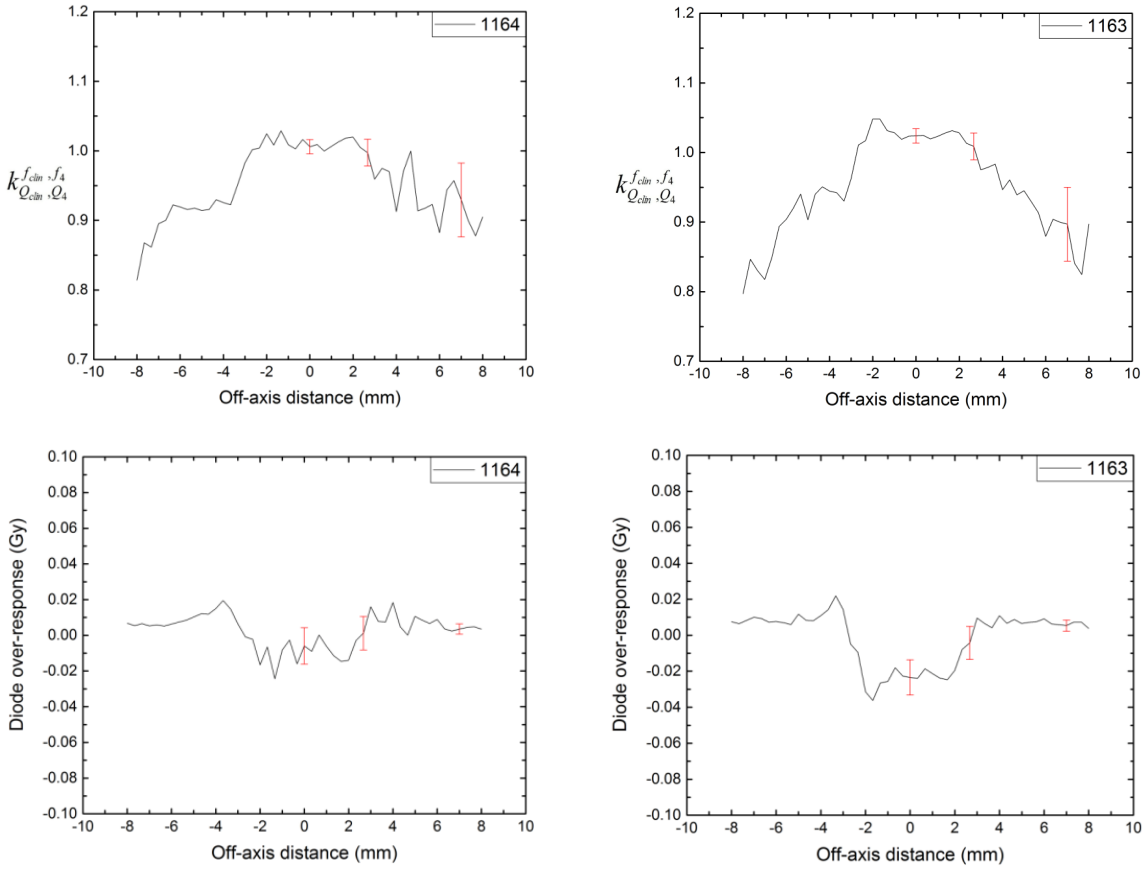

(a) *(b)*

Figure 4.15: (a) 1164 diode off-axis k profile and over-response of uncorrected readings in a 0.5x0.5cm² field, at 5 cm deep, 100 cm SSD. (b) 1163 diode off-axis k profile and over-response of uncorrected readings in the same field and depth. Statistical uncertainties shown are ± 2 s.d.

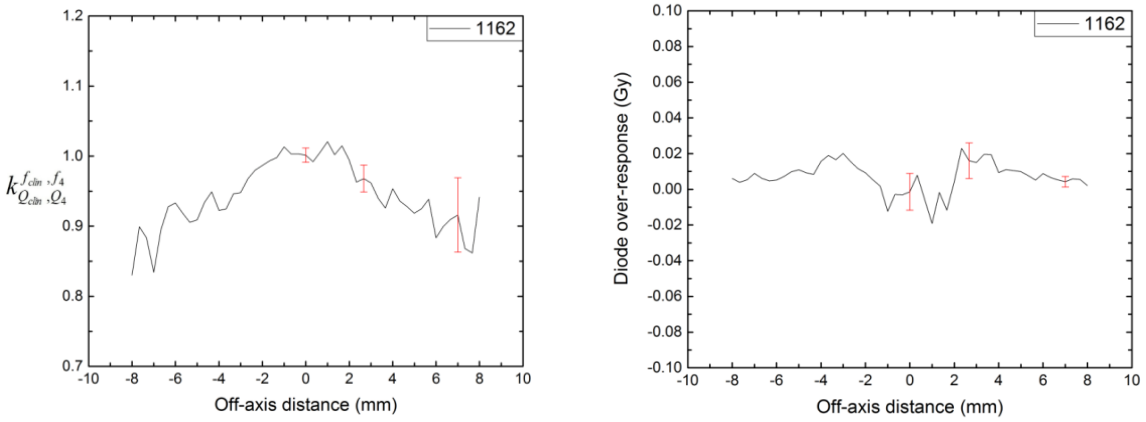

Figure 4.16: 1162 diode off-axis k profile (left) and over-response of uncorrected readings (right), 0.5x0.5 cm² field, 5cm deep, 100 cm SSD. Statistical uncertainties shown are ± 2 s.d.

The off-axis *k* profiles of all the detectors (of the first set) in a 0.5x0.5 cm^2 field, at **15 cm** deep in water were plotted too; some selected diode off-axis *k* profiles are presented in figures 4.17 and 4.18 to demonstrate that detectors which perform well at 5 cm deep (e.g. Prototype and 1163 diodes), show similar responses at an in-water depth of 15 cm too and are suitable for measurements at both depths. The same method was followed to obtain the off-axis *k* profiles, and the error bars (2 s.d.) indicate again the signal to noise ratio. The asymmetries observed in the off-axis *k* profile plots are due to noise (as previously discussed in chapter 3) and mainly in the low dose regions of the *k* profiles.

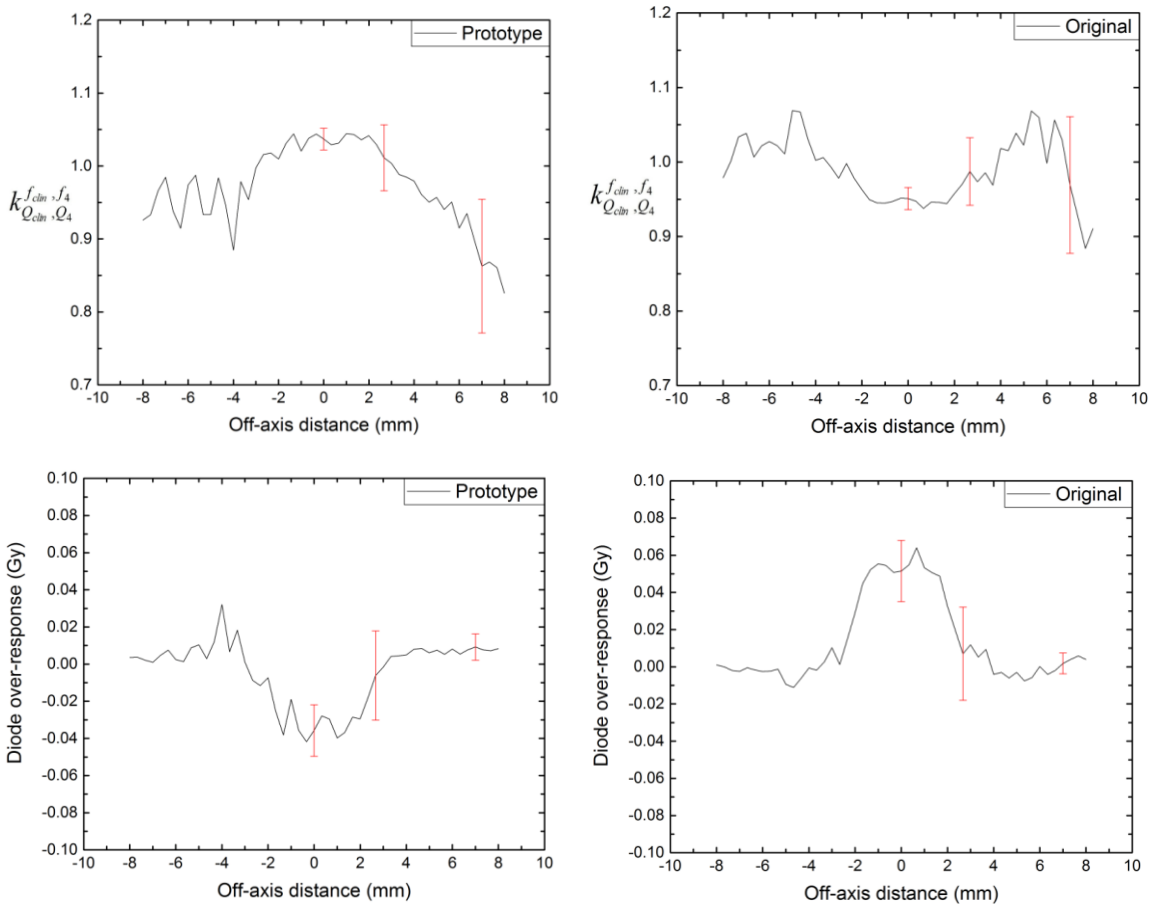

*Figure 4.17: Prototype 1 mm air-gap (a) and no air-gap Original (b) diodes off-axis k profile, X-jaw, and over-response of uncorrected readings in a 0.5x0.5 cm^2 field, at **15 cm deep**, 100 cm SSD. All error bars show statistical uncertainties at the 2 s.d. level. The modified (1 mm air-gap) Prototype diode performs significantly better than the no air-gap detector at this depth too.*

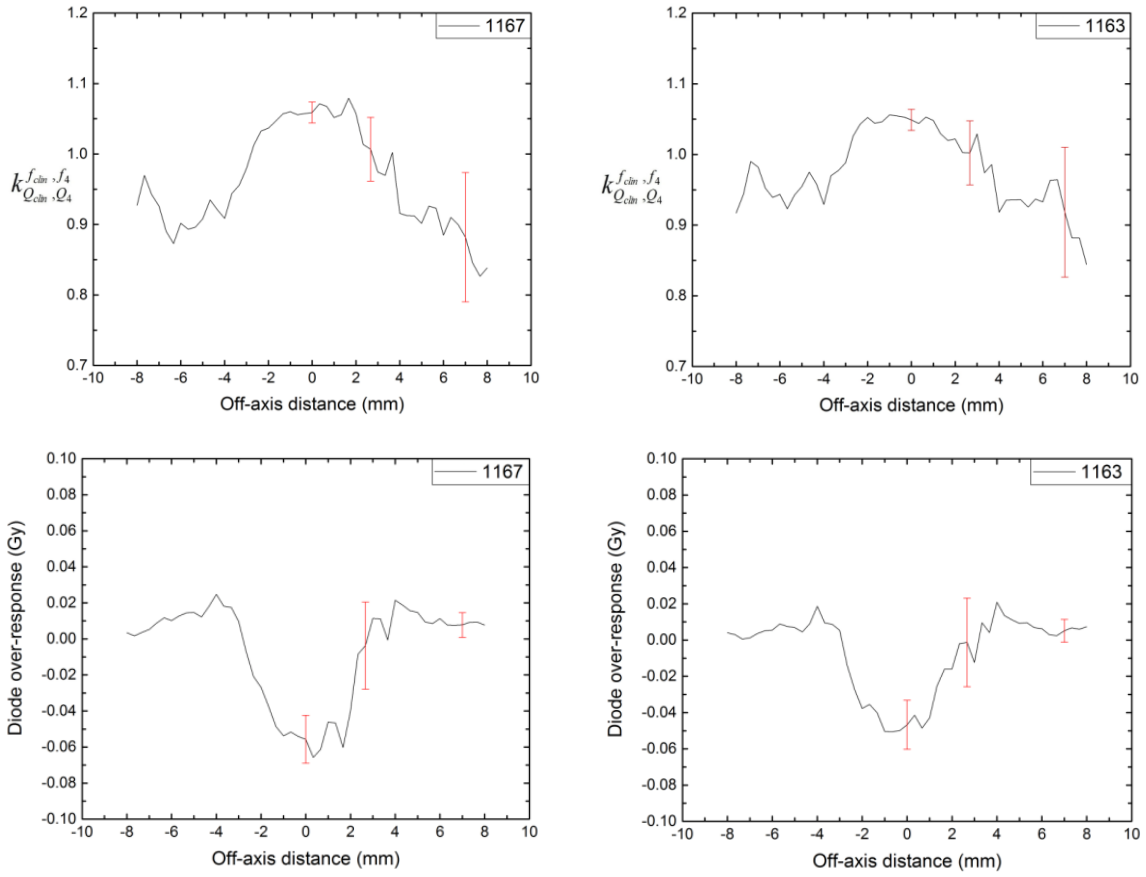

Figure 4.18: 1167 (a) and 1163 (b) diodes off-axis k profile, X-jaw, and over-response of uncorrected readings in a ***0.5x0.5 cm²*** *field, at* ***15 cm deep****, 100 cm SSD. Statistical uncertainties shown are ± 2 s.d. The 1163 diode performs better, i.e. k values across the 0.5 cm field much closer to one, than the 1167 detector.*

The off-axis *k* profiles for the (modified) Prototype diode and the Original un-modified diode in a **0.7x0.7 cm²** field, at 5 cm deep, are presented in figure 4.19 as a comparison between the two detectors. Again the Prototype diode (1 mm air-gap) seems to perform better than the Original detector (no air-gap), since its maximum dose error is within 2% (in contrast to the Original which is around 8%). Results for the rest of the detectors are very similar to the other fields measured, with the (*k* factor very close to 1.00) diodes performing better than the ones with *k* values far from 1.00.

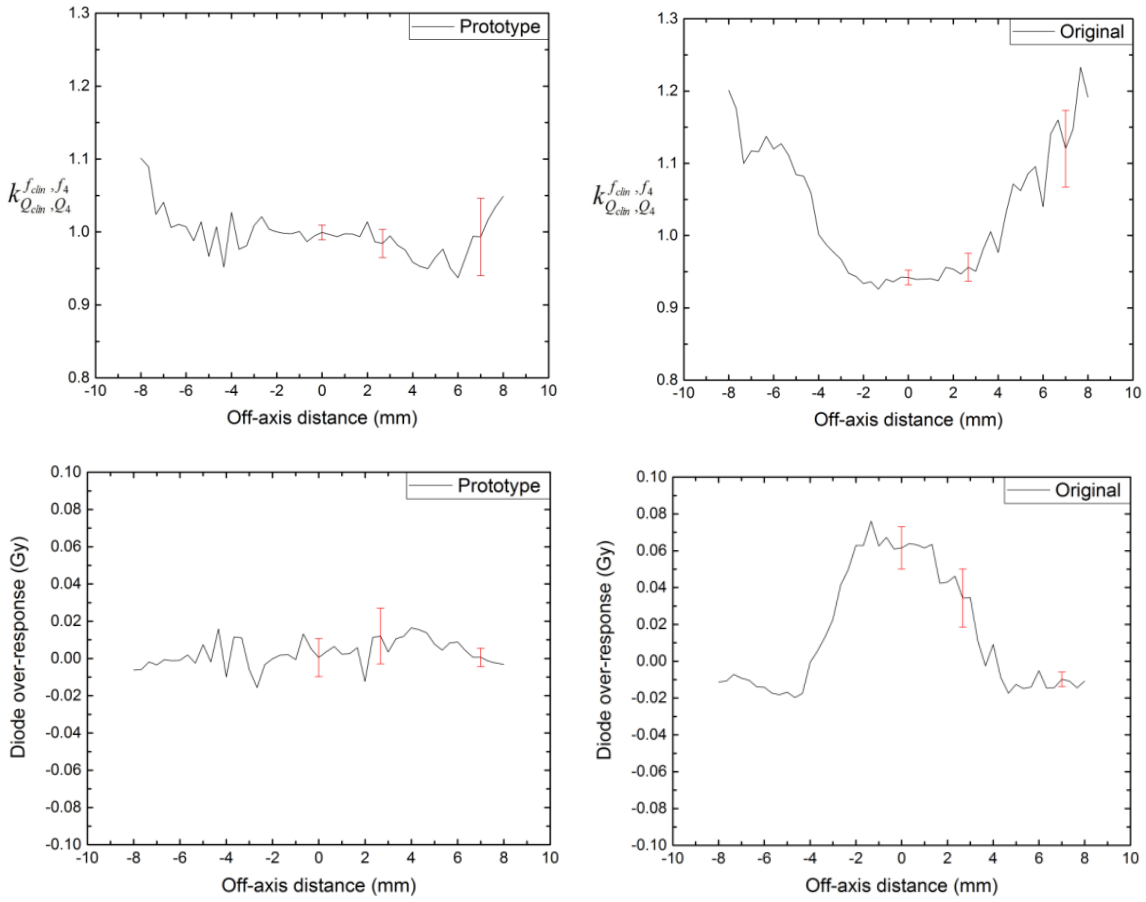

*Figure 4.19: Prototype 1 mm air-gap (a) and no air-gap Original (b) diodes off-axis k profile, X-jaw, and over-response of uncorrected readings in a **0.7x0.7 cm²** field, at **5 cm deep** and 100 cm SSD. All error bars show statistical uncertainties at the 2 s.d. level.*

4.4 Monte-Carlo results

4.4.1 On-axis $k_{Q_{0.5,4\ cm}}^{0.5,4\ cm}$ correction factors

The on-axis $k_{Q_{0.5,4\ \mathrm{cm}}}^{0.5,4\ \mathrm{cm}}$ factors calculated for the 15 MV beam model, at 5 cm deep in water, are summarised in table 4.2. Correction factors were calculated only for the no air-gap type 60017 Original diode, the "old" (1 mm air-gap) Prototype and the two modified detectors that showed the best performance according to the 6 MV Monte-Carlo data analysis.

Air-gap thickness (mm)	Detector	**Real air-gap** $k_{Q_{0.5,4\ cm}}^{0.5,4\ cm}$	**Wider air-gap** $k_{Q_{0.5,4\ cm}}^{0.5,4\ cm}$
-	60017 Original	0.896 ± 0.005	-
1	1 mm air-gap Prototype	-	0.978 ± 0.006
1.4	1166	-	1.009 ± 0.006
1.6	1167	1.006 ± 0.006	-

*Table 4.2: k correction values calculated for the 15 MV beam model, for on-axis readings made at an in-water depth of **5 cm in a 0.5×0.5 cm^2** field, using a detector calibrated in a 4×4 cm^2 field. Uncertainties are shown at the ± 2 s.d. level. Calculations were completed only for selected detector models based on the 6 MV results.*

With the sensitive volume of the detectors at 15 cm deep in the virtual water-tank, and keeping the same reference conditions (4x4 cm^2 field, at 5 cm deep), on-axis corrections factors were calculated again to ensure that the modified 1166 Wider and 1167 Real detectors perform well at a greater depth too. The detector models representing the density compensated diodes show a substantially improved response compared to the (no air-gap) Original diode detector model (table 4.3).

Air-gap thickness (mm)	Detector	**Real air-gap** $k_{Q_{0.5,4\ cm}}^{0.5,4\ cm}$	**Wider air-gap** $k_{Q_{0.5,4\ cm}}^{0.5,4\ cm}$
-	60017 Original	0.900 ± 0.005	-
1	1 mm air-gap Prototype	-	0.978 ± 0.006
1.4	1166	-	1.007 ± 0.006
1.6	1167	1.003 ± 0.006	-

*Table 4.3: k correction values calculated for the 15 MV beam model, for on-axis readings made at an in-water depth of **15 cm in a 0.5×0.5 cm^2 field**, using a detector calibrated in a 4×4 cm^2 field. Uncertainties are shown at the ± 2 s.d. level. The 1166 Wider and 1167 Real diodes perform well at a greater depth too, resulting in their k values being within 1% of 1.00.*

4.4.2 Percentage depth dose curves (PDDs) and EPOM shift analysis

The MC calculated PDD data, in a 0.5x0.5 cm^2 field, for the water voxel (DOSXYZnrc code used), and the 60017 Original and 1167 Real diodes (using the egs_chamber code) are shown in figure 4.20. All data were at first plotted against the real depth the detector's sensitive volume lies below the water surface (4.20a) and then with the "kick" points shifted at zero depth (4.20b) and last by applying a fixed 1.33 mm shift (4.20c).

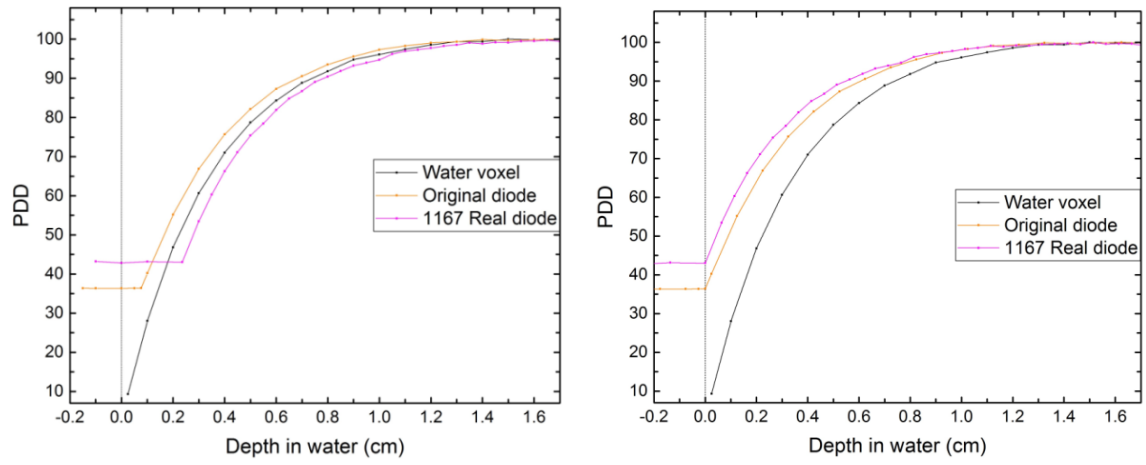

(a)

(b)

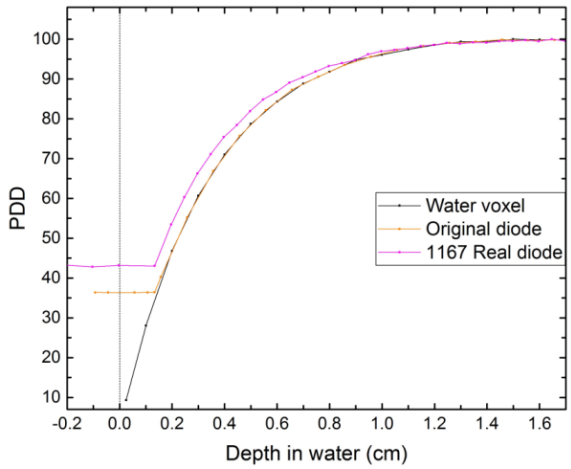

(c)

Figure 4.20: MC calculated PDD data for a 15 MV beam. In part (a) the detectors' reading is plotted against the depth of the sensitive volume in water with the "kick" point occurring for each detector when it is first submerged. In part (b) all detectors PDD data are shifted so the "kick" occurs at zero depth in water. In part (c) the same data is plotted, but now with all detector readings shifted by 1.33 mm. The Original diode PDD curve is perfectly aligned with the water voxel PDD data; whereas, a 0.54 mm distance between the 1167 Real diode and the water voxel PDD can be seen in the build-up region of the curves meaning the air-gap added slightly affects the detector's EPOM.

Similarly to the experimental data analysis and the 6 MV Monte-Carlo results, the PDD curves of the water voxel and the corrected (shifted) 1167 Real diode were again plotted, focusing now on greater depths in water, to confirm the validity of the observed "pre-d_{max}" 0.54 mm shift. The same normalisation method (curves normalised to the three highest values "window") was used for the 15 MV data, to ensure that the value of maximum dose is not biased due to noise close to d_{max}. The ± 2 s.d. statistical uncertainties were added to the plots in figure 4.21.

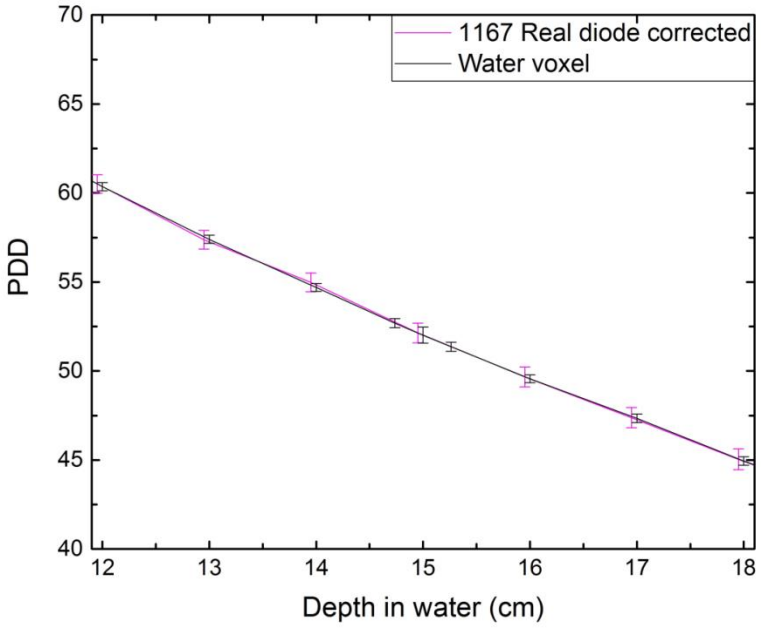

Figure 4.21: The water voxel PDD and the corrected (0.54 mm shift applied) 1167 Real diode PDD. The two PDD curves overlay well in this region, thus no additional shift is required to the diode PDD apart from the 0.54 mm one already applied.

4.4.3 Off-axis $k_{Q_{0.5,4\,cm}}^{0.5,4\,cm}$ profiles

As for the 6 MV beam model, MC simulations were run with the detector's sensitive volume at various positions off the central axis of the beam, at 5 and 15 cm deep in water to obtain the data for the off-axis *k* profiles in a 15 MV beam as well. Since the 1167 Real diode was the one showing the best performance at both depths in a 6 MV beam, a comparison between its off-axis response and the response of the (un-modified)

Original diode, at both 5 and 15 cm deep, is presented here. In figure 4.22, the off-axis *k* profiles and the diode over-response graphs are shown at 5 cm deep for both detectors, and figure 4.23 shows MC results at 15 cm deep in water. From both figures it can be concluded that adding an air-gap significantly improves the off-axis response of the diode at both 5 and 15 cm deep compared to the Original un-modified diode. The ± 2 s.d. statistical uncertainties (red error bars) of the MC calculations are included in the following plots.

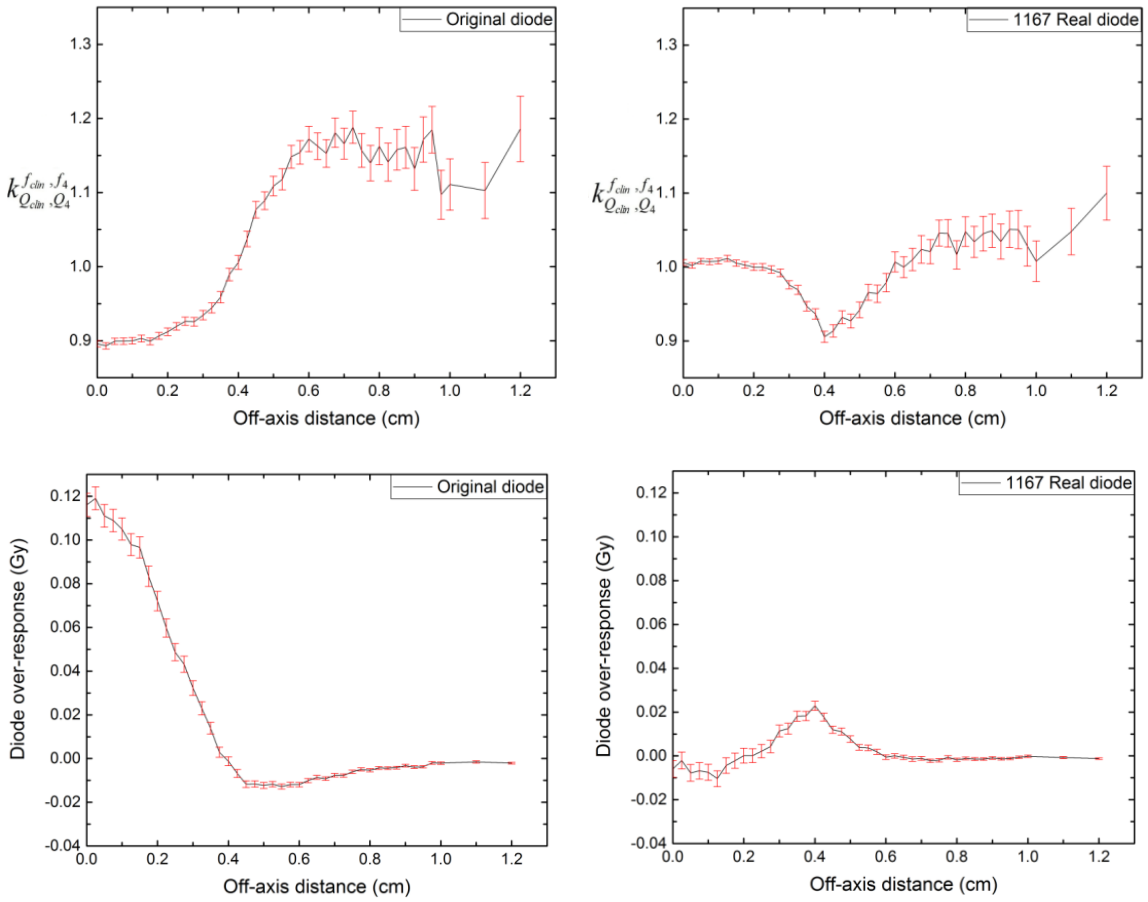

*Figure 4.22: (a) Simulation data for the Original diode off-axis k profile across a 0.5x0.5 cm² field at **5 cm deep** and 15 MV energy and the over-response of uncorrected readings when a dose of 1 Gy was delivered on-axis. (b) Simulation data for the 1167 Real diode off-axis k profile across a 0.5x0.5 cm² field at **5 cm deep** and 15 MV energy and the over-response of uncorrected readings when a dose of 1 Gy was delivered on-axis.*

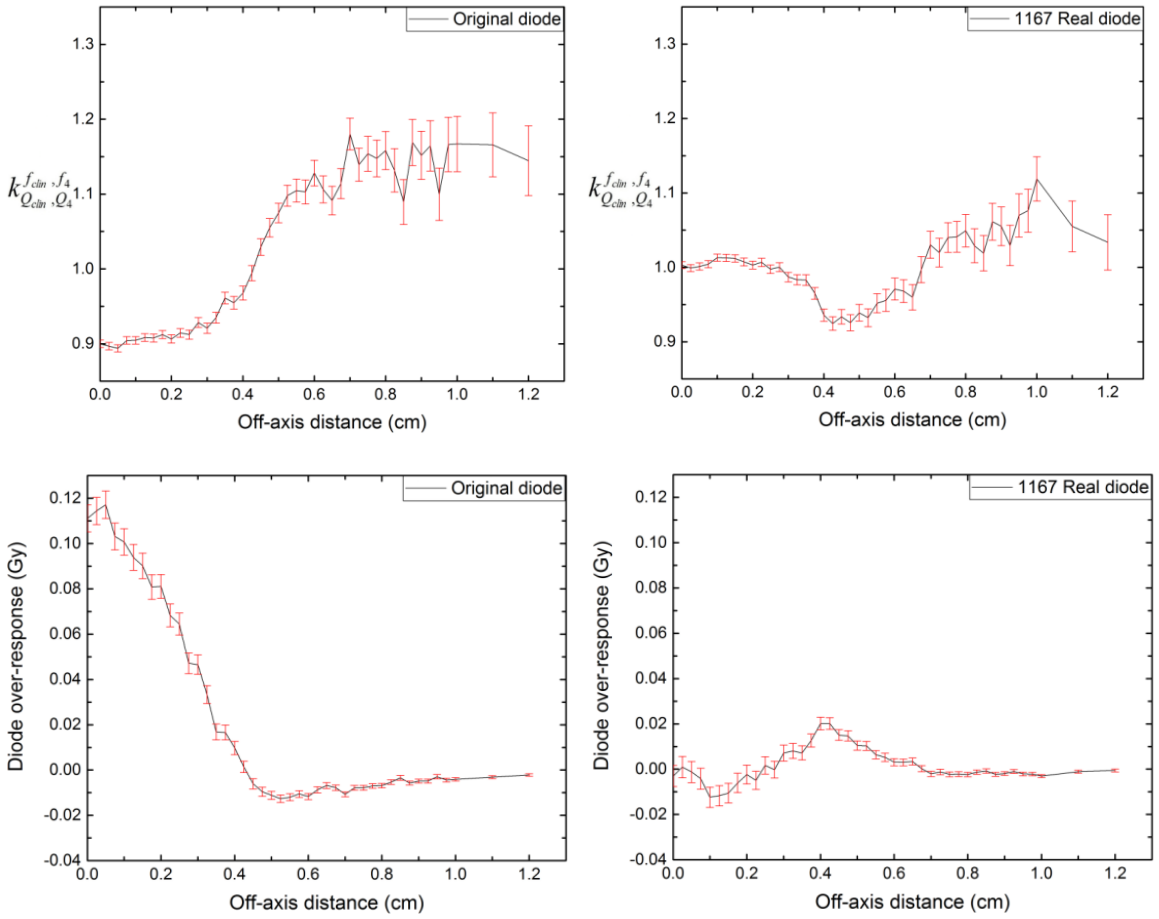

*Figure 4.23: (a) Simulation data for the original diode off-axis k profile across a 0.5x0.5 cm² field at **15 cm deep** and 15 MV energy and the over-response of uncorrected readings when a dose of 1 Gy was delivered on-axis. (b) Simulation data for the 1167 Real diode off-axis k profile across a 0.5x0.5 cm² field at **15 cm deep** and 15 MV energy and the over-response of uncorrected readings when a dose of 1 Gy was delivered on-axis. No over-response reading for the 1167 Real diode is more than 2%.*

4.5 Discussion of 15 MV results

The PTW silicon diodes of the first set have been experimentally characterised in a 15 MV photon beam and specific MC calculations have been completed for selected diode models of the same set as well. The data presented in this chapter (on-axis *k* values, depth doses and off-axis *k* profiles) confirm the findings of the 6 MV data (chapter 3) regarding the (air-gap based) mass-density compensation method: the inclusion of thin air-gaps above the sensitive silicon substantially improves the detector response at this higher beam energy too.

At depths of both 5 and 15 cm, the experimentally determined on-axis *k* values for the 1162 - 1167 modified didoes do not change progressively with the air-gap thickness, an issue previously encountered and discussed in chapter 3 (sections 3.3.4 and 3.5) and attributed to the un-controlled thickness of the denser material, compared to unit density water, present above the active region of the detectors (micro-CT image, figure 3.31). As for the 6 MV data, the Original and 1166 diodes are the two extremes with the *k* values for the rest of the detectors lying somewhere in between. The similar findings with the 6 MV data for the modified detectors imply that nothing was wrong with our experimental measurements in a 6 MV beam, since the detectors behave the same way. In figure 4.24 the 6 MV $k_{Q_{0.5,4\ cm}}^{0.5,4\ cm}$ values, at 5 cm deep, are plotted versus the detector air-gap thickness showing that for the experimental results (left plot) the curve is not monotonic (unexpected results for some of the *k* values on the basis of the air-gap thicknesses, also discussed in chapter 3). This is not the case for the computationally calculated *k* values (right plot) which increase while the thickness of the air-gap increases.

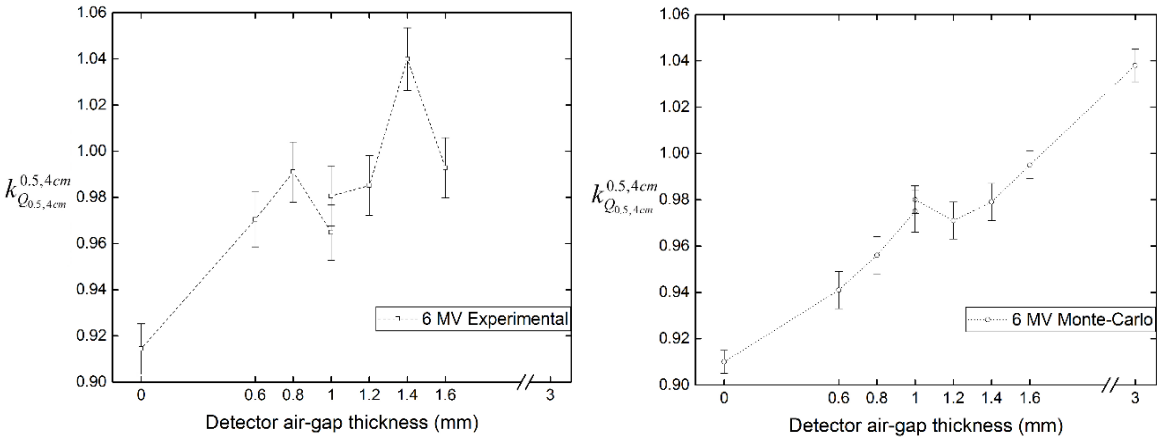

<u>Figure 4.24:</u> Experimentally determined (left) and MC calculated (right) 6 MV on-axis $k_{Q_{0.5,4\ cm}}^{0.5,4\ cm}$ values, at 5 cm deep, for all the diodes of the first set plotted against the air-gap thickness. The curve of the experimental values (left) is not monotonic, whereas for the MC results k values change progressively with the air-gap thickness. The MC calculated k value for the imaginary (3 mm thick air-gap) detector model is also added to the plot on the right.

The 6 MV experimental on-axis $k_{Q_{0.5,4\ cm}}^{0.5,4\ cm}$ values are now plotted in the same graph with the 15 MV experimental results (presented in section 4.3.1 of this chapter), both against the detector air-gap thickness, to demonstrate that the curves are similar at both beam energies (figure 4.25), meaning that the detectors behave in the same way at 6 and 15 MV. The measurements for the results presented in figure 4.25 are totally independent: different EBT3 films, based on two different calibration curves, were used to obtain the dose at a specific point in water at 6 and 15 MV.

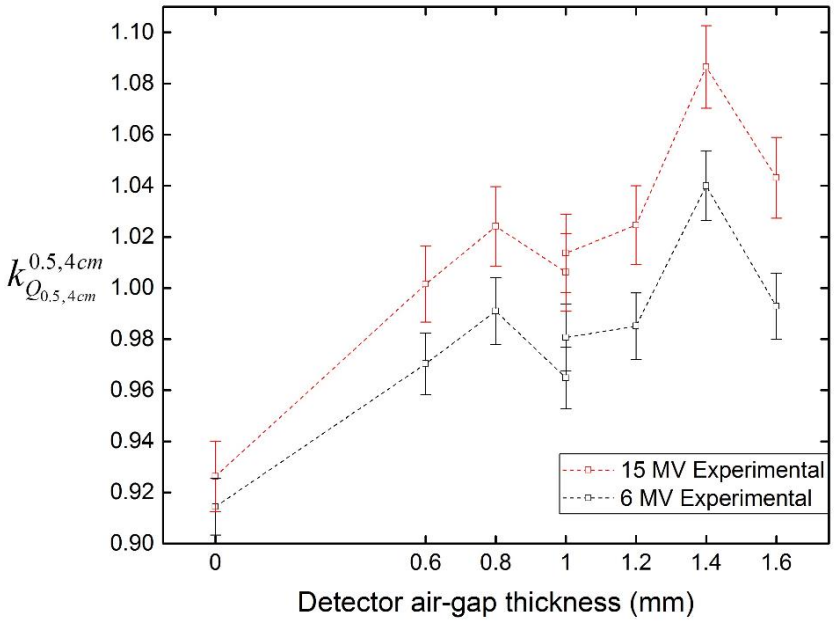

<u>Figure 4.25:</u> 6 MV and 15 MV on-axis k correction factors, at 5 cm deep and 100 cm SSD, in a 0.5x0.5 cm^2 field, plotted versus the different detector air-gap thickness. All the detectors of the first set show a similar behaviour at both beam energies.

From the experimental PDD data presented in this chapter it can be concluded that the different air-gaps added in the diodes do not affect the overall shape of the PDD curves in the 15 MV beam (figure 4.3). However, from figures 4.4 and 4.5 it can be concluded that there are some slight shifts to the modified detector EPOMs relative to the un-modified diode. In summary, the PDD analysis showed that the PDDs of the diodes are not substantially affected by the inclusion of air-gaps within the detectors (for both the 6

MV and 15 MV data), since all the EPOM shifts are less than 0.5 mm (tables 3.1 and 4.1). The reason for the visible structures in figure 4.8 (only for the diodes 1166 and 1167 and only for the 15 MV data) is not entirely clear; they can possibly be attributed to the output variation of the linac, but in any case the effect is very small. Regarding the Monte-Carlo PDD analysis, the 6 MV findings remain valid for the 15 MV beam energy as well, with the Original diode PDD perfectly matching the water voxel PDD and a small, 0.54 mm, shift necessary for the (modified) 1167 Real diode model.

From the experimental off-axis *k* profiles presented in this chapter it can be concluded that the modified detectors perform better than the (no air-gap) Original diode, a result in full agreement with the 6 MV data. Furthermore, as in a 6 MV photon beam, detectors that show good response on-axis, i.e. *k* values within ± 3.5% of 1.00, seem to perform well off-axis too at both 5 and 15 cm deep in a 15 MV beam. From the MC calculated off-axis *k* profiles (figures 4.22 and 4.23) it is evident that the 1167 Real diode (1.6 mm air-gap) substantially outperforms the Original detector (no air-gap) at both depths with none of its over-response readings more than 2%.

4.6 Conclusions

The experimental and computational results presented in this chapter show similar findings in a 15 MV beam for the (Type No. 60017) detectors as already observed in a 6 MV beam, and that in the 15 MV beam the (small-field) effects are slightly larger due to the existence of electrons with higher energies that travel further in water compared to ones produced by a 6 MV beam. The validity of the mass-density compensation method at this substantially higher beam energy is also confirmed, along with the same discrepancies in the response of the modified 1162 - 1167 diodes, on the basis of their air-gap thickness, because of the unexpected design issues previously discussed in detail. As a result, the experimental and computational evaluation of the performance of new improved detectors (Type No. 60023) manufactured by PTW, in both 6 and 15 MV photon beams, is presented in chapter 5.

Chapter 5

New detectors – 6 and 15 MV results

5.1 Introduction

The detailed experimental and computational characterisation of the original set of PTW silicon diodes (Type No. 60017 diodes) has revealed unexpected design issues (discussed in the previous three chapters and shown by the micro-CT imaging of the detectors, figure 3.31) which affected the detector response and caused discrepancies in the experimentally determined *k* values with respect to air-gap thicknesses. Following the testing of the 60017 PTW diodes, fundamental modifications were made in the design of the first set of dosimetry diodes leading to a second set of detectors – i.e. the Type No. 60023 PTW diodes – that have been tested both experimentally and computationally in the course of this project. The second set of PTW detectors comprises the un-modified 1518_36 diode (with no air-gap added), and the modified 1518_30, 1518_29 and 1518_26 diode detectors with 0.6, 0.8 and 1 mm thick air-gaps, respectively.

The sensitive volume of the 60023 PTW diode detectors is a very thin disc of silicon in contact with a larger silicon cuboid, and lies perpendicular to the detector long axis (as previously illustrated in chapter 2, figure 2.2). More materials with densities closer to 1 g cm^{-3} were used in these new detectors in the close proximity of the sensitive volume, to avoid – as much as possible – perturbation of the electron fluence. Moreover, the amounts of any existing materials whose densities differ from unity were better controlled, so that their thickness was kept constant and not variable between the four improved 60023 PTW diodes. Based on the mass-density compensation method (Underwood *et al* 2013b) air-gaps of different thickness were introduced above the sensitive silicon of the three modified type 60023 diodes (1518_26, 1518_29 and

1518_30). The air-gap was added between the main body of the detector and its plastic outer casing, resulting in a "compact" density compensated silicon diode detector without the need to add a removable and adjustable "air cap", as was previously done by Charles *et al* (2014).

The experimental and Monte-Carlo data presented in this chapter provide information about the response of the new PTW (Type No. 60023) silicon diodes in small and wider radiation fields, and comprise on-axis *k* values (under the Alfonso *et al* 2008 formalism), percentage depth doses (PDD curves) and off-axis *k* profiles, at both 6 and 15 MV, in accordance with the results of chapters 3 and 4 for the original set of detectors.

5.2 Methods

Using a 6 MV photon beam, produced by the Varian "TrueBeam" linac (Varian, Palo Alto, CA) located in the VT2 room at CCC, a preliminary set of experimental measurements were made to determine on-axis *k* values (according to Eq. 1.10) in a 0.5x0.5 cm^2 field, relative to a 4x4 cm^2 field, at 5 cm deep in the "Blue Phantom 2" water tank for all the new PTW 60023 diode detectors. This was done to check that the detector *k* correction factors varied monotonically with air-gap thickness, which would confirm that for these detectors variability in other components was less important.

The thicknesses of the air-gaps introduced in the type 60023 diodes were revealed by the manufacturer (PTW). Experimental and computational results described below confirm the monotonic variation of on-axis *k* values with air-gap for this detector type. Furthermore, these results show that in fact the best *k* values (i.e. closer to 1.00) were obtained only using the no air-gap (1518_36) and 0.6 mm air-gap (1518_30) diode detectors, and consequently the other two detectors with larger air-gaps were eliminated from further studies. This reduction in the number of detectors tested was useful both for minimising the experimental measurements and subsequent data analysis, and limiting the number of time-consuming MC calculations.

Exactly the same experimental methods described in detail in chapter 2 were followed for the characterisation of the 1518_30 and 1518_36 diodes both in 6 and 15 MV photon beams. Measurements were made with the two diode detectors (positioned vertically to the water surface, parallel to the beam axis) and EBT3 gafchromic film both at 5 and 15 cm deep in the water tank, in several clinical field sizes specified just by the collimator jaws, keeping the MLCs of the linac fully retracted throughout the whole experimental process and without using a reference detector at any point.

The measurements made with the improved Type No. 60023 PTW diodes, and presented in this chapter, are totally independent from the experimental work completed for the original set of detectors; the characterisation of the new set of diodes was done two years later than the work regarding the first set of detectors tested within this project. Consequently, two different calibration curves were generated using EBT3 films within the MATLAB software (one for each beam energy, method and details of calibration curves discussed in chapter 2, section 2.2.5.2).

The response of the 1518_36 and 1518_30 diodes has also been computationally evaluated using 6 MV (Underwood *et al* 2013a) and 15 MV beam models (Scott *et al* 2008). MC simulations were completed within the egs_chamber user-code (Wulff *et al* 2008) for both detector models: thirteen different materials were simulated in total to "build" each of the 60023 diode models, according to the manufacturer's confidential blueprints, and one of these media was then assigned to every one of the many specified "regions" constituting the geometry of the detector model.

MC studies of the response of the no air-gap 1518_36 and 0.6 mm air-gap 1518_30 diodes were carried out for a 0.5x0.5 cm^2 (small clinical) field and for a 4x4 cm^2 (machine-specific reference) field using the phase-space files previously created for the 6 MV (Underwood *et al* 2013a) and 15 MV (Scott *et al* 2008) beam models. Additional MC simulations were performed for both detector models in a 0.7x0.7 cm^2 (small) field both at 6 and 15 MV. The phase-space files used for the 6 MV and 15 MV 0.7x0.7 cm^2 fields contain 3.7 x 10^7 and 1.2 x 10^7 particles, respectively. Both 0.7x0.7 cm^2 phase-space files were created within the BEAMnrc (Rogers *et al* 2011) MC system, using the

previously experimentally validated beam models of Underwood *et al* (2013a) (6 MV) and Scott *et al* (2008) (15 MV).

The DOSXYZnrc (Rogers *et al* 2011) MC user-code was used again to score the energy deposition in specific water voxels of a 50x50x50 cm^3 virtual water tank. A water voxel of 0.25x0.25x0.5 mm^3 in dimensions was chosen to obtain the on-axis dose and beam profiles, at both 5 and 15 cm deep (100 cm SSD), in the small-fields (0.5 and 0.7 cm square fields), whereas a 2x2x0.5 mm^3 water voxel was used to calculate the on-axis dose at depths of 5 and 15 cm (100 cm SSD) in the reference field (4x4 cm^2). ECUT and PCUT values of 0.521 MeV and 0.001 MeV were set for all the DOSXYZnrc and egs_chamber MC simulations.

Finally, an additional detector model was created within the egs_chamber (Wulff *et al* 2008) user-code, using the EGS++ geometry package, representing an "imaginary type 60023" diode with an air-gap of 0.3 mm in thickness above the sensitive silicon. On-axis *k* values were computationally calculated for this imaginary 0.3 mm air-gap diode detector in 0.5 and 0.7 cm square fields, relative to a 4x4 cm field, for both beam energies (6 and 15 MV), only at 5 cm deep in water.

5.3 New PTW 60023 diode detectors – 6 MV experimental results

5.3.1 On-axis $k_{Q_{clin},Q_{msr}}^{f_{clin},f_{msr}}$ correction factors

The 6 MV experimentally determined on-axis $k_{Q_{0.5,4\ \mathrm{cm}}}^{0.5,4\ \mathrm{cm}}$ values, at 5 cm deep and 100 cm SSD, for all the new PTW 60023 diode detectors are plotted against their air-gap thicknesses in figure 5.1. The (no air-gap) 1518_36 and the (0.6 mm air-gap) 1518_30 diodes perform better, i.e. *k* values closer to 1.00, compared to the other two detectors (0.8 mm air-gap 1518_29 and 1.0 mm air-gap 1518_29). Furthermore, the no-air gap version of the new detector, the 1518_36 diode, has a *k* factor considerably closer to one than that of the type 60017 Original no air-gap detector. From figure 5.1 it can also be concluded that the calculated *k* values change progressively with the air-gap thickness

meaning there are no issues with the design of the improved 60023 PTW detectors (as in the case of the modified 1162 - 1167 type 60017 diodes of the first set).

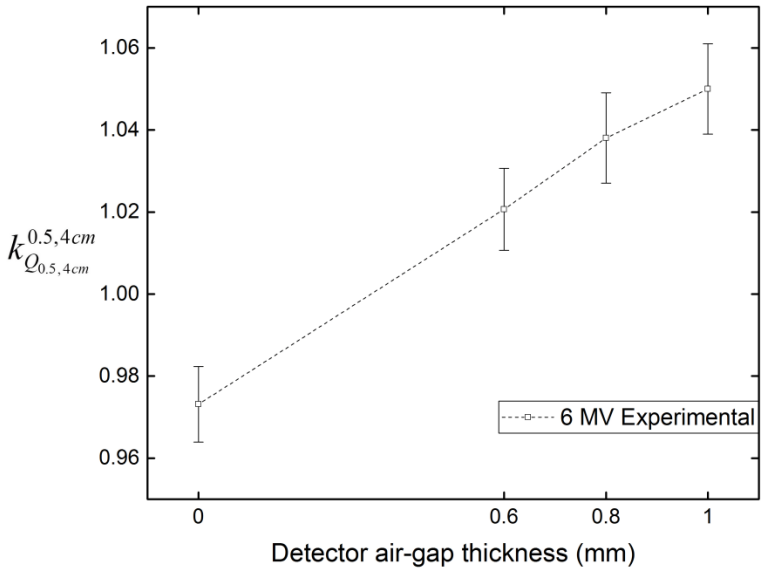

Figure 5.1: Experimentally calculated on-axis k correction factors for all the PTW 60023 diodes in a 0.5x0.5 cm^2 field, at 5 cm deep and 100 cm SSD. k values are plotted versus the detector air-gap thickness, 1518_36: no air-gap, 1518_30: 0.6 mm, 1518_29: 0.8 mm and 1518_26: 1.0 mm air-gap. The 1518_36 and 1518_30 diodes perform better than the rest of the detector on-axis, with the no air-gap 1518_36 detector over-reading (k < 1) by about 2.8% and the 0.6 mm air gap 1518_30 diode under-responding (k > 1) by ~ 2%, relative to the dose absorbed by a point of water at the same depth.

The Alfonso *et al* (2008) on-axis $k_{Q_{clin},Q_{msr}}^{f_{clin},f_{msr}}$ correction factors for the no air-gap 1518_36 diode and the modified (0.6 mm air-gap) 1518_30 detector experimentally determined in various clinical field sizes, relative to a 4x4 cm^2 field, are shown in figure 5.2. The values were obtained with both detectors and EBT3 films in a 6 MV photon beam, at 5 cm deep and 100 cm SSD, in the "Blue Phantom 2" water tank. Experimental statistical uncertainties are shown at the ± 2 s.d. level.

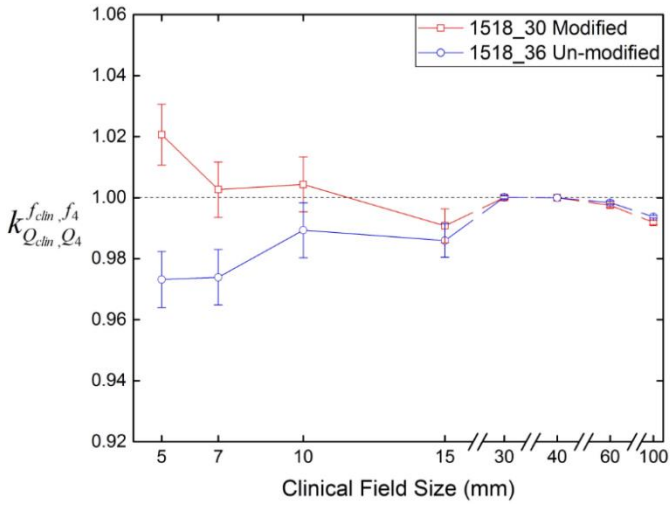

*Figure 5.2: Experimental results for the on-axis correction factors for a **6 MV** photon beam at **5 cm deep** in water. All values were calculated using a 4x4 cm^2 as the machine-specific reference field, also measured at 5 cm deep; the correction factor for this field at 5 cm deep is by definition equal to one for both detectors tested. Error bars show two standard deviations statistical uncertainties.*

Similar trends can be observed for the experimentally determined on-axis *k* values at 15 cm deep in water. Again the no air-gap detector (1518_36) seems to over-respond while the modified 1518_30 diode appears to be a little over-corrected after adding the 0.6 mm air-gap. Results are presented in figure 5.3, with all *k* values plotted against the various clinical fields measured.

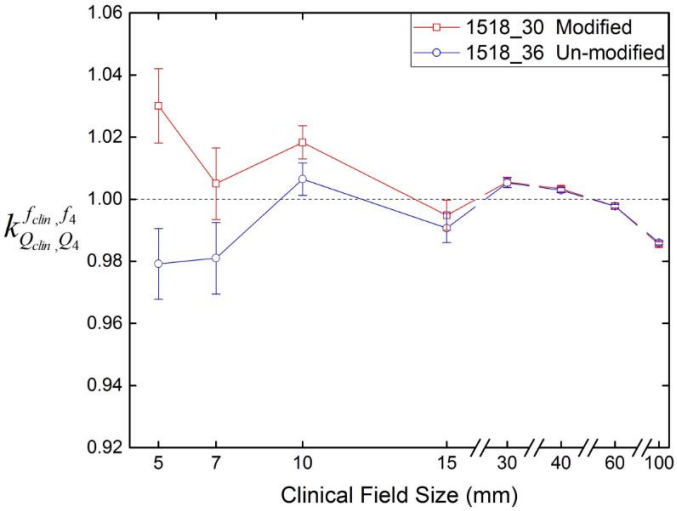

*Figure 5.3: Experimental results for the on-axis correction factors for a **6 MV** beam at **15 cm deep** in water. All values are calculated using a 4x4 cm^2 machine specific reference (msr) field, measured at 5 cm deep. Both detectors behave similarly at this greater depth in water. Error bars show two standard deviations statistical uncertainties.*

5.3.2 Percentage depth dose curves (PDDs) – EPOM shift

PDD data were acquired using both diode detectors in the smallest field measured, i.e. 0.5x0.5 cm^2, for a 6 MV beam. The PDD curves are plotted, focusing on the build-up region, (figure 5.4) after applying the 0.95 mm shift based on the information regarding the location of the EPOM in the no air-gap 1518_36 detector. The curves were measured at a spatial resolution of ~ 0.3 mm and thus the location of the "kick" could be corrected within ± 0.15 mm. Both PDD curves were normalised to the three highest values "window", a better method than just normalising to 100% at d_{max} because it is not so influenced by noise close to the d_{max} point. A -0.23 mm distance difference between the two PDD curves (PDD shift) can be seen in figure 5.4, meaning that the EPOM shift of the modified detector, relative to the detector with no air-gap, has the opposite sign than the PDD shift; the EPOM of the modified 1518_30 diode lies at 0.95 + 0.23 = 1.18 mm below the top surface of the detector.

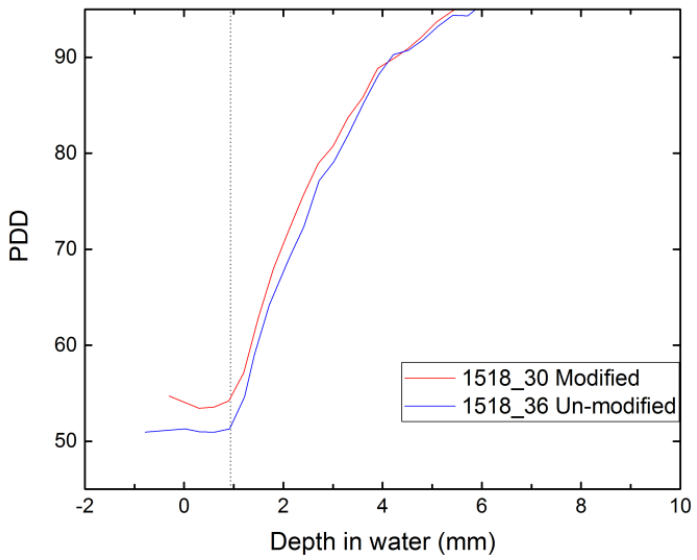

*Figure 5.4: PDD data obtained both with the un-modified (no air-gap) 1518_36 diode and the 1518_30 modified detector in a **0.5x0.5 cm^2** field at **6 MV**, with each "kick" shifted to a depth of 0.95 mm (dashed line). The calculated distance difference (0.23 mm) between the two curves in the build-up region, at 80% of the maximum dose, means that the air-gap added in the 1518_30 diode slightly changes the location of the detector's EPOM. Consequently, the EPOM shift of the 1518_30 diode is **+0.23 mm**.*

In figure 5.5 both PDD curves in the same field (0.5x0.5 cm^2) are plotted but now after applying a 0.23 mm shift to the curve of the 1518_30 modified detector and focusing at a greater depth in water. The two curves overlay, indicating that the PDD shift is the same in the build-up region and at depth, as might be expected for an effect resulting from an EPOM shift.

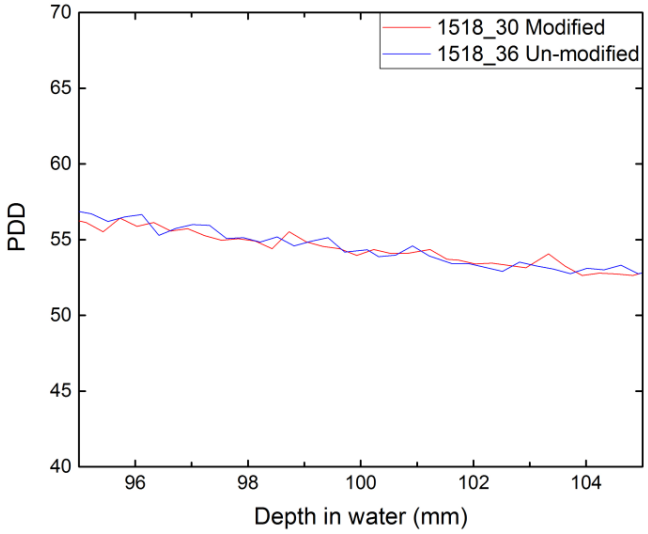

Figure 5.5: The (no air-gap) 1518_36 detector PDD and the corrected (0.23 mm shift applied) 1518_30 diode PDD, in a 0.5x0.5 cm^2 field. The curves overlay in this region, beyond the d_{max} point, no additional shift is required apart from the 0.23 mm one already applied to the curve of the 1518_30 diode.

5.3.3 Off-axis $k_{Q_{0.5,4\ cm}}^{0.5,4\ cm}$ beam profiles

6 MV beam profiles (in-line and cross-line directions) were obtained in a 0.5x0.5 cm^2 field, at 5 and 15 cm deep, from measurements made using both diodes (1518_36 and 1518_30) and EBT3 gafchromic films. The off-axis k profiles in the cross-line direction (X- pair of linac jaws defining the field at the edges the detectors move through) for the smallest field measured experimentally, i.e. the 0.5x0.5 cm^2 in which the detectors behave the most non-ideally, were plotted and results showing the response of the 1518_36 and 1518_30 detectors across the field, at 5 cm deep, are shown in figure 5.6.

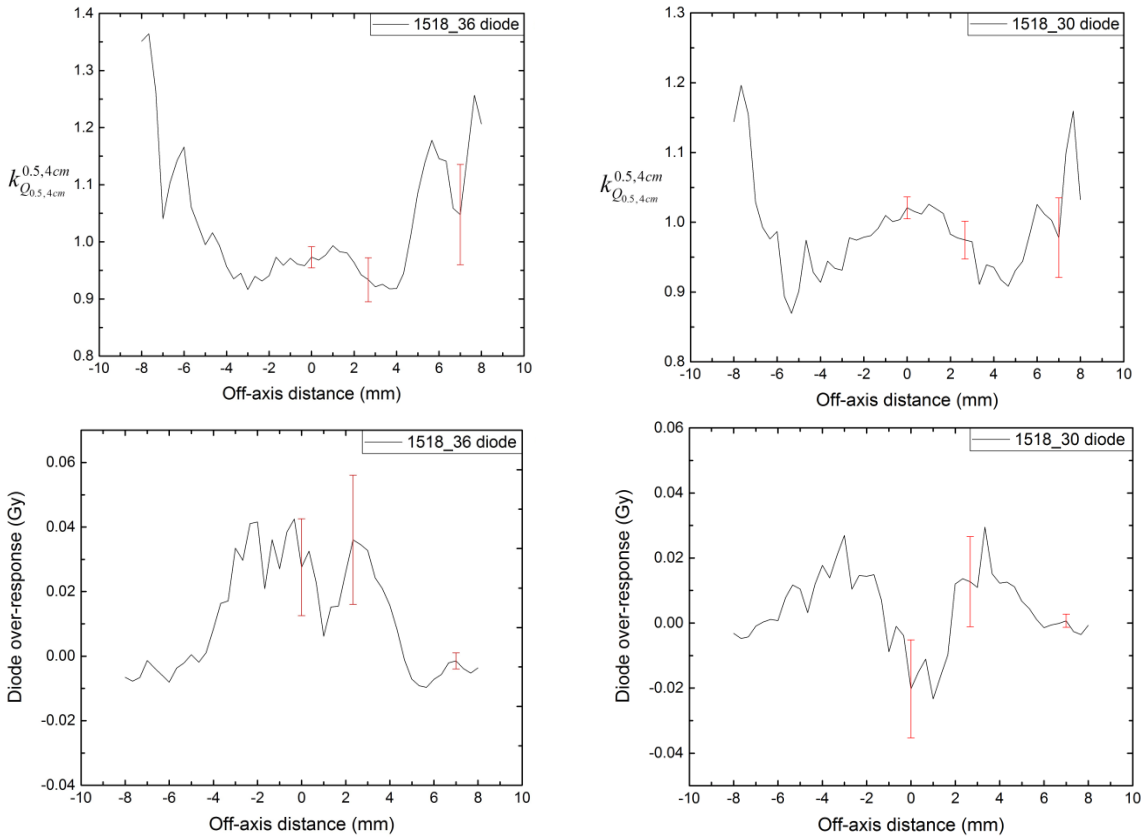

(a) *(b)*

Figure 5.6: Experimental data using EBT3 film and diodes, X-jaw, showing the detector response (a) of the 1518_36 un-modified diode and (b) of the 1518_30 modified detector, across a ***0.5x0.5 cm^2*** *field at* ***5 cm deep****, 100 cm SSD, in a* ***6 MV*** *photon beam. The top plots show the k correction factor (relative to a 4x4 cm^2 field) at various positions off-axis (off-axis k profile). The bottom plots show the over-response of the uncorrected readings of the diode detectors when a dose of 1 Gy was delivered on-axis. All error bars show statistical uncertainties at the ± 2 s.d. level.*

The off-axis *k* profiles of the 1518_36 and 1518_30 diodes in the same field (0.5x0.5 cm^2) but now at 15 cm deep in water are presented in figure 5.7. Similar observations can be made at both depths, with the un-modified 1518_36 detector, with no air-gap added, behaving as a slightly over-dense detector, and the (0.6 mm air-gap) 1518_30 diode behaving as a fractionally under-dense detector and slightly under-responding in the interior of the small field compared to EBT3 film.

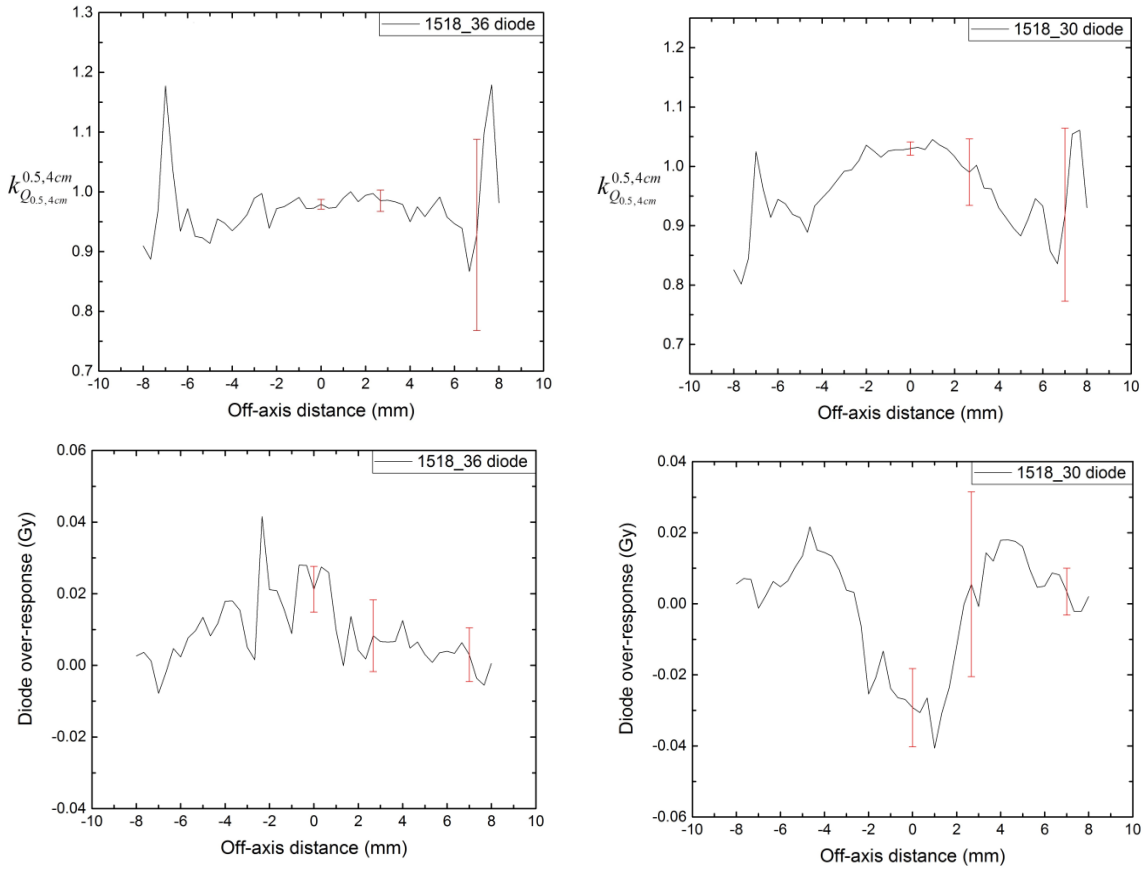

(a) *(b)*

*Figure 5.7: (a) 1518_36 diode off-axis k profile and over-response of uncorrected readings (when a dose of 1 Gy was delivered on-axis) in a **0.5x0.5 cm²** field, at **15 cm deep** and 100 cm SSD, in a **6 MV** photon beam. (b) 1518_30 diode off-axis k profile and over-response of uncorrected readings (when a dose of 1 Gy was delivered on-axis) in the same field and depth. Statistical uncertainties shown are ± 2 s.d.*

5.4 New PTW 60023 diode detectors – 6 MV Monte-Carlo results

5.4.1 On-axis $k_{Q_{clin},Q_{msr}}^{f_{clin},f_{msr}}$ correction factors

On-axis $k_{Q_{clin},Q_{msr}}^{f_{clin},f_{msr}}$ correction values (Eq. 1.10) have been computationally calculated using the 6 MV beam model for both the (no air-gap) 1518_36 diode and the 1518_30 modified detector in 0.5x0.5 and 0.7x0.7 cm^2 fields[1], at 5 cm deep and 100 cm SSD. The MC results presented in table 5.1 are reassuringly similar to the experimental ones,

[1] Correction factors were calculated only in 0.5 and 0.7 cm square fields, because these fields are the ones in which the detectors behave most non-ideally.

suggesting that the real detectors are very close to their design. The *k* values for the (0.3 mm air-gap) imaginary type 60023 diode model, in both fields, are also included.

Air-gap thickness (mm)	Detector	On-axis $k_{Q_{0.5,4\ cm}}^{0.5,4\ cm}$ value	On-axis $k_{Q_{0.7,4\ cm}}^{0.7,4\ cm}$ value
-	1518_36 un-modified	0.979 ± 0.006	0.977 ± 0.006
0.3	Imaginary type 60023	1.007 ± 0.006	0.995 ± 0.006
0.6	1518_30 modified	1.029 ± 0.006	1.002 ± 0.006

*Table 5.1: k correction values calculated for the **6 MV** beam model, for on-axis readings made at an in-water depth of **5 cm** in both small fields, using a detector calibrated in a 4×4 cm^2 field. Uncertainties are shown at the ± 2 s.d. level. The no air-gap 1518_36 diode behaves as a slightly over-dense dosimeter in both fields, whereas the modified 1518_30 diode is a little over-corrected. The 0.3 mm air-gap variant of the 60023 PTW diodes performs best on-axis, since both its k values lie within ± 1% of 1.00.*

With the sensitive volume of the detectors at 15 cm deep in the virtual water-tank and the same reference conditions (4x4 cm2 field, at 5 cm deep and 100 cm SSD), on-axis corrections factors were calculated again to computationally evaluate the response of the 60023 diodes at this greater depth as well. Similar trends are observed for the detectors at both depths (5 and 15 cm deep) with the no air-gap 1518_36 detector behaving as a slightly over-dense dosimeter (though not nearly so much as the un-modified 60017 Original diode of the first set) and the 1518_30 modified diode being a little over-corrected, driving its *k* value to about 4% higher than 1.00 (detector under-reads relative to the dose absorbed by a point of water) at 15 cm deep in a 0.5 square field.

Air-gap thickness (mm)	Detector	On-axis $k_{Q_{0.5,4\ cm}}^{0.5,4\ cm}$ value	On-axis $k_{Q_{0.7,4\ cm}}^{0.7,4\ cm}$ value
-	1518_36 un-modified	0.987 ± 0.008	0.988 ± 0.007
0.6	1518_30 modified	1.038 ± 0.008	1.012 ± 0.008

*Table 5.2: k correction values calculated for the 6 MV beam model, for on-axis readings made at an in-water depth of **15 cm** in a **0.5×0.5** and a **0.7x0.7 cm² field**, using a detector calibrated in a 4×4 cm² field. Uncertainties are shown at the ±2 s.d. level.*

5.4.2 Percentage depth dose curves (PDDs)

The PDD data, in a 0.5x0.5 cm^2 field, computationally calculated at 6 MV in water voxels (using the DOSXYZnrc user-code) and for the PTW 60023 diode detectors (completed within the egs_chamber code) are presented in figure 5.8. As for the original set of detectors the reading of each diode was plotted at first against the real depth of the detector's sensitive volume in water (part 5.8a). In part 5.8b (top right plot) the detector readings are shifted so that each "kick" is occurring at zero depth in water and in the last part (5.8c) of the figure by applying a fixed 0.95 mm shift.

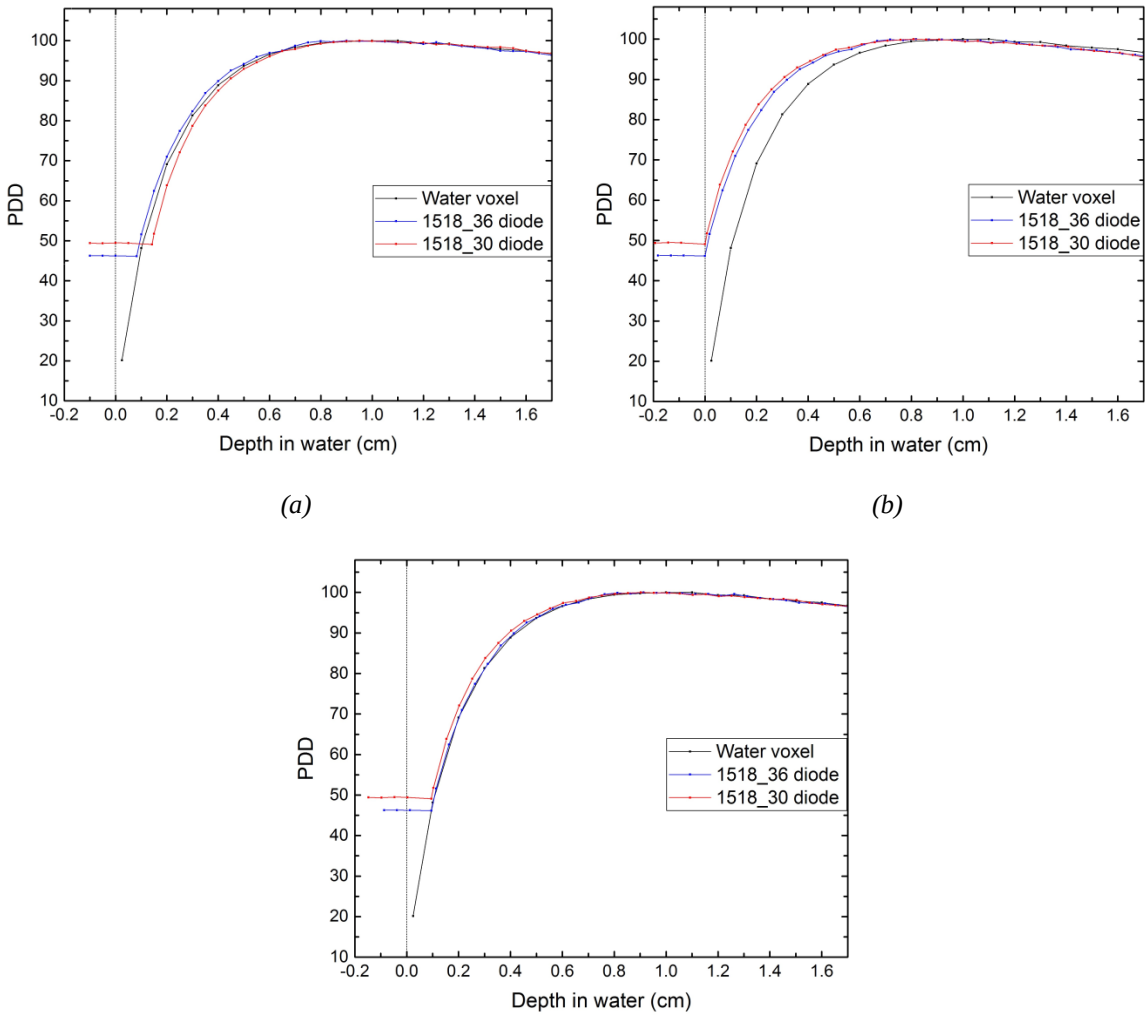

*Figure 5.8: MC calculated PDD data for a **6 MV** beam model. In part (a) the detectors' reading is plotted against the real depth of the sensitive volume in water with the "kick" point occurring for each detector when it is first submerged. In part (b) all detectors PDD data are shifted so the "kick" occurs at zero depth in water. In part (c) the same data is plotted, but now with all detector readings shifted by 0.95 mm. The (no air-gap) 1518_36 diode PDD curve is perfectly aligned with the water voxel PDD data; whereas, a 0.24 mm distance between the 1518_30 modified diode and the water voxel PDD can be noticed in the build-up region of the curves meaning the air-gap added slightly affects the detector's EPOM.*

The 0.24 mm shift observed in figure 5.8 (part c) is strikingly similar to the 0.23 mm shift determined experimentally (section 5.3.2). The PDD data of the water voxel and the 1518_30 modified detector were plotted again but now after applying the observed "pre-d_{max}" shift correction to the whole of the diode PDD curve. A comparison of the two PDD curves indicating the matching of the curves at greater depths is shown in

figure 5.9. Error bars showing 2 s.d. statistical uncertainties for both the water voxel and the 1518_30 detector data were added to the plot to demonstrate that any mismatch between the curves is within the noise limits. Both PDD curves were normalised to the "window" of the three highest values.

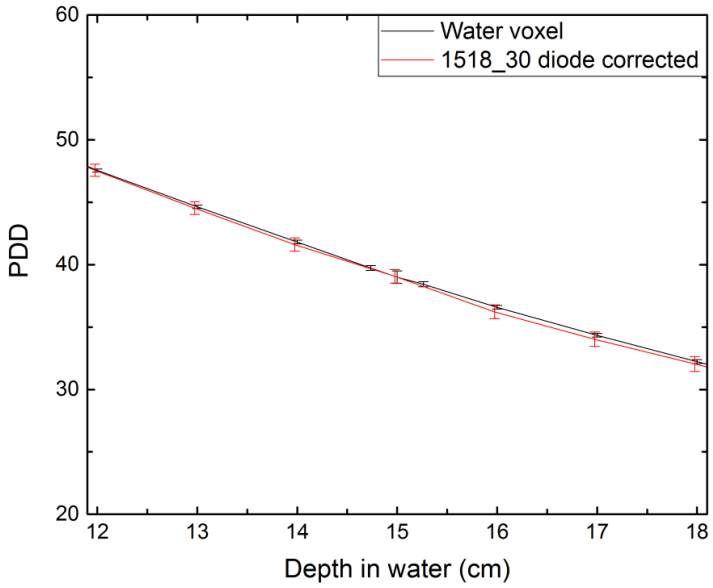

Figure 5.9 : The water voxel PDD and the corrected (0.24 mm shift applied) 1518_30 diode PDD. The two PDD curves overlay well in this region; therefore, no additional shift is required to the diode PDD apart from the 0.24 mm one already applied to the curve.

5.4.3 Off-axis $k_{Q_{clin},Q_{msr}}^{f_{clin},f_{msr}}$ profiles

The off-axis *k* (Eq. 1.10) profiles for both detector models were plotted, at 5 and 15 cm deep, in a 0.5x0.5 cm^2 field showing the detector response at various distances from the central axis of the beam (figures 5.10 and 5.11). Both detectors perform well at 5 cm deep in water, with no over-response reading more than 3% for any of them. At a depth of 15 cm, the computed response of the (no air-gap) 1518_36 diode detector seems to outperform the modified 1518_30 diode based on the bottom plots (over-response of uncorrected diode readings) in figure 5.11.

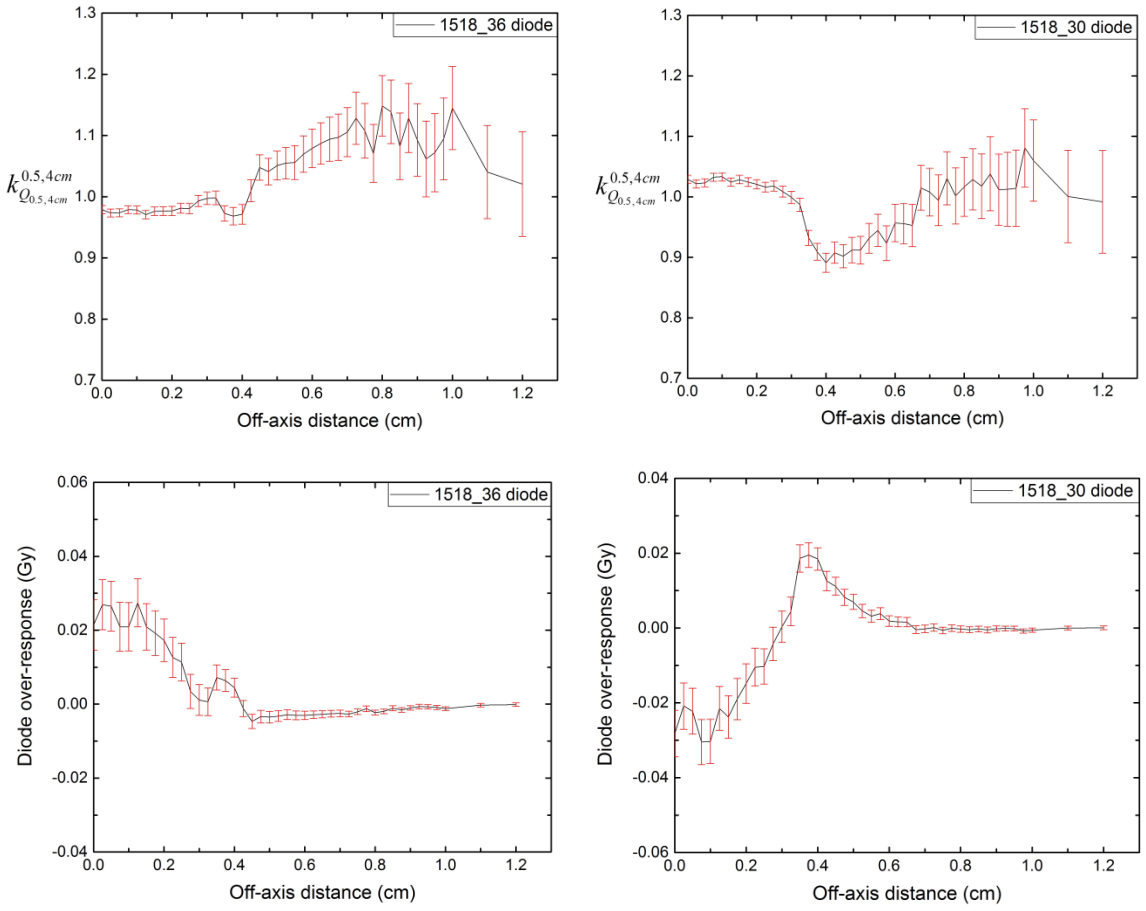

(a) *(b)*

Figure 5.10: (a) ***6 MV*** *simulation data for the no air-gap 1518_36 diode off-axis k profile across a* ***0.5x0.5 cm^2*** *field at* ***5 cm deep****, 100 cm SSD and the over-response of uncorrected readings when a dose of 1 Gy was deliverd on-axis. (b) Simulation data for the 1518_30 modified diode off-axis k profile across a* ***0.5x0.5 cm^2*** *field (same depth and beam energy) and the over-response of uncorrected readings.*

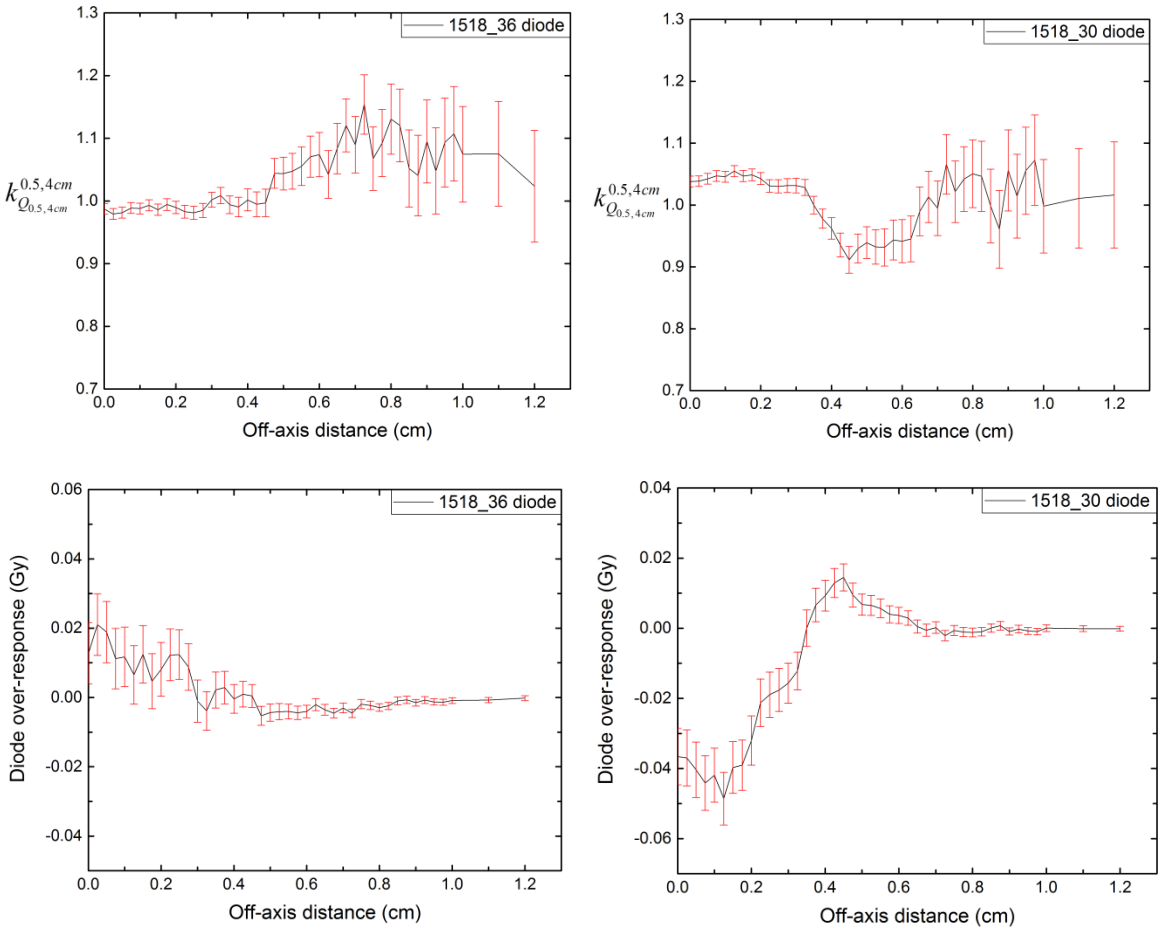

Figure 5.11: (a) Simulation data for the 1518_36 diode off-axis k profile across a ***0.5x0.5 cm²*** *field at* ***15 cm deep*** *and* ***6 MV*** *energy and the over-response of uncorrected readings. (b)* ***6 MV*** *simulation data for the 1518_30 modified diode off-axis k profile across in the same field and depth and the over-response of uncorrected readings. At this greater depth the computed response of the no air-gap 1518_36 diode is better than the 0.6 mm air-gap 1518_30 detector.*

5.5 New PTW 60023 diode detectors – 15 MV experimental results

Following the 6 MV experimental results presented in section 5.3 of this chapter, on-axis *k* values, PDD data and off-axis *k* profiles for the 1518_36 and 1518_30 diodes at a substantially higher beam energy (15 MV) are presented next (sections 5.5.1, 5.5.2 and 5.5.3).

5.5.1 On-axis $k_{Q_{clin},Q_{msr}}^{f_{clin},f_{msr}}$ correction factors

In figure 5.12 the Alfonso *et al* (2008) on-axis $k_{Q_{clin},Q_{msr}}^{f_{clin},f_{msr}}$ correction factors (Eq. 1.10) for the 1518_36 and 1518_30 diodes are presented. All *k* values were calculated at 5 cm deep in water for a 15 MV photon beam and are plotted against the various clinical fields measured with their statistical uncertainties shown at the ± 2 s.d. level. The reference conditions (4x4 cm^2 field, 200 MUs, 100 cm SSD and 5 cm depth) are exactly the same as for the 6 MV data.

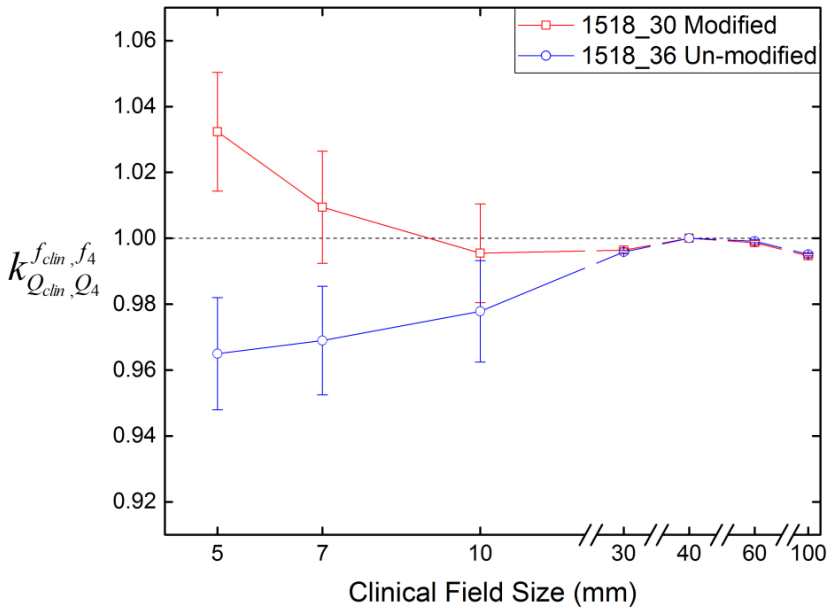

*Figure 5.12: Experimentally determined on-axis k values for a **15 MV** photon beam at **5 cm deep** in water and 100 cm SSD. A 4x4cm² field was used as the machine-specific reference field, also at 5 cm deep. Error bars show two standard deviations statistical uncertainties. 1518_30: 0.6 mm air-gap, 1518_36: no air-gap diode.*

15 MV experimental Alfonso *et al* (2008) on-axis correction factors, now with the EBT3 films used and the (top of the) sensitive volume of both diodes at 15 cm deep in water in the different clinical fields measured, are shown in figure 5.13.

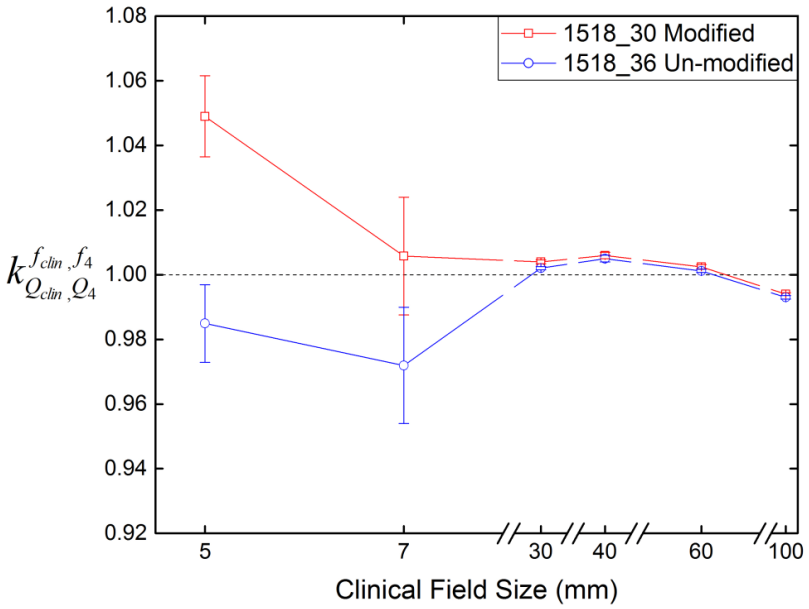

*Figure 5.13: Experimental on-axis k values for a **15 MV** beam at **15 cm deep**, 100 cm SSD, in various clinical fields relative to a 4x4 cm^2 field. Error bars show two standard deviations statistical uncertainties. 1518_30: 0.6 mm air-gap, 1518_36: no air-gap diode.*

In agreement with the 6 MV results, the 1518_30 diode under-reads – thus, requiring a correction factor greater than 1.00 – in small fields (compared to the dose absorbed by a point of water) at depths of both 5 and 15 cm. On the other hand, the (no air-gap) 1518_36 diode detector behaves as a slightly over-dense dosimeter resulting in over-estimation of the measured dose by ~ 3.5% at 5 cm deep, and by ~ 2% at 15 cm deep in water.

5.5.2 Percentage depth dose curves (PDDs) – EPOM shift

Experimental PDD data were obtained with both PTW 60023 diode detectors in a 0.5x0.5 cm^2 field at 15 MV. The PDD curves were plotted, focusing on the build-up region, to measure the distance difference between them (PDD shift), at 80% of the maximum dose (figure 5.14). A +0.22 mm shift needs to applied to the PDD curve of the 1518_30 diode to match the PDD curve of the no air-gap 1518_36 detector, meaning

that the EPOM shift of this diode is thus +0.22 mm relative to the EPOM of the no air-gap detector, corresponding to 1.17 mm below the top surface of the detector.

The same PDD data were plotted again, demonstrating that at greater depths in water (beyond the d_{max} point) the two PDD curves overlay; there is no obvious shift after the d_{max} point for the 1518_30 modified diode. These graphs are not included here to avoid presenting excessive amount of data leading to similar conclusions.

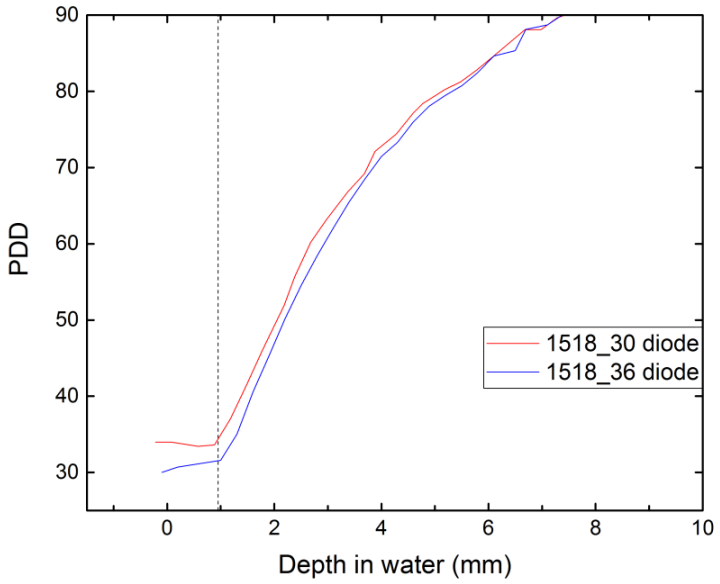

*Figure 5.14: 15 MV PDD curves for the **0.5x.5 cm²** field with the "kicks" of both diodes shifted to a depth of 0.95 mm (dashed line). A small PDD shift (~ 0.22 mm) between the 0.6 mm air-gap 1518_30 diode and the no-air gap 1518_36 detector, at 80% of the maximum dose, can be seen in the build-up region of the curves, thus concluding that the air-gap added in the 1518_30 diode slightly affects the dosimeter's EPOM.*

5.5.3 Off-axis $k_{Q_{0.5,4\ cm}}^{0.5,4\ cm}$ profiles

For the smallest field measured (0.5x0.5 cm^2) – the one in which the detectors behave most non-ideally – off-axis *k* profiles (with the detectors calibrated in a 4x4 cm^2 field) were plotted for both diode detectors, at 5 and 15 cm deep in water. In-line and cross-line beam profiles have been measured using both diode detectors of the second set (1518_36 and 1518_30 diodes) and EBT3 films. The point of the film with the

maximum value of dose was used as the origin of the film profile (x=0) and off-axis *k* profiles were plotted after applying an appropriate shift (not greater than 0.5 mm for any of the detectors) to the diode profile to get the best match between the two profiles. Figure 5.15 shows the results for the off-axis $k_{Q_{0.5,4\ \mathrm{cm}}}^{0.5,4\ \mathrm{cm}}$ profiles of both diodes (1518_36 and 1518_30) in the cross-line direction (field defined by the X-jaws in this direction), at 5 cm deep in water.

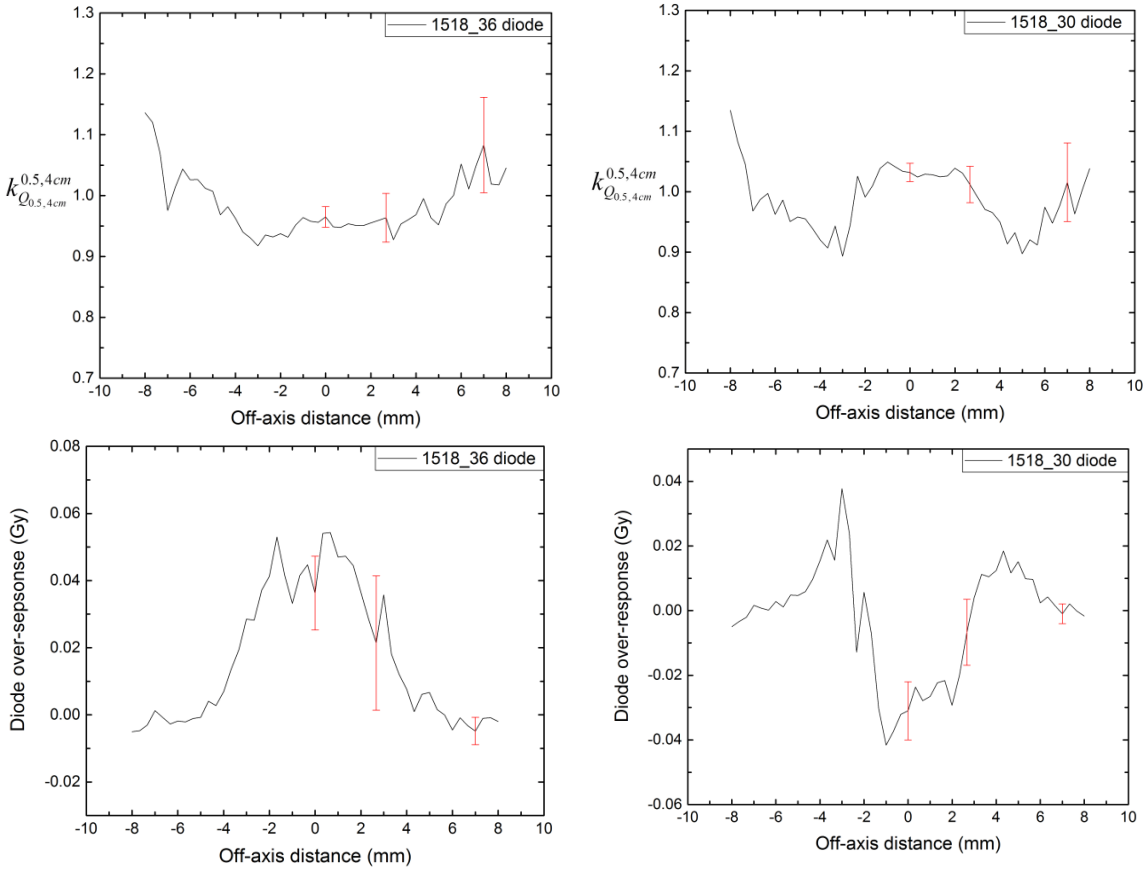

Figure 5.15: Experimental data using EBT3 film and the type 60023 PTW diodes, X-jaw, showing the detector response (a) of the 1518_36 no air-gap diode and (b) of the 1518_30 modified detector, across a ***0.5x0.5 cm^2*** *field at* ***5 cm deep****, 100 cm SSD, in a* ***15 MV*** *photon beam. The top plots show the k correction factor (relative to a 4x4 cm^2 field) at various positions off-axis (off-axis k profile). The bottom plots show the over-response of the uncorrected readings of the diode detectors when a dose of 1 Gy was delivered on-axis. All error bars indicate the signal to noise ratio at the 2 s.d. level.*

The off-axis $k_{Q_{0.5,4\ \mathrm{cm}}}^{0.5,4\ \mathrm{cm}}$ profiles of both the 1518_36 and 1518_30 diodes, in the 0.5x0.5 cm^2 field, at 15 cm deep in water are presented next (figure 5.16).

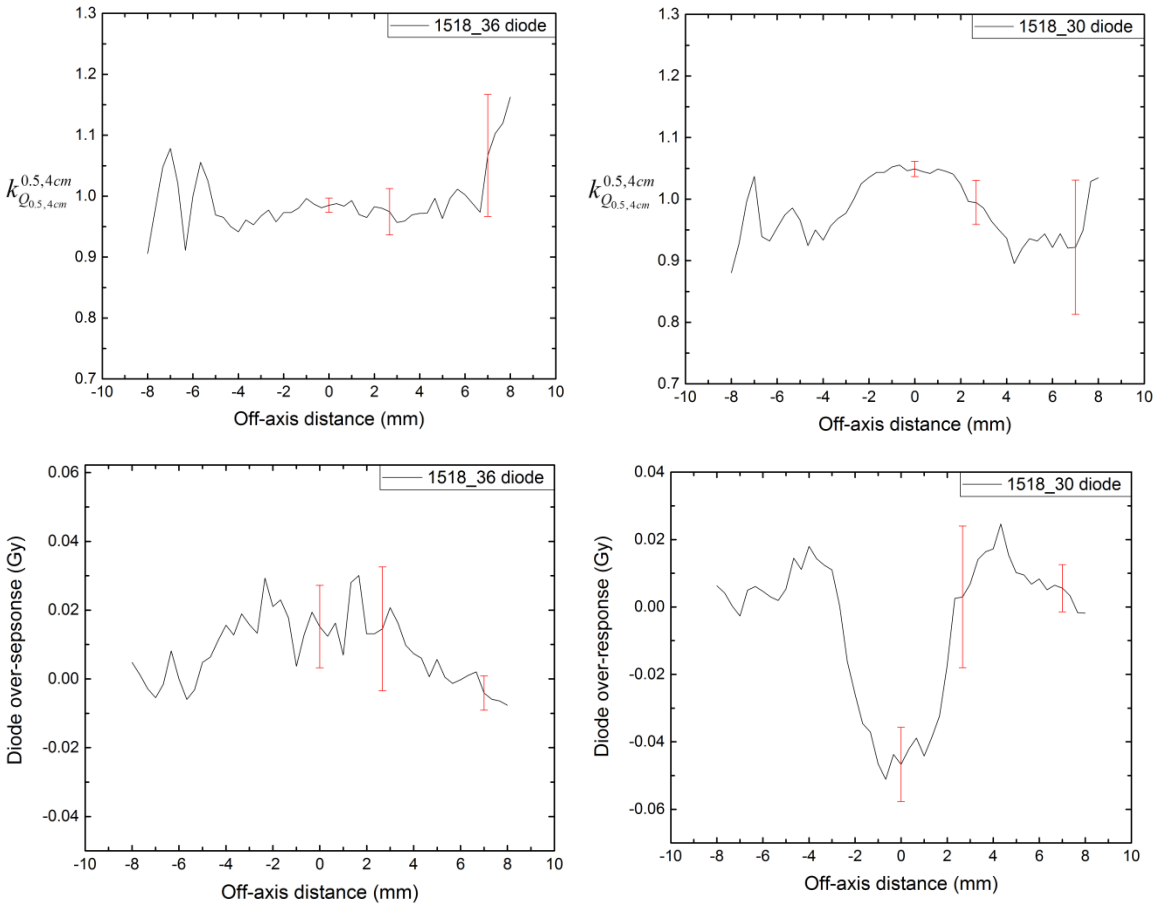

*Figure 5.16: No air-gap 1518_36 (a) and 0.6 mm air-gap 1518_30 (b) diodes off-axis k profiles, X-jaw, and over-response of uncorrected readings in a **0.5x0.5 cm^2** field, at **15 cm deep**, 100 cm SSD and **15 MV**. The over-response graphs show the over-response of the uncorrected readings of the diode detectors when a dose of 1 Gy was delivered on-axis. Statistical uncertainties shown are ± 2 s.d.*

5.6 New PTW 60023 diode detectors – 15 MV Monte-Carlo results

5.6.1 On-axis $k_{Q_{clin},Q_{msr}}^{f_{clin},f_{msr}}$ correction factors

The on-axis performance of the new PTW 60023 diodes (1518_36 and 1518_30 detectors) in a 15 MV photon beam has been computationally evaluated by calculating the on-axis $k_{Q_{clin},Q_{msr}}^{f_{clin},f_{msr}}$ correction factors (Eq. 1.10) in 0.5 and 0.7 cm square fields, at both 5 and 15 cm deep in water (tables 5.3 and 5.4). The no air-gap 1518_36 diode behaves as an over-dense detector at both depths, whereas the inclusion of a 0.6 mm air-gap in the 1518_30 detector seems to be a slightly excessive correction, causing the modified diode to under-respond (thus, requiring a correction factor greater than 1) by about 4% at both depths in a 0.5cm square field. The MC calculated on-axis *k* values are in good agreement with the experimental ones, both at 5 and 15 cm deep.

The MC calculated *k* correction values in both small fields, at 5 cm deep, for the imaginary type 60023 detector with a 0.3 mm air-gap are also included in table 5.3. In agreement with the 6 MV computational calculations (section 5.4.1), the 0.3 mm air-gap seems to be the optimum air-gap thickness for the type 60023 PTW diode detectors since all *k* values calculated for this detector model lie within ± 1% of 1.00 at both beam energies.

Air-gap thickness (mm)	Detector	On-axis $k_{Q_{0.5,4\ cm}}^{0.5,4\ cm}$ value	On-axis $k_{Q_{0.7,4\ cm}}^{0.7,4\ cm}$ value
-	1518_36 un-modified	0.978 ± 0.007	0.984 ± 0.007
0.3	Imaginary type 60023	1.009 ± 0.007	1.003 ± 0.007
0.6	1518_30 modified	1.041 ± 0.007	1.020 ± 0.007

*Table 5.3: k correction values calculated for the **15 MV** beam model, for on-axis readings at **5 cm deep** in water in **0.5 and 0.7 cm** square fields, with the detectors calibrated in a 4x4 cm^2 field. Uncertainties are shown at the ± 2 s.d. level.*

Air-gap thickness (mm)	Detector	On-axis $k_{Q_{0.5,4\ cm}}^{0.5,4\ cm}$ value	On-axis $k_{Q_{0.7,4\ cm}}^{0.7,4\ cm}$ value
-	1518_36 un-modified	0.985 ± 0.008	0.984 ± 0.008
0.6	1518_30 modified	1.043 ± 0.008	1.017 ± 0.008

*Table 5.4: k correction values calculated for the **15 MV** beam model, for on-axis readings at 1**5 cm deep** in water in **0.5 and 0.7 cm** square fields, with the detectors calibrated in a 4x4 cm^2 field. Uncertainties are shown at the ± 2 s.d. level.*

5.6.2 Percentage depth dose curves (PDDs) and EPOM shift analysis

The simulation PDD data, in a 0.5x0.5 cm^2 field, for the water voxel (DOSXYZnrc code), and the (no air-gap) 1518_36 and the (0.6 mm air-gag) 1518_30 diodes (egs_chamber code) are presented in figure 5.17. Exactly the same analysis as for the computational 6 MV PDD data (section 5.4.2 of this chapter) was done, concluding that the inclusion of the air-gap slightly affects the location of the EPOM (0.2 mm EPOM shift) of the modified detector.

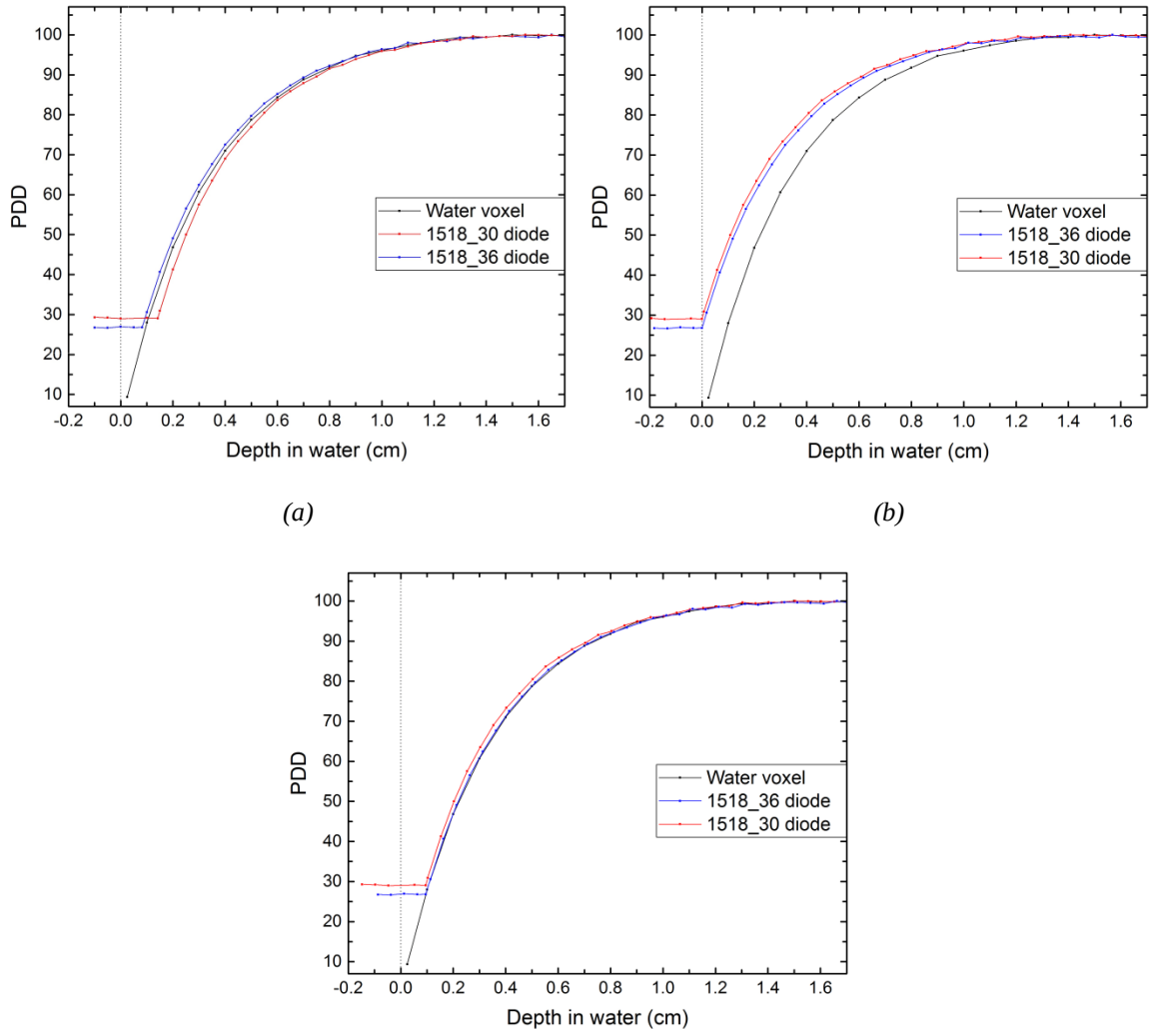

*Figure 5.17: MC calculated PDD data for a **15 MV** beam in a **0.5x0.5 cm^2** field. In part (a) the detectors' reading is plotted against the real depth of the sensitive volume in water with the "kick" point occurring for each detector when it is first submerged. In part (b) all detectors PDD data are shifted so the "kick" occurs at zero depth in water. In part (c) the same data is plotted, but now with all detector readings shifted by 0.95 mm. The no-air gap 1518_36 diode PDD curve is perfectly aligned with the water voxel PDD data; whereas, a 0.2 mm distance between the 1518_30 modified diode and the water voxel PDD can be seen in the build-up region of the curves meaning the air-gap added slightly affects the instrument's EPOM.*

A comparison between the water voxel PDD curve and the corrected (0.2 mm PDD shift applied relative to the un-modified detector) PDD curve of the 1518_30 modified detector, at greater depths beyond the d_{max} point, is presented in figure 5.18. The two

curves overlay well in this region and therefore no additional shift is required apart from the one already applied to the diode PDD curve.

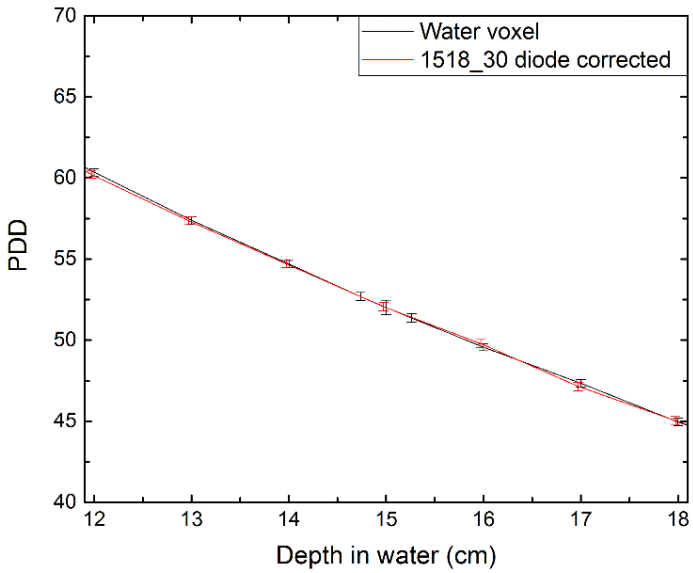

Figure 5.18: The water voxel PDD and the corrected (0.2 mm shift applied) 1518_30 modified diode PDD. The two PDD curves overlay well in this region, thus no additional shift is required to the diode PDD apart from the 0.2 mm one already applied.

5.6.3 Off-axis $k_{Q_{0.5,4\ \mathrm{cm}}}^{0.5,4\ \mathrm{cm}}$ profiles

MC simulations were completed within the egs_chamber user-code for a 15 MV photon beam model to evaluate the response of both the un-modified 1518_36 diode and the (0.6 mm air-gap) 1518_30 diode detector off the beam central axis. Half profiles were computed at both 5 and 15 cm deep in the virtual water tank using both detector models since it can be assumed that the profiles are completely symmetrical. The results for the off-axis *k* profiles, plotted for both diodes at both 5 and 15 cm deep, are presented in figures 5.19 and 5.20. In both figures, the bottom plots illustrate the over-response of the uncorrected diode readings when a dose of 1 Gy was delivered on-axis.

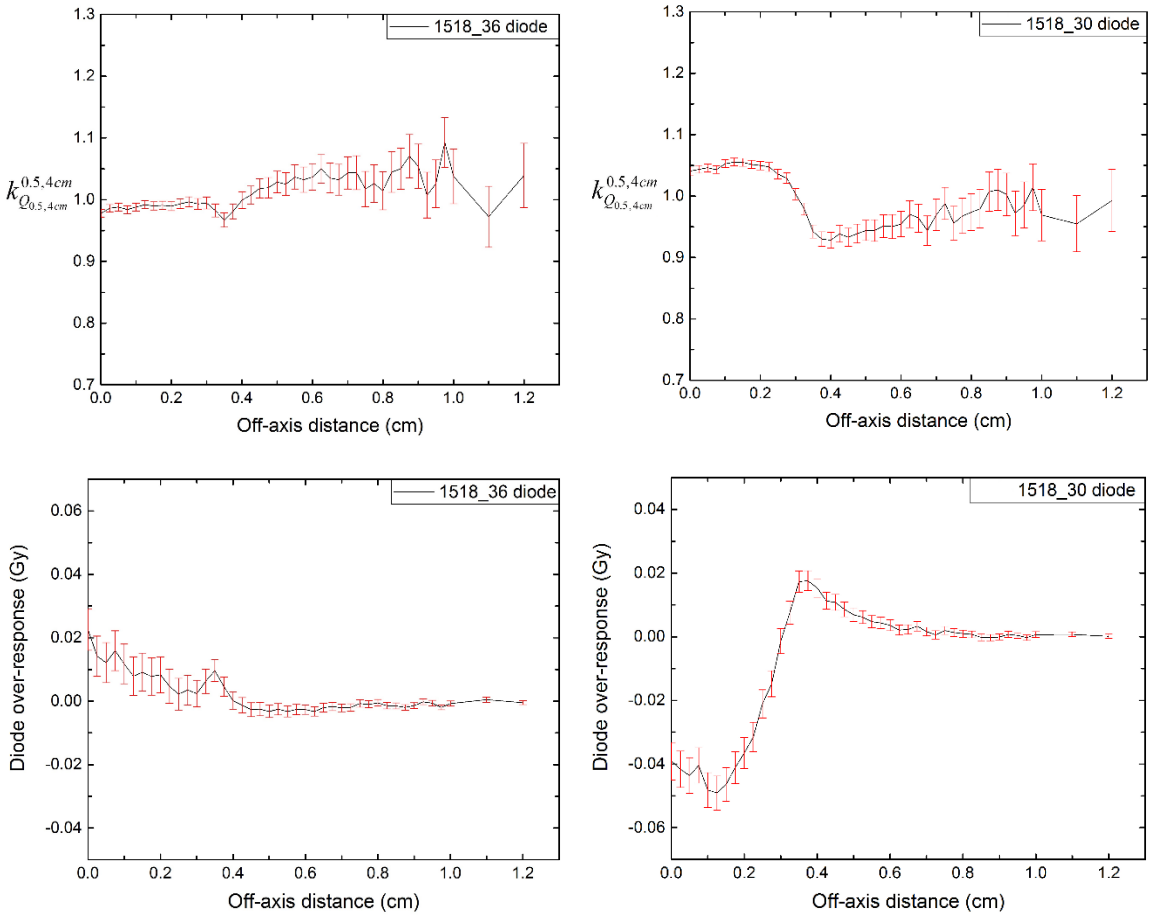

*Figure 5.19: (a) Monte-Carlo data for the no air-gap 1518_36 diode off-axis k profile across a **0.5x0.5 cm^2** field at **5 cm deep** at **15 MV** energy and the over-response of uncorrected readings. (b) Monte-Carlo data for the 0.6 mm air-gap 1518_30 modified diode off-axis k profile across a 0.5x0.5 cm^2 field at **5 cm deep** and **15 MV** energy and the over-response of uncorrected readings. Uncertainties are shown at the ± 2 s.d. level.*

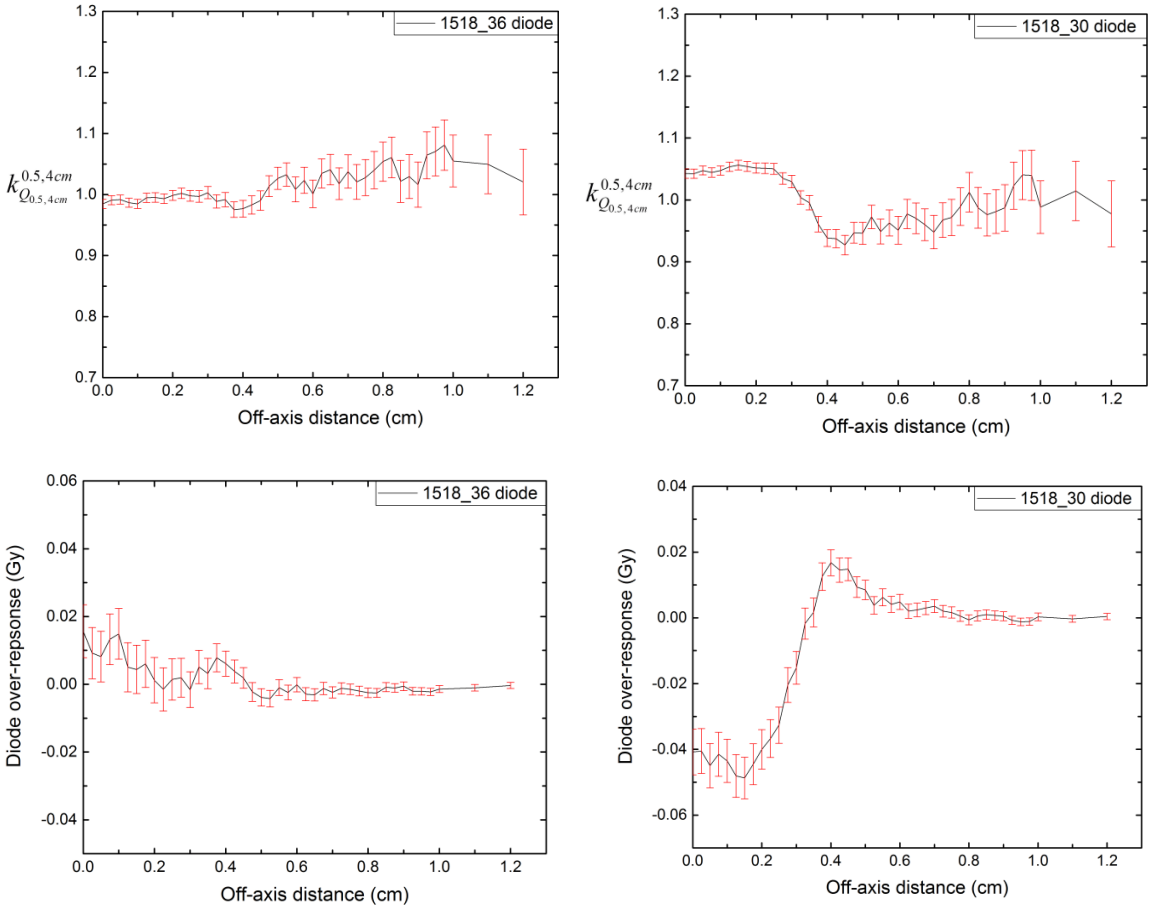

*Figure 5.20: (a) Monte-Carlo data for the no air-gap 1518_36 diode off-axis k profile across a **0.5x0.5 cm**^{2} field at 1**5 cm deep** at **15 MV** energy and the over-response of uncorrected readings. (b) Monte-Carlo data for the 0.6 mm air-gap 1518_30 modified diode off-axis k profile across a 0.5x0.5 cm^2 field at 1**5 cm deep** and **15 MV** energy and the over-response of uncorrected readings. All error bars show 2 s.d. statistical uncertainties.*

5.7 Discussion of PTW 60023 diodes results

The 6 MV on-axis *k* corrections factors for all the PTW 60023 diodes (presented in figure 5.1), in a 0.5x0.5 cm^2 field, demonstrate that *k* values increase progressively while the air-gap thickness increases, meaning that there are no (unexpected) issues with the design of the improved 60023 PTW detectors (like the issues discussed in previous chapters regarding the modified 1162 - 1167 type 60017 diodes of the first set). In addition, MC calculated and experimentally determined results are very similar,

indicating that the detector design and physical realization are closely matched for the PTW type 60023 diodes. Figure 5.21 shows a direct comparison of the 6 MV experimental and Monte-Carlo on-axis $k_{Q_{0.5,4\text{ cm}}}^{0.5,4\text{ cm}}$ values, at 5 cm deep in water, for both the type 60017 (first set of detectors) and the improved type 60023 silicon diodes. Significant discrepancies (up to 6%) between experiment and simulation can be observed for the type 60017 diodes, whereas experimental *k* values for the type 60023 diodes differ less than 1% from the computational ones.

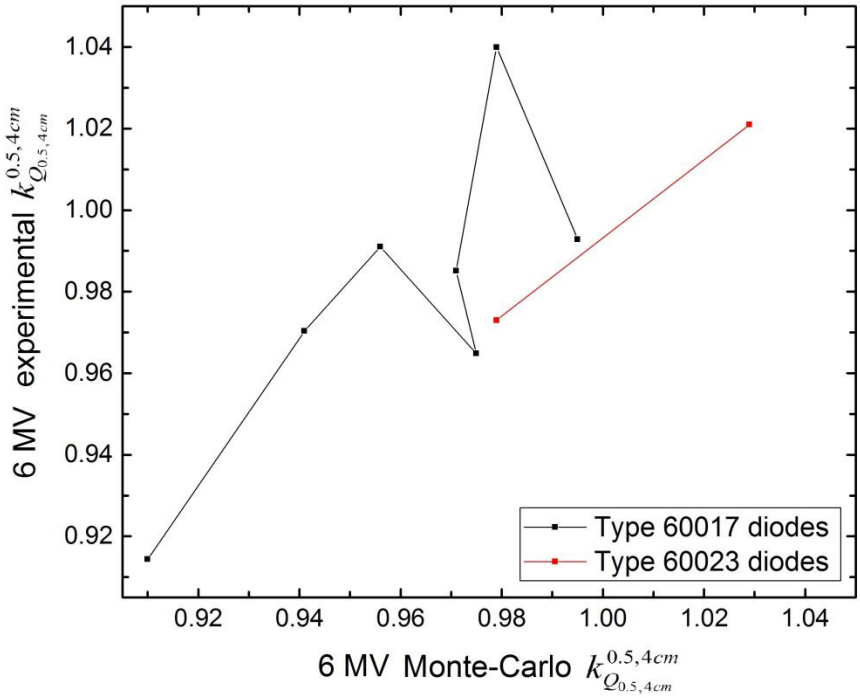

Figure 5.21: A comparison of the 6 MV experimental and MC on-axis $k_{Q_{0.5,4\text{ cm}}}^{0.5,4\text{ cm}}$ values, at 5 cm deep in water and 100 cm SSD, for both the 60017 and 60023 diode detectors. For the type 60023 diodes experimental and Monte-Carlo results are in agreement within 1%.

From both the 6 and 15 MV experimentally determined on-axis *k* values, at both 5 and 15 cm deep, (figures 5.2, 5.3 and 5.12, 5.13) it is evident that the two PTW 60023 improved detectors characterised in this chapter, i.e. the no air-gap 1518_36 and the 0.6 mm air-gap 1518_30 diodes, perform well on-axis with none of their *k* values differing more than 4% from 1.00. However, by comparing their on-axis response it can be

concluded that the no air-gap detector (1518_36) seems to behave as a slightly over-dense dosimeter (though not nearly so much as the PTW 60017 Original diode of the first set of detectors), while the modified 1518_30 diode appears to be a little over-corrected, thus under-reading relative to the dose absorbed by a point of water in a small field (e.g. 0.5 or 0.7 square fields) at the same depth.

The conclusions regarding the on-axis response of the two PTW 60023 diode detectors are confirmed by the computational work presented in this chapter (sections 5.4.1 and 5.6.1); there is very good agreement – all values agree within 1.5% – between the experimentally determined and the computationally calculated on-axis *k* values for both diode detectors in the small (0.5x0.5 and 0.7x0.7 cm^2) fields at both depths, in 6 and 15 MV photon beams. Moreover, the MC calculations for the on-axis *k* values confirmed our assumption that a modified type 60023 PTW diode detector, with a thinner air-gap than the 0.6 mm one added in the 1518_30 detector, would be the detector that performs best; all on-axis *k* values calculated for the imaginary (type 60023) diode model with a 0.3 mm air-gap lie within ± 1% of 1.00, at both 6 and 15 MV.

The experimental PDD analysis presented in this chapter (sections 5.3.2 and 5.5.2) showed that introducing a thin air-gap (of the order of fractions of a mm) above the PTW 60023 diode's sensitive volume (based on the "mass-density" compensation method of Underwood *et al* 2013b) does not change the overall shape of the measured PDD curve. However, the inclusion of the air-gap slightly affects the location of the detector's EPOM, causing EPOM shifts of the order of fractions of a millimeter. Monte-Carlo calculated PDD curves presented in figures 5.8 (6 MV) and 5.17 (15 MV) validate this observation: at both beam energies the no air-gap 1518_36 diode PDD curve is perfectly aligned with the water voxel PDD, whereas a 0.24 mm and a 0.20 mm distance can be seen between the 1518_30 modified diode and the water voxel PDD curves at 6 MV and 15 MV, respectively.

Regarding the experimental off-axis *k* profiles for the 1518_36 and 1518_30 diodes, in a 0.5x0.5 cm^2 field, similar trends are observed at both 5 and 15 cm deep in water and for both beam energies (6 and 15 MV). The no air-gap detector (over-dense dosimeter) seems to over-respond, while the modified 1518_30 diode under-reads compared to the

EBT3 film. The MC results for the off-axis *k* profiles indicate that the (no air-gap) 1518_36 diode slightly outperforms the modified 1518_30 detector – especially at 15 cm deep in water – with no over-response reading more than ~ 2%, either at 5 or 15 cm deep in water at both beam energies.

In general, the MC results for the two PTW 60023 diodes show that the no air-gap detector is right to within about 2% both on and off-axis, at depths of 5 and 15 cm in water, at both 6 and 15 MV. The experimental results for the same detector demonstrate that its response is right to within 4% at 6 MV and 5 % at 15 MV when measuring dose on and off-axis in a small (0.5x0.5 cm^2) field, at 5 and 15 cm deep. Finally, both the experimental and computational results presented in this chapter suggest the potential for further improvement by introducing a 0.3 mm air-gap above the sensitive silicon of the un-modified type 60023 PTW diode detector.

5.8 Conclusions

The Type No. 60023 PTW diode detectors have been characterised and their response has been both experimentally and computationally evaluated in 6 and 15 MV photon beams. In contrast to the first set of detectors (i.e. the modified type 60017 PTW diodes) no design issues have been encountered in this improved set of detectors, with their experimental results not revealing any unexpected pattern on the basis of the air-gap thicknesses and being in good agreement with MC calculations. Furthermore, the design of these detectors has been significantly improved since all on-axis *k* values for the no air-gap detector lie closer to 1.00 (within ± 3.5%) compared to the PTW 60017 Original diode that is over-responding by about 9% in a 0.5x0.5 cm^2 field, at 6 MV.

Experimental and MC results for the on-axis response of the PTW 60023 diodes in 6 and 15 MV beams demonstrate that both detectors work well as small-field dosimeters, with none of their *k* values differing more than ~ 4% from 1.00. The no air-gap 60023 diode behaves as a slightly over-dense detector, substantially better though than the PTW Original 60017 diode due to the improvements in its design, while the modified type 60023 detector slightly under-responds because of the inclusion of a 0.6 mm air-gap

above its sensitive volume. Furthermore, introducing the 0.6 mm thick air-gap causes a small (of the order of fractions of a millimeter) EPOM shift to the modified PTW 60023 diode relative to the detector with no air-gap, a result experimentally determined first and then computationally confirmed, at both 6 and 15 MV. Finally, from the experimental off-axis response of the two diodes, at 6 and 15 MV, it can be concluded that the no air-gap diode marginally over-responds and the modified detector under-responds, compared to EBT3 film, in the interior of a small (i.e. 0.5x0.5 cm^2) field, with the no air-gap diode slightly outperforming the modified 60023 detector, especially at 15 cm deep. MC data generally show the no air-gap type 60023 detector responding correctly to within about 2% everywhere, while the noisier experimental results show a maximum error of about 5%. Both MC and experimental results suggest that a 60023 diode with a thin intermediate air-gap of approximately 0.3 mm thickness should perform optimally.

Chapter 6

Non-standard 6 MV MC calculations – oblique incidence and a 0.3x0.3 cm^2 field

6.1 Introduction

The performance of both the type No. 60017 (original set of detectors) and 60023 (improved set of detectors) PTW diodes has been experimentally and computationally evaluated in small photon fields, and results both at 6 and 15 MV are presented in chapters 3, 4 and 5 of this thesis. For the purpose of this chapter MC simulations were completed using four detector models in total (representing two diodes from each set of PTW detectors): the (un-modified) Original 60017 diode and the 1.6 mm air-gap type 60017 diode (original set of detectors), and the un-modified (no air-gap) and the 0.6 mm air-gap type 60023 diodes (new set of detectors). Using the EGSnrc system (Kawrakow *et al* 2011) additional MC studies of the response of these four PTW diodes in a 6 MV beam were carried out, exploring even more non-standard situations, and their results are the subject of this chapter.

More specifically, the on-axis detector response was evaluated at the center of a 0.5x0.5 cm^2 field with the diodes oriented at a range of angles relative to the beam axis (oblique incidence). By tilting the dosimeters at various angles, the charged particle fluence passes through different paths en route to the sensitive volume, in terms of stopping powers and densities of the materials present, compared to the case that the instrument is conventionally aligned with the beam axis, thus substantially affecting the detector's reading. Furthermore, Alfonso *et al* (2008) on-axis *k* correction factors were computationally calculated in a 0.3x0.3 cm^2 clinical field, relative to a 4x4 cm^2 field, for all the detectors tested within this chapter. In this (very) small field the effects causing

significant issues in small-field dosimetry – i.e. breakdown of LCPE on the beam axis and (partial) occlusion of the primary photon source, as described in section 1.2.1 of chapter 1 – are larger compared to the 0.5x0.5 cm^2 field, and the determination of dose is even more influenced by the size of the detector's sensitive volume (volume averaging effect).

All data presented in this chapter are the result of purely computational work; no experimental measurements were made either with the detectors tilted, or at the center of a 0.3x0.3 cm^2 field since it is very difficult to set such a small field in reality using the collimator jaws of a linac, or to place the detectors in the water tank oriented at a well-defined angle relative to the beam axis.

6.2 Methods

MC calculations were completed using the egs_chamber (Wulff *et al* 2008) user-code to further explore the response of PTW silicon diodes under even more non-standard conditions, in a 6 MV photon beam. The detectors tested are the Original 60017 diode, the (no air-gap) type 60023 un-modified diode (serial No. 1518_36), and the two modified diodes that perform best according to the results presented in previous chapters, i.e. the 1.6 mm air-gap type 60017 diode (serial No. 1167) and the 0.6 mm air-gap type 60023 diode (serial No. 1518_30).

The detectors were positioned in a 50x50x50 cm^3 virtual water tank, at the centre (on-axis) of a 0.5x0.5 cm^2 clinical field, at 5 cm deep and 100 cm SSD, and static measurement (sensitive volume) dose values were obtained with the axis of the detectors lying at 30º, 45º, 60º and 90º relative to the beam axis (oblique incidence). Similar MC simulations were performed with the detectors tilted at the same range of angles (relative to the beam axis), but now in a 4x4 cm^2 field (f_{msr}), at 5 cm deep and 100 cm SSD.

On-axis *k* values (Eq. 1.10) were computationally calculated for the four detector models (mentioned above) in a 0.5x0.5 cm^2 field, relative to a 4x4 cm^2 field, in two different ways: a) with the detectors tilted both in the (small) clinical and the reference field; and

b) with the detectors tilted only in the small field, while keeping them conventionally aligned with the beam axis in the 4x4 cm^2 reference field.

In order to evaluate the on-axis response of the un-modified (no air-gap) type 60017 and 60023 detectors, and the 0.6 mm air-gap (type 60023) and 1.6 mm air-gap (type 60017) diodes in a 0.3x0.3 cm^2 field, on-axis $k_{Q_{0.3,4\ \mathrm{cm}}}^{0.3,4\ \mathrm{cm}}$ correction factors (under the Alfonso *et al* 2008 formalism) were computationally calculated at 5 cm deep in water. For the small clinical field, the dose absorbed by a 0.25x0.25x0.5 mm^3 water voxel whose centre lay on-axis at 5 cm deep in a 50x50x50 cm^3 water tank and in the absence of a detector was calculated using the DOSXYZnrc user-code (Rogers *et al* 2011). Detector sensitive volume doses were calculated within the egs_chamber user-code (Wulff *et al* 2008) with all the detectors conventionally aligned parallel to the beam and positioned on-axis with their sensitive volumes at a depth of 5 cm in water (SSD = 100 cm).

The 6 MV beam model of Underwood *et al* (2013a) was used again to create a (sufficiently large) phase-space file for the 0.3x0.3 cm^2 field within the BEAMnrc (Rogers *et al* 2011) MC system. The phase-space file generated contains 1.1 x 10^7 particles and was used as a source of particles both for DOSXYZnrc and egs_chamber MC simulations.

Throughout the computational work completed in the course of this chapter, global energy cut-off values of ECUT = 0.521 MeV and PCUT = 0.001 MeV were set both for the DOSXYZnrc and egs_chamber simulations, while all radiation transport parameters and variance reduction techniques were maintained the same, in accordance with the computational work presented in previous chapters (details discussed in sections 2.3.2 and 2.3.3 of chapter 2).

6.3 Results

6.3.1 6 MV on-axis $k_{Q_{0.5,4\ \mathrm{cm}}}^{0.5,4\ \mathrm{cm}}$ correction factors – oblique incidence

The 6 MV on-axis *k* correction factors (Eq. 1.10), calculated at 5 cm deep in a 0.5x0.5 cm^2 clinical field relative to a 4x4 cm^2 field, for the type 60017 diodes are graphically presented in figure 6.1. $k_{Q_{0.5,4\ \mathrm{cm}}}^{0.5,4\ \mathrm{cm}}$ values calculated with the two detectors tilted in both fields (black lines in figure 6.1) and with the diodes tilted only in the small field (shown in red colour) are plotted against the various angles (in degrees) relative to the beam axis. A 90º rotation aligns the axis of the dosimeter with the y-axis in the water tank co-ordinate system.

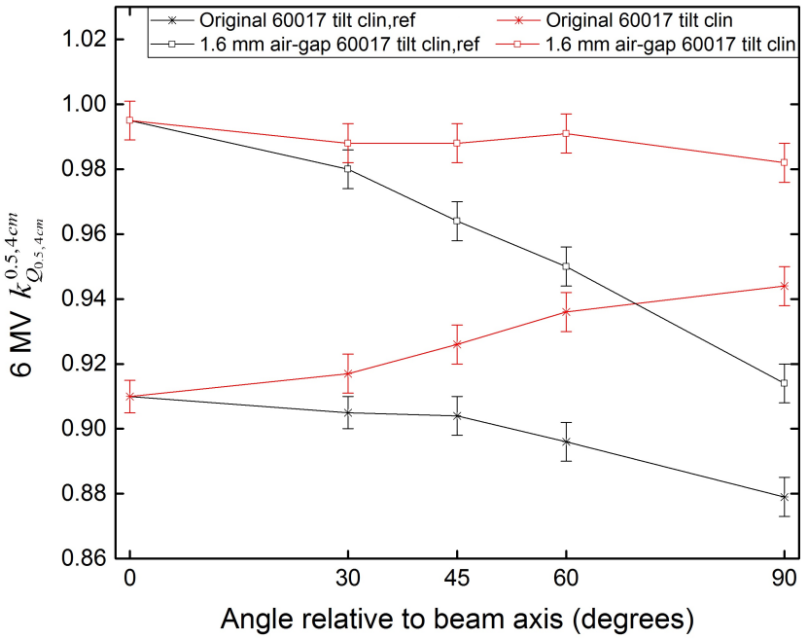

*Figure 6.1: k correction values calculated for the 6 MV beam model in a **0.5x0.5 cm²** field, at 5 cm deep and 100 cm SSD, for the (un-modified) Original and the 1.6 mm air-gap **type 60017** diode detectors. k values shown in black colour were calculated using data obtained with the detectors tilted in both the clinical and reference fields whereas, correction factors shown in red were calculated using the detector readings acquired with the dosimeters tilted only in the small clinical field. Error bars indicate two standard deviations statistical uncertainties.*

From figure 6.1 it can be concluded that changes on Original 60017 diode $k_{Q_{0.5,4\ cm}}^{0.5,4\ cm}$ values are of similar scale (relative to the 0.910 value calculated with the detector conventionally positioned parallel to the beam axis in both fields, i.e. at zero degrees)

when the dosimeter is either tilted in the clinical field only or tilted in both the small and reference fields. Both ways, calculated *k* correction factors are far from 1.00 (more than 6%) for this over-dense detector. On the contrary, the 1.6 mm air-gap type 60017 modified detector behaves much better when tilted only in the small field and conventionally aligned with the beam axis in the reference 4x4 cm^2 field, with all its measured *k* values being within ± 2% of 1.00, even when the diode is positioned at 90º relative to the beam axis.

To further clarify results regarding the on-axis *k* values presented in figure 6.1, the response of both (type 60017) diode detectors in the clinical (0.5x0.5 cm^2) and reference (4x4 cm^2) fields – rather than the *k* correction factors – is shown with the dosimeters oriented at 30º, 45º, 60º and 90º relative to the beam axis (figure 6.2). All detector readings are normalised to the reading of each detector obtained when the instrument is aligned parallel to the beam (detector at zero degrees relative to the beam axis).

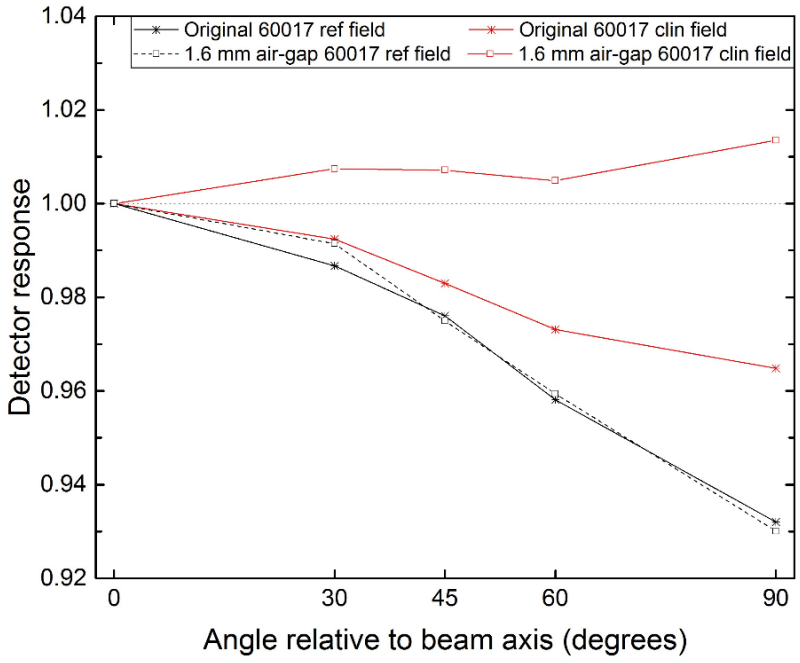

Figure 6.2: Detector response of the (no air-gap) Original and 1.6 mm air-gap ***type 60017*** *diodes in the 0.5x0.5 cm^2 (data shown in red) clinical field and in the 4x4 cm^2 (shown in black) reference field, at 6 MV and 5 cm deep (SSD = 100 cm). All values are normalised to the response of each detector oriented at zero degrees relative to the beam axis. Error bars are not included to improve visibility of the graphs.*

In figure 6.2 it can be seen that the detector response in the reference field changes in a very similar way for the two type 60017 diodes when oriented at an angle relative to the beam axis; both detectors "lose" (about the same amount of) signal as the tilting angle increases, resulting in a ~ 7% lower reading when the dosimeters are tilted at a 90º angle relative to the beam axis. On the other hand, the two detectors behave differently in the (0.5x0.5 cm^2) clinical field, with the un-modified Original diode reading lower – though not so much as in the 4x4 cm^2 field – as the angle between the detector axis and the beam axis increases, but the 1.6 mm air-gap modified diode measuring relatively constant values of dose as the angle changes, with a maximum deviation from the zero degrees reading, of about 1.3%, when the detector is aligned with the y-axis (i.e. tilted at an angle of 90º relative to the beam axis).

Similar graphs are presented next showing the MC calculated on-axis *k* values (figure 6.3) for the PTW type 60023 diode detectors and the change in the detector response (figure 6.4) when these two dosimeters are oriented at 30º, 45º, 60º and 90º relative to the beam central axis.

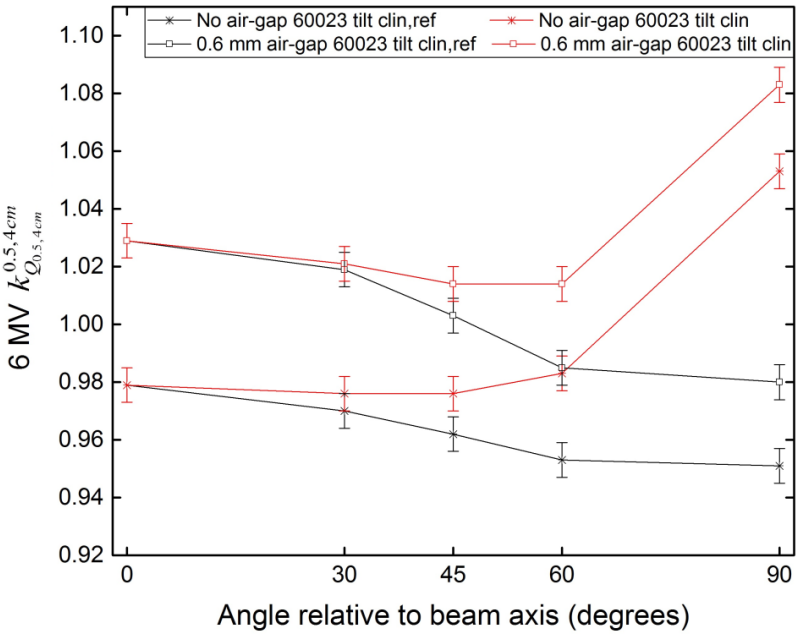

Figure 6.3: k correction values calculated for the 6 MV beam model in a ***0.5x0.5 cm²*** *field, at 5 cm deep and 100 cm SSD, for the un-modified (no air-gap) and the 0.6 mm air-gap* ***type 60023*** *diode detectors. k values shown in black were calculated using data obtained with the detectors tilted in both the clinical and reference fields whereas, correction factors shown in red were calculated using the detector readings acquired with the dosimeters tilted only in the small clinical field. Error bars show two standard deviations statistical uncertainties.*

Figure 6.3 illustrates that the calculated *k* values for both type 60023 diodes increase substantially (i.e. dosimeters under-respond) when the detectors are oriented at an angle of 90º relative to the beam axis in the clinical field and at zero degrees in the reference field (data shown in red). On the other hand, *k* values do not change dramatically when the detectors are tilted only in the clinical field at angles of 30º, 45º and 60º relative to the beam axis. For instance, the $k_{Q_{0.5,4\ \mathrm{cm}}}^{0.5,4\ \mathrm{cm}}$ (60º tilt in the clinical field only) differs by about 0.5% and 1.5%, compared to the zero degrees *k* values, for the no air-gap 60023 and the 0.6 mm air-gap 60023 diode, respectively.

When the 60023 diode detectors are oriented obliquely in both the clinical and reference fields (data shown in black in figure 6.3), the calculated values of $k_{Q_{0.5,4\ cm}}^{0.5,4\ cm}$ are lower compared to the zero degrees orientation in the reference field, even when the detector axis is at 90º relative to the beam axis in the small field, and the 0.6 mm air gap 60023 detector seems to outperform the un-modified (no air-gap) detector. But in contrast with results obtained for the 1.6 mm air-gap type 60017 detector, the modified type 60023 diode, with a 0.6 mm air-gap added, performs better (i.e. has *k* values closer to 1.00) when tilted both in the clinical and reference fields.

The observations discussed above can be explained and better understood by the detector response data (normalised to response at zero degrees) presented in figure 6.4, for both type 60023 diodes. In agreement with the type 60017 detectors (figure 6.2) it can be concluded that there is more variation of detector response with angle in the large field than in the small one, and this difference drives the variation of *k* with angle (at least when the detectors are set at the same angle in both large and small fields).

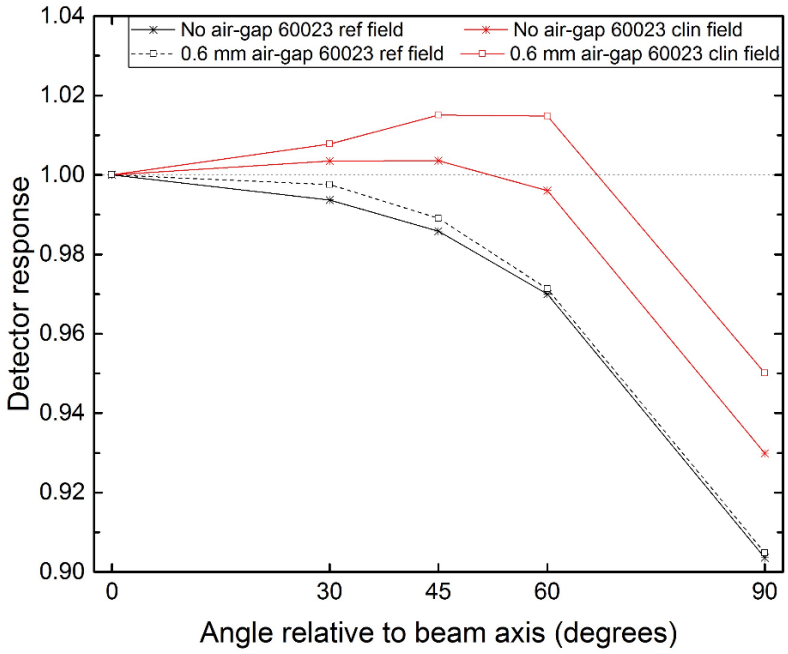

*Figure 6.4: Detector response of the no air-gap and the 0.6 mm air-gap **type 60023** diodes in the 0.5x0.5 cm^2 (data shown in red) clinical field and in the 4x4 cm^2 (shown in black colour) reference field, at 6 MV and 5 cm deep (SSD = 100 cm). All values are normalised to the response of each detector oriented at zero degrees relative to the beam axis. Error bars are not included, to improve visibility of the graphs.*

6.3.2 6 MV on-axis $k_{Q_{0.3,4\ cm}}^{0.3,4\ cm}$ correction factors

The 6 MV computationally-calculated Alfonso *et al* (2008) on-axis $k_{Q_{0.3,4\ cm}}^{0.3,4\ cm}$ values, at 5 cm deep and 100 cm SSD, are shown in table 6.1 for the PTW 60017 Original and the (modified) 1.6 mm air-gap diodes.

Air-gap Thickness (mm)	Detector	On-axis $k_{Q_{0.3,4\ cm}}^{0.3,4\ cm}$ value
-	60017 Original	0.894 ± 0.005
1.6	60017 1.6 mm air-gap	1.027 ± 0.006

*Table 6.1: k correction values calculated for the Original and the modified type 60017 diodes, for on-axis readings at 5 cm deep and 100 cm SSD, in a **0.3x0.3 cm^2** field relative to a 4x4 cm^2 field, at 6 MV. Uncertainties are shown at the ±2 s.d. level.*

The low (about 10.5% different from 1.00) on-axis $k_{Q_{0.3,4\ \mathrm{cm}}}^{0.3,4\ \mathrm{cm}}$ value calculated for the no air-gap PTW 60017 Original diode can be attributed to the high density of the sensitive silicon of the dosimeter, which causes the detector to substantially over-respond (relative to the dose absorbed by a point of water at the same depth) in this (very) small field, thus requiring a correction factor smaller than 1.00. On the other hand, the k = 1.027 ± 0.006 value for the modified (1.6 mm air-gap added) type 60017 diode can be thought as the result of two combined effects, both driving the correction factor to a value greater than one: the under-response of this much less dense detector – due to the existence of the 1.6 mm thick air-gap (density compensation) – and the volume averaging because of the (comparable to the field-size) dimensions of the sensitive silicon.

The on-axis $k_{Q_{0.3,4\ \mathrm{cm}}}^{0.3,4\ \mathrm{cm}}$ correction factors for the type 60023 diode detectors are summarised in table 6.2. The un-modified (no air-gap) detector has a k value (surprisingly) close to one, while the 0.6 mm air-gap type 60023 modified diode seems to under-read (k > 1) in the 0.3x0.3 cm^2 field by about 8% compared to the dose absorbed by a point of water, with the influence of the volume averaging effect on the k values being more noticeable for the type 60023 diodes compared to the type 60017 detectors.

Air-gap Thickness (mm)	Detector	On-axis $\boldsymbol{k_{Q_{0.3,4\ \mathrm{cm}}}^{0.3,4\ \mathrm{cm}}}$ value
-	60023 un-modified	0.993 ± 0.006
0.6	60023 0.6 mm air-gap	1.079 ± 0.006

*Table 6.2: k correction values calculated for the no air-gap and the (0.6 mm air-gap) modified type 60023 diode detectors, for on-axis readings at 5 cm deep and 100 cm SSD, in a **0.3x0.3 cm^2** field relative to a 4x4 cm^2 field, at 6 MV. Uncertainties are shown at the ±2 s.d. level.*

The 6 MV on-axis $k_{Q_{0.3,4\ \mathrm{cm}}}^{0.3,4\ \mathrm{cm}}$ values, shown in tables 6.1 and 6.2, are graphically presented in figure 6.5 along with the (6 MV) correction factors in a 0.5x0.5 cm^2 field for the same detectors.

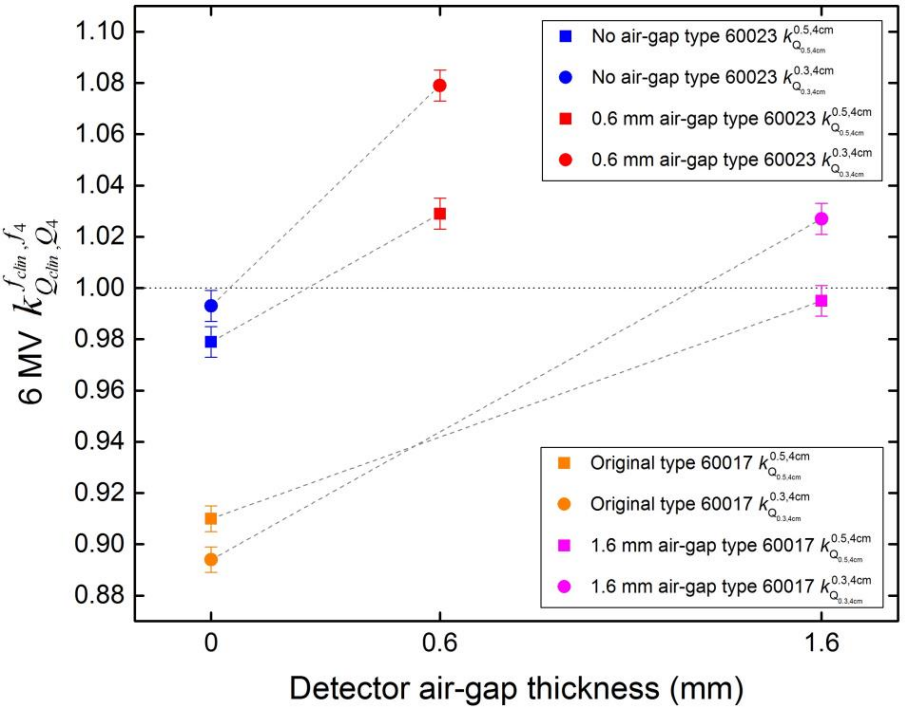

Figure 6.5: 6 MV k correction factors calculated for the type 60017 and 60023 diodes, in 0.3x0.3 (circles) and 0.5x0.5 cm^2 (squares) clinical fields, relative to a 4x4 cm^2 field, at 5 cm deep and 100 cm SSD. Statistical uncertainties are shown at the ± 2 s.d. level.

It is evident from figure 6.5 that the on-axis $k_{Q_{0.3,4\ \mathrm{cm}}}^{0.3,4\ \mathrm{cm}}$ correction factors for both the type 60017 and 60023 modified detectors (1.6 and 0.6 mm thick air-gaps, respectively) are increased compared to the values calculated in a 0.5x0.5 cm^2 (clinical) field for the same detectors. This is also the case for the (un-modified) no air-gap type 60023 diode whose *k* value increases by about 1.5% between the two small fields. On the other hand, the un-modified Original type 60017 diode exhibits a different behavior with its on-axis $k_{Q_{0.3,4\ \mathrm{cm}}}^{0.3,4\ \mathrm{cm}}$ value being ~ 2% lower than the correction factor calculated in a 0.5 cm square field, relative to a 4x4 cm^2 field.

6.4 Discussion of results

On-axis *k* correction factors have been computationally calculated, at 6 MV, for two no air-gap silicon diodes (i.e. the PTW 60017 Original diode and the no air-gap type 60023 detector) and for the 1.6 mm air-gap type 60017 and 0.6 mm air-gap type 60023 silicon diodes investigating their response under non-standard conditions: with the detectors oriented at a range of angles relative to the beam axis, and at the centre of a (very) small, i.e. 0.3x0.3 cm^2, radiation field.

The results from the MC studies regarding the oblique incidence show that the two type 60017 detectors behave in different ways (figure 6.1); if we calculate $k_{Q_{0.5,4\ \mathrm{cm}}}^{0.5,4\ \mathrm{cm}}$ for the (no air-gap) Original diode using dose values obtained either when the detector is tilted in both the clinical and reference fields or in the small field only, the scale of variation of *k* from the value of 0.910 – i.e. the value calculated with the detector conventionally aligned with the beam axis – is similar and all *k* values are far from 1.00. Contrariwise, the modified (1.6 mm air-gap) type 60017 diode shows a much more consistent behavior, with *k* values close to unity (i.e. within ± 2%), when tilted only in the clinical and not in both fields. By tilting the modified (1.6 mm air-gap) type 60017 diode in both fields the calculated on-axis $k_{Q_{0.5,4\ \mathrm{cm}}}^{0.5,4\ \mathrm{cm}}$ values significantly deviate from 1.00 reaching a value of 0.914 ± 0.006 (2 s.d.) when the detector is oriented at 90º relative to the beam axis. These findings are explained by the data presented in figure 6.2 showing that although the detector response changes in a very similar way for both diodes in the 4x4 cm^2 field, this is not the case in the clinical (0.5x0.5 cm^2) field.

Figure 6.3 demonstrates that the type 60023 diodes perform better when tilted in both the clinical and reference fields. The on-axis $k_{Q_{0.5,4\ \mathrm{cm}}}^{0.5,4\ \mathrm{cm}}$ values for the (modified) 0.6 mm air-gap 60023 detector are closer to one (no *k* value at any angle differs more than 3% from 1.00) when calculated using diode readings obtained with the instrument tilted in both fields, rather than in the clinical field only (as is the case for the type 60017 modified detector), meaning that a PTW type 60023 density compensated small-field dosimeter requires tilting in both fields to measure dose under oblique incidence conditions. It is worth mentioning that there is a substantial increase, of about 6%, on the

$k_{Q_{0.5,4\ \mathrm{cm}}}^{0.5,4\ \mathrm{cm}}$ values of both type 60023 diodes when the dosimeters are tilted only in the clinical field at a 90º angle relative to the beam axis, compared to the $k_{Q_{0.5,4\ \mathrm{cm}}}^{0.5,4\ \mathrm{cm}}$ values calculated with the detectors aligned parallel to the beam. This result is in agreement with the MC data published by Underwood *et al* (2013a), with figure 9b of that paper showing a similar increase on the *k* value for the PTW 60012 Ediode. A possible explanation for this particularly significant effect at 90º for the 60023 diodes could be the change in the interface of the sensitive volume while the dosimeters are tilted. When the detector is conventionally aligned parallel to the beam axis most of the electrons (traveling mainly onwards) pass through a low density (i.e. 1.045 g/cm^3) material to reach the sensitive volume which is above a silicon cuboid (i.e. a material of 2.33 g/cm^3 density). When the detector is tilted at 90º relative to the beam axis, a large amount of the electrons that travel onwards need to pass through the high density silicon cuboid before reaching the sensitive volume of the dosimeter. The reason for not seeing the same effect at the rest of the detector orientations tested (i.e. the different angles) is that even when the diode is tilted at an angle of 60º relative to the beam axis, electrons (contributing to the measured dose) travel through a very similar path with the zero degrees orientation, i.e. through a low density material to reach the sensitive volume above the silicon cuboid.

Finally, by considering the graphs showing the detector response as a function of the tilting angle (relative to the beam axis) for both the 60017 and 60023 detectors (figures 6.2 and 6.4) it can be concluded that the oblique incidence affects more the diode readings in the reference, i.e. 4x4 cm^2 field, than in the small clinical 0.5x0.5 cm^2 field, the difference between the level of effect in the two fields driving the variation of $k_{Q_{0.5,4\ \mathrm{cm}}}^{0.5,4\ \mathrm{cm}}$ with detector angle when the detector is oriented obliquely in both fields.

Computational data presented in tables 6.1 and 6.2 and figure 6.5 about the $k_{Q_{0.3,4\ \mathrm{cm}}}^{0.3,4\ \mathrm{cm}}$ values, at 5 cm deep, for the four diodes tested show the importance of the volume averaging effect (strongly depended on the sensitive volume dimensions of the detector used) when measuring dose in small radiation fields. In a (very) small field, such as 0.3x0.3 cm^2, two conflicting effects substantially influence the response of a dosimeter:

over-response due to the high density (compared to the 1 g cm^{-3} density of water) of the sensitive material[1] which means a decrease in the calculated *k* value; and volume averaging effect, happening because the size of the detector is comparable to the dimensions of the photon field, which causes the on-axis *k* value to increase.

The $k_{Q_{0.3,4\ \mathrm{cm}}}^{0.3,4\ \mathrm{cm}}$ value equal to 0.894 ± 0.005 for the Original 60017 diode (~ 2% lower than the *k* in the 0.5x0.5 cm^2 field for the same detector) can be explained as the result of measuring the dose in an even smaller field using a very dense (non-corrected in terms of density compensation) detector. The high density of silicon (compared to water) plays a more dominant role than the volume averaging effect, limiting the diffusion of electrons which contribute to the measured dose, and thus causing an even greater over-response of the detector in the 0.3x0.3 cm^2 field, compared to the 0.5x0.5 cm^2 field measured in previous chapters. The (more than) 3% increase on the *k* value of the 1.6 mm air-gap type 60017 diode, between a 0.5 and a 0.3 cm square clinical field, can be attributed mainly to volume averaging.

Similarly to the modified (1.6 mm air-gap) 60017 detector, the *k* values for both type 60023 diodes see a 1.4% (no air-gap 60023 detector) and ~ 5% (0.6 mm air-gap 60023 diode) increase when switching from a 0.5 to a 0.3 cm square clinical field. This also can be explained considering the influence of the volume averaging effect, which causes the detectors to under-estimate more the measured dose in the smaller (i.e. 0.3x0.3 cm^2) field and therefore, pushes the calculated *k* values higher, especially for the slightly over-corrected modified (0.6 mm air-gap added) 60023 detector. Finally, the calculated $k_{Q_{0.3,4\ \mathrm{cm}}}^{0.3,4\ \mathrm{cm}}$ correction factors of the two modified detectors (60017 and 60023) differ by 5%, the detector with the thinner air-gap (0.6 mm for the type 60023 versus 1.6 mm for the type 60017) requiring as a correction the higher value of the two. At first sight this is surprising, but it can be explained by the fact that the type 60023 modified diode is

[1] And of other non-sensitive materials in the close proximity of the active volume as well, as discussed in chapter 1.

overall a "less dense"[2] detector compared to the type 60017 modified one, and it also has a slightly wider sensitive volume, increasing volume-averaging.

6.5 Conclusions

The MC results presented in this chapter, regarding the oblique incidence, demonstrate that the 1.6 mm air-gap modified 60017 diode performs substantially better when tilted in the clinical field and oriented at zero degrees (relative to the beam axis) in the reference field, while the on-axis $k_{Q_{0.5,4\text{ cm}}}^{0.5,4\text{ cm}}$ values for (un-modified) Original 60017 diode lie far from one, regardless of the detector orientation in either the small or the reference field. In contrast, the type 60023 diodes perform better when the detectors are tilted in both the clinical and machine-specific reference fields, with computational on-axis $k_{Q_{0.5,4\text{ cm}}}^{0.5,4\text{ cm}}$ results for the no air-gap and 0.6 mm air-gap diodes suggesting that a detector with an intermediate air-gap and tilted in both fields would work best.

The 6 MV computationally-calculated on axis $k_{Q_{0.3,4\text{ cm}}}^{0.3,4\text{ cm}}$ correction factors show that the PTW 60017 Original diode over-responds even more in this smaller field (compared to the 0.5x0.5 cm^2 field). On the contrary, the $k_{Q_{0.3,4\text{ cm}}}^{0.3,4\text{ cm}}$ value for the 1.6 mm air-gap 60017 detector is about 3.2% higher than the correction factor calculated for the same detector, at the same depth, in a 0.5x0.5 cm^2 clinical field (figure 6.5). The $k_{Q_{0.3,4\text{ cm}}}^{0.3,4\text{ cm}}$ values for the type 60023 detectors are higher compared to the values calculated for a 0.5x0.5 cm^2 clinical field, relative to a 4x4 cm^2, due to volume averaging, and MC calculations show that the no air-gap detector performs best, with a *k* value very close to 1.00 (i.e. 0.993 ± 0.006).

[2] The type 60023 diodes contain more materials with densities closer to 1 g cm^{-3} compared to the type 60017 detectors, in which materials with densities significantly higher than one exist in the close proximity of the sensitive volume.

Chapter 7

Conclusions and further work

In the course of this project two different sets of unshielded silicon diodes (PTW Type No. 60017 and 60023 diode detectors) have been both experimentally and computationally characterised at 6 and 15 MV. This work investigates the consequences of deliberately introducing thin air-gaps above the sensitive volume of silicon diodes, based on the "mass-density compensation" method (Underwood *et al* 2012, 2013b), trying to identify the optimum air-gap thickness for a correction-free density compensated diode detector, suitable for dosimetry in small non-equilibrium radiation fields. Unlike the work of Charles *et al* (2014), where a removable and adjustable "air-cap" was used to improve the response of the PTW 60017 Original diode, all the modified diodes characterised within this project were built with an air-gap between the main body of the detector and its RW3 outer casing, resulting in a "compact" density compensated silicon diode detector.

A set of density-compensated detectors based on the no air-gap PTW 60017 Original diode (first set of diodes) was tested, but with narrower 3.6 mm wide air-gaps compared to the 4.7 mm wide air-gap diodes characterised by Underwood *et al* (2015), followed by the detailed characterisation of a new improved set of PTW type 60023 silicon diodes. This thesis provides a more comprehensive experimental and computational testing of the performance of the PTW diode detectors compared to the work done by previous groups (Charles *et al* 2014, Underwood *et al* 2015): detectors' on- and off-axis response was evaluated at 5 and 15 cm depths in both 6 and 15 MV beams, using a 4×4 cm^2 reference field rather than the 10×10cm^2 field of Underwood *et al* 2015 to minimize spectral effects. Furthermore, MC calculations were completed investigating the on-axis response of selected detectors in a very small (i.e. 0.3x0.3 cm^2) field and at the centre of

a 0.5x0.5 cm^2 field with the dosimeters oriented at a range of angles relative to the beam axis.

Chapter 3 of this thesis demonstrated that detector response improves substantially via the air-gap based "mass-density compensation" principle (Underwood *et al* 2013b), confirming findings from previous groups (Charles *et al* 2013, 2014 and Underwood *et al* 2015). Results presented in the same chapter for the on-axis *k* correction factors for the (no air-gap) PTW 60017 Original and the 1 mm air-gap "old" Prototype diodes agree within ± 1% with the values reported by Underwood *et al* (2015) for the same detectors, after allowing for a change in calibration field from 10x10 to 4x4 cm^2. However, the detailed characterisation of the modified PTW type 60017 diodes revealed unexpected design issues, regarding non-sensitive materials of the detectors, which led to unexpected results: experimental on-axis *k* values did not vary monotonically with air-gap thickness. This caused substantial discrepancies between experimentally-determined and computationally-calculated *k* values in a 0.5x0.5 cm^2 field, since the computationally-derived *k* values did vary monotonically with air-gap. These discrepancies existed both at 5 and 15 cm deep in water, and made it impossible to identify in reality the optimum air-gap thickness for the type 60017 detectors.

However, the experimental and MC results presented in Chapter 3 did show that the detectors which performed well on- and off-axis at 5 cm deep (i.e. *k* values lie within about ± 2% of 1.00), also worked well at 15 cm deep in water, both on and off the beam central axis. The latter finding is of great importance because it means that there is a potential to use the same small-field dosimeter to accurately determine dose at various depths in water and positions across the measured field.

The conclusions of Chapter 4 are twofold. Firstly, 15 MV experimentally-determined on axis *k* factors for the modified type 60017 diodes varied in the same way – i.e. not monotonically with air-gap thickness – as in a 6 MV beam, at depths of both 5 and 15 cm. This confirms the existence of significant design issues in the type 60017 modified detectors, and at the same time confirms the experimental findings at 6 MV. Secondly, both experimental and computational results of this chapter indicate that the PTW 60017 detectors behave quite similarly at 6 and 15 MV, on and off-axis. The detectors that

work well at 6 MV perform well at 15 MV too, and thus the (air-gap based) density compensation method is validated at this substantially higher beam energy, with the only difference being the slightly larger (small-field) effects due to the existence of electrons with higher energies that travel further in water compared to ones produced by a 6 MV beam.

Following the testing of the PTW type 60017 diode detectors and considering the results of Chapters 3 (6 MV) and 4 (15 MV), PTW made fundamental modifications to the design of the first set of detectors, leading to the second set of silicon diodes, i.e. the PTW Type No. 60023 detectors, characterised within this project. The experimental and computational evaluation of the performance of the type 60023 diodes was the subject of Chapter 5 in this thesis.

Three main conclusions can be deduced from the results presented in Chapter 5. Firstly, experimentally-determined on-axis *k* values for these detectors increase progressively while the air-gap thickness increases and they are in agreement with the MC results both at 6 and 15 MV, at both depths in water, indicating that there are no issues with the design of the type 60023 diodes. In addition, by using more materials with densities closer to 1 g cm^3 (i.e. the density of water) and better controlling the thicknesses of any non-water equivalent materials the overall design of the new PTW diodes was substantially improved, which is proven by the fact that the zero air-gap 60023 diode requires on-axis *k* correction factors considerably closer to 1.00 than those required for the PTW 60017 Original diode in all the small (clinical) fields measured. Secondly, both the (un-modified) no air-gap and 0.6 mm air-gap type 60023 diodes perform well when used as small-field dosimeters with none of their (either experimentally-determined or computationally-calculated) *k* values differing more than ~ 4% from one. In general, both computational and experimental results demonstrate that the no air-gap 60023 detector marginally outperforms the modified (0.6 mm air-gap) 60023 diode. MC results show the no air-gap 60023 diode responding correctly to within about 2% everywhere, while the (noisier) experimental results show a maximum error of ~ 5% for the same detector. Finally, by comparing the response of these two PTW 60023 detectors it can be concluded that the no air-gap diode behaves as a slightly over-dense dosimeter, while

the 0.6 mm air-gap detector seems to be a little over-corrected, suggesting that an air-gap of around 0.3 mm may be optimal.

The last results chapter of this thesis (Chapter 6) describes the results of further computational work performed using a 6 MV beam model. MC studies of the response of specific PTW silicon diode detectors of the two sets of diodes (type 60017 and 60023 detectors) were carried out to examine even more non-standard situations. The on-axis response of the dosimeters was evaluated when they were tilted – relative to the beam axis – in either the clinical (i.e. 0.5x0.5 cm^2) field only or tilted in both the small and reference (i.e. 4x4 cm^2) fields, and then with the detectors (conventionally aligned with the beam axis) at the centre of a 0.3x0.3 cm^2 field.

In Chapter 6 a significant difference in the response of the type 60017 and 60023 diodes, regarding the oblique incidence, is highlighted; both the no air-gap and the modified (0.6 mm air-gap) PTW 60023 detectors show angular robustness if the dosimeters are tilted in both the clinical and reference fields. On the other hand, the modified (1.6 mm air-gap) 60017 PTW diode performs substantially better when tilted only in the small (clinical) field and conventionally aligned with the beam axis in the reference field, while the on-axis response of the (no air-gap) PTW 60017 Original diode, which anyway is poor with *k* values differing by ~ 9% from one, is not improved by operating obliquely either in the clinical field only, or both in the small and reference fields.

Finally, as previously discussed the un-modified (no air-gap) 60023 diode performs best overall – with on-axis *k* values being within about ± 3% (experimentally) and ± 2% (computationally) of 1.00 in a 0.5x0.5 cm^2 field – a finding that is still valid in an even smaller (i.e. 0.3x0.3 cm^2) field considering the computationally-calculated on-axis correction factor ($k_{Q_{0.3,4\ \mathrm{cm}}}^{0.3,4\ \mathrm{cm}}$ = 0.993 ± 0.006) presented in Chapter 6.

Following this detailed characterisation of the type 60017 and 60023 PTW diode detectors at 6 and 15 MV, research in the field of small-field dosimetry can potentially be taken further forward by evaluating the response of silicon diodes when a magnetic field is applied (MRI linacs), and further investigating how (and to what extent) the

electrons contributing to the measured dose are affected by the existence of the magnetic field.

In conclusion, the experimental and computational work presented in this thesis demonstrated that the (un-modified) no air-gap type 60023 PTW silicon diode is a robust and accurate small-field detector, compared to the no air-gap type 60017 PTW diode, which performs well on- and off-axis at 6 and 15 MV in fields as small as 0.5x0.5 cm^2, at both 5 and 15 cm deep in water. Furthermore, this dosimeter continues to respond accurately (on-axis k = 0.993 ± 0.006) in an even smaller (i.e. 0.3x0.3 cm^2) field, and when oriented at various angles (ranging from 0 to 90º) relative to the beam axis with the condition that the detector is tilted in both the clinical and reference fields. The inclusion of a small air-gap above the sensitive silicon, but thinner than 0.6 mm which is an over-correction, may potentially further improve detector response and more closely approach a correction-free diode detector for small-field dosimetry.

Bibliography

AAPM (2010) Stereotactic body radiation therapy: The report of AAPM Task Group 101 Med. Phys. **37** pp.4078–101

AAPM (1999) AAPM's TG-51 protocol for clinical reference dosimetry of high-energy photon and electron beams Med. Phys. **26** pp.1847–1870

Alfonso R, Andreo P, Capote R., Saiful Huq M., Kilby W., Kjäll P., Mackie T. R., Palmans H., Rosser K., Seuntjens J., Ullrich W. and Vatnitsky S. (2008) A new formalism for reference dosimetry of small and nonstandard fields *Med. Phys.* **35** pp.5179–86

Allison J., Amako K., Apostolakis J., Araujo H., Dubois P. A. and Asai M (2006) Geant4 developments and applications *IEEE Trans. Nucl. Sci.* **53** 270–8

Andreo P. and Benmakhlouf H. (2017) Role of the density, density effect and mean excitation energy in solid-state detectors for small photon fields *Phys. Med. Biol.* **62** pp.1518–32

Andreo P. (2017) The physics of small megavoltage photon beam dosimetry *Radiother. Oncol.* **126** pp.205–13

Andreo P. and Benmakhlouf H. (2018) Comment on 'Origins of the changing detector response in small megavoltage photon radiation fields' *Phys. Med. Biol.* **63** p.198001

Attix F. H. (1986a) Ionizing Radiation. *Introduction to radiological physics and radiation dosimetry* New York: Wiley

Attix F. H. (1986b) Cavity Theory. *Introduction to radiological physics and radiation dosimetry* New York: Wiley

Attix F. H. (1986c) Dosimetry by Pulse-Mode Detectors, Semiconductor Detectors for Dosimetry. *Introduction to radiological physics and radiation dosimetry* New York: Wiley

Baró J., Sempau J., Fernández-Varea J. M. and Salvat F. (1995) PENELOPE: An algorithm for Monte Carlo simulation of the penetration and energy loss of electrons and positrons in matter *Nuclear Instruments and Methods in Physics Research Section B: Beam Interactions with Materials and Atoms* **100** pp.31–46

Beddar A. S., Mason D. J. and O'Brien P.F. (1994) Absorbed dose perturbation caused by diodes for small field photon dosimetry *Med. Phys.* **21** pp.1075-79

Benmakhlouf H. and Andreo P. (2017) Spectral distribution of particle fluence in small field detectors and its implication on small field dosimetry *Med. Phys.* **44** pp.713–24

Benmakhlouf H., Sempau J. and Andreo P. (2014) Output correction factors for nine small field detectors in 6 MV radiation therapy photon beams

Bouchard H., Seuntjens J., Carrier J. and Kawrakow I. (2009) Ionization chamber gradient effects in nonstandard beam configurations *Med. Phys.* **36** pp.4654–63

Bouchard H., Seuntjens J. (2004) Ionization chamber-based reference dosimetry of intensity modulated radiation beams *Med. Phys.* **31** pp.2454–65

Boyer A. L. and Schultheiss T. (1988) Effects of dosimetric and clinical uncertainty on complication-free local tumor control *Radiother. Oncol.* **11** pp.65–71

Bragg W. H. (1912) Studies in Radioactivity New York: Macmillan

Brown F. B. (2003) *MCNP – A general Monte Carlo particle transport code* Number Version 5, Report LA-UR-03. Los Alamos National Laboratory

Burlin T. E. (1966) A general theory of cavity ionisation *Br. J. Radiol.* **39** pp.727–34

Cancer Research UK (2018) *Cancer Statistics for the UK* [online] Available at: https://www.cancerresearchuk.org/health-professional/cancer-statistics-for-the-uk [Accessed 10 Sep. 2018]

Charles P. H., Cranmer-Sargison G., Thwaites D. I., Kairn T., Crowe S. B., Pedrazzini G., Aland T., Kenny J., Langton C. M. and Trapp J. V. (2014) Design and experimental testing of air slab caps which convert commercial electron diodes into dual purpose, correction-free diodes for small field dosimetry *Med. Phys.* **41** 101701

Charles P. H., Crowe S. B., Kairn T., Knight R. T., Hill B., Kenny J., Langton C. M. and Trapp J. V. (2013) Monte Carlo-based diode design for correction-less small field dosimetry *Phys. Med. Biol.* **58** pp.4501–12

Cranmer-Sargison G., Weston S., Evans J. A., Sidhu N. P. and Thwaites D. I. (2012) Monte Carlo modelling of diode detectors for small field MV photon dosimetry: detector model simplification and the sensitivity of correction factors to source parameterization *Phys. Med. Biol.* **57** pp.5141–5153

Clark C., Aird E., Bolton S., Miles E., Nisbet A., Snaith J., Thomas R., Venables K. and Thwaites D. (2015) Radiotherapy dosimetry audit: three decades of improving standards and accuracy in UK clinical practice and trials. *The British Journal of Radiology*, **88**(1055) p.20150251

Crop F., Reynaert N., Pittomvils G., Paelinck L., De Wagter C., Vakaet L. and Thierens H. (2009) The influence of small field sizes, penumbra, spot size and measurement depth on perturbation factors for microionization chambers *Phys. Med. Biol.* **54** pp.2951–69

Das I. J., Ding G. X. and Ahnesjö A. 2007 Small fields: Nonequilibrium radiation dosimetry *Med. Phys.* **35** pp.206-215

Ding G. X. and Ding F. (2012) Beam characteristics and stopping-power ratios of small radiosurgery photon beams *Phys. Med. Biol.* **57** pp.5509–21

Derreumaux S., Etard C., Huet C., Trompier F., Clairand I., Bottollier-Depois J. F., Aubert B. and Gourmelon, P. (2008) Lessons from recent accidents in radiation therapy in France *Rad. Prot. Dosim.* **131** pp.130–5

Fenwick J. D., Georgiou G., Rowbottom C. G., Underwood T. S. A., Kumar S. and Nahum A. E. (2018a) Origins of the changing detector response in small megavoltage photon radiation fields *Phys. Med. Biol.* **63** 125003 (13pp.)

Fenwick J. D., Georgiou G., Rowbottom C. G., Underwood T. S. A. and Kumar S. (2018b) Reply to comment on 'origins of the changing detector response in small megavoltage photon radiation fields' *Phys. Med. Biol.* **63** 198002 (5pp.)

Francescon P., Beddar S., Satariano N. and Das I. J. (2014) Variation of $k_{Q_{clin},Q_{msr}}^{f_{clin},f_{msr}}$ for the small-field dosimetric parameters percentage depth dose, tissue-maximum ratio, and off-axis ratio *Med. Phys.* **41** 101708

Francescon P., Kilby W., Satariano N. and Cora S. (2012) Monte Carlo simulated correction factors for machine specific reference field dose calibration and output factor measurement using fixed and iris collimators on the CyberKnife system *Phys. Med. Biol.* **57** pp.3741–58

Francescon P., Cora S. and Satariano N. (2011) Calculation of $k_{Q_{clin},Q_{msr}}^{f_{clin},f_{msr}}$ for several small detectors and for two linear accelerators using Monte Carlo simulations *Med. Phys.* **38** pp.6513–6527

Gray L. H. (1936) An ionization method for the absolute measurement of gamma-ray energy *Proc. R. Soc.* **A156** pp.578–96

Gray L. H. (1929) The absorption of penetrating radiation *Proc. R. Soc.* **A122** pp.647–68

Hamilton A. J., Lulu B.A., Fosmire H., Stea B. and Cassady J.R. (1995) Preliminary clinical experience with linear accelerator-based spinal stereotactic radiosurgery *Neurosyrgery* **36** pp.311-19

IAEA (2017) *Dosimetry of Small Static Fields Used in Radiotherapy: An International Code of Practice for Reference and Relative Dose Determination* Technical Report Series 484 (Vienna: International Atomic Energy Agency)

IAEA (2016) *Accuracy Requirements and Uncertainties in Radiotherapy* IAEA Human Health series No. 31 (Vienna: International Atomic Energy Agency)

IAEA (2000) *Absorbed Dose Determination in External Beam Radiotherapy: An International Code of Practice for Dosimetry Based on Standards of Absorbed Dose to Water* Technical Report series 398 (Vienna: International Atomic Energy Agency)

ICRU (1998) *Fundamental Quantities and Units for Ionising Radiation* Report vol. 60 (Bethesda, MD: International Commission on Radiation Units and Measurements)

ICRU (1984) *Radiation Dosimetry; Electron Beams with Energies Between 1 and 50 MeV* Report vol. 35 (Bethesda, MD: International Commission on Radiation Units and Measurements)

ICRU (1980) *Ratiadion Quantities and Units* Report vol. 33 (Bethesda, MD: International Commission on Radiation Units and Measurements)

IPEM (2010) *Small field MV photon dosimetry Report* vol. 103 (York, UK: Institute of physics and Engineering in Medicine)

IPSM (1990) Code of Practice for high-energy photon therapy dosimetry based on the NPL absorbed dose calibration service *Phys. Med. Biol.* **35** pp.1355–60

Jabbari K., Anvar H. S., Tavakoli M. B. and Amouheidari A. (2013) Monte Carlo Simulation of Siemens ONCOR Linear Accelerator with BEAMnrc and DOSXYZnrc Code *Journal of Med. Signals & Sensors* **3** (8pp.)

Jenkins T. M., Nelson W. R., Rindi A., Nahum A. E. and Rogers D. W. O. (ed) 1988 Monte Carlo Transport of Electrons and Photons (New York: Plenum Press)

Kawrakow I., Mainegra-Hing E., Rogers D. W. O., Tessier F. and Walters B. R. B. (2011) *NRCC Report PIRS-701*; The EGSnrc code system: Monte Carlo simulation of electron and photon transport (Ottawa: National Research Council of Canada)

Kawrakow I., Mainegra-Hing E. and Rogers D. W. O. (2006) *NRCC Report Pirs-877*; EGSnrcMP: The Multi-Platform Environment for EGSnrc (Ottawa: National Research Council of Canada)

Kawrakow I. (2005) *NRCC Report PIRS-899*; egspp: the EGSnrc C++ class library (Ottawa: National Research Council of Canada)

Khan F. M. (2010a) Part III: Modern Radiation Therapy, Intensity modulated Radiation Therapy – The physics of radiation therapy 4th ed. Philadelphia: Lippincott Williams & Wilkins

Khan F. M. (2010b) Part III: Modern Radiation Therapy, Stereotactic Radiosurgery – The physics of radiation therapy 4th ed. Philadelphia: Lippincott Williams & Wilkins

Knoll G. F. (2010a) Chapter 11: Semiconductor Diode Detectors – Radiation detection and measurement 4th ed. Hoboken, N.J.: Wiley

Knoll G. F. (2010b) Chapter 8: Scintillation Detector Properties – Radiation detection and measurement 4th ed. Hoboken, N.J.: Wiley

Landau D. P., Binder K. (2009) A guide to Monte Carlo simulations in statistical physics 3rd ed. Cambridge: Cambridge University Press

Lewis D., Micke A., Yu X. and Chan M. F. (2012) An efficient protocol for radiochromic film dosimetry combining calibration and measurement in a single scan *Med. Phys.* **39 (10)** pp.6339–50

Li S., Rashid A., He S. and Djajaputra D. (2004) A new approach in dose measurement and error analysis for narrow photon beams (beamlets) shaped by different multileaf collimators using a small detector *Med. Phys.* **31** pp.2020–32

Lo S. S., Bin S. T., Jiade J. L. and Schefter T. E. (2012) Introduction. Stereotactic Body Radiation Therapy Berlin: Springer

McKerracher C. and Thwaites D. I. (2002) Verification of the dose to the isocentre in stereotactic plans *Radiother. Oncol.* **64** pp.97–107

McKerracher C. and Thwaites D. I. (1999) Assessment of new small-field detectors against standard-field detectors for practical stereotactic beam data acquisition *Phys. Med. Biol.* **44** pp.2143–60

Micke A., Lewis D. F. and Yu X. (2011) Multichannel film dosimetry with nonuniformity correction Med. Phys. **38(5)** pp.2523–34

Mobit P. N., Nahum A. E. And Mayles P. (1997) A Monte Carlo study of the quality dependence of diamond thermoluminescent dosimeters in radiotherapy beams *Phys. Med. Biol.* **42** pp.1913–27

Nahum A. E. (2009) Cavity theory, stopping-power ratios, correction factors *AAPM Summer School Proc.*, Clinical Dosimetry Measurements in Radiotherapy (ed.) D. W. O. Rogers and J. E. Cygler *Madison, WI: Medical Physics Publishing* pp.91–136

Nahum A. E. (2007) Principles and basic concepts in radiation dosimetry. *Handbook of Radiotherapy Physics—Theory and Practice* (ed.) P. Mayles, A. E. Nahum and J. C. Rosenwald London: Taylor and Francis

Nahum A. E. (1978) Water / air mass stopping power ratios for megavoltage photon and electron beams *Phys. Med. Biol.* **23** pp.24–38

Office for National Statistics UK (2018) Deaths - Office for National Statistics [online] Available at: https://www.ons.gov.uk/peoplepopulationandcommunity/birthsdeathsandmarriages/deaths [Accessed 10 Sep. 2018]

Pantelis E., Moutsatsos A., Zourari K., Petrokokkinos L., Sakelliou L., Kilby W., Antypas C., Papagiannis P., Karaiskos P. and Georgiou E (2012) On the output factor measurements of the CyberKnife iris collimator small fields: experimental determination of the $k_{Q_{clin},Q_{msr}}^{f_{clin},f_{msr}}$ factor for microchamber and diode detectors *Med. Phys.* **39** pp.4875–85

Papaconstadopoulos P., Hegyi G., Seuntjens J. and Devic S. (2014) A protocol for EBT3 radiochromic film dosimetry using reflection scanning *Med. Phys.* **41** 122101 (6pp.)

Physics NIST (2018) *Stopping Power and Range Tables for Electrons* [online] Available at: https://physics.nist.gov/cgi-bin/Star/e_table.pl [Accessed 15 Sep. 2018]

PTW (2018) Ionizing Radiation Detectors, Including Codes of Practice; *PTW Manual* (Freiburg, Germany)

Rogers D. W. O., Walters B. and Kawrakow I. (2011) *NRCC Report No. 0509 (A) rev L*; BEAMnrc Users Manual (Ottawa: National Research Council of Canada)

Rogers D. W. O. (2006) Fifty years of Monte Carlo simulations for medical physics *Phys. Med. Biol.* **51** pp.R287–R301

Sánchez-Doblado F., Andreo P., Capote R., Leal A., Perucha M., Arráns R., Núnez L., Mainegra E., Lagares J. I. and Carrasco E. (2003) Ionization chamber dosimetry of small photon fields: a Monte Carlo study on stopping-power ratios for radiosurgery and IMRT beams *Phys. Med. Biol.* **48** pp.2081–99

Scott A. J. D., Kumar S., Nahum A. E. and Fenwick J. D. (2012) Characterizing the influence of detector density on dosimeter response in non-equilibrium small photon fields *Phys. Med. Biol.* **57** pp.4461–76

Scott A. J. D., Nahum A. E. and Fenwick J. D. (2008) Using a Monte Carlo model to predict dosimetric properties of small radiotherapy photon fields *Med. Phys.* **35** pp.4671–84

Solberg T. D., Siddon R. L. and Kavanagh B. (2012) Historical Development of Stereotactic Ablative Radiotherapy. Stereotactic Body Radiation Therapy Berlin: Springer

Spencer L. V. and Attix F. H. (1955) A theory of cavity ionization *Radiation Research* **3** pp.239–54

Stark R. (2007) The Status and Future of Medical and Industrial Accelerator Technologies *IEEE International Vacuum Electronics Conference*

Timmerman R. D. and Kavanagh B. D. (2005) Stereotactic Body Radiation Therapy *Curr. Probl. Cancer* **29** pp.120–57

Tsoulfanidis N. (1995) Measurement and detection of radiation 2nd ed. Washington, DC: Taylor & Francis

Uematsu M., Shioda A., Tahara K., Fukui T., Yamamoto F., Tsumatori G., Ozeki Y., Aoki T., Watanabe M. and Kusano S. (1998) Focal, high dose, and fractionated modified stereotactic radiation therapy for lung patients: a preliminary experience *Cancer* **82** pp. 1062–70

Underwood T. S. A., Thompson J., Bird L., Scott A. J. D., Patmore P., Winter H. C., Hill M. A. and Fenwick J. D. (2015) Validation of a prototype DiodeAir for small field dosimetry *Phys. Med. Biol.* **60** pp.2939–53

Underwood T. S. A., Winter H. C., Hill M. A. and Fenwick J. D. (2013a) Detector density and small field dosimetry: integral versus point dose measurement schemes *Med. Phys.* **40** 082102 (16pp.)

Underwood T. S. A., Winter H. C., Hill M. A. and Fenwick J. D. (2013b) Mass-density compensation can improve the performance of a range of different detectors under non-equilibrium conditions *Phys. Med. Biol.* **58** pp.8295–310

Underwood T. S. A. (2013) The dosimetry of small, megavoltage photon fields: correction factors, dose area products and detector designs Ph.D., University of Oxford

Underwood T. S. A., Winter H. C., Fenwick J. D. and Hill M. A. (2012) OC-0512 modifying detector designs for small field dosimetry *Radiother. Oncol.* **103** S206

Williams J. and Thwaites D. I. (2000) Radiotherapy physics: In practice. 2nd ed. Oxford: Oxford University Press

Wulff J., Zink K. and Kawrakow I. (2008) Efficiency improvements for ion chamber calculations in high energy photon beams Med. Phys. **35** pp.1328-36

Yu C. X. (1995) Intensity-modulated arc therapy with dynamic multileaf collimation: an alternative to tomotherapy *Phys. Med. Biol.* **40** pp.1435-49